DISSERTATION

THE EFFECTS OF ENVIRONMENTAL FLOW ON THE INTERNAL DYNAMICS OF TROPICAL CYCLONES

Submitted by

Gabriel Jason Williams, Jr.

Department of Atmospheric Science

In partial fulfillment of the requirements

For the Degree of Doctor of Philosophy

Colorado State University

Fort Collins, Colorado

Summer 2012

Doctoral Committee:

Advisor: Wayne H. Schubert

Sue van den Heever
Eric D. Maloney
Gerhard Danglemayr

ABSTRACT

THE EFFECTS OF ENVIRONMENTAL FLOW ON THE INTERNAL DYNAMICS OF TROPICAL CYCLONES

This dissertation focuses on two projects that examine the interaction between the internal dynamics of tropical cyclones and the large-scale environmental flow using a hierarchy of numerical model simulations.

Diabatic heating from deep moist convection in the hurricane eyewall produces a towering annular structure of elevated potential vorticity (PV) called a hollow PV tower. For the first project, the three-dimensional rearrangement of hurricane-like hollow PV towers is examined in an idealized framework. For the adiabatic PV tower in the absence of environmental flow, barotropic instability causes air parcels with high PV to be mixed into the eye preferentially at lower levels, where unstable PV wave growth rates are the largest. When the diabatic forcing is included, diabatic PV production accompanies the inward mixing at low levels, and similarly diabatic PV destruction accompanies the outflow at upper-levels. The largest variation in PV is produced when the diabatic forcing is placed within the radius of maximum winds (RMW) due to its ability to efficiently extract kinetic energy from the specified heating source.

For the adiabatic PV tower in vertical shear, the initial response of the vortex to the vertical shear is to tilt downshear and rotate cyclonically about the mid-level center. The cyclonic precession of the vortex around the center demonstrates the existence of an azimuthal wavenumber-1

quasimode that prevents the vertical alignment of the vortex. When the effects of diabatic forcing are included, the increase in inertial stability causes the resonant damping of the quasimode to become more efficient, leading to the emission of sheared vortex Rossby waves (VRWs) and vortex alignment. Generally, it is shown that the vortex response to vertical shear depends sensitively on the Rossby deformation radius, Rossby penetration depth, and the vortex beta Rossby number of the vortex.

For the second project, we examine the development of shock-like structures in the tropical cyclone boundary layer for a stationary and slowly moving tropical cyclone. Using a twodimensional slab boundary layer model and a three-dimensional boundary layer model, we show that both boundary layer models approximate the nonlinear viscous Burgers' equation in the tropical cyclone boundary layer. For the stationary tropical cyclone, radial inflow creates a circular shock near the surface while vertical mixing communicates the shock throughout the boundary layer. The peak Ekman pumping occurs at a height of 600 m, which is also the location of maximum turbulent transport, consistent with Hurricane Hugo (1989). For a moving TC, the asymmetry in the frictional drag causes an asymmetry in the boundary layer response. As the translation speed of the TC increases, the nonlinear asymmetric advective interactions amplify, leading to an anticyclonic spiral in the vertical velocity field and pronounced inflow in the right-front quadrant of the storm.

ACKNOWLEDGEMENTS

First and foremost, I am grateful to my advisor, Dr. Wayne Schubert for his advice, support, and ability to explain the dynamics of nonlinear atmospheric processes in simple terms. I would like to thank my committee members, Dr. Sue van den Heever, Dr. Eric Maloney, and Dr. Gerhard Dangelmayr, for serving and for their helpful comments during this research.

Numerous people have provided comments and assistance in this research. I thank the current and former members of the Schubert research group staff for their comments and assistance: Mr. Brian McNoldy, Mr. Richard Taft, and Mrs. Gail Cordova. I am particularly grateful to Mr. Richard Taft for providing computer and programming assistance over the course of this research. I also thank the current and former Schubert research group for their useful discussions, in particular, Dr. Jonathan Vigh, Dr. Kate Musgrave and Dr. Levi Silvers for introducing me to hurricane dynamics and providing numerous discussions on atmospheric dynamics.

Finally, I would like to thank my family and friends for their support. In particular, I would like to express my deepest gratitude to my wife Alicia Williams for her patience and support and I would like to thank my extended church family for their prayers and support throughout this long process. Financial support for this research has been provided by the National Science Foundation under the Science and Technology Center for Multi-Scale Modeling of Atmospheric Processes (CMMAP), managed by Colorado State University cooperation agreement No. ATM-0425247.

TABLE OF CONTENTS

Chapter 1

INTRODUCTION

1.1 Motivation

Significant progress has been made in the last two decades in the studies of tropical cyclone (TC) structure and intensity changes, especially those processes in the TC inner core region. The dynamics of the TC core is believed to be the key to TC structure and intensity changes. Some important internal processes are wave-mean flow interaction due to convectively coupled vortex Rossby waves (Montgomery and Kallenbach, 1997; Moller and Montgomery, 1999), potential vorticity (PV) mixing between the eyewall and eye (Schubert et al., 1999; Kossin and Schubert, 2001; Montgomery et al., 2002), vortex Rossby-wave breaking and inner spiral rain bands (Guinn and Schubert, 1993; Chen and Yau, 2001; Wang 2008), and eyewall replacement cycles (Willoughby et al., 1982; Houze et al., 2007).

Although studies in recent years have revealed the role of inner core dynamics in TC genesis, structure, and intensity changes, most of them have been limited to dry dynamics or idealized simulations with full physics models in the absence of environmental flow. Future studies are required to understand the response of the internal dynamics and the TC intensity to environmental forcing. However, no studies in the literature focus on the effect of PV mixing and the propagation of VRWs in the inner core of TCs as a means of understanding the dynamical mechanisms that cause TCs to intensify in response to environmental forcing. This study outlines a research strategy for addressing these issues. First, this study will examine the evolution of inner core asymmetries of a sheared vortex from a purely adiabatic sense in order to isolate the dry dynamics since previous

work has demonstrated that there is an intrinsic ability of the vortex to dampen its tilt and precession frequency without the presence of moisture (Schecter et al. 2002; Reasor et al. 2004). Secondly, this study will examine the effect of diabatic forcing on the evolution of inner core asymmetries of a sheared vortex.

1.2 Vortex Rossby Wave Theory and Applications

Geophysical vortices commonly arise and often persist for lengthy intervals in the atmosphere and ocean, especially in circumstances influenced by Earth's rotation and stable density stratification. A central component in vortex dynamics is the fact that perturbed vortices with smooth and approximately monotonic radial vorticity profiles tend to relax back towards a stationary state with decay of the asymmetric components and accompanying changes in the radial and vertical profiles of the azimuthal vertical flow. This relaxation process is an essential feature of the persistence of vortices and is called vortex axisymmetrization. This process can be advectively nonlinear for large initial perturbations, and it is ultimately dissipative as the asymmetric components irreversibly evolve towards very small scales. For monotonic vorticity profiles, the axisymmetrization process is accompanied by outward-propagating waves whose restoring mechanism is associated with the radial gradient of vorticity. Because of their resemblance to the Rossby waves in the mid-latitude large-scale motion, these waves are termed as VRWs. A VRW can be either barotropic (2D) or baroclinic (3D) (see Figure 1.1). Each is excited by deforming the mean PV distribution with a specific pair of vertical (m) and azimuthal (n) wave numbers. In time, the deformed PV structure spins about the vertical axis with a constant angular phase velocity ω_R/n. The wave frequency ω_R generally increases with n (Schecter and Montgomery 2004).

Tropical cyclones are localized geophysical vortices with elevated cyclonic PV concentrated in the inner core region near the RMW with large radial gradients. Any radial perturbation of an air parcel would experience a restoring force due to the presence of PV gradients and generate VRWs

in the inner core region of the TC. This concept was originally proposed by MacDonald (1968) to explain the existence of inner spiral rain bands in TCs. Guinn and Schubert (1993) provide insight into the dynamics of inner spiral bands by demonstrating that those that develop in a shallow water primitive equation model can be understood as slowly evolving sheared PV disturbances associated with the advective (low-frequency) component of the flow.

A formal theory for the propagation and interaction of VRWs with the mean flow was first presented by Montgomery and Kallenbach (1997) and later generalized by McWilliams et al. (2003). They showed that the axisymmetrization of PV anomalies, such as those generated through moist-convective processes, by the strong horizontal shear of the mean vortex was accompanied by outward-propagating VRWs that accelerated the tangential winds near the radius of wave excitation. They suggested that VRWs are responsible for the initiation of the inner spiral rainbands and can affect the structure and intensity of the mean vortex by wave-mean flow interaction. Montgomery and Enagonio (1998) and Moller and Montgomery (1999, 2000) used a three-dimensional quasi-geostrophic model and a fully nonlinear asymmetric balance model, respectively, to show that tropical cyclogenesis and intensification could occur through the axisymmetrization and ingestion of like-signed PV anomalies by a parent vortex with a monopole vorticity structure. Furthermore, through the continual injection of PV pulses (to simulate the effects of ongoing convection), Moller and Montgomery (2000) showed that an initially tropical storm-strength vortex could develop a warm core and attain hurricane strength on realistic time scales.

Tropical cyclones exhibiting monopoles of vorticity are, however, likely to occur only during the tropical storm and weak hurricane stages of development, while rapidly intensifying or mature hurricanes with well developed eyewalls usually exhibit rings of elevated PV on the inner edge of the eyewall (Kossin and Eastin 2001; Mallen et al. 2005). Using the hydrostatic primitive equations with explicit treatment of cloud microphysics, Wang (2001, 2002a,b) showed that the asymmetric structure within 70 km of the center of his modeled vortex with an annular tower of PV was dom-

inated by wavenumber 1 and 2 VRWs. Consistent with the findings of Reasor et al. (2000), the VRWs have a spiral structure in relative vorticity with maximum amplitudes near the RMW, and propagate upwind around the eyewall relative to the tangential flow of the azimuthal mean cyclone. The waves tilt outward with height and have a coherent structure in the mid-lower troposphere. Similar results were found by Chen et al. (2003), who showed that the leading modes in wave activity in the core were VRWs, generated in the lower eyewall through diabatic heating. The waves were found to be well coupled to convection as the enhanced vertical velocity associated with the wave led to the appearance of inner spiral rain bands (Chen and Yau 2001; Wang 2002b). Such a coupling between the VRWs and the eyewall convection can result in polygonal eyewalls and eyewall breakdown.

Unlike their monopole vortex counterparts discussed previously, numerical simulations of vortices with annular PV rings have failed to document a consistent influence of VRWs on the intensity of the mean vortex. Chen and Yau (2001), Moller and Shapiro (2002), and Chen et al. (2003) documented maximum VRW activity near the RMW, and the transport of high angular momentum and PV by the VRWs radially inward, from the eyewall toward the eye. This inward transport of high vorticity by VRWs was associated with intensification, as the maximum tangential wind spin-up occurred just inside the RMW, causing the RMW to propagate inward with time and leading to contraction of the eyewall. On the other hand, Wang (2002b) and Chen and Yau (2003) found VRW mean flow interactions tended to inhibit strengthening as the VRWs acted to spin up the tangential winds directly in the eye and decelerate the winds at the RMW.

Given the numerous amount of numerical modeling studies dealing with VRWs in recent years, it is somewhat surprising that only a handful of observational studies have examined convective asymmetries in the core of TCs and evaluated whether they exhibit the properties of the VRWs seen in numerical models. Muramatsu (1986) documented 15 h of counterclockwise-rotating eyewall shapes in Typhoon Wynne (1980). He made an analogy between polygonal eyewalls and the

multiple vortices sometimes seen rotating around the inside of a parent tornado vortex, and noted barotropic instability as a possible cause of both phenomena. Kuo et al. (1999) and Reasor et al. (2000) documented elliptical eyewalls in Typhoon Herb (1996) and Hurricane Olivia (1994), respectively. Both studies noted elliptical eyewalls that rotated at approximately half the maximum tangential wind speed with deep convection located at the ends of the major axis of the ellipse.

The most complete observational investigation of asymmetric vorticity dynamics and VRWs in the core of a tropical cyclone was carried out by Reasor et al. (2000) in Hurricane Olivia (1994). They examined the low-wavenumber asymmetric structure and evolution of Hurricane Olivia's (1994) inner core, which has been observed by airborne dual-Doppler radar with 30-min time resolution for 3.5 h, during which the hurricane was weakening. They found that vertical shear over the hurricane core increased dramatically during the observation period, leading to an azimuthal wavenumber-1 convective asymmetry oriented along the maximum vertical shear vector. The asymmetry in relative vorticity, however, was dominated by an azimuthal wavenumber-2 feature below a height of 3 km, and by a wavenumber-1 pattern above this height. The asymmetry was characterized by a wavenumber-2 discrete vortex Rossby edge wave, which they suggested resulted from barotropic instability in the symmetric vortex. Propagation of the wavenumber-2 VRW around the eyewall offered a physical explanation for the storm eye rotation with a period of 50 min, about twice that for a parcel being advected by the azimuthal flow near the RMW around the storm. Trailing vorticity bands with radial wavelengths of 510 km were observed within about 20 km of the hurricane center. These vorticity bands were ascribed to axisymmetrizing vortex Rossby waves and might contribute to the observed rain-bands of similar radial wavelengths.

Motivated by the success of other observational studies in documenting VRWs in the core of tropical cyclones and the finding that the VRWs are well coupled to convection (Chen and Yau 2001; Reasor et al. 2000), Corbosiero et al. (2006) conducted an examination of the high spatial and temporal resolution radar dataset from Hurricane Elena (1985) to look for VRW activity. From

the study, they discovered that as the storm rapidly intensified, Elena developed a ring-like vorticity profile similar to those shown to support barotropic instability by Schubert et al. (1999) and Reasor et al. (2000), with large radial gradients of vorticity on either side of the maximum. They demonstrated that the eyewall took on an elliptical shape that rotated with the speed of a wavenumber-2 PV edge wave and the evolution of Elena's reflectivity and vorticity structure indicates that barotropic instability was realized and asymmetric mixing did occur in the core of Elena.

1.3 Mixing in Barotropically Unstable Vortices

Further complicating the dynamics in TCs with elevated rings of vorticity in the eyewall is the possibility of barotropic instability. Schubert et al. (1999) showed that an annular vorticity structure contains counter-propagating VRWs with respect to the flow on its inner and outer vorticity gradients. If these waves became phase locked, they grew in concert and led to the exponential instability of the ring, whereby the eyewall vorticity pooled into discrete areas, creating mesovortices. Depending on the initial conditions of the PV ring, the mesovortices either merged over time and relaxed to a monopole (Schubert et al. 1999; Chen and Yau 2003), or remained separate to form a quasi-steady rotating lattice of vortices that gave the appearance of elliptical (two mesovortices) or polygonal (four or more mesovortices) eyewalls (Kossin and Schubert 2001). To explain why these PV rings break down into specific mesovortex structures, Hendricks et al. (2009) explored the end states of unstable ring vortices with varying shape and structure. Figure 1.2 demonstrates the theoretical mathematical solutions to the eigenvalue problems on the top of the figure and the actual physical results from model integrations at the bottom of the picture. The theory proposed by Hendricks et al. (2009) centers around the idea that the preferential development of one wavenumber over another is determined by two new vortex parameters: a ring thickness parameter (δ), and a ratio of inner vorticity to the average vorticity inside from the center of the vortex to the edge of the ring of high vorticity (γ).

Hendricks et al. (2009) also catalogued the mesovortex end state structures of these model runs, shown in Figure 1.3. While the evolution of the initial state into a monopole in quite a number of cases is not surprising, the stable end states that yield ellipitical eyewalls, polygonal eyewalls, and mesovortices are quite interesting. These results are far more the exception than the rule, and they generally exist for rings that are of moderate thickness. For smaller γ, polygonal eyewalls are favored, whereas for larger γ, elliptical eyewalls are favored. Hendricks et al. (2009) pointed out that, in general, it is not possible to predict accurately end states analytically; however, the use of vortex minimum enstrophy and maximum entropy approaches have yielded some insight (Schubert et al. 1999). In these experiments, the asymmetric mixing by the mesovortices between the eye and eyewall brought high eyewall vorticity into the eye and low vorticity from the eye outward. To conserve angular momentum during such a rearrangement, some high eyewall vorticity was also mixed outward, taking the form of vorticity filaments, or spiral bands with VRW characteristics (Kuo et al. 1999; Schubert et al. 1999).

In uniform and favorable environments for hurricanes, the mixing and asymmetries that result from barotropic instability events can have substantial impacts on the intensity of a mature hurricane. In the idealized studies of Schubert et al. (1999) and Nolan and Montgomery (2002), it was demonstrated that barotropic instability and vorticity mixing can decrease the maximum wind speed. Nolan and Montgomery (2002) and Nolan and Grasso (2003) provided an extensive look into thermal and vorticity perturbations on tropical storm-like, Category 1 hurricane-like, and Category 3 hurricane-like vortices. They saw that these perturbations outside the core in stronger tropical cyclones generally cause a weakening. Unstable modes draw energy for their growth from the mean vortex, and all dynamical impacts can sufficiently be explained by their impact on the symmetric mode of the vortex.

Another way in which barotropic instability can weaken a hurricane was demonstrated in the high-resolution, full-physics hurricane simulations described in Yang et al. (2007). Comparing axisymmetric and 3D hurricane simulations, Yang et al. found that their 3D storm was weaker than the axisymmetric counterpart. In particular, PV mixing in the 3D simulation reduced the tilt of the eyewall, leading to downdrafts that were warmer and moister than those underneath the tilted eyewall of their axisymmetric simulation. The weaker downdrafts in the 3D simulation led to a smaller air–sea entropy deficit near the radius of maximum winds, which reduced the energy input into the storm.

Kwon and Frank (2008) showed that in a moist baroclinic vortex, the internal eddies generated from their barotropically-unstable vortex created only slight fluctuations in intensity in time. The results changed noticeably from their dry vortex (Kwon and Frank 2005), as the main energetic pathway changed from barotropic eddy processes to interactions between mean potential and mean kinetic energy. Rozoff et al. (2009) showed that diabatic processes, through low-level convergence, constantly rebuild the low-level structure of tropical cyclones. Despite that, there is still mixing during breakdown events. Using the simulations of Hurricane Bonnie by Braun (2006), Cram et al. (2007) demonstrated with trajectory analysis that eye-eyewall mixing is a fairly common phenomenon. At the lowest levels, air is advected out of the eye. That air is in turn replenished by supergradient winds that overshoot the eyewall and enter the eye. The outflow of high entropy air out of the eye, they argue, lends credence to a "superintensity" theory as suggested by Persing and Montgomery (2003) and Braun (2002). Thus, a range of hurricane models and observations implies that barotropic instability and vorticity mixing can impact hurricane intensity in a number of direct and indirect ways.

Extending the barotropic results to three-dimensions, Hendricks and Schubert (2010) examined the three-dimensional adiabatic rearrangement of two 3D annular structures of potential vorticity (one with large δ and one with small δ) called hollow PV towers. For both hollow tow-

ers, dynamic instability caused air parcels with high PV to be mixed into the eye preferentially at lower levels, where unstable PV wave growth rates are the largest. The mixing at lower and middle levels was most rapid for the breakdown of the thin hollow tower, consistent with previous barotropic results (e.g. Schubert et al. 1999; Hendricks et al. 2009). For both hollow towers, the rearrangement of PV affected the tropical cyclone structure by causing a preferential shift inward of absolute angular momentum at low levels and by causing warm anomalies in the center of the vortex. This suggests that eyewall tilt and hurricane eye temperature inversion is partially dynamically controlled.

Observational studies have confirmed the barotropic modeling results of Schubert et al. (1999) and Kossin and Schubert (2001) by documenting the existence of multiple mesovortices in the eye and substantial mixing between the eye and eyewall. Kossin et al. (2002, 2004) and Kossin and Schubert (2001) showed clear photographic and satellite imagery of low-level vortical swirls in the eyes of multiple Atlantic and Pacific basin tropical cyclones that closely resembled the long-lived mesovortices of Kossin and Schubert (2001). Using flight-level reconnaissance data, Kossin and Eastin (2001) showed that the radial profiles of vorticity and equivalent potential temperature can undergo a rapid transition from a barotropically unstable regime with maximum values of vorticity and equivalent potential temperature in the eyewall, to a stable regime with both maxima in the eye. Knaff et al. (2003) found that the development of annular hurricanes was systematically preceded by a dramatic asymmetric mixing event between the eye and the eyewall involving one or more mesovortices.

1.4 Dynamics of Sheared Adiabatic Vortices

Recent theoretical studies, however, have attempted to elucidate the role that dry-adiabatic dynamics play in the non-axisymmetric vortex response to impinging vertical shear. Using initially barotropic vortices, Jones (1995) showed that an initially tilted vortex tends to resist vertical shear

by cyclonically precessing upshear and tilting over slowly in comparison to the time scale of the differential advection. The resiliency of the vortex to the environmental shear is dependent upon the vortex size, vortex strength, and the value of the Coriolis parameter. Larger and stronger vortices at higher latitudes were all more resistant to tilt displacement than those that were smaller and weaker at lower latitudes. Jones (2000) revisited the vortex-in-shear concept with a baroclinic vortex. She found that the lower parts of the storm behaved like a barotropic vortex, but the upper parts of the storm (where the radial PV gradient is weaker) were merely advected by the background wind. The distance that the upper part of the storm moves is dependent upon the parameters discussed previously. Jones (2004) discussed resiliency mechanisms which include rotation of a tilted vortex such that when the vortex is tilted upshear the vertical shear effectively constrains and reduces the tilt, and when it is downshear the environment will enhance the tilt.

Smith et al. (2000) used quasigeostrophic arguments to explain the evolution seen in Jones (1995). They used a two-layer model to address the coupling of two vortices. The top layer was forced with a background flow while the bottom layer remained quiescent. As the top layer was advected, the bottom layer and the top layer interacted with each other and caused a mutual rotation and advection downstream. The strength of this coupling was based upon the penetration depth. As the penetration depth increased, so did the coupling. They showed that in the quasigeostrophic limit, the advection of each vortex can be expressed simply as the cross-flow caused by the symmetric component of the wind from the other vortex. However, when increasing the Rossby number to greater than unity, this interaction became more complicated as the penetration depth calculation became radially dependent upon the structure of each vortex. Despite this fact, they argue that to a first degree, vortex interaction can be explained as the cross-vortex flow induced by separate vortices across the cores of other vortices.

Recent theoretical studies explain, from different perspectives, the evolution of an initially tilted or vertically sheared geophysical vortex using VRW theory (Reasor and Montgomery 2001; Schecter et al. 2002; Reasor et al. 2004; Schecter and Montgomery 2003, 2004). In the linear VRW formalism, the precession of the vortex and its alignment can be represented as the propagation and amplitude decay of VRW disturbances that propagate on the radial potential-vorticity-gradient of the azimuthal mean vortex. For simplicity, the initial vortex is assumed to be barotropic. Depending on the mean vortex Rossby number and the ratio of the horizontal scale of the vortex to the far-field internal Rossby deformation radius, the tilt decay for TC-like vortices occurs either via outward-propagating sheared VRW disturbances or resonance damping of a VRW quasi mode (see Reasor et al. 2004 for further details). The sheared route of tilt decay is analogous to the familiar Thomson/Orr decay mechanism for sheared disturbances (Thomson 1887; Orr 1907; Montgomery and Kallenbach 1997; McWilliams et al. 2003). In the resonant damping route the tilt decay rate is proportional to the negative radial gradient of potential vorticity at a critical radius beyond the RMW, where the precession frequency of the vortex tilt matches the rotation rate of the mean azimuthal flow (see Figure 1.4 for more details).

Linear VRW theory includes the possibility of a growing tilt asymmetry. If the radial PV gradient is positive at the critical radius then the VRW representing the tilt asymmetry will grow exponentially in time, with an e-folding time scale that is comparable to the advective time scale of the vortex core (Schecter et al. 2002; Reasor et al. 2004). Reasor et al. (2004) demonstrated that this indeed occurred for the ”standard“ vortex profile used in the Jones (1995) benchmark simulation. This standard vortex, in addition to weaker versions that retain the same non-dimensional shape, form a class of idealized vortex profiles based upon Smith (1990) that were utilized in 9 out of 10 Jones (1995) simulations and 2 of the 4 simulations in Jones (2000). Here, the positive radial PV gradient at the critical radius of the Smith (1990) vortex and consequent tilt instability originates from the transition of cyclonic to anticyclonic relative vorticity not far beyond the RMW. In contrast to Jones (1995), the tilted vortices in Reasor et al. (2004) realigned because the family of vortices considered

there, including the Gaussian PV distribution, possessed monotonically decreasing radial distributions of positive PV and consequently, sufficiently negative radial PV gradients at the critical radius.

The tilt asymmetry can also grow in amplitude by a vortex-Rossby/inertia-buoyancy (RIB) wave instability. If the rotation rate of the core is sufficiently large compared to the Coriolis frequency, and if the mean radial PV gradient at the critical radius is sufficiently weak (or zero, as in the case of a pure Rankine vortex), VRW-induced phase mixing centered at the critical radius is insufficient to suppress a frequency matching with an outward-propagating inertiabuoyancy wave. The composite RIB disturbance yields an exponentially growing core tilt asymmetry whose e-folding time scale can again be comparable to the advective time scale of the vortex core (Schecter and Montgomery 2004). A sufficiently negative radial PV gradient at the critical radius, however, can suppress this instability altogether (according to linear theory), preserving asymmetric balanced flow and maintaining a nearly erect vortex (Reasor et al. 2004; Schecter and Montgomery 2004). Clearly, the stable or unstable vortex response to vertical wind shear in these idealized (adiabatic) TC models is critically dependent on its radial structure.

One major difference between the two theories still seems to be the location of the forced vertical motion. Jones (2004) finds it to be left of the vortex tilt (consistent with previous work) and finds that the tilt rotates with time whereas Reasor et al. (2004) find that the tilt is steady at downshear-left (contrary to other authors) where presumably the forced positive vertical motion is located. As Jones (2004) points out, perhaps the definition of vortex center used to define ”tilt” is critical in determining which mechanism might be working.

1.5 The Effect of Moist Convection on the Dynamics of Sheared Vortices

In tropical cyclones, latent heat release aloft and surface convergence allows for the constant regeneration of the annular ring of PV at the lowest levels of the storm through vorticity conservation

budgets. As the winds converge radially and speed up tangentially, they continually rebuild the vorticity ring inside of the RMW. Dry dynamical modeling generally does not include this heat source aloft; thus a symmetric secondary circulation that is needed to maintain the ring does not form. The radial flow accumulates moisture and heat as it traverses the ocean (Rotunno and Emanuel 1987), thus providing the moisture necessary for the latent heat release and the surface convergence to maintain the ring.

Jones (1995) demonstrated that when a vortex is sheared, there is a wavenumber-1 response of the vortex in the potential temperature fields and in the vertical velocity fields. Frank and Ritchie (1999) presented a cursory look at a full-physics vortex in both easterly and westerly vertical shear. The vertical profile they used was cosine-shaped with a magnitude of 3 m/s. They discovered that at initial times (6-12 hr), the vertical velocity field mimicked the findings of Jones (1995). As integrations progressed, the vertical columns began to saturate, and the primary vertical motion moved to the downshear-left quadrant. Maximum tangential winds became located in the upshear-left quadrant. When additional background flow was added to the storm, the storm behaved somewhat differently. There was another convective maximum in the front-right quadrant of storm motion after the storm had intensified and convection was more symmetrically distributed around the eyewall of the vortex. These results were later confirmed through the observational analysis of Corbosiero and Molinari (2002, 2003).

Frank and Ritchie (2001) readdressed the problem of a full-physics vortex in shear by modifying the shear forcing. On top of a control run, they forced the storm with 5 m/s, 10 m/s, and 15 m/s shear, respectively. In both the 5 m/s and 10 m/s cases, the storms developed convective asymmetries downshear-left and eventually weakened to an intensity that was lower than at the time at which the shear forcing was imposed. They found that the convective asymmetry precedes any appreciable tilt, arguing that the convective asymmetry is due to differential vorticity advection in the vertical caused by the shear. The 10 m/s forcing weakened the vortex about 24 hours sooner

than did the 5 m/s, whereas the 15 m/s shear tore the storm apart. They argue that the shear weakens from a top-down perspective: the shear ventilates the upper level warm core through erosion of upper-level PV. The evolution of the strength of their hurricane-like vortices and the precipitation anomalies agree with the historical perspective provided by DeMaria (1996), which states that excessive shear will almost universally weaken a storm.

An alternative theory to the top-down theory of Frank and Ritchie (2001) is the bottom-up theory proposed by Riemer et al. (2010). They use the Carnot engine analogy that was first presented by Emanuel (1986), where tropical cyclones can be thought of as an engine that expends energy gathered through sea-surface latent heat flux. They argue that enhanced downdrafts from the outflow of the storm and from the shear-induced stationary band complex (Corbosiero and Molinari 2002, 2003) cause a larger downward flux of low θ_e air already present at the mid-levels in the tropical cyclone. This drier air interferes with the low-level boundary-layer air. While this argument is thermodynamically appealing, it is not without certain limitations. As was shown in Bryan and Rotunno (2010), the model used by Riemer et al. (2010) is already prone to overly strong tropical cyclones when compared with reality, and this is likely due to improper eddy parameterizations in the boundary layer. Any conclusions drawn by Riemer et al. (2010) with regards to the boundary layer in their simulations must keep this limitation in mind.

In terms of vortex resiliency theory, when moist processes are included, the sheared TC problem becomes more complicated, but Reasor et al. (2004) argue that the tilt dynamics is still controlled in a first approximation by dry adiabatic dynamics. When a hurricane-strength barotropic vortex with a realistic Rossby deformation radius is subject to a simple tilt perturbation (azimuthal and vertical wavenumber-one asymmetry), the critical radius is found to lie between one and four RMW distances (Schecter and Montgomery 2003; Reasor et al. 2004). Guided by accepted reasoning that moist processes in the eyewall region give rise to a reduced effective static stability (e.g., Emanuel et al. 1987; Montgomery and Farrell 1992; Shapiro and Montgomery 1993), the critical

radius should reside radially inward from its dry estimate (Reasor et al. 2000). Extending these ideas to a moist vortex, Schecter and Montgomery (2007) investigated the effects of parameterized moisture on rapidly rotating vortices and discovered three basic points. First, when simulating a category 3 hurricane-like vortex, the moist physics slowed the development of its most unstable mode (wavenumber 3) compared to its dry counterpart. Second, moisture acts to suppress discrete vortex Rossby wave development and the resultant inertia-gravity wave emission by reducing the static stability at the RMW, where the vortex is most moist. Third, as a result of the second point, vortex resiliency – the resistance of the vortex to tilting – is improved.

Using a high-resolution numerical simulation of Hurricane Erin (2001), Wu and Braun (2006) and Braun and Wu (2007) investigated the response of the storm to ambient shear (here, shear is defined as the winds at 200 mb minus the winds at 850 mb). At the time of the shearing event, Erin was on the Category 2-3 threshold. The wavenumber-1 structure of precipitation did not become dominant until shear surpassed 5 m/s. They also found that there was explosive convection related to mesovortex passage through the shear zone. They argue that the reason for enhanced convection is due to convergence trailing the mesovortex caused by their induced flows and amplified by additional convergence caused by the low-level wind of the environment. They also noted that the shear is much higher in the model than it was in the observations, so that might lead to differences in the evolution of their vortex when compared with the actual observations. The displacement of the center of the storm at 9.3 km from the surface at 72 hours is 42 km. This unrealistic tilt tends to be 4 times greater than the greatest amount of tilt observed by a weaker storm in moderate shear (Reasor et al. 2009) or in observations (Corbosiero and Molinari, 2002 and 2003), where tilts are on the order of 10 km.

Davis et al. (2008) used the Advanced Research WRF to model six hurricanes in the north Atlantic from the 2005 and 2006 hurricane seasons to investigate their responses to shear as the storms underwent extratropical transition. They determined three methods through which the storms re-

sisted vertical shear. The first is vortex precession. That is, after shearing, the vortices tilted in the direction of the shear and then oriented themselves between downshear and downshear-left. The second mechanism was diabatic heating that cancelled the effect of tilting. This ultimately led to a formation of a new center downshear-left under the precipitation maximum. The third mechanism was a transient baroclinic development that occurred when an upper-tropospheric PV anomaly, such as a trough, was positioned upshear from the hurricane vortex. This produced intensification of the storm in a baroclinic sense, and the surface circulation was greatly weakened. Davis et al. (2008) also suggested that diabatic responses in sheared storms are due to PV advection associated with the tilt itself. If the vortex precesses then the diabatic processes will be favored downshear left to reduce tilt. If the vortex tilts without rotation, then the main convective band will be downtilt.

1.6 Objectives and Organization of Dissertation

The research performed in this study includes the analysis of the evolution of sheared hollow PV towers simulated in an adiabatic hydrostatic primitive equation model and in a full physics framework. Because the radial gradient of PV changes sign in a hollow PV tower, the vortex satisfies the Charney-Stern necessary condition for combined barotropic-baroclinic instability. This work will combine the work in sheared vortex dynamics of Jones (1995, 2000b, 2004), Frank and Ritchie (1999), Schecter et al. (2002), and Reasor et al. (2004) with the work in dynamical breakdown of the vortex ring of Schubert et al. (1999), Rozoff et al. (2009), and Hendricks and Schubert (2010). A variety of methods will be used to quantify the evolution of the vortices PV palinstrophy, penetration depth, vortex beta number, and Rossby deformation radius. The goals of this research are to address the following questions:

- How does inner core mixing of PV affect tilt precession?
- How do the shear forcing and the profile of shear affect the evolution of the inner-core instability?

- How do non-conservative processes, such as surface friction, vertical diffusion, and diabatic heating, affect inner core mixing of PV and tilt precession?

The vortex Rossby wave damping mechanism suggested by Reasor et al. (2004) and Schecter et al. (2002) appears to be valid in stable, monotonic vortices, which are used in their studies. In stable vortices, the asymmetries produced by vertical shear initiate waves instead of instability, and the waves (vortex Rossby waves) will eventually decay with time. However, since the PV structure of mature TCs resembles a hollow PV tower and satisfies the necessary condition for combined barotropic-baroclinic instability, it is expected that the response of the vortex to vertical shear will be somewhat different from that of a stably structured vortex, although the VRW damping mechanisms still play a role in some regions of an unstable vortex. In unstable cases the perturbations created by vertical shear tend to grow with time at the expense of the energy of a mean vortex, so the intensity of the vortex will decrease.

Chapter 2 will present the results of the adiabatic sheared hollow PV tower experiments. An overview of the model used for these experiments and the analysis techniques will be presented as well. The conclusions from these experiments will build upon the theoretical studies of dry sheared vortices mentioned previously. Chapter 3 will show the effect of diabatic forcing on the evolution of sheared PV towers. An overview of the model used for these experiments will be presented as well. The conclusions from these experiments will extend the results from Hendricks and Schubert (2010) and will also upon the theoretical studies of dry sheared vortices.

Chapters 4 and 5 will address the effect of vortex translation on the development of boundary layer jets in a tropical cyclone. Low-level wind maxima have been frequently observed in the boundary layer of tropical cyclones. Kepert (2001) and Kepert and Wang (2001) describe a physical mechanism for producing such a jet in which strong inward advection of angular momentum leads to supergradient flow. The processes that maintain the necessary inflow against the outward acceleration due to gradient wind imbalance were identified as being vertical diffusion, vertical advection,

and horizontal advection. In these chapters, the emphasis is on interpreting these observations in terms of shock-like structures that emerge from the fact that the boundary layer model contains an embedded Burgers' equation. The goals of these chapters are to address the following questions:

- How does the spatial distribution of vorticity affect the spatial distribution of Ekman pumping in the boundary layer?
- How does the thermodynamics structure of the boundary layer depend upon the translation velocity and the spatial distribution of vorticity?
- How does vortex translation affect the development of shock-like structures in the tropical cyclone boundary layer?

A historical background on the hurricane boundary layer and overview of the model used in this will be given. A summary of the work done in this research and ideas for future research will be presented in Chapter 6.

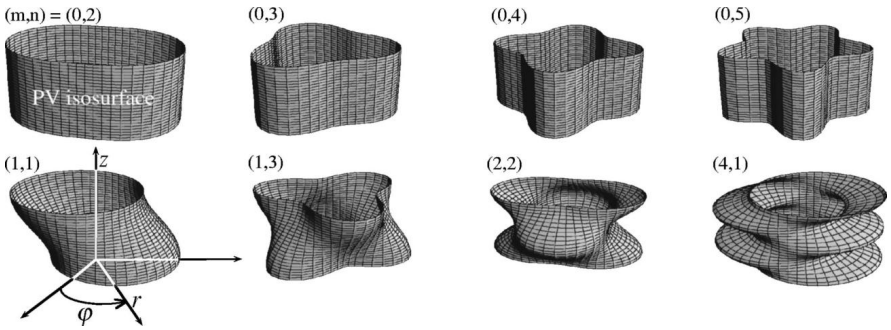

Figure 1.1: Deformed PV isosurfaces corresponding to a selection of barotropic (top row) and baroclinic (bottom row) VRWs. The wave amplitudes are exaggerated for clarity (Schecter and Montgomery 2004)

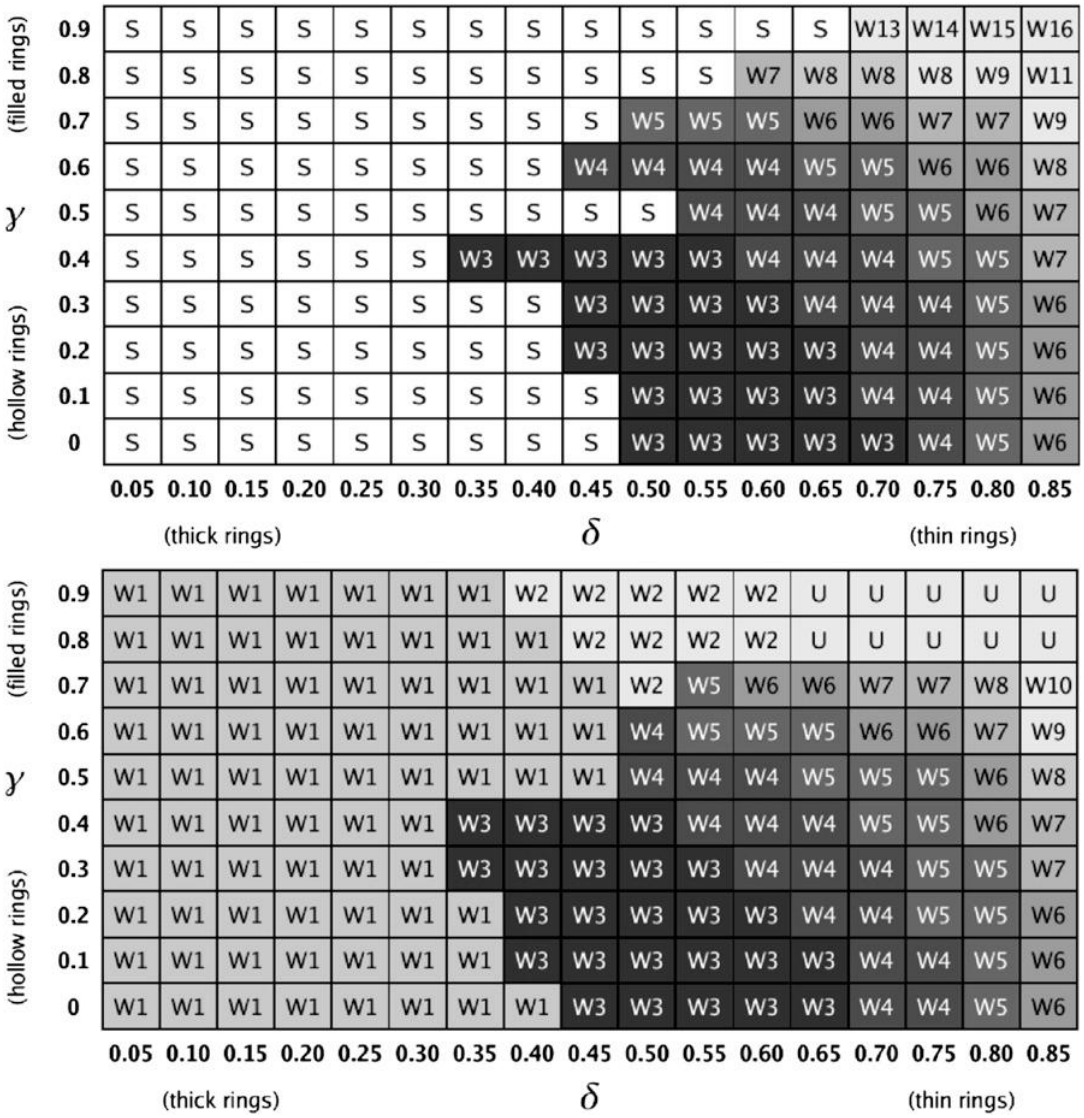

Figure 1.2: Fastest-growing wavenumber instability using the linear analysis of Schubert et al. (1999). In the top, the "S" denotes that the vortex was stable to exponentially growing perturbations of all azimuthal wavenumbers. The "U" in the bottom panel signifies that the initial wavenumber of the instability was undetermined. (Hendricks et al. 2009)

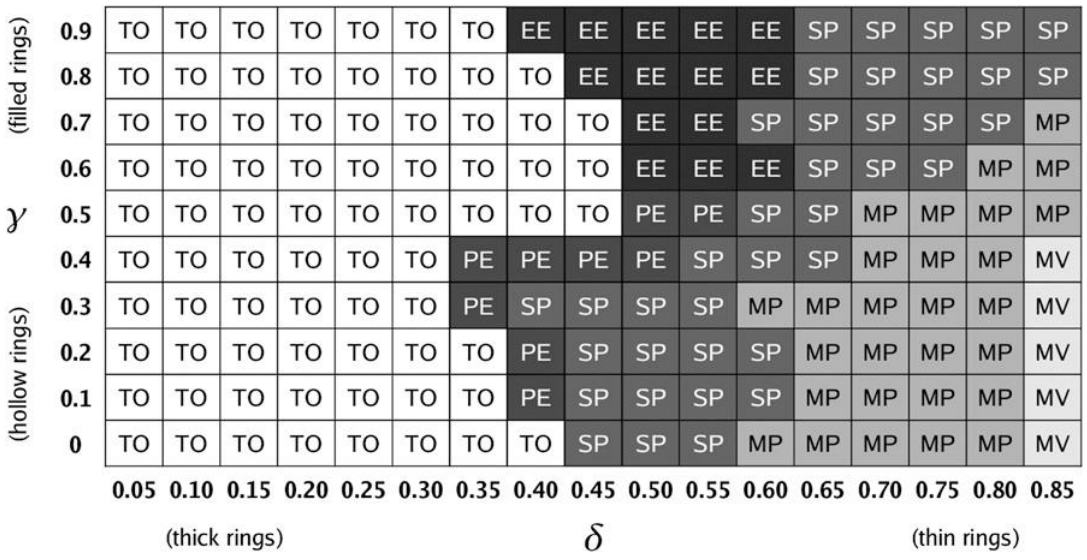

Figure 1.3: End states (t = 48 h) observed after nonlinear mixing (Hendricks et al. (2009)

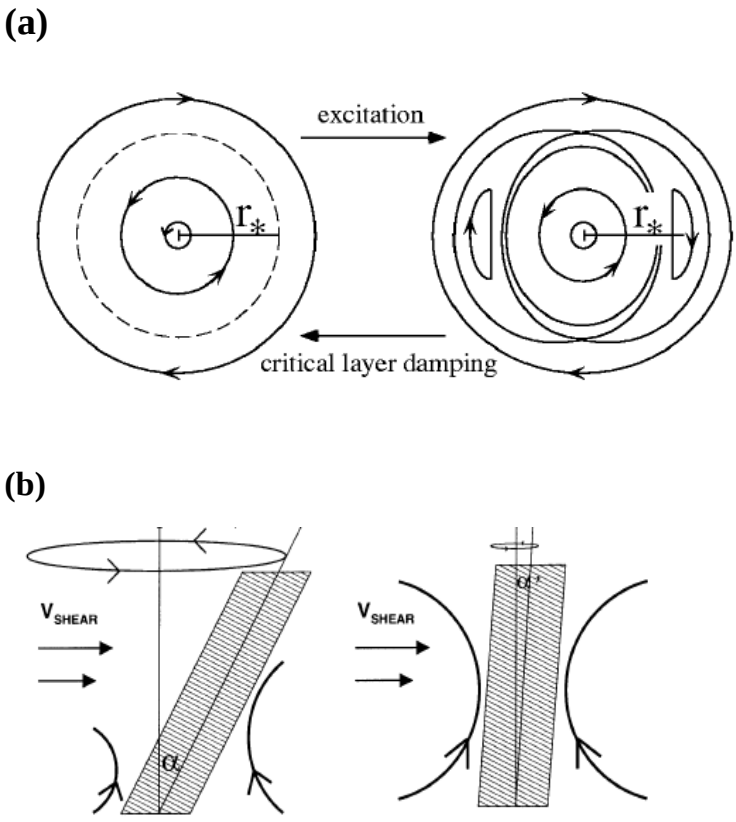

Figure 1.4: (a) Streamlines of the horizontal flow (in a rotating frame) at an arbitrary height z. Stirring of PV at the critical radius $r_\star$ causes the discrete VRW to decay, and the vortex to symmetrize. (b) Schematic of TC alignment mechanism when the TC vortex is tilted by vertical shear. VRW damping counters differential advection of the TC by the vertical shear flow by reducing the tilt angle α. For sufficiently strong VRW damping, a quasi-aligned vortex ($\alpha' \ll \alpha$) is possible.

Chapter 2

ADIABATIC SHEARED HOLLOW PV TOWERS

2.1 Methodology

2.1.1 Overview of Model

For these experiments, we consider adiabatic, quasi-hydrostatic motions of a compressible atmosphere on an f-plane. The numerical model used here is based on the three-dimensional hydrostatic primitive equations in isentropic coordinates *(x,y,θ)*, where *x* and *y* are in the zonal and meridional directions, respectively, and θ is the potential temperature. The governing equations are given by:

$$\frac{Du}{Dt} = fv - \frac{\partial M}{\partial x}, \tag{2.1}$$

$$\frac{Dv}{Dt} = -fu - \frac{\partial M}{\partial y}, \tag{2.2}$$

$$\frac{\partial \sigma}{\partial t} + \frac{\partial(\sigma u)}{\partial x} + \frac{\partial(\sigma v)}{\partial y} = 0, \tag{2.3}$$

$$\frac{\partial M}{\partial \theta} = \Pi, \tag{2.4}$$

$$\Phi(x, y, \theta) = \Phi(x, y, \theta_s) - \int_{\Pi_s}^{\Pi(x,y,\theta)} \theta d\Pi', \tag{2.5}$$

where *u* and *v* are the velocity components in the *x* and *y* directions, $\sigma = g^{-1}(\partial p/\partial\theta)$ is the pseudo-density, $M = \theta\Pi + \Phi$ is the Montgomery potential, $\Pi(p) = c_p(p/p_0)^{\kappa}$ is the Exner function, Φ is the geopotential, and *f* is the Coriolis parameter set at $5\times10^{-5}\ s^{-1}$. Since we are considering purely adiabatic motions, the material derivative simplifies to $D/Dt = \partial/\partial t + u(\partial/\partial x) + v(\partial/\partial y)$. Therefore, three-dimensional advection becomes essentially two-dimensional in θ-coordinates, which is one of the chief advantages of the isentropic coordinate system.

The model is vertically discretized using the Charney-Phillips (CP) grid. Here, the prognostic variables *u*, *v*, σ are carried on integer layers, whereas pressure and potential temperature are carried on the half-integer levels. The Lorenz (L) grid, which carries momentum and potential temperature on the same level, is not used because it has an extra degree of freedom in the vertical for potential temperature. Arakawa and Moorthi (1988) showed that a spurious amplification of short waves existed in the Lorenz grid when simulating baroclinic instability of an idealized midlatitude zonal jet. The model top is assumed to be both an isentropic and an isobaric surface, with θ_T = 360 K and p_T = 106 hPa. The lower boundary is assumed to be the isentropic surface θ_B = 298 K, along which the pressure is variable in *(x,y,t)*.

The model is horizontally discretized using the Arakawa C grid with a doubly periodic boundary horizontal domain. Since inertia-gravity waves can be generated during PV mixing, a sponge layer was used near the lateral boundaries to minimize the false reappearance of these waves in the interior region of the model. More information on the model discretization and the model characteristics can be found in Appendix A.

2.1.2 Experimental Design

Since the primary goal of this chapter is to investigate the adiabatic evolution of sheared hollow PV towers, we will examine the effect of zonal, unidirectional shear on three-dimensional

adiabatic PV rearrangement. The hollow PV tower will be based on the initial conditions from Hendricks and Schubert (2010). The initial condition for the relative vorticity has the separable form $\zeta(r,\phi,\theta) = [\zeta_{sym}(r) + \zeta_{pert}(r,\phi)]F(\theta)$, where the radial structure of the axisymmetric part is given by:

$$\zeta_{sym}(r) = \begin{cases} 0 & r \le r_1 \\ \zeta_2 S\left(\frac{r_2 - r}{r_2 - r_1}\right) & r_1 \le r \le r_2 \\ \zeta_2 & r_2 \le r \le r_3 \\ \zeta_2 S\left(\frac{r - r_3}{r_4 - r_3}\right) + \zeta_3 S\left(\frac{r_4 - r}{r_4 - r_3}\right) & r_3 \le r \le r_4 \\ \zeta_3 & r \ge r_4 \end{cases} \tag{2.6}$$

and the vertical structure is given by

$$F(\theta) = \begin{cases} 1 & \theta_B \le \theta \le \theta_{ref} \\ \exp\left[-\frac{1}{2}\left(\frac{\theta - \theta_{ref}}{20K}\right)^2 \right] & \theta_{ref} \le \theta \le \theta_T \end{cases} \tag{2.7}$$

Here, $S(s) = 1 - 3s^2 + 2s^3$ is a cubic shape function that provides smooth transition zones, and θ_{ref} = 302 K. For the hollow tower, ζ_2 = 0.00257 s^{-1} and r_1, r_2, r_3, r_4 = 23, 27, 38, 42 km, respectively. This gives a maximum initial velocity of approximately 30 m/s. Because of the doubly periodic boundary conditions, the net circulation around the domain boundary vanishes on each isentropic surface, i.e., the horizontal average of the isentropic relative vorticity vanishes on each isentropic surface. Thus, after specification of r_1, r_2, r_3, r_4, and ζ_2, the constant ζ_3 is determined in such a way as to make the domain average of $\zeta_{sym}(r)$ vanish. The unbalanced, weak perturbation used to help initiate the instability process is given by

$$\zeta_{pert}(r) = \zeta_{amp} \sum_{n=1}^{12} \cos(n\phi + \phi_n) \times \begin{cases} 0 & r < r_1 \\ \zeta_2 S\left(\frac{r_2 - r}{r_2 - r_1}\right) & r_1 < r < r_2 \\ \zeta_2 & r_2 < r < r_3 \\ \zeta_2 S\left(\frac{r - r_3}{r_4 - r_3}\right) + \zeta_3 S\left(\frac{r_4 - r}{r_4 - r_3}\right) & r_3 < r < r_4 \\ \zeta_3 & r > r_4 \end{cases} \tag{2.8}$$

where $\zeta_{amp} = 10^{-5} s^{-1}$ and ϕ_n is a random phase factor.

2.2 Control Experiment: Adiabatic Rearrangement of a Hollow PV Tower

Before discussing the nonlinear evolution of each hollow tower, it is insightful to examine how small amplitude unstable PV waves grow in each layer. The linear stability analysis of Schubert et al. (1999) indicates that, in a barotropic context, the unstable vorticity wave growth rate is a function of the average inner-core vorticity (average vorticity over the region $0 \leq r \leq r_4$), azimuthal wavenumber, ring thickness, and the ring hollowness (i.e., the ratio of eye vorticity to average inner-core vorticity). Generally speaking, the largest growth rates occur for disturbances on thinner and hollower rings, and there is also a tendency for the most unstable mode to be at a higher azimuthal wavenumber (Hendricks et al. 2009). We expect these barotropic results to be an adequate general guide to the present hollow PV tower experiments.

Since unstable wave growth rates are directly proportional to the average inner-core vorticity, then we expect that the rearrangement of PV for a baroclinic hollow PV tower will occur more rapidly near the surface than at the upper layers because the vorticity (and radial shear of the tangential wind) is larger there. Furthermore, the existence of vertical shear in the baroclinic hollow PV tower allows for the possibility of a combined barotropic-baroclinic instability with disturbance PV tilting against both the horizontal and vertical shear of the tangential wind. Since the vertical shear of the tangential wind in these vortices (and, in nature) is much smaller than the radial shear, we expect that the instability will be mostly barotropic in nature (cf. Nolan and Montgomery 2002).

The initial condition for the hollow tower for the $\theta = 304$ K and $\theta = 341$ K surfaces are shown in Fig. 2.1 and Fig. 2.2. The hollow tower was constructed with a thickness parameter $\delta = (r_1 + r_2)/(r_3 + r_4) \approx 0.625$ and an average inner-core vorticity of $\gamma = \zeta_1/\zeta_{av} = 0$. Given these parameters, Hendricks et al. (2009) suggest that this hollow PV tower will be most unstable to wavenumber-3 and will symmetrize into a monopole within 48 hours. The PV is concentrated in the radial zone of cyclonic shear and curvature vorticity between $r = 20$ and $r = 40$ km, and is maximized at 305 K, even though the vortex winds are maximum at 302 K. PV is maximized at 305 K because of the balanced pseudodensity field, which has increased static stability above the surface.

Figure 2.3 shows the unforced evolution of the PV tower at *t* = 4 hr. At this time, the most unstable wavenumber $n = 3$ is visible on the $\theta = 304$ K surface. As the inner PV wave breaks cyclonically, PV becomes pooled into three regions, and low PV air from the eye is drawn into the eyewall in the form of filaments. The growth of the unstable mode is a result of counter-propagating VRWs. The VRWs exist on the highest PV gradients of the vortex - at approximately 25 km and 40 km radius. The inner VRW is propagating with the mean flow, while the outer VRW is propagating against the mean flow due to change in radial gradient of PV.

Figure 2.4 shows the PV tower at *t* = 6 hr. As the wave-breaking stage continues, interior particles with low and intermediate PV are drawn into the high PV ring. This low and intermediate PV fluid spirals cyclonically into and carves up the high vorticity fluid in the original annular ring. Figure 2.5 shows the PV tower at *t* = 10 hr. Here we see two consequences of the withdrawal of intermediate and low PV fluid: a decrease in the area of the inner PV region and a tightening of the PV gradient on the inner edge of the PV ring. Figure 2.6 shows the PV tower at *t* = 14 hr. At this time, the central region of low PV moves off-center. The remaining patch of low PV circles the vortex approximately every 4 hours, as high PV begins to move towards the center, shown in Figure 2.7. From 20 hr to 36 hours, the patch of low PV continues to circle the vortex, while the patch of high PV settles into the vortex center, accompanied by its associated trailing spiral bands of PV

(shown in Figure 2.8 and 2.9). At this time, the PV ring at $\theta = 341$ K shows a hint of a slower growing wavenumber 3 mode. The end state of the PV tower is given in Figure 2.10. At this time, the low level PV ring has nearly symmetrized to a monopole, while the upper level ring is beginning to break down at azimuthal wavenumber 3. In response to mixing, a bridge of high PV now crosses the eye at approximately θ = 305 K. Above θ = 332 K, PV rings are just beginning to break down, but mixing has not yet occurred between the eyewall and the eye. The tangential wind structure of the end state PV tower is given in Figure 2.11. In response to mixing, the mean tangential velocity has increased in the eye region and decreased in eyewall region.

In order to quantify the nonlinear mixing event, we will use the integral quantities palinstrophy and enstrophy:

$$P = \iint \frac{\nabla\zeta \cdot \nabla\zeta}{2}\, dxdy \tag{2.9}$$

$$Z = \iint \frac{\zeta^2}{2}\, dxdy \tag{2.10}$$

In general terms, palinstrophy measures the tightness of vorticity gradients. During nonlinear mixing, palinstrophy will increase. When mixing has ceased and unstable vortices evolve to monopole states, palinstrophy will decrease. Also, there is an intimate relationship between palinstrophy, enstrophy, and energy. The two integral relations that relate palinstrophy, enstrophy, and energy are:

$$\frac{dE}{dt} = -2\nu Z \tag{2.11}$$

$$\frac{dZ}{dt} = -2\nu P \tag{2.12}$$

where $E = \iint \frac{u^2 + v^2}{2}\, dxdy$ is the energy and ν is the diffusion coefficient. The diffusion term on the right-hand side of (2.10) controls the spectral blocking associated with the enstrophy cascade to higher wavenumbers. Using these relations, an increase in palinstrophy will decrease the

enstrophy, which would indicate a less rapid decrease in energy. Figure 2.12 shows the time series of enstrophy, palinstrophy, energy, and angular momentum at θ = 305 K. During the period between 5 and 10 hours, there is an increase of palinstrophy ($\approx$ 15 percent) and an associated decay of enstrophy. During this 5 hour interval, approximately 15 percent of the original enstrophy is sent to small scales where it is dissipated. In contrast, the angular momentum and kinetic energy are nearly conserved. For example, at t = 24 h, the angular momentum, kinetic energy, and enstrophy are 99.9 percent, 98.7 percent, and 51.5 percent of their respective initial values. Between 24 and 36 hours, there is a slow decrease in palinstrophy, as the PV ring symmetrizes to a monopole.

Figure 2.13-2.15 shows the evolution of the hollow PV tower at θ = 304 K in terms of the differential form of palinstrophy. At the start, the highest values of palinstrophy are, as expected, on the edges of the ring, as the initial profile prescribes sharp vorticity gradients between the ring and the lower values of vorticity directly outside the ring. The largest values of vorticity tend to exist where the mesovortices are being sheared by the differential rotation of the vortex. Furthermore, the stretching and folding of vorticity turns the high vorticity ring into an area of enstrophy cascade, leading to a tightening of PV gradients. For this vortex, the palinstrophy maximizes at approximately 6 hours, which indicates that the horizontal nonlinear mixing maximizes at this point. As the PV tower begins to symmetrize to a monopole, the magnitude of palinstrophy begins to decrease.

The effects of internal mixing should be to lower central pressure and to lower the mean maximum tangential velocity (Kossin and Schubert 2001; Hendricks et al. 2009). The hollow tower had an initial intensity of $v_{max} = 30.9$ m/s and $p_{min} = 1014.35$ hPa. At t = 36 hours, the new values were $v_{max} = 27.25$ m/s and $p_{min} = 1001.7$ hPa. For this hollow tower, the maximum mean tangential winds and minimum central pressure decreased in tandem during PV mixing, consistent with the results from Hendricks et al. (2010).

2.3 Adiabatic Rearrangement of a Hollow PV Tower in Zonal Shear

For this experiment, we will look at the adiabatic rearrangement of PV for a hollow tower in vertical shear. This experiment is meant to simulate the conservative dynamics and resiliency of a rapidly rotating barotropically unstable vortex during an episode of external vertical shear. Previous studies (e.g., Reasor et al. 2004) have looked at the vertical alignment of a barotropic, monotonically stable vortex in the low-Rossby number (Ro ≤ 1) regime. This experiment will look at the vertical alignment of a high Rossby number (Ro ≈ 50), barotropically unstable vortex in unidirectional vertical shear.

In this experiment, we will use the same initial conditions as in the control experiment, except the background environmental wind will have the simple zonal shear:

$$U(p) = u_0 \cos\left(\pi \frac{p}{p_t}\right) \tag{2.13}$$

where p is the pressure and p_t is the pressure at the top of the model domain. Therefore, the background wind is $-u_0$ at the surface and u_0 at the model top. In order for the tilt asymmetry induced by shear to remain a perturbation on the mean vortex, we use weak shear for this experiment. Here, $u_0 = 2$ m/s.

The evolution of the hollow PV tower is shown in Figs. 2.16-2.24. At mid-levels, the speed of the vortex motion is close to the speed of the environmental flow. At the surface, the vortex moves significantly slower than the surface environmental flow. At the upper levels, the vortex moves faster than the environmental slow. In general, the vertical tilt of the vortex increases with time, but is much smaller than that which would be implied by simple advection by the basic flow. (This would lead to a separation of 518 km between the vortex center at $\theta = 298$ K and $\theta = 365$ K after 36 hours.)

Figures 2.25-2.29 looks at the PV evolution for the $\theta = 305$ K and $\theta = 341$ K surfaces. Here it can be seen that the initial motion at the surface has a northward component, while the motion of the upper-level vortex has a southward component, shown in Fig. 2.25. This results in the development of a NW-SE tilt in the vortex after 6 hours, shown in Fig. 2.26. The continued rotation then leads to the lower-level center moving southward and the upper-level center moving northwards after 20 hours, as shown in Figure 2.27. This suggests that the upper- and lower-level centers rotate cyclonically about the mid-level center. At the end of 36 hours, the vortex has developed a distinct N-S vertical tilt, with upper-level PV being advected by the shear. The results from these simulations are consistent with Wang and Holland (1996) and Jones (2000). When a baroclinic vortex is tilted by vertical shear, the initial response of the vortex to the vertical shear is to tilt downshear. The upper- and lower-level centers then began to rotate cyclonically about the midlevel center, causing both leftward and rightward movement relative to the shear vector.

Figure 2.29 shows the time series of enstrophy, palinstrophy, energy, and angular momentum at θ = 304 K. As in the control experiment, there is an increase of palinstrophy with an associated decay of enstrophy. However, the nonlinear mixing occurs earlier in the model simulation and during the mixing phase, more enstrophy is sent to smaller scales. During the period between 5 and 10 hours, there is an increase of palinstrophy ($\approx$ 15 percent) and an associated decay of enstrophy to smaller scales($\approx$ 20 percent of the original enstrophy). In contrast to the control experiment, there is a noticeable dissipation of kinetic energy. For example, at t = 24 h, kinetic energy and enstrophy are 91.2 percent and 54.4 percent of their respective initial values. Between 24 and 36 hours, there is a slow decrease in palinstrophy, as the PV ring symmetrizes to a monopole. This suggest that shear forcing has an effect on nonlinear mixing and enstrophy cascade.

Figure 2.30-2.33 shows the evolution of the hollow PV tower at θ = 304 K in terms of the differential form of palinstrophy. At the start, the highest values of palinstrophy are, as expected, on the edges of the ring, as the initial profile prescribes sharp vorticity gradients between the ring

and the lower values of vorticity directly outside the ring. In contrast, the palinstrophy maximizes at approximately 5 hours, indicating that shear forcing causes horizontal nonlinear mixing to occur earlier. Because more enstrophy is sent to smaller scales, the vortex symmetrizes quicker to a monopole state, causing a rapid decrease in palinstrophy.

As in the control experiment, the effects of internal mixing should be to lower central pressure and to lower the mean maximum tangential velocity (Kossin and Schubert 2001; Hendricks et al. 2009). The hollow tower had an initial intensity of $v_{max} = 30.9$ m/s and $p_{min} = 1014.35$ hPa. At *t* = 36 hours, the new values were $v_{max} = 22.6$ m/s and $p_{min} = 1001.3$ hPa. For the vortex in shear simulation, there was a greater decrease in maximum tangential velocity mostly likely due to the dissipation of kinetic energy in the vortex.

Contrary to prior studies on vortex alignment, the upper-level vortex anomalies began to develop independently from the lower-level vortex anomalies and the vortex fails to vertically align. To determine the reason for this, we use three diagnostics: penetration depth, Rossby deformation radius, and vortex beta Rossby number.

2.3.1 Influence of Penetration Depth

In θ-coordinates, the penetration depth is defined as (Hoskins et al. 1985):

$$\Delta\theta = L\left[\frac{pI}{\kappa\sigma\frac{\partial M}{\partial\theta}}\right]^{1/2} \tag{2.14}$$

where *L* is the horizontal length scale of the disturbance, *p* is the pressure, $I = \sqrt{(f + 2v/r)(f + \zeta)}$ is the inertial stability, σ is the pseudodensity, and *M* is the Montgomery streamfunction. The penetration depth is the depth at which the inertial effects of the vortex are felt. In θ-coordinates, $\Delta\theta$ measures the vertical penetration of the induced flow structure above or below the location of a PV anomaly. As a result, the penetration depth is directly related to the inertial stability of the vortex.

For these experiments, the penetration depth will be applied to the RMW. Since a simple zonal tilt will cause positive wavenumber-1 anomalies with the vortex and negative wavenumber-1 anomalies opposite the tilt, each anomaly at the different isentropic layers has its own induced flow which will affect the flow on different isentropic layers. The penetration depth gives a description of strength of the induced flow and the strength of the coupling between different isentropic layers.

Since the inertial stability of the vortex decreases with height, the vertical penetration of the induced flow also decreases with height. In particular, above the $\theta = 326$ K, the penetration depth is very weak. Therefore, the PV anomaly in the upper-troposphere is not felt strongly by the lower-troposphere. For this reason, the PV rings above the $\theta = 326$ K surface move independently from the PV rings below the $\theta = 326$ K and are advected by the mean flow. This result is consistent with the results seen by Smith et al. (2000), who used a two-layer model to explain the motion seen in Jones et al. (1995). Using quasigeostrophic arguments, Smith et al. (2000) showed that the co-rotation of their two vortices is due to induced flow caused by the PV anomalies associated with each vortex. This induced flow is related to the penetration depth - the stronger the depth, the more tightly the vortices rotated about one another. When the inertial flow of the vortices is not felt on each other, then they move apart. After mixing, the mean tangential wind decreases, thus decreasing the depth to which the inertial flow of each individual level is felt, so the tilt will increase preferentially in the upper-troposphere.

2.3.2 Influence of Internal Rossby Deformation Radius

In θ-coordinates, the internal Rossby radius of deformation for a rapidly rotating vortex, λ_R, is defined as (Hoskins et al. 1985):

$$\lambda_R = \Delta\theta \left[\frac{pI}{\kappa\sigma \frac{\partial M}{\partial \theta}} \right]^{-1/2} \tag{2.15}$$

where $\Delta\theta$ is the vertical depth of the vortex. In previous studies on vortex alignment, the vortex was assumed to be quasi-geostrophic (e.g. Ro ≤ 1), and thus, the Rossby deformation radius, λ_R,

was independent of the inertial stability

$$\lambda_R \approx \frac{\Delta\theta}{f}\left[\frac{g\kappa\sigma}{p}\frac{\partial M}{\partial\theta}\right]. \tag{2.16}$$

Therefore, the internal Rossby deformation radius depends only on static stability, vertical vortex depth, and planetary vorticity. Reasor and Montgomery (2001) discovered that the rate of alignment for a tilted quasi-geostrophic vortex depends upon the internal Rossby deformation radius. For internal Rossby deformation radius larger than the horizontal scale of the tilted vortex, an azimuthal wavenumber-1 quasi-mode exists (Reasor and Montgomery 2001). The quasi-mode is characterized by its steady cyclonic propagation, long lifetime, and resistance to differential rotation, behaving much like a discrete VRW. The quasi-mode traps disturbance energy causing the vortex to precess, or corotate, and thus prevents alignment. For internal Rossby deformation radius smaller than the horizontal vortex scale, the quasi-mode disappears into the continuous spectrum of VRWs and alignment proceeds through the irreversible redistribution of PV by the sheared VRWs.

However, for a rapidly rotating vortex, the internal Rossby deformation radius depends inversely upon the inertial stability of the vortex. Therefore, for strongly rotating vortices, the internal Rossby deformation radius decreases, increasing the rate of alignment for the vortex through sheared VRWs. Figure 2.34 shows the time series of the internal Rossby deformation radius for 5 isentropic layers and the expected internal Rossby deformation radius from quasigeostrophic theory. From this figure, we see that internal Rossby deformation radius decreases by a factor of 5-8 from its quasigeostrophic value. Therefore, we expect a faster alignment rate (or a stronger resistance to vertical shear) for the hollow PV tower in the lower troposphere and since the inertial stability is much weaker in the upper-troposphere, we expect a slower alignment rate (or a weaker resistance to vertical shear).

Although the vortex used in this experiment is in the high Rossby number regime, the ratio of the horizontal scale to the internal Rossby deformation radius, L/λ_R, is approximately 0.2,

which means that the wavenumber-1 quasi-mode dominates the vortex resisting vertical alignment. Schecter et al. (2002) proposed a theory for the rate at which a quasigeostrophic vortex realigns after being tilted by an episode of external vertical shear. The initial tilt is viewed as the excitation of a three-dimensional vortex Rossby mode which decays exponentially with time during its early evolution. The decay rate is proportional to the PV gradient at a critical radius, where the fluid rotation is resonant with the mode, and depends upon the internal Rossby deformation radius. Based on their arguments, when the Rossby deformation radius increases, then the critical radius for damping moves outwards. To see this, we note the Moller and Montgomery (2000) derived the dispersion relation for a baroclinic wavelike disturbance that propagates on a three-dimensional stably-stratified barotropic circular vortex in gradient wind and hydrostatic balance:

$$\omega = n\Omega + \frac{n}{R}\frac{\bar{\xi}}{\bar{q}}\frac{\partial\bar{q}/\partial r|_{r=R}}{k^2 + n^2/R^2 + \gamma^2} \tag{2.17}$$

where *n*, *m*, and *k* are the azimuthal, vertical, and radial wavenumbers, respectively; ω is the local wave frequency; R is the reference frequency; $\bar{\xi}$ is the mean inertial parameter; $\bar{q}$ is the mean PV; $\bar{\Omega}$ is the mean angular velocity; and γ is the inverse local Rossby deformation radius. The corresponding expression for the radial group velocity is:

$$C_{gr} = \frac{\partial\omega}{\partial k} = -\frac{2kn}{R}\frac{\bar{\xi}}{\bar{q}}\frac{\partial\bar{q}/\partial r|_{r=R}}{(k^2 + n^2/R^2 + \gamma^2)^2}. \tag{2.18}$$

By integrating C_{gr} in time and letting $t \to \infty$, we obtain the stagnation radius:

$$r_s = R + \frac{\bar{\xi}\partial\bar{q}/\partial r|_{r=R}}{\bar{q}R\partial\bar{\Omega}/\partial r|_{r=R}}\frac{1}{k^2 + n^2/R^2 + \gamma^2} \tag{2.19}$$

Therefore, as the Rossby deformation radius increases, γ decreases and r_s increases. Since the internal Rossby deformation radius increases during the model simulation, the critical radius will move to an area of lesser PV gradient and thus critical layer damping will decrease. This means that the resonance damping loses its efficiency and thus the quasi-mode amplitude slowly decays. This is observed in our experiments since the vortex reaches a quasi-steady downshear tilt state.

2.3.3 *Influence of Vortex Beta Rossby Number*

The internal Rossby deformation radius also affects another parameter called the vortex beta Rossby number, R_β (Moller and Montgomery 2000; Enagonio and Montgomery 2001). Mathematically, it is defined as the ratio of the nonlinear terms in the PV equation to the effective "beta" terms involving the mean PV gradient of the basic-state vortex. Whereas the vortex itself is the perturbation in the problem of vortex motion on a β plane (Montgomery et al. 1999), here the perturbation is the departure from vertical alignment. In studies of vortex motion the beta Rossby number is large compared to unity, signifying a large perturbation. The vortex in external vertical shear is characterized by beta Rossby numbers smaller than unity, signifying a small perturbation. In the nondivergent limit, the vortex beta Rossby number scales as:

$$R_\beta \approx \frac{V'}{L'^2 \frac{d\bar{\zeta}}{dr}} \tag{2.20}$$

where V' is the perturbation velocity amplitude and L' the perturbation horizontal scale. R_β provides a measure of how important nonlinear advection is compared to the VRW restoring mechanism. For R_β much less than unity, perturbations on an everywhere monotonic mean vortex are expected to disperse as VRWs. Conversely, for R_β much greater than unity, the dynamics are dominated by nonlinear (wave-wave and wave-mean flow) processes. R_β can increase by increasing the strength of the perturbation, decreasing the perturbation length scale, or weakening the mean vorticity gradient. For this reason, vortex alignment, in view of the R_β, depends on the mean vortex structure as well as the perturbation strength. In terms of vertical shear, as vertical shear increases on a vortex, R_β increase until the nonlinear (wave-wave and wave-mean flow) processes dominate over the VRW restoring mechanism, causing the vortex to shear apart. This is observed in our vortex simulations. Since the upper-level PV rings have relatively small mean vorticity gradients, nonlinear processes tend to dominate over the VRW restoring mechanism, preventing realignment.

Reasor and Montgomery (2001) demonstrated that as λ_R tends to 0, R_β tends to 0, implying that the VRW restoring mechanism dominates over nonlinear advection. Another consequence of this dependence of R_β on λ_R is that the linear VRW dynamics will accurately capture the alignment process for a wider range of shear strength, the larger λ_R is. Our results are consistent with these observations. As PV evolves during the model simulation, we see sheared VRWs superposed on an azimuthal wavenumber-1 quasimode. While nonlinear effects modify the vortex structure by counteracting the sheared VRW dispersion, the underlying azimuthal wavenumber-1 quasimode dominates the PV evolution.

The nonlinear effects caused by vertical shear are seen in an internal oscillation as the new center develops from the mixing process. When the vortex mixes, there is an internal oscillation as the new center develops from the mixing. The shear forcing causes a damping of the unstable mode by extracting energy from the mean and increasing wavenumber 1. This is seen in the time series of palinstrophy in Figure 2.29. This results in a slight change in internal mixing. Additionally, since wavenumber 1 grows more quickly, the internal mixing happens more quickly, as verified in Figure 2.30.

2.4 Summary and Application to Tropical Cyclones

Here, we have studied the evolution of a baroclinic hollow PV tower in zero environmental flow and in external zonal shear. For the baroclinic hollow PV tower in zero environmental flow, barotropic instability caused air parcels with high PV to be mixed into the eye preferentially at lower levels, where unstable PV wave growth rates are the largest. During the model simulation, little mixing is found to occur at upper levels. The rearrangement of PV affect the structure and intensity of the vortex by causing a simultaneous decrease in minimum central pressure and maximum tangential velocity and by forming a PV bridge at lower levels.

For the baroclinic hollow PV tower in zonal shear, the shear forcing caused an internal oscillation (wavenumber-1 structure) and a damping of the unstable mode during the nonlinear mixing of the vortex. The initial response of the vortex to the vertical shear is to tilt downshear. The upper- and lower-level centers then began to rotate cyclonically about the midlevel center, causing both leftward and rightward movement relative to the vertical shear. The cyclonic precession of the vortex around the center demonstrates the existence of an azimuthal wavenumber-1 quasimode that prevents the vertical alignment of the vortex. Because of the radial structure of our vortex, the resonant damping of the quasimode, as in Schecter et al. (2002), becomes very efficient as the critical radius moves outward to a region of weakened PV gradient. The persistence of the quasi-mode also demonstrates that nonlinear advection does not play a dominant role in the vertical alignment process. Since L/λ_R and R_β are small, the vortex in shear can be described in terms of linear VRW theory.

The results from these experiments can be extended to tropical cyclones. At lower levels, observed hurricane eyes typically have a temperature inversion that separates the moist cloudy air below from the clear dry air above. The height of the inversion can vary but typically it is near 850 hPa. As a consequence of PV mixing between the eyewall and eye, significant structural change has been shown to occur in our idealized simulations. When PV is advected in a quasi-balanced flow, the invertibility principle indicates that new balanced wind and mass fields quickly adjust to support the new PV distribution. At any given time and spatial point, the PV can be considered to be the product of two factors: the isentropic absolute vorticity $(f + \zeta)$ and the static stability $-g(\partial\theta/\partial p)$. When the PV mixing process enhances the PV at low levels in the eye, we should expect this local PV increase to show up as simultaneous increases in both the isentropic absolute vorticity and static stability. In this sense, the mixing of high PV into the core at low levels can result in high static stability there. Thus, there is the possibility that the hurricane eye temperature inversion discussed above may be at least partially under the dynamical control of the PV mixing process.

Our experiments also show that shear forcing creates an internal oscillation within the core of the vortex and weakens nonlinear mixing through the vortex evolution. This suggests that shear forcing inhibits the formation of the lower-level PV bridge, which may help to explain why shear forcing inhibits the formation and maintenance of the warm core structure in a TC. In real hurricanes, the thermally indirect transverse circulation associated with eyewall diabatic heating induces eye warming through subsidence. In the absence of environmental flow, PV mixing complements diabatic processes, and thus helps to explain why observed eye temperature inversions near 850 hPa are so strong. Shear forcing may cause PV mixing to compete with diabatic processes, inhibiting strong low-level eye temperature inversions.

For typical tropical conditions, the global internal deformation radius is on the order of 1000 km. For horizontal vortex scales on the order of 100 km, then L/λ_R falls well within the quasi-mode regime. If the alignment dynamics at large Rossby number depends on the local deformation radius, then we might anticipate that tropical cyclones under vertical shear will resist vertical shear by radiation of sheared VRWs or by resonant damping of the quasi-mode structure. In particular, our results imply that strong tropical cyclones efficiently radiate sheared VRWs in order to resist vertical shear. Also, since strong tropical cyclones will also have strong PV gradients outside of the RMW, this suggests that strong tropical cyclones also have strong decay rates of the quasi-mode structure induced by the vertical tilt. From this analysis, it appears that vertical shear acts as a VRW generator when it interacts with a tropical cyclone. The quasi-mode propagation causes the vortex to precess, and its decay leads to slow alignment. When the inertial stability of a tropical cyclone increases such that the horizontal scale is a non-negligible fraction of the global internal deformation scale, then the inviscid damping of the sheared VRWs leads to rapid reduction of the tilt.

Lastly, the invisid damping mechanism by linear VRW depends on the details of the vortex profile. In our experiments, there was an approximate steady-state tilt to the left of the shear vector. Previous studies (e.g., Smith et al. 2000) give the impression that the precessing solution is a typical

solution in the limit of small initial tilt (or in our case, weak vertical shear). These results indicate that while the downshear-left tilt orientation is the one that minimizes the net vertical shear, and thus would appear to be an optimal solution, the possibility of the downshear-left solution depends on the details of the vortex profile. Although quantitative mesoscale observations of hurricane tilt are fairly limited, the consensus thus far appears to be that hurricanes do not precess continually when forced by vertical shear. When a hurricane is forced by vertical shear, the observations suggest that the vortex tilt is generally oriented downshear to downshear-left when the decay rate of the quasi-mode is non-negligible, consistent with our results. This suggests that the downshear-left location of convective asymmetry observed in hurricanes forced by vertical shear may be in the first approximation a consequence of dry adiabatic VRW dynamics.

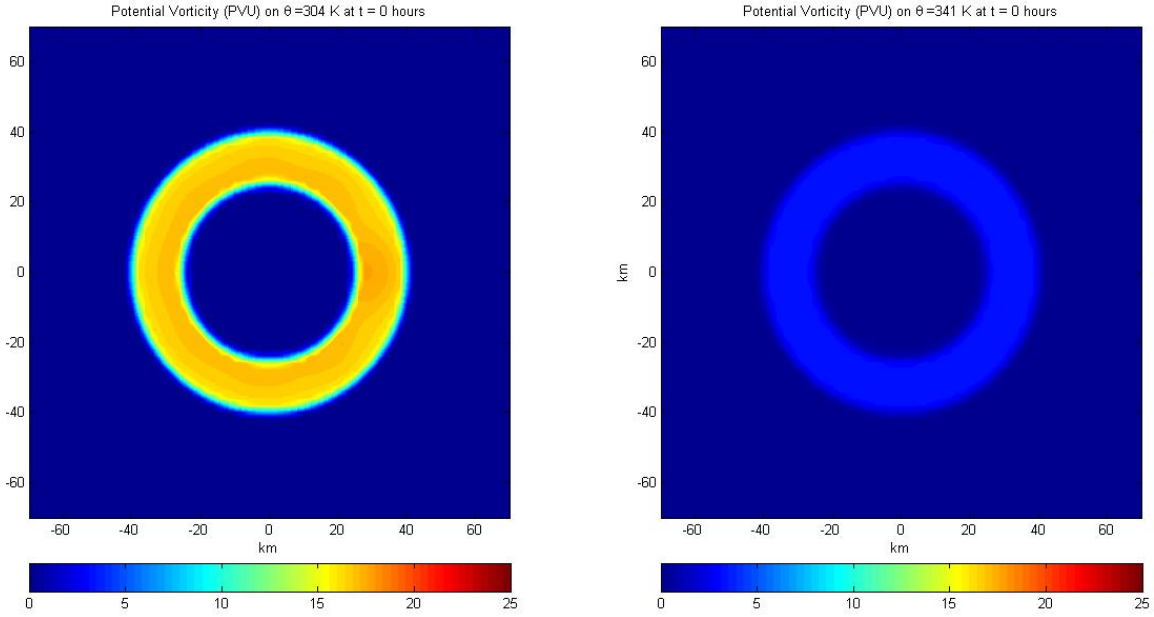

Figure 2.1: The initial condition for the hollow PV tower.

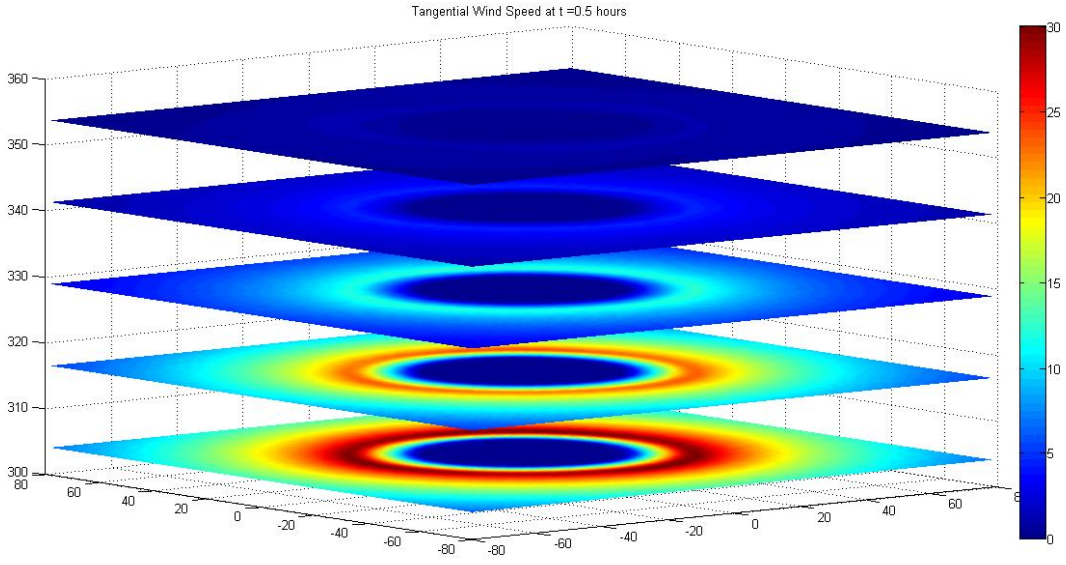

Figure 2.2: Tangential wind structure for the hollow PV tower.

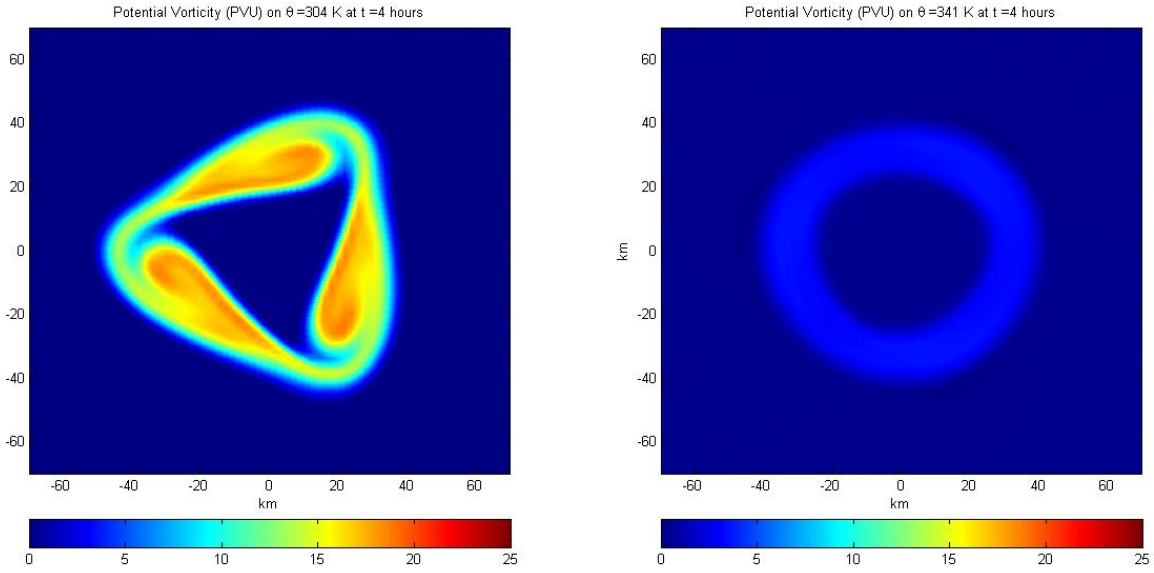

Figure 2.3: PV Evolution of $\theta = 304$ K and $\theta = 341$ at 4 hours.

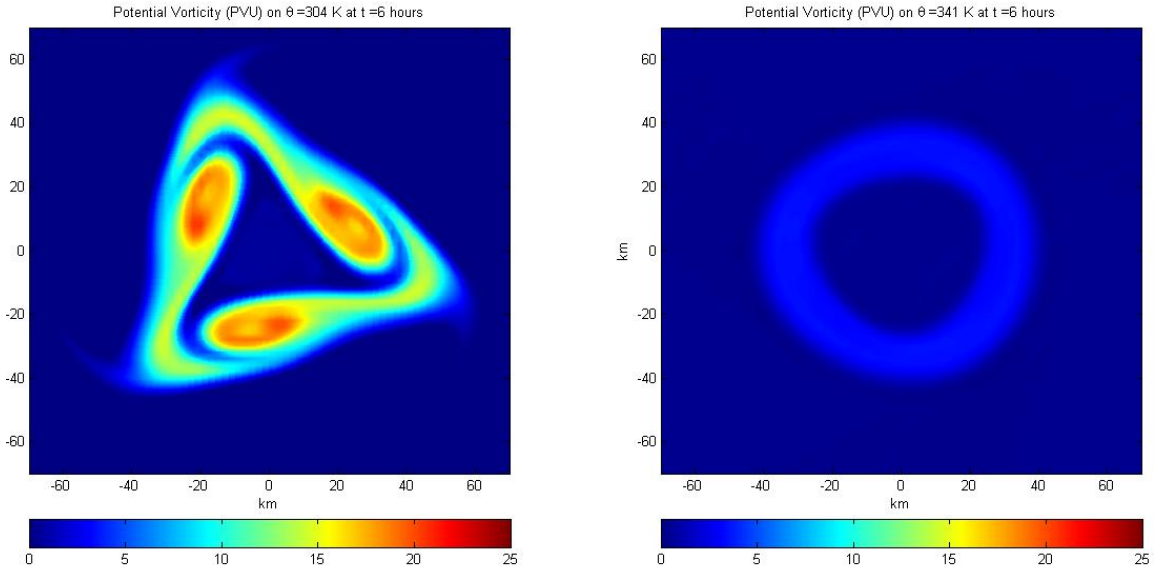

Figure 2.4: PV Evolution of $\theta = 304$ K and $\theta = 341$ at 6 hours.

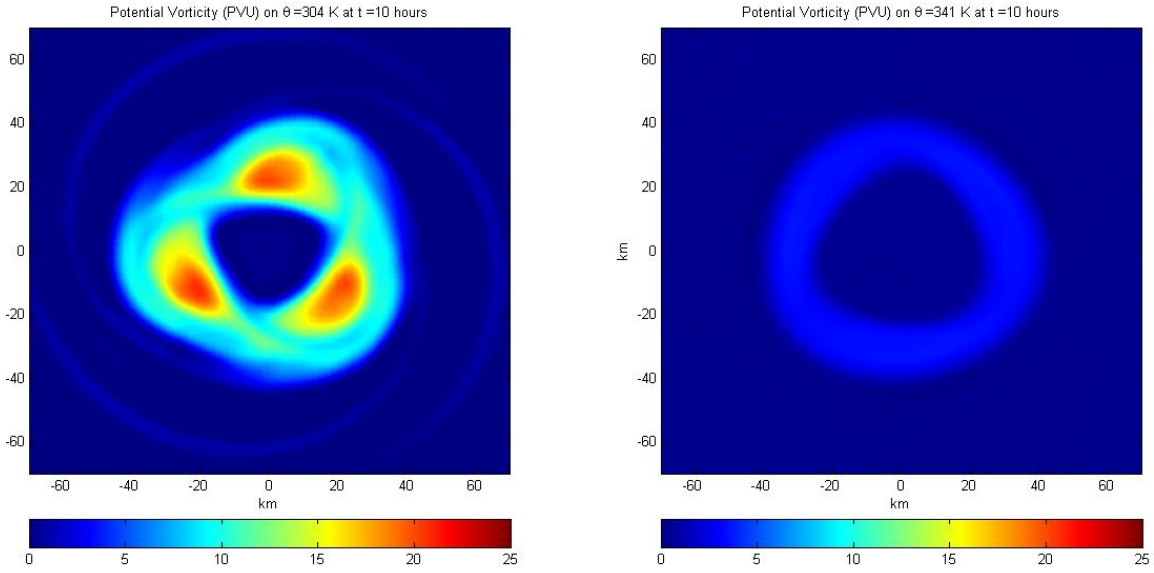

Figure 2.5: PV Evolution of $\theta = 304$ K and $\theta = 341$ at 10 hours.

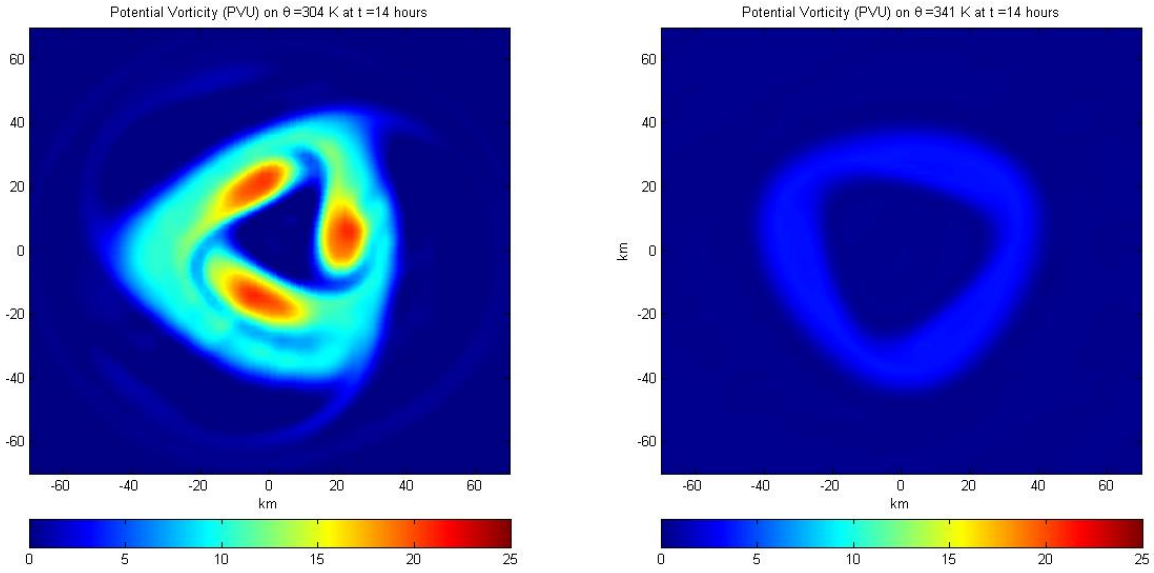

Figure 2.6: PV Evolution of $\theta = 304$ K and $\theta = 341$ at 14 hours.

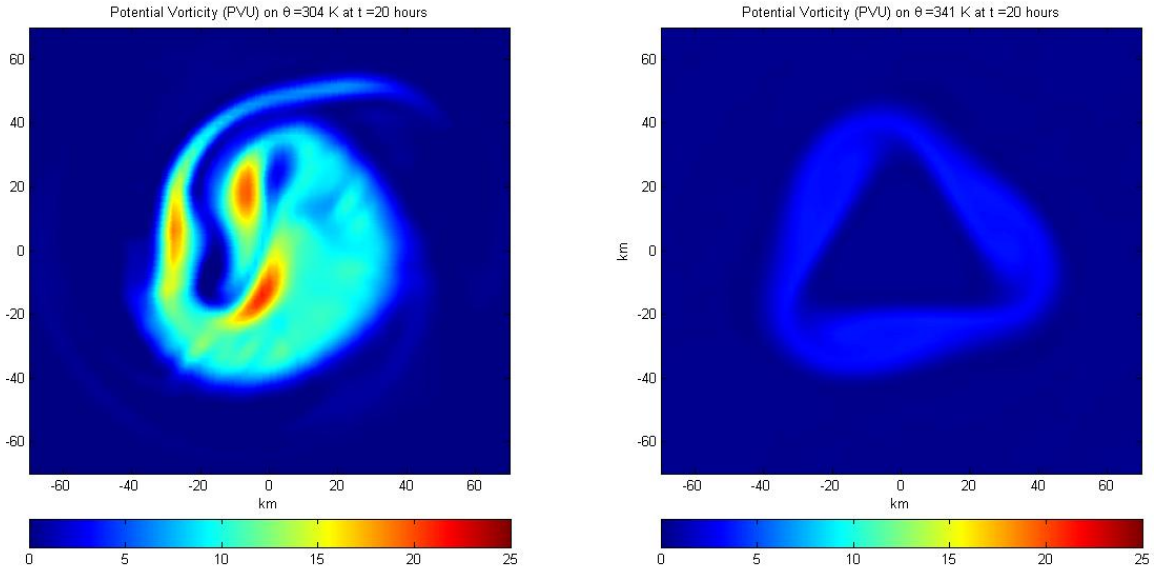

Figure 2.7: PV Evolution of $\theta = 304$ K and $\theta = 341$ at 20 hours.

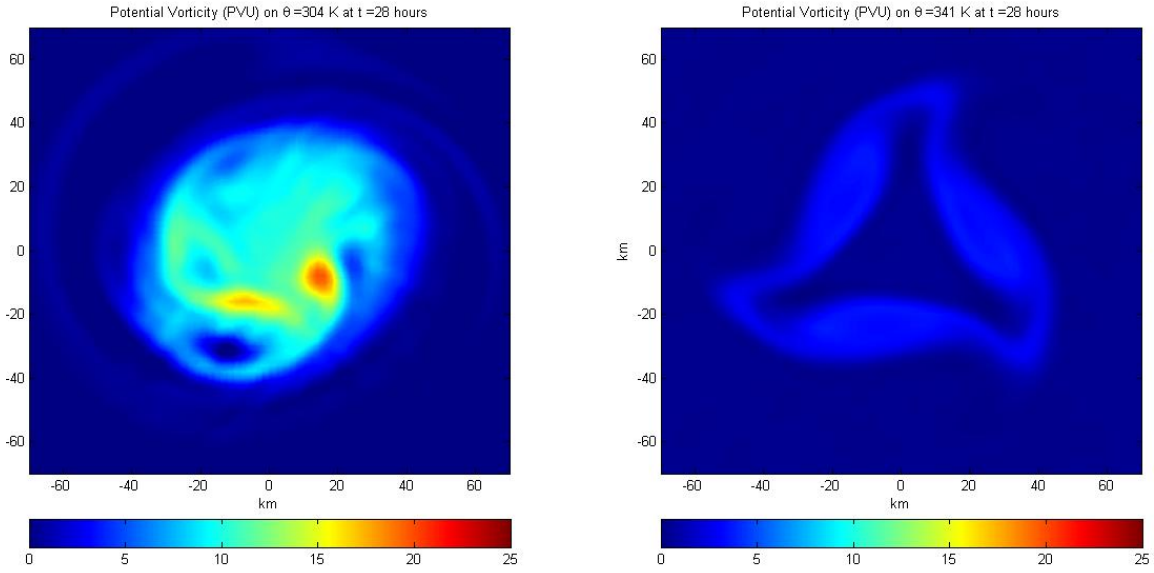

Figure 2.8: PV Evolution of $\theta = 304$ K and $\theta = 341$ at 28 hours.

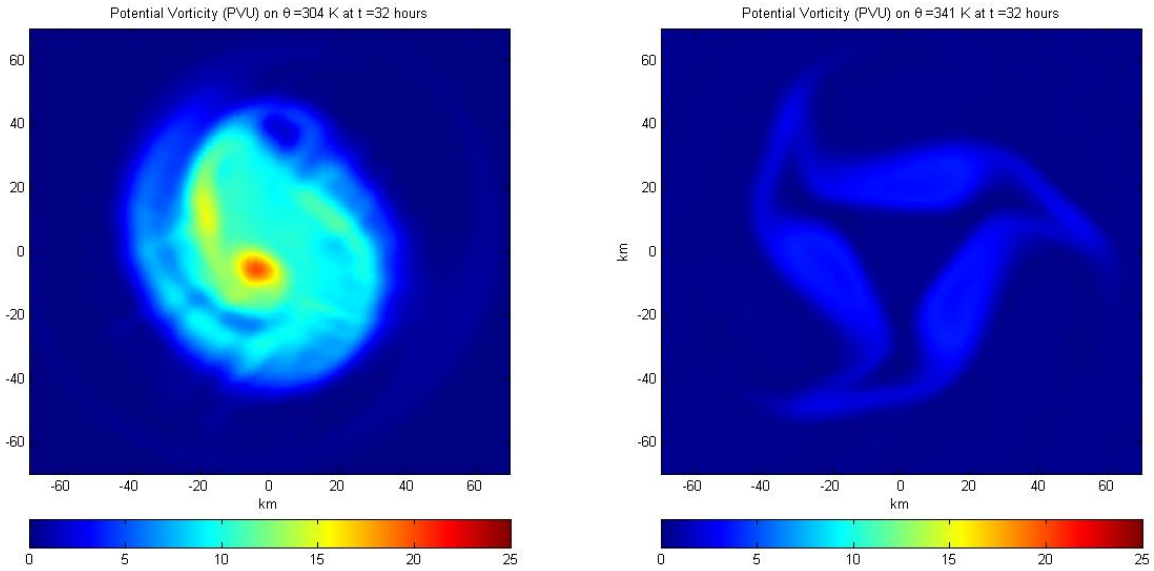

Figure 2.9: PV evolution of $\theta = 304$ K and $\theta = 341$ at 32 hours.

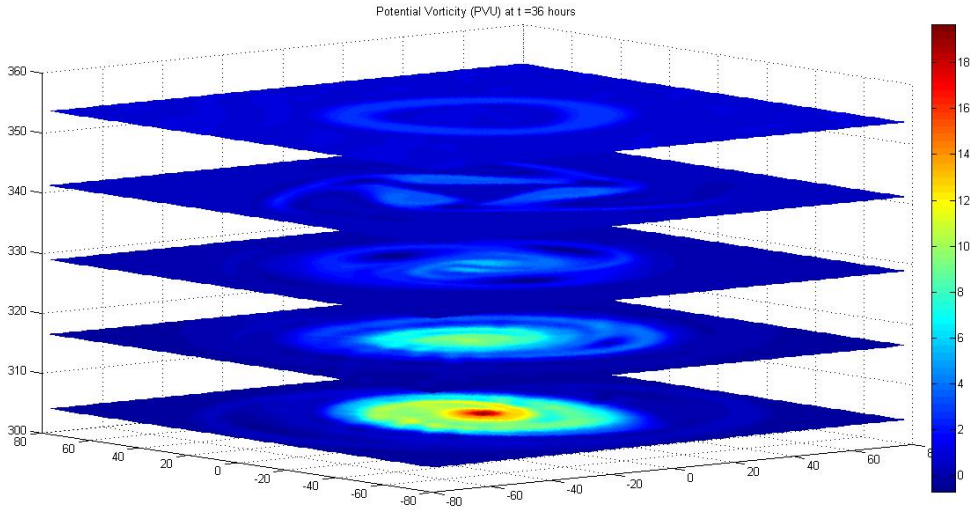

Figure 2.10: End state of hollow PV tower at 36 hours.

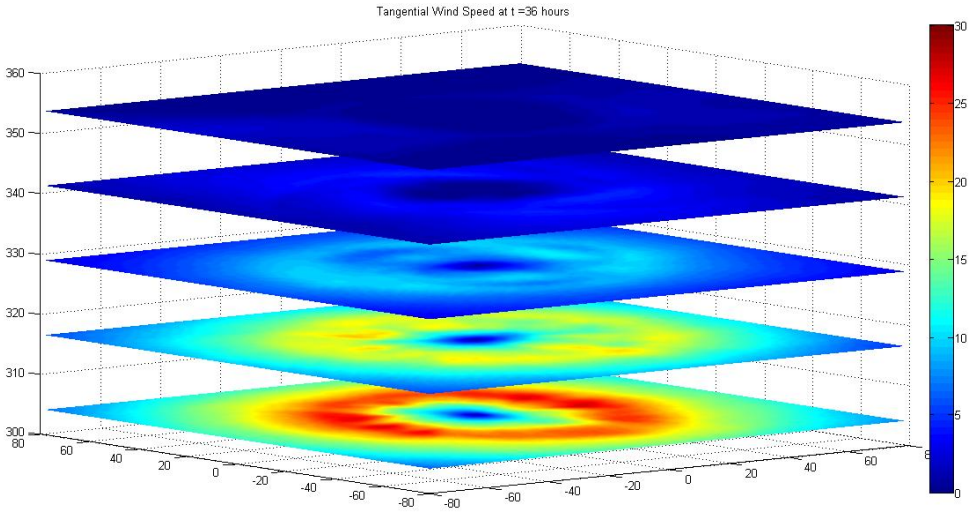

Figure 2.11: Tangential wind of hollow tower at 36 hours.

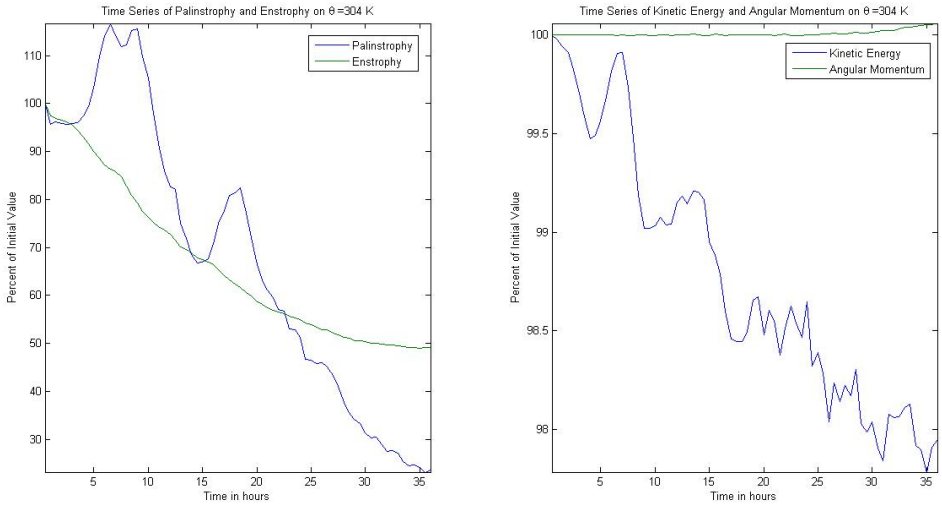

Figure 2.12: Time series of palinstrophy, enstrophy, kinetic energy, and angular momentum.

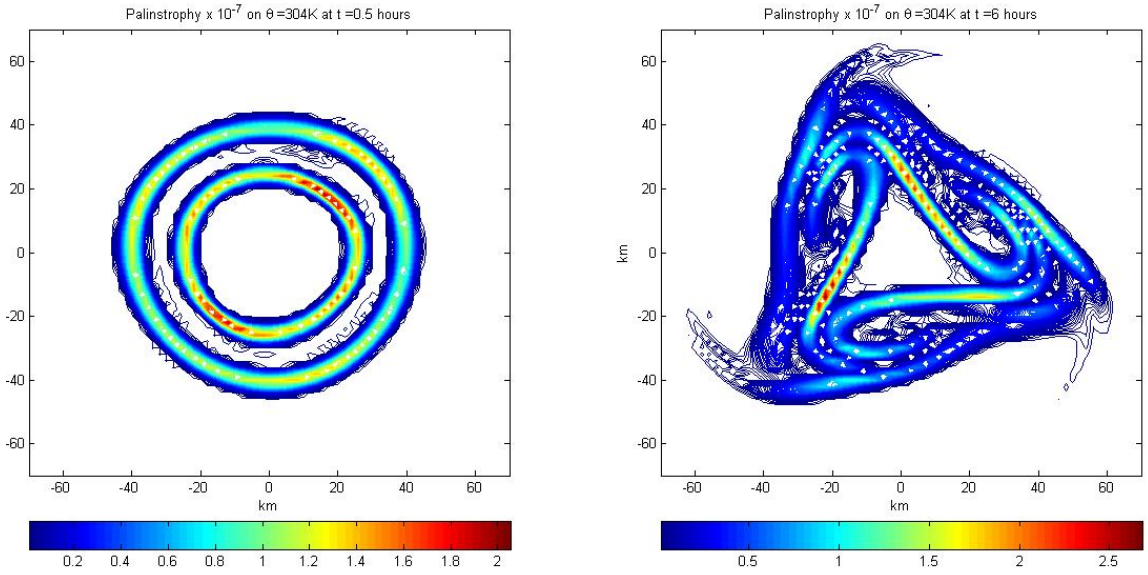

Figure 2.13: Palinstrophy at 0 hours and 6 hours.

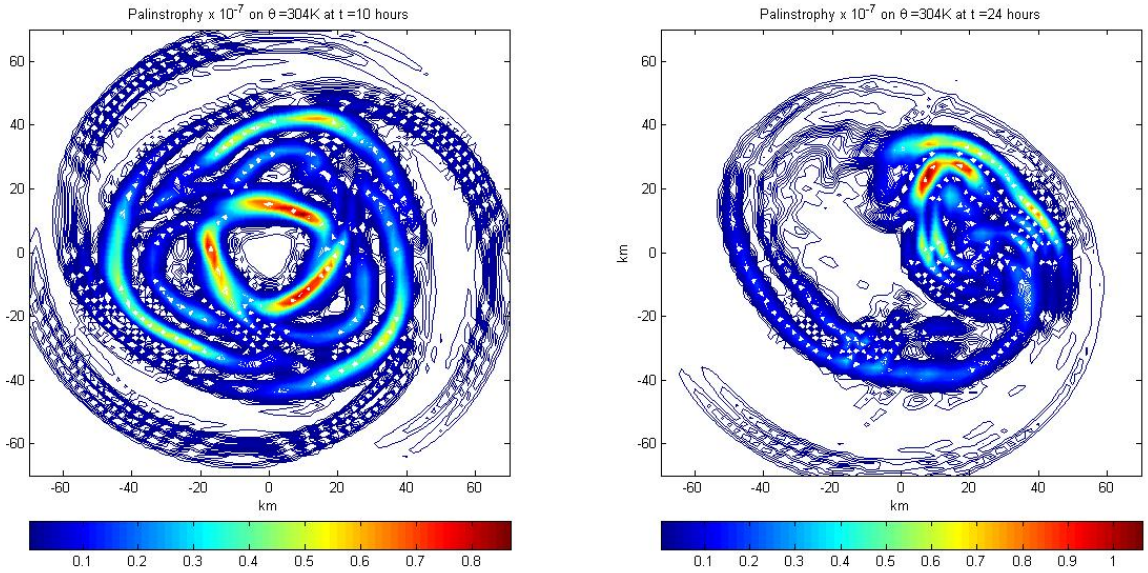

Figure 2.14: Palinstrophy at 10 hours and 24 hours.

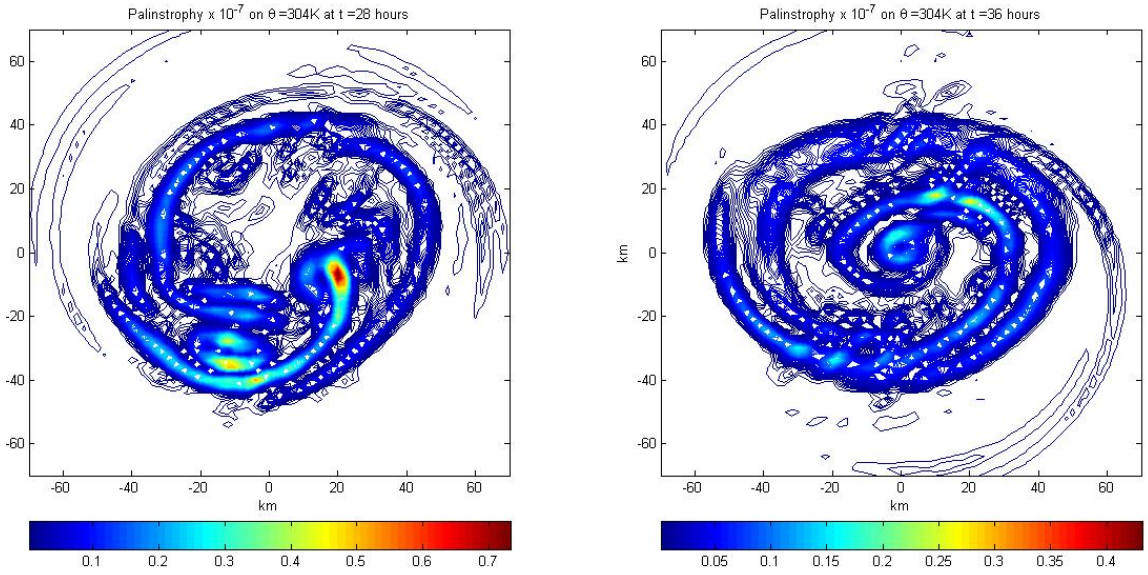

Figure 2.15: Palinstrophy at 28 hours and 36 hours.

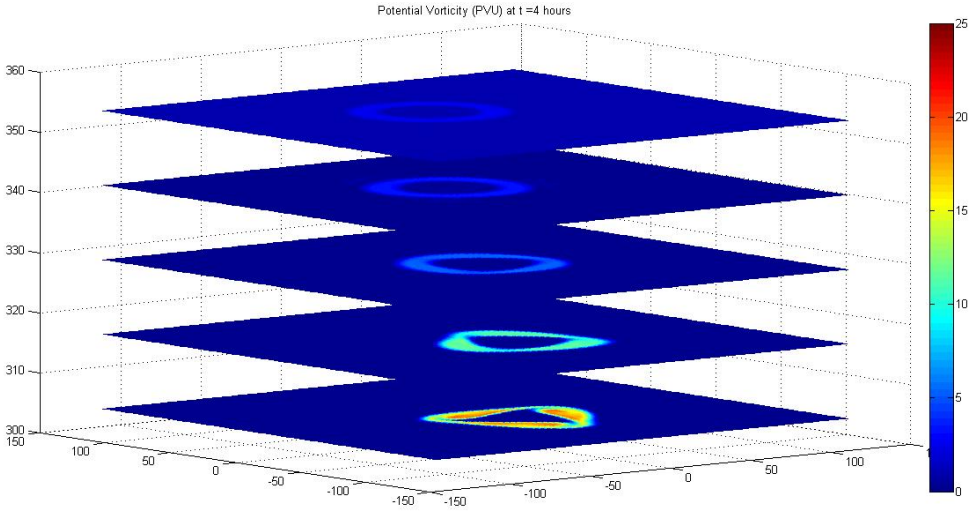

Figure 2.16: PV evolution at 4 hours.

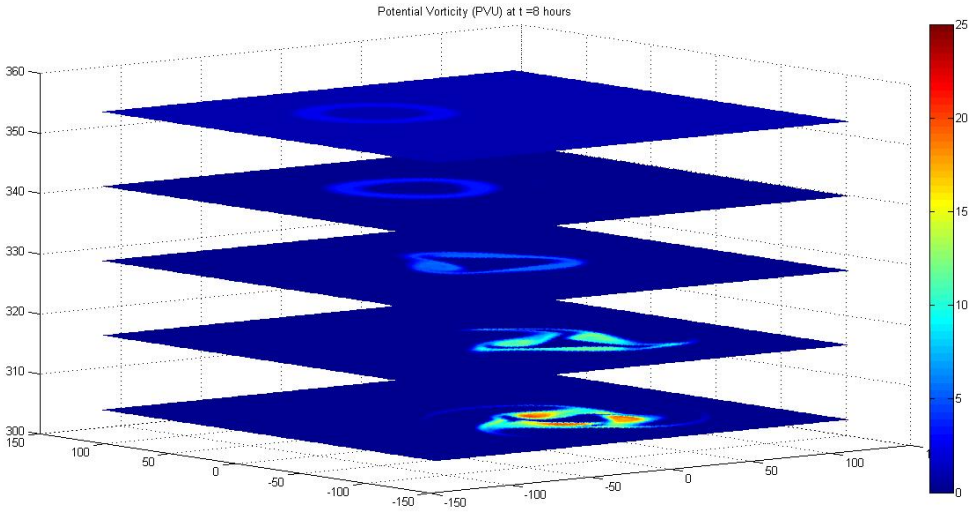

Figure 2.17: PV evolution at 8 hours.

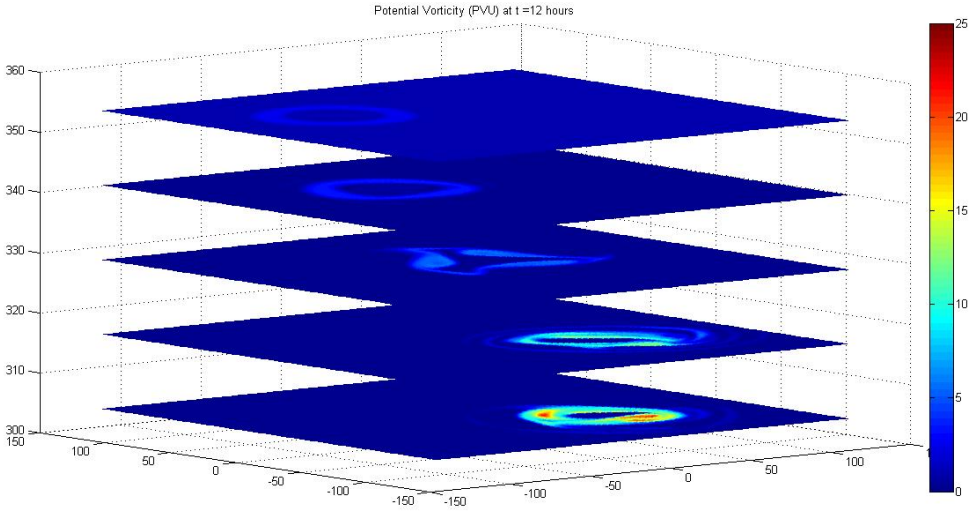

Figure 2.18: PV evolution at 12 hours.

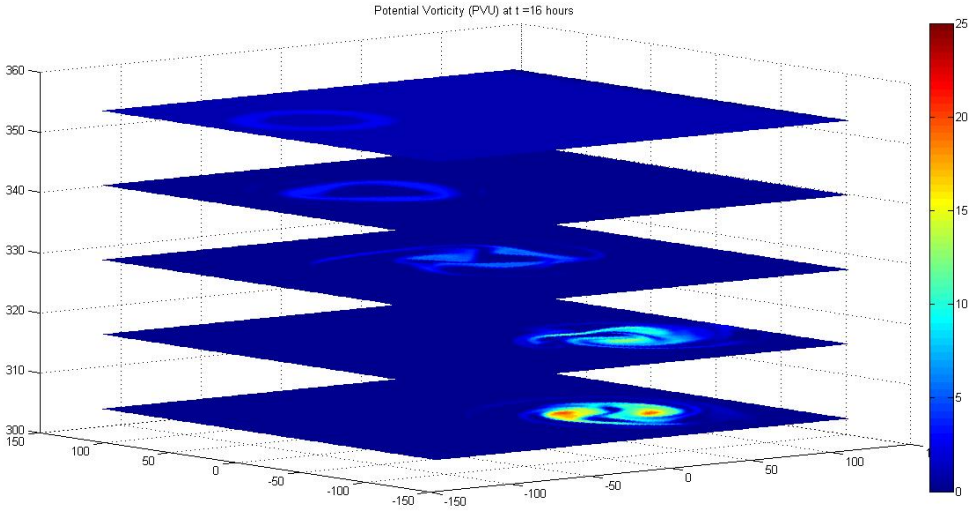

Figure 2.19: PV evolution at 16 hours.

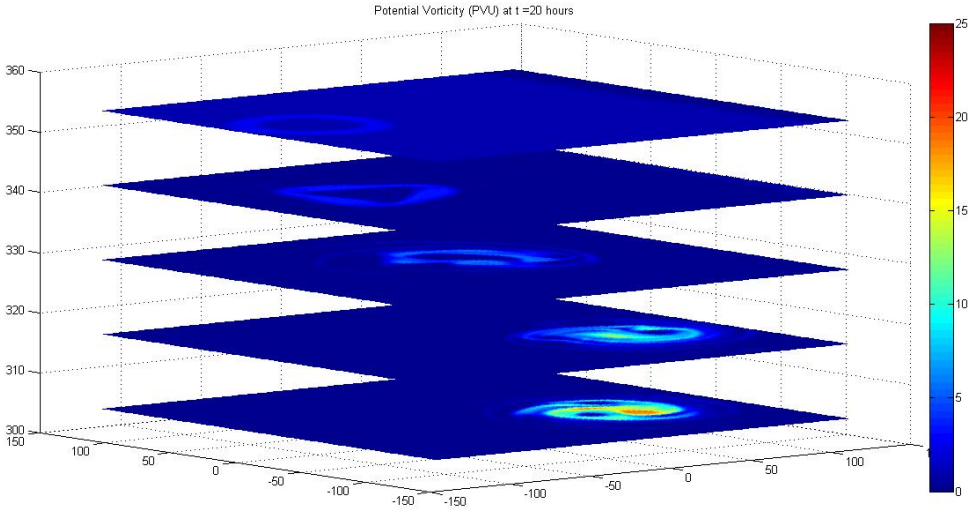

Figure 2.20: PV evolution at 20 hours.

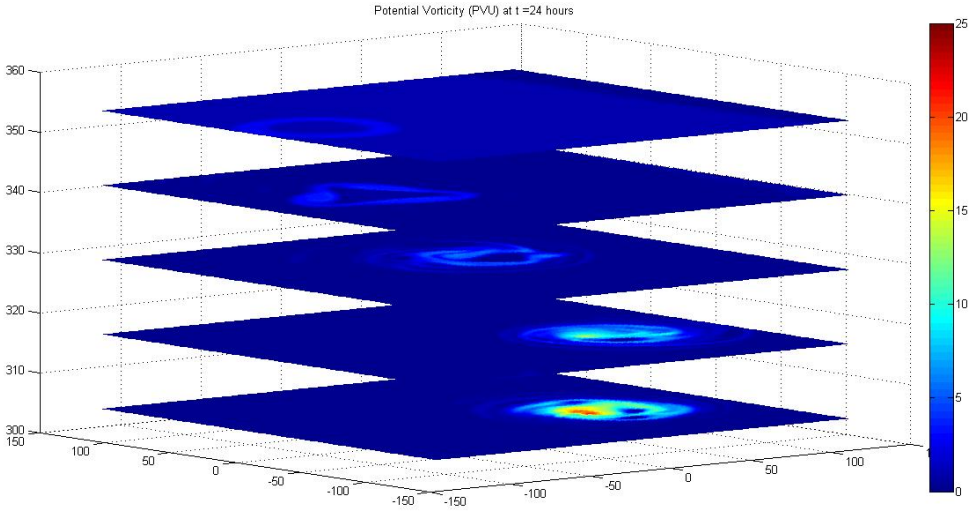

Figure 2.21: PV evolution at 24 hours.

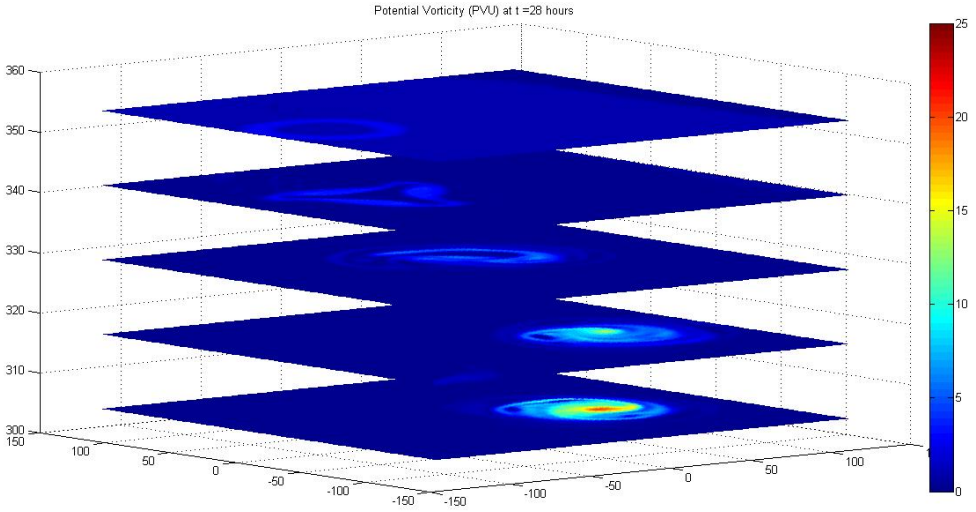

Figure 2.22: PV evolution at 28 hours.

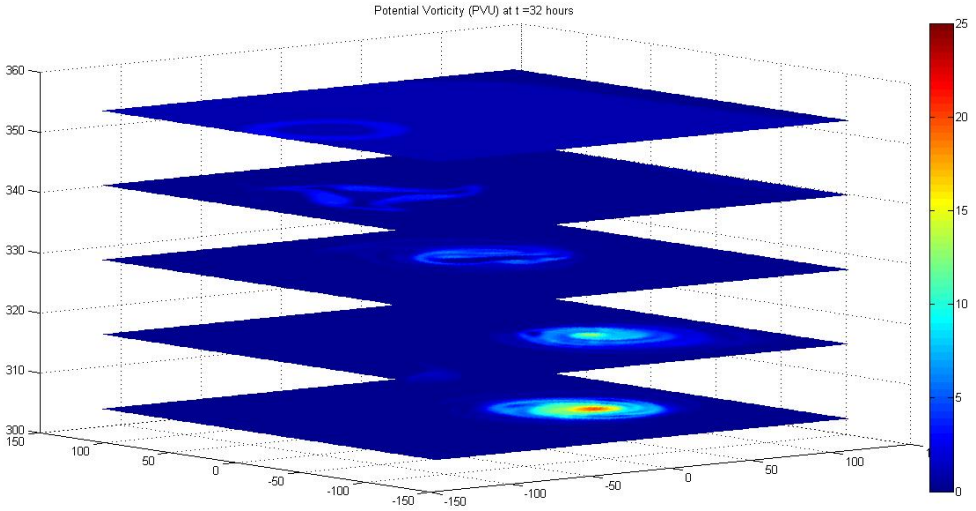

Figure 2.23: PV evolution at 32 hours.

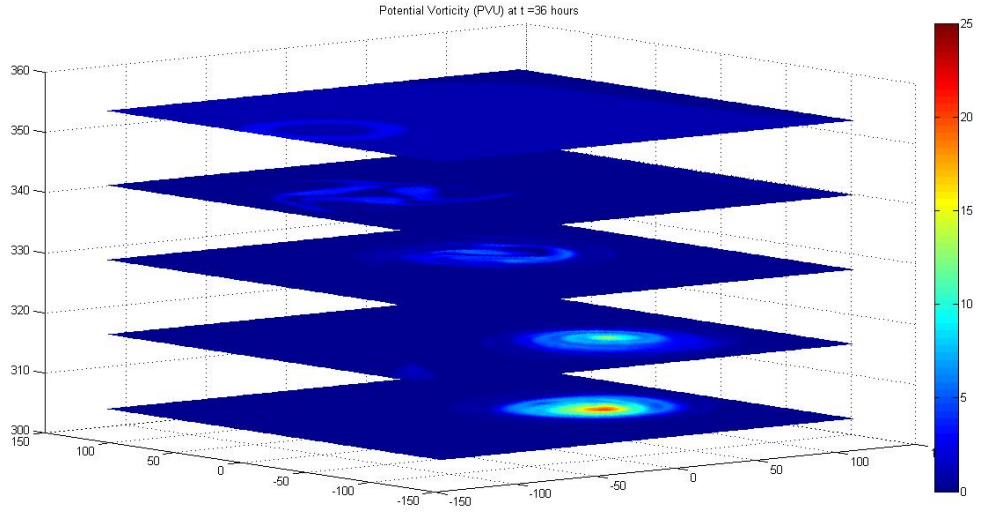

Figure 2.24: PV evolution at 36 hours.

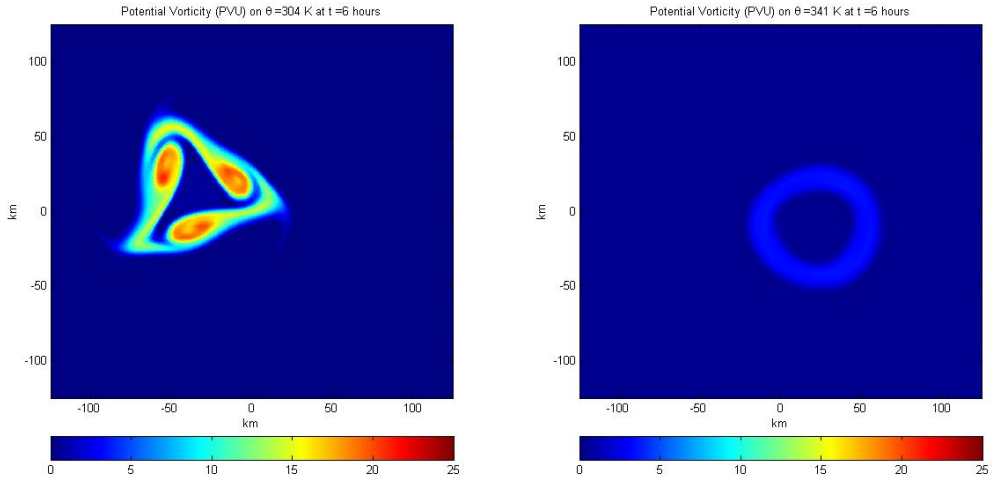

Figure 2.25: PV evolution of $\theta = 304$ K and $\theta = 341$ K at 6 hours.

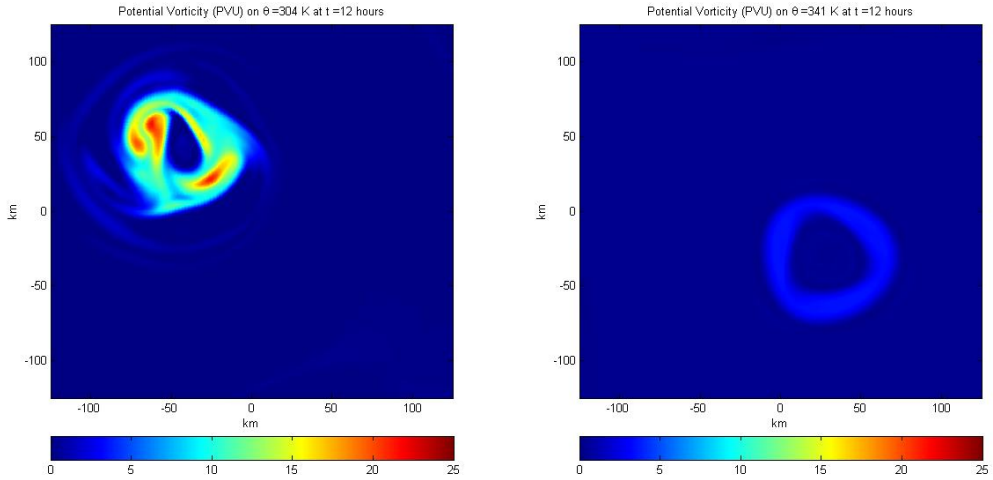

Figure 2.26: PV evolution of $\theta = 304$ K and $\theta = 341$ K at 12 hours.

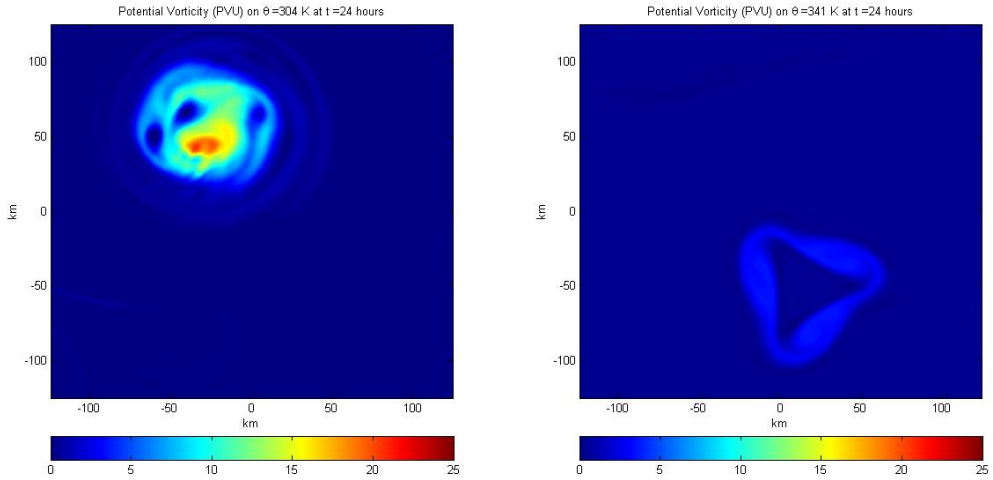

Figure 2.27: PV evolution of $\theta = 304$ K and $\theta = 341$ K at 24 hours.

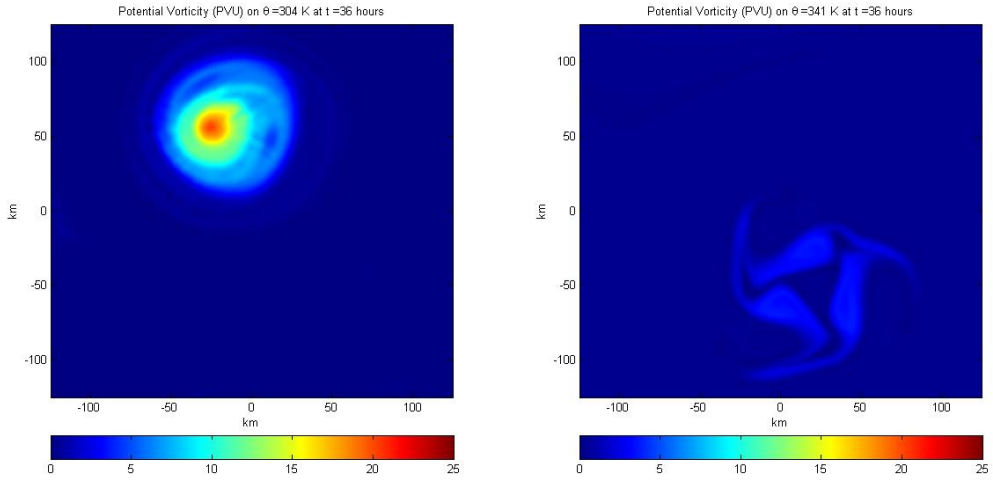

Figure 2.28: PV evolution of $\theta = 304$ K and $\theta = 341$ K at 36 hours.

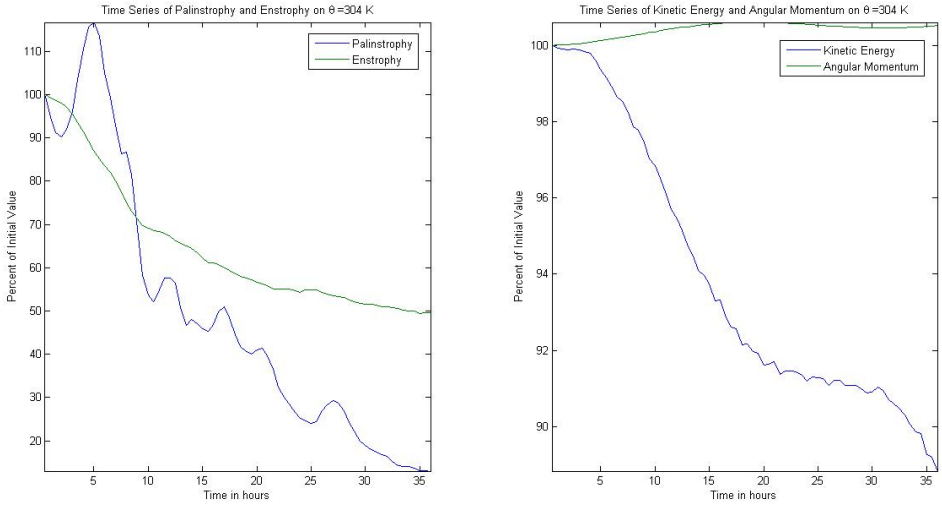

Figure 2.29: Time series of palinstrophy, enstrophy, kinetic energy, and angular momentum.

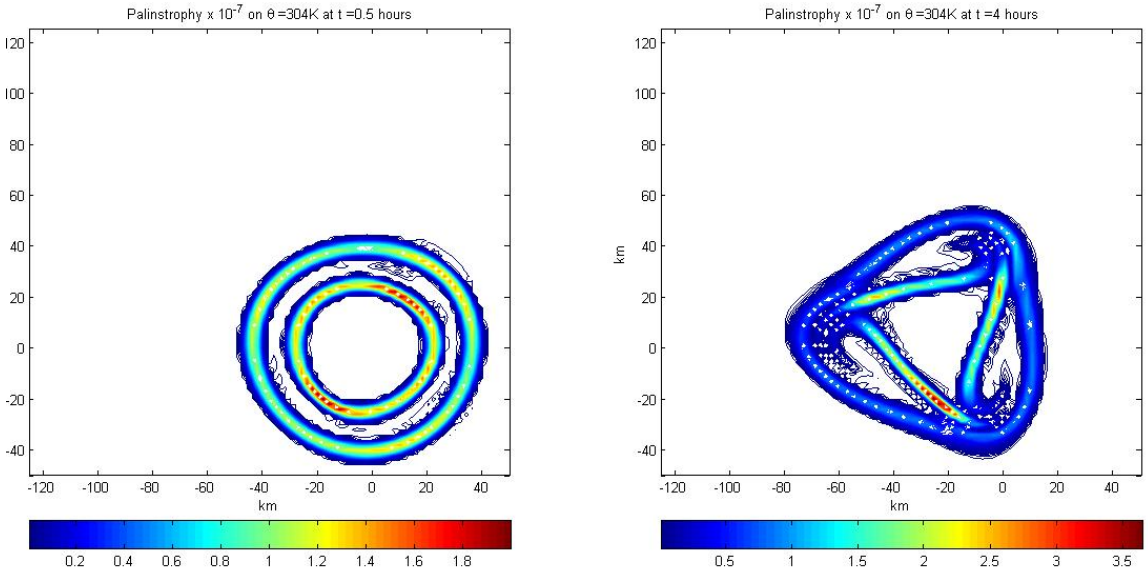

Figure 2.30: Palinstrophy at 0 hours and 4 hours.

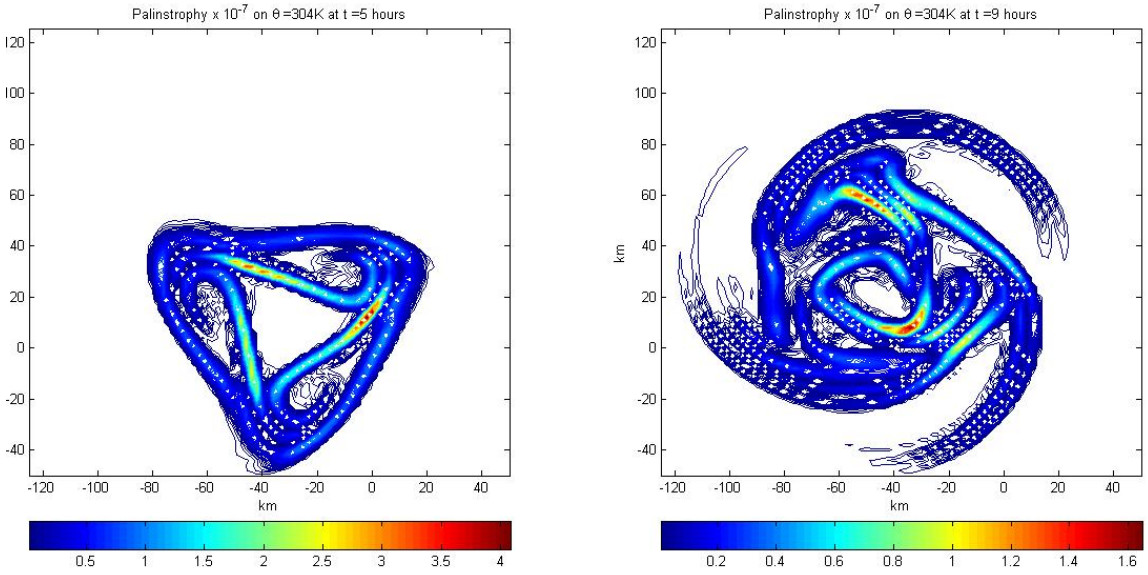

Figure 2.31: Palinstrophy at 5 hours and 9 hours.

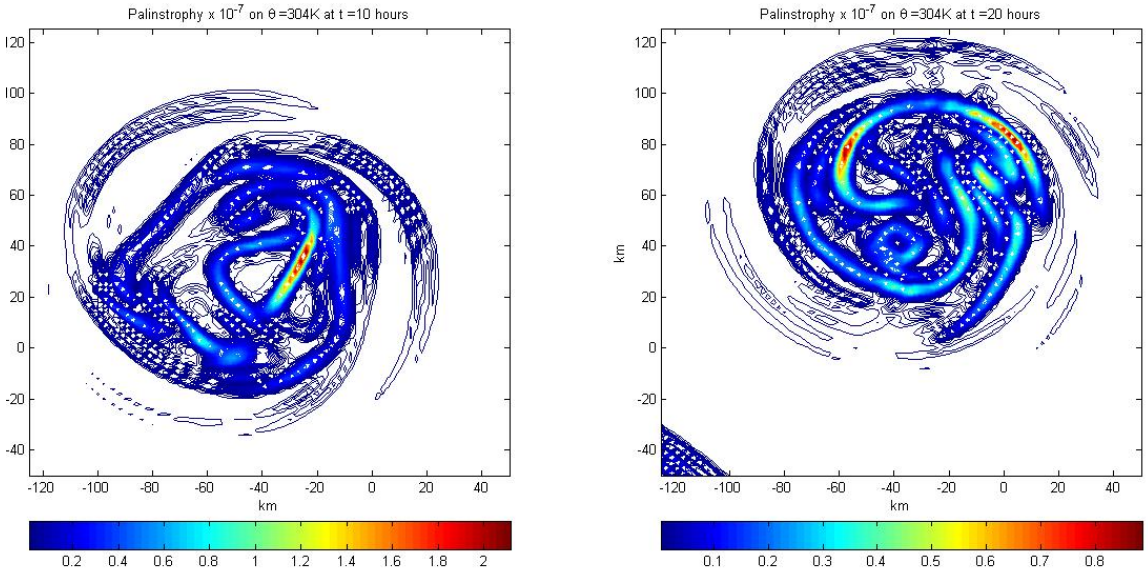

Figure 2.32: Palinstrophy at 10 hours and 20 hours.

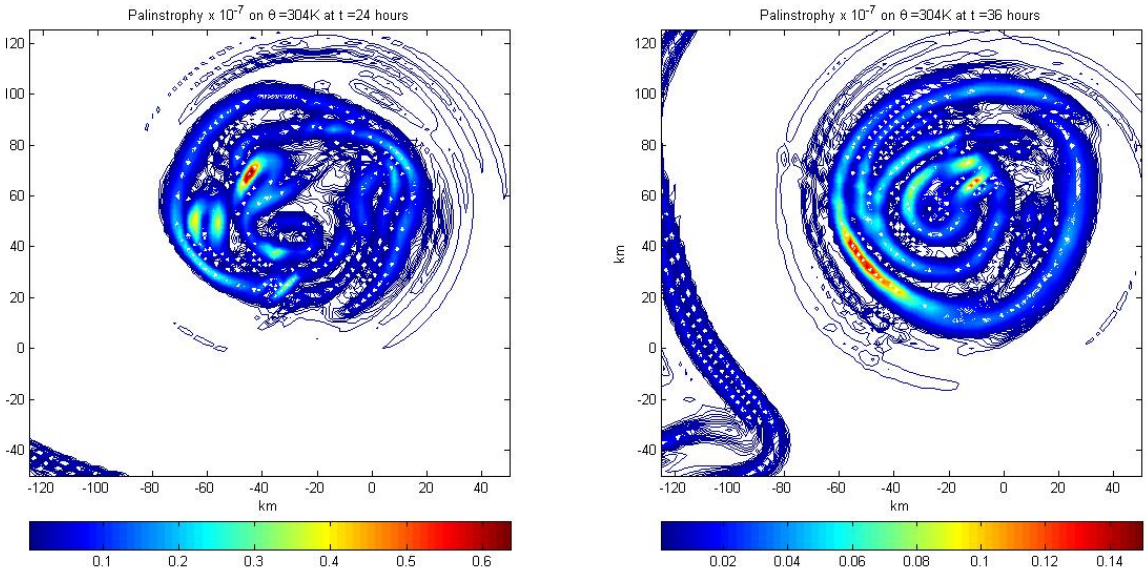

Figure 2.33: Palinstrophy at 24 hours and 36 hours.

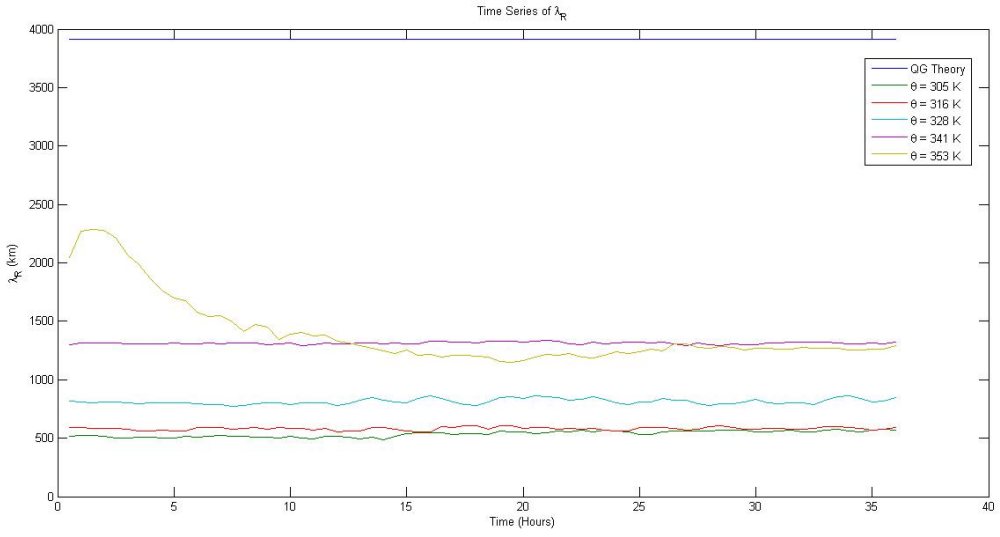

Figure 2.34: Time series of internal Rossby deformation radius

Chapter 3

THE EFFECT OF NONCONSERVATIVE PROCESSES ON SHEARED HOLLOW PV TOWERS

The previous chapter examined the adiabatic rearrangement of a hollow PV tower under simple vertical shear. Although the insight gained from that analysis is useful, the dry adiabatic framework used there to examine PV mixing is an oversimplication of the real atmosphere. The PV structure in real hurricanes is also influenced by the nonconservative effects of moist convection, surface friction, and vertical diffusion, which were neglected in the previous chapter. In particular diabatic PV production (and thus, an increase in inertial stability and/or static stability) would tend to accompany the inward mixing at low levels, and similarly diabatic PV destruction (and thus, a decrease in inertial stability and/or static stability) would likely accompany the outflow at middle to upper levels. Furthermore, diabatic effects create a secondary circulation (not present in the previous chapter) causing PV to be increased locally when there is vertical mass divergence and vice-versa. This chapter studies PV mixing in more complex scenarios. In this chapter, we examine the effect of nonconservative forcing (such as diabatic heating, vertical diffusion, and surface friction) on the evolution of sheared hollow PV towers.

This chapter is organized in following way. Section 3.2 examines the effect of static diabatic forcing on the evolution of hollow PV towers. Section 3.3 examines the effect of nonconservative processes (diabatic heating, vertical diffusion, and surface friction) on the evolution of sheared hollow PV towers. Finally, Section 3.4 summarizes these results and their application for tropical cyclones.

3.1 The Effect of Static Diabatic Forcing on the Evolution of Hollow PV Towers

3.1.1 Overview of Numerical Model

For these experiments, we consider adiabatic, quasi-hydrostatic motions of a compressible atmosphere on an f-plane. The numerical model used here is based on the three-dimensional hydrostatic primitive equations in isentropic coordinates used in Chapter 2. The governing equations are given by:

$$\frac{Du}{Dt} = fv - \frac{\partial M}{\partial x}, \tag{3.1}$$

$$\frac{Dv}{Dt} = -fu - \frac{\partial M}{\partial y}, \tag{3.2}$$

$$\frac{\partial m}{\partial t} + \frac{\partial (mu)}{\partial x} + \frac{\partial (mv)}{\partial y} + \frac{\partial (m\dot{\theta})}{\partial \theta} = 0, \tag{3.3}$$

$$\frac{\partial M}{\partial \theta} = \Pi, \tag{3.4}$$

$$\Phi(x, y, \theta) = \Phi(x, y, \theta_s) - \int_{\Pi_s}^{\Pi(x,y,\theta)} \theta d\Pi', \tag{3.5}$$

where *u* and *v* are the velocity components in the *x* and *y* directions, $m = g^{-1}(\partial p/\partial \theta)$ is the pseudodensity, $M = \theta\Pi + \Phi$ is the Montgomery potential, $\Pi(p) = c_p(p/p_0)^{\kappa}$ is the Exner function, Φ is the geopotential, and f is the Coriolis parameter set at $5 \times 10^{-5}\ s^{-1}$. Since we are studying the role of diabatic forcing on hollow PV towers, we will use the full material derivative: $D/Dt = \partial/\partial t + u(\partial/\partial x) + v(\partial/\partial y) + \dot{\theta}(\partial/\partial \theta)$ where $\dot{\theta} = Q/\Pi$ is the diabatic heating rate. Therefore, the effect of diabatic forcing enters as a vertical advection term in the θ-coordinate model.

The vertical structure of heating in convectively active, intense tropical cyclones typically exhibit a first vertical internal mode structure. Therefore, we assume the diabatic heating Q has the separable form

$$\frac{Q(r,\sigma)}{c_p} = \hat{Q}(r)\exp(-\alpha\sigma)\sin(\pi\sigma). \tag{3.6}$$

where $\sigma = \dfrac{p - p_{top}}{p_s - p_{top}} = \dfrac{p - p_{top}}{p_\star}$, $p_\star = p_s - p_{top}$, p_s, and p_{top} are the surface and top pressures, and p_{top} is a constant, taken here to be 100 mb. Choosing α = 0.554 places the maximum heating at 500 mb, which proves to be a good approximation to the Yanai et al. (1973) heating profile. The vertical distribution of diabatic heating is given in Figure 3.1. To specify the $\hat{Q}(r)$ term in (3.1), we assume that the diabatic heating has the form of an annular ring with smooth edges

$$\hat{Q}(r) = \hat{Q}_{ew}\begin{cases} 0 & r \le r_1 \\ S\left(\frac{r_2 - r}{r_2 - r_1}\right) & r_1 \le r \le r_2 \\ 1 & r_2 \le r \le r_3 \\ S\left(\frac{r - r_3}{r_4 - r_3}\right) + \zeta_3 S\left(\frac{r_4 - r}{r_4 - r_3}\right) & r_3 \le r \le r_4 \\ 0 & r \ge r_4 \end{cases} \tag{3.7}$$

where $S(s) = 1 - 3s^2 + 2s^3$ is the cubic interpolating function satisfying $S(0) = 1$, $S(1) = 0$, $S'(0) = 0 = S'(1)$, and r_1, r_2, r_3, r_4 are specified constants. The eyewall diabatic heating, denoted by $\hat{Q}_{ew}$, is determined from r_1, r_2, r_3, r_4 by imposing the constraint that the domain-averaged diabatic heating is fixed to 0.40 K day^{-1}. Imposing this constraint on $\hat{Q}(r)$, Musgrave et al. (2011) show that the eyewall diabatic heating is given by

$$\hat{Q}_{ew} = c_p \cdot G \cdot (0.40 K day^{-1}), \tag{3.8}$$

where G is a geometric factor given by

$$G = \frac{10(200km)^2}{(3r_3^2 + 4r_3r_4 + 3r_4^2) - (3r_1^2 + 4r_1r_2 + 3r_2^2)}. \tag{3.9}$$

Because the radial structure of diabatic forcing remains fixed during the vortex evolution, we refer to this as static diabatic forcing. To determine how the radial location of diabatic heating affects the evolution of hollow PV towers, we will use 3 diabatic forcing profiles, shown in Table 3.1 and Figure 3.2. The hollow PV tower will be based on the initial conditions from Chapter 2. The initial

condition for the relative vorticity has the separable form $\zeta(r, \phi, \theta) = [\zeta_{sym}(r) + \zeta_{pert}(r, \phi)]F(\theta)$, where $\zeta_{sym}(r)$, $F(\theta)$, and ζ_{pert} are given by (2.5), (2.6), and (2.7), respectively. For the hollow tower in these experiments, ζ_2 = 0.00125 s^{-1} and r_1, r_2, r_3, r_4 = 23, 27, 38, 42 km, respectively. This gives a maximum initial velocity of approximately 15 m s^{-1}.

3.1.2 Control Experiment

The initial condition for the hollow tower for the $\theta = 304$ K and $\theta = 341$ K surfaces are shown in Fig. 3.3. The PV is concentrated in the radial zone of cyclonic shear and curvature vorticity between $r = 20$ and $r = 40$ km, and is maximized at 305 K, even though the vortex winds are maximum at 302 K. Figure 3.4 shows the evolution of the PV tower at *t* = 8 hr. At this time, the most unstable wavenumber $n = 3$ is visible on the $\theta = 304$ K surface. As mentioned in Chapter 2, the growth of the unstable mode is a result of counter-propagating VRWs. The VRWs exist on the highest PV gradients of the vortex - at approximately 25 km and 40 km radius. The inner VRW is propagating with the mean flow, while the outer VRW is propagating against the mean flow due to change in radial gradient of PV.

Figure 3.5 shows the PV tower at *t* = 14 hr. As the wave-breaking stage continues, interior particles with low and intermediate PV are drawn into the high PV ring. This low and intermediate PV fluid spirals cyclonically into and carves up the high vorticity fluid in the original annular ring. Figure 3.6 shows the PV tower at *t* = 18 hr. Here we see two consequences of the withdrawal of intermediate and low PV fluid: a decrease in the area of the inner PV region and a tightening of the PV gradient on the inner edge of the PV ring. Figure 3.7 shows the PV tower at *t* = 28 hr. At this time, the central region of low PV moves off-center. The remaining patch of low PV circles the vortex approximately every 4 hours, as high PV begins to move towards the center. From 28 hr to 36 hours, the patch of low PV continues to circle the vortex, while the patch of high PV settles into the vortex center, accompanied by its associated trailing spiral bands of PV. At this time, the most unstable wavenumber $n = 3$ is visible on the $\theta = 341$ K surface, as shown in

Figure 3.8. Figure 3.9 shows the time evolution of maximum tangential velocity at $\theta = 304$ K, maximum potential vorticity at $\theta = 304$ K, and minimum surface pressure. In response to mixing, the mean tangential velocity has decreased in the eyewall region and the minimum surface pressure has decreased, consistent with the results in Chapter 2.

3.1.3 DH1: Static Heating Inside the RMW

For Case 1, the diabatic heating profile has the form of an annular ring located inside of the RMW of the mean vortex. Figure 3.10 shows the time evolution of maximum tangential velocity at $\theta = 304$ K, maximum potential vorticity at $\theta = 304$ K, and minimum surface pressure. From this figure, we see that heating within the RMW produces an increase of maximum tangential velocity (approximately 9 m s^{-1} over 36 hours), a dramatic increase in maximum PV (approximately 28 PVU over 36 hours), and a rapid decrease in minimum surface pressure (approximately 10 mb over 36 hours).

Figures 3.11-3.15 show the PV evolution for the $\theta = 305$ K and $\theta = 341$ K surfaces. Because of the vertical structure of the diabatic heating profile, the $\theta = 305$ K surface shows an increase in PV during the model simulation, whereas the $\theta = 341$ K surface shows a decrease in PV during the model simulation. For the $\theta = 304$ K surface, we see a contraction of the RMW, consistent with the results of Vigh and Schubert (2009) and Musgrave et al. (2011). The contraction of the RMW and the increase of V_{max} leads to an increase in the overall vortex circulation and the inertial stability within the core of the vortex. Based on the analysis of Schubert et al. (1999), as the relative vorticity increases, the unstable vorticity wave growth rate also increases. Therefore, the hollow PV tower in Case 1 relaxes to a monopole at a faster rate than in the corresponding adiabatic PV tower. DH1 relaxes to a monopole within 24 hours whereas the corresponding adiabatic PV tower relaxes to a monopole within 36 hours.

For the $\theta = 341$ K surface, we see an expansion of the RMW and a thinning of the PV ring. As the RMW increases, a ring of negative PV develops in the core of the vortex. Based on the analysis of Schubert et al. (1999), as the outer ring of PV thins, the unstable vorticity wave growth rate occurs at higher wavenumbers. For this reason, the outer PV ring at the $\theta = 341$ K surface breaks down at azimuthal wavenumber 5. As the tangential velocity increases near the surface, the Rossby length decreases and the Rossby depth increases. This suggests that the secondary circulation produced by the diabatic heating will be suppressed by the large inertial stability of the vortex.

Hack and Schubert (1986) describe the nonlinear response of atmospheric vortices to diabatic heating using the concept of energy efficiency. Specifically, the fraction of the total energy generation that is partitioned to KE generation for the large-scale circulation is dependent on the position of the heating relative to the inertial stability. Because the diabatic heating profile is located within the RMW in the region of high inertial stability, the vortex efficiently extracts kinetic energy from the specified heating source. As the large-scale atmospheric vortex grows in intensity due to increases in PV and relative vorticity, its ability to extract kinetic energy from the specified heating source also increases. This increase in efficiency contributes to a nonlinear coupling between the large-scale circulation and its response to diabatic heating.

3.1.4 DH2: Static Heating Across the RMW

For Case 2, the diabatic heating profile has the form of an annular ring that is stretched across the RMW of the mean vortex. Figure 3.16 shows the time evolution of maximum tangential velocity at $\theta = 304$ K, maximum potential vorticity at $\theta = 304$ K, and minimum surface pressure. From this figure, we see that heating within the RMW produces a modest increase of maximum tangential velocity (approximately 2 m s^{-1} over 36 hours), a small increase in maximum PV (approximately 10 PVU over 36 hours), and decrease in minimum surface pressure (approximately 2.5 mb over 36 hours). Although the variation in maximum tangential wind, maximum PV, and minimum surface pressure are larger than the control experiment, we see here that the diabatic heating in DH2

is less efficient in strengthening the vortex circulation than DH1. Figures 3.17-3.21 shows the PV evolution for the $\theta = 305$ K and $\theta = 341$ K surfaces. As before, because of the vertical structure of the diabatic heating profile, the $\theta = 305$ K surface shows an increase in PV during the model simulation, whereas the $\theta = 341$ K surface shows a decrease in PV during the model simulation. For the $\theta = 304$ K surface, we see a slight expansion of the RMW before unstable PV wave growth mixes high PV into the eye region, consistent with the results of Musgrave et al. (2011). As in DH1, the increase of V_{max} leads to an increase in the overall vortex circulation, an increase in the inertial stability within the core of the vortex, and an increase in the unstable vorticity wave growth rate. However, since the increase of V_{max} is small, the increase in vorticity wave growth rate is also small. DH1 relaxes to a monopole within 24 hours whereas DH2 relaxes to a monopole within 32 hours.

For the $\theta = 341$ K surface, we see a slight contraction of RMW and a thinning of the PV ring. As the RMW decreases, a ring of negative PV develops outside of the vortex core. The outer PV ring undergoes a breakdown at azimuthal wavenumber 3 and during the model simulation, the outer ring elongates into three large anticyclonic gyres. Based on the analysis of Schubert et al. (1999), as the inner ring of PV thins, the unstable vorticity wave growth rate occurs at higher wavenumbers. Therefore, the inner ring undergoes a breakdown at azimuthal wavenumber 5. Since this is a relatively weak vortex, the Rossby length is large and the Rossby depth is small. This suggests that the secondary circulation produced by the diabatic heating will be horizontally elongated, as shown by the anticyclonic gyres produced in the outflow layers. Following the energy efficiency argument of Hack and Schubert (1986), because the diabatic heating profile is located just outside the RMW, the vortex inefficiently extracts kinetic energy from the specified heating source. Therefore, even though a secondary circulation develops due to heating source, the heating source does not efficiently amplify the mean vortex circulation. Therefore, there is little coupling between the large-scale circulation and the diabatic heating source.

3.1.5 DH3: Static Heating Outside the RMW

For Case 3, the diabatic heating profile has the form of an annular ring that is outside the RMW of the mean vortex. Figure 3.22 shows the time evolution of maximum tangential velocity at $\theta = 304$ K, maximum potential vorticity at $\theta = 304$ K, and minimum surface pressure. This figure shows that diabatic heating partially or completely outside the RMW has little effect on the intensity of the mean vortex compared to the control experiment. Therefore, the diabatic heating in DH3 is extremely ineffective in strengthening the primary circulation of the vortex.

Figures 3.23-3.27 show the PV evolution for the $\theta = 305$ K and $\theta = 341$ K surfaces. For the $\theta = 304$ K surface, the evolution of PV is similar to evolution of PV for the control experiment. This demonstrates that there is little to no increase in vorticity of PV in the heating region or in the mean vortex, consistent with Musgrave et al. (2011). However, DH3 relaxes to a monopole at a slower rate than in the control experiment. For the $\theta = 341$ K surface, we see the thinning of the PV ring. During the model simulation, a thin ring of negative PV develops outside of the vortex core. The outer PV ring undergoes a breakdown at azimuthal wavenumber 4 and during the model simulation, the outer ring elongates into four large anticyclonic gyres. There is an increase of PV on the outer edge of the inner PV ring which causes unstable vorticity wave growth at higher wavenumbers. Therefore, the inner ring undergoes a breakdown at azimuthal wavenumber 4 and during the model simulation, the inner ring begins to elongate to form four large cyclonic gyres near the RMW. The large scale gyres in the outflow layer are due to the fact that the Rossby length is large and the Rossby depth is small for DH3.

Similar to DH2, the conversion of total potential energy to the kinetic energy of the balanced flow becomes less efficient as the heating is removed from the region of highest inertial stability. Since the energy efficiency depends on the position of the heating relative to the inertial stability, the location of the heating profile creates an inefficient energy partition. In this case, the extraction of kinetic energy from the specified heating source is virtually non-existent as the PV evolution of

DH3 is very similar to the PV evolution of the control experiment. As the vortex circulation weakens, its ability to extract kinetic energy from the specified heating source also decreases. Therefore, the heating profile causes no noticeable effect on the vortex.

This study examined the response of an idealized vortex to a ring of diabatic heating. The vortex response was assessed based on the location of the heating: within the RMW, stretched across the RMW, or outside the RMW. The vortex response, particularly in intensity, is extremely sensitive to the placement of the diabatic heating. Any heating contained within the RMW produces a sharp increase in intensity, corresponding to the deepening stage of a tropical cyclone and also providing the most likely scenario for rapid intensification of the idealized TC. The placement of the heating within the high inertial stability region within the RMW is still the most efficient overall at converting the energy from the heat source into kinetic energy.

3.2 The Effect of Nonconservative Processes on Sheared Hollow PV Towers

In the previous section, we demonstrated how the location of static diabatic heating affects the evolution of a hollow PV tower. However, since the radial structure of static diabatic heating remains fixed as the vortex evolves, there are two primary weaknesses with the simple diabatic forcing used in the previous section. First, the diabatic heating remains as an annular structure as the hollow PV tower undergoes barotropic-baroclinic instability. Even though the increase of PV can be especially rapid in the lower troposphere near the eyewall leading to a hollow PV tower, it is unrealistic to assume that the radial structure of the diabatic heating remains fixed throughout the PV mixing process. Second and most importantly, because the diabatic heating has a fixed radial structure, the diabatic heating cannot interact with the primary and secondary circulation of the vortex. In this section, we illustrate how nonconservative forcing (diabatic heating, surface friction, and vertical diffusion) affects the evolution of sheared hollow PV towers.

3.2.1 Overview of Numerical Model

For these experiments, we consider hydrostatic motions of a dry, compressible atmosphere on an f-plane. The numerical model used here is based on the three-dimensional hydrostatic primitive equations in sigma coordinates *(x,y,σ)*, where *x* and *y* are in the zonal and meridional directions, respectively, and

$$\sigma = \frac{p - p_{top}}{p_s - p_{top}} = \frac{p - p_{top}}{p_\star}, \tag{3.10}$$

where $p_\star = p_s - p_{top}$, p_s, and p_{top} are the surface and top pressures, and p_{top} is a constant, taken here to be 100 mb. Then the upper and lower boundary conditions are $\dot{\sigma} = 0$ at $\sigma = 0$ and $\sigma = 1$, where $\dot{\sigma} = D\sigma/Dt$ is the vertical σ-velocity and D/Dt is the material derivative. The governing equations are given by:

$$\frac{Du}{Dt} = fv - \frac{\partial \Phi}{\partial x} - \frac{RT\sigma}{p}\frac{\partial p_\star}{\partial x}, \tag{3.11}$$

$$\frac{Dv}{Dt} = -fu - \frac{\partial \Phi}{\partial y} - \frac{RT\sigma}{p}\frac{\partial p_\star}{\partial y}, \tag{3.12}$$

$$\frac{D\theta}{Dt} = \frac{Q}{\Pi}, \tag{3.13}$$

$$\frac{\partial p_\star}{\partial t} = -\int_0^1 \left(\frac{\partial u p_\star}{\partial x} + \frac{\partial v p_\star}{\partial y}\right) d\sigma, \tag{3.14}$$

$$p_\star \dot{\sigma} = \sigma \frac{\partial p_\star}{\partial t} - \int_0^\sigma \left(\frac{\partial u p_\star}{\partial x} + \frac{\partial v p_\star}{\partial y}\right) d\sigma, \tag{3.15}$$

$$\frac{\partial \Phi}{\partial \sigma} = -\frac{RTp_\star}{p}, \tag{3.16}$$

where *R* is the specific gas constant for dry air, Φ is the geopotential, and Q is the specified heat source. The remaining variables have their usual meaning. The model is vertically discretized using

the Charney-Phillips (CP) grid. In this grid, horizontal velocities and geopotential are carried on integer layers, whereas potential temperature and vertical mass fluxes are carried on the half-integer levels. The vertical discrete equations are designed to satisfy the four constraints advocated by Arakawa and Lamb (1977). The model is horizontally discretized using the Arakawa C grid with a doubly periodic boundary domain and horizontal advection is discretized using the fifth-order upstream scheme. More information on the model discretization and the model characteristics can be found in Appendix B.

Moist processes are not included explictly in this model, instead diabatic heating is parameterized using the CISK-type parameterization from Wang and Holland (1995).

$$Q = \begin{cases} \alpha\eta(\sigma)\zeta_B & \zeta_B > 0 \\ 0 & \zeta_B < 0 \end{cases} \tag{3.17}$$

where ζ_B is the relative vorticity at the lowest model level, α is the heating amplitude, and $\eta(\sigma)$ is the vertical heating distribution,

$$\eta(\sigma) = b\sin(\pi\sigma)\exp(-\delta\sigma), \tag{3.18}$$

where b and δ are non-dimensional parameters which define the scale and shape of the vertical heating profile. The vertical distribution of heating is given by Figure 3.28. This heating profile enables the diabatic heating to interact directly with the primary circulation through boundary layer convergence. Wang and Holland (1995) used this heating profile to investigate the binary interaction of tropical cyclones. In their paper, they found that the heating profile is relatively insensitive to variations in the vertical distribution of heating, but the vortex is sensitive to changes in amplitude. For this reason, we choose weak diabatic heating for our simulations ($\alpha = 0.35$) and choose the vertical distribution of heating such that the diabatic heating maximizes in the mid-troposphere ($b = 0.675$ and $\delta = 0.65$). Even though the weaknesses of the CISK parameterization have been well-documented, this heating profile gives a first approximation of how interactive diabatic heating

affects the evolution of a hollow PV tower. The initial condition for the relative vorticity has the separable form $\zeta(r, \phi, \sigma) = [\zeta_{sym}(r) + \zeta_{pert}(r, \phi)]F(\sigma)$, where $\zeta_{sym}(r)$ and ζ_{pert} are given by (2.5) and (2.7), respectively. The vertical structure is given by

$$F(\sigma) = \begin{cases} \sin\left(\frac{\pi}{2} \times \frac{\sigma - \sigma_u}{1 - \sigma_u}\right) & \sigma > \sigma_u \\ 0 & \sigma \leq \sigma_u. \end{cases} \tag{3.19}$$

For the hollow tower in these experiments, ζ_2 = 0.00125 s^{-1} and r_1, r_2, r_3, r_4 = 23, 27, 38, 42 km, respectively. This gives a maximum initial velocity of approximately 15 m/s. In this section, we perform two experiments: a hollow PV tower in the absence of environmental flow (labeled CH0) and a hollow PV tower in simple zonal shear (labeled CH1).

3.2.2 CH0: Nonconservative Forcing in the Absence of Environmental Flow

Figure 3.29 shows the time evolution of maximum relative vorticity at $\sigma = 0.93$, maximum potential vorticity at $\sigma = 0.93$, and minimum surface pressure of experiment CH0. Because the diabatic forcing is proportional to boundary layer convergence, this implies that the location of the heating is within the RMW of the vortex. This produces a large increase of relative vorticity (and thus inertial stability) and potential vorticity, while causing a decrease in minimum surface pressure, consistent with the results of DH0.

Figures 3.30-3.35 show the PV evolution for the $\sigma = 0.21$ and $\sigma = 0.93$ surfaces. Because of the vertical structure of the diabatic heating, the $\sigma = 0.93$ surface shows an increase in PV during the model simulation, whereas the $\sigma = 0.21$ surface shows a decrease in PV during the model simulation. For the $\sigma = 0.93$ surface, we see a contraction of the RMW, consistent with the results of DH0. The contraction of the RMW and the increase of relative vorticity leads to an increase in the overall vortex circulation and the inertial stability within the core of the vortex. Moreover, the PV ring for the $\sigma = 0.93$ surface relaxes to a monopole with 18 hours, a faster rate than DH0. This indicates that surface friction enhances inward PV mixing of the hollow tower and makes the PV

tower more susceptible to breakdown and mixing. For the $\sigma = 0.21$ K surface, we see an expansion of the RMW, similar to DH0. However, in contrast to DH0, the vortex maintains its ring thickness. Therefore, the PV ring on this surface breaks down at azimuthal wavenumber-3. This shows that vertical diffusion helps to maintain the overall structure of the PV tower by transporting momentum and PV from the mid-troposphere to the upper-troposphere. Due to the increase of static stability, the Rossby length decreases and the Rossby depth increases. Although the direct effects of friction are confined primarily to the boundary layer, the inner core is indirectly affected by boundary layer friction through the secondary circulation resulting from Ekman pumping. As the vortex (and the diabatic heating through boundary layer convergence) continues to increase in strength, the vertical extent and upward penetration of Ekman pumping also increases, resulting in a deeper secondary circulation.

Similar to DH0, we can also use the energy efficiency argument to describe the nonlinear response of atmospheric vortices to diabatic heating. Even though boundary layer frictional inflow and vertical diffusion cause a sink to PV, the location of diabatic heating enables a net growth of vorticity (and thus PV) throughout the model simulation. Because the diabatic heating profile is located within the RMW in the region of high inertial stability, the vortex efficiently extracts kinetic energy from the specified heating source. This efficient extraction of kinetic energy from the diabatic heating enables a net increase in the strength of the vortex. As the large-scale atmospheric vortex grows in intensity due to increases in PV and relative vorticity, its ability to extract kinetic energy from the specified heating source also increases. This increase in efficiency contributes to a nonlinear coupling between the large-scale circulation and its response to diabatic heating.

3.2.3 CH1: Nonconservative Forcing under Zonal Shear

For this experiment, we will look at the effect of diabatic forcing on the dynamics of a hollow PV tower in vertical shear. This experiment is meant to simulate the resiliency of a high Rossby number, barotropically unstable vortex during an episode of external vertical shear including the

effects of diabatic forcing. Previous studies (e.g., Jones 1995) have looked at the vertical alignment of a monotonically stable vortex. This experiment will extend these studies by examining the vertical alignment of a rapidly rotating, barotropically unstable vortex in unidirectional vertical shear. In this experiment, we will use the same initial conditions as in the control experiment, except the background environmental wind will have the simple zonal shear:

$$U(\sigma) = u_0 \cos(\pi\sigma) \tag{3.20}$$

Therefore, the background wind is $-u_0$ at the surface and u_0 at the model top. As in Chapter 2, $u_0 = 2$ m/s for this experiment.

Figure 3.36 shows the time evolution of maximum relative vorticity at $\sigma = 0.93$, maximum potential vorticity at $\sigma = 0.93$, and minimum surface pressure of CH1. Similar to CH0, the diabatic forcing produces a large increase of relative vorticity (and thus inertial stability) and potential vorticity, while causing a decrease in minimum surface pressure. The evolution of the hollow PV tower is shown in Figs. 3.36-3.40. At mid-levels, the speed of the vortex motion is close to the speed of the environmental flow. At the surface, the vortex moves significantly slower than the surface environmental flow. At the upper levels, the vortex moves faster than the environmental slow. In general, the vertical tilt of the vortex increases with time, but is much smaller than that which would be implied by simple advection by the basic flow.

Figures 3.41-3.45 look at the PV evolution for the $\sigma = 0.21$ and $\sigma = 0.93$ surfaces. Here it can be seen that the initial motion at the surface has a northward component, while the motion of the upper-level vortex has a southward component, shown in Fig. 3.41. This results in the development of a NW-SE tilt in the vortex after 12 hours, shown in Fig. 3.42. The continued rotation then leads to the lower-level center moving southward and the upper-level center moving northwards after 24 hours, as shown in Figure 3.43. This suggests that the upper- and lower-level centers rotate cyclonically about the mid-level center. The results from these simulations are consistent with the

adiabatic vortex-in-shear simulations presented in Chapter 2. The major difference is that at the end of 30 hours, the vortex has returned to vertical alignment, whereas in Chapter 2, the vortex develops a distinct N-S tilt. Contrary to the results of Chapter 2, the vortex vertically aligns within the model simulation time. To determine the reason for this, we use three diagnostics: penetration depth, Rossby deformation radius, and vortex beta Rossby number.

The penetration depth for our vortex is given by:

$$H \approx \frac{IL}{N} \tag{3.21}$$

where $I = \sqrt{(f + 2v/r)(f + \zeta)}$ is the inertial stability, L is the horizontal scale of the flow, and N is the Brunt-Vaisala frequency. Since the inertial stability of the vortex decreases with height, the vertical penetration of the induced flow also decreases with height. In particular, above the $\sigma = 0.5$ surface, the penetration depth is very weak. Therefore, upper-level PV anomalies have a negligible impact on lower-level PV anomalies. Furthermore, since the inertial stability of the upper-level PV anomalies continues to decrease during the model simulation, the penetration depth also decreases for the upper-level PV anomalies. This implies that the induced flow from upper-level anomalies becomes weaker over time. In contrast, below the $\sigma = 0.5$ surface, the penetration depth is larger. Therefore, lower-level PV anomalies will have an important impact on lower-level PV anomalies. Since the inertial stability of the lower-level PV anomalies continues to increase during the model simulation, the penetration depth also increases for the lower-level PV anomalies. This implies that the induced flow from the lower-level anomalies amplifies over the model simulation time.

For this vortex, lower-level PV anomalies drive the alignment rate of the vortex, and as the diabatic heating increases the strength of the vortex, the upward penetration of lower level PV anomalies and Ekman pumping also increases. These results are also consistent with the results seen by Smith et al. (2000). Using quasigeostrophic arguments, Smith et al. (2000) showed that the co-rotation of their two vortices is due to induced flow caused by the PV anomalies associated with

each vortex. Since the PV anomalies near the surface are increasing in magnitude, the co-rotation rate of the upper and lower level PV anomalies will also increase, leading to vertical alignment. The Rossby radius of deformation for our vortex is given by:

$$R_D \approx \frac{NH}{I} \tag{3.22}$$

where H is the vertical depth of the vortex. As mentioned in Chapter 2, Reasor and Montgomery (2001) discovered that the rate of alignment for a tilted quasi-geostrophic vortex depends upon the internal Rossby deformation radius. For internal Rossby deformation radius larger than the horizontal scale of the tilted vortex, an azimuthal wavenumber-1 quasi-mode exists, which causes a steady cyclonic propagation of the vortex and resistance to differential rotation. For internal Rossby deformation radius smaller than the horizontal vortex scale, the quasi-mode disappears into the continuous spectrum of VRWs and alignment proceeds through the irreversible redistribution of PV by the sheared VRWs.

Since diabatic heating causes the inertial stability of the vortex to increase, the Rossby deformation radius decreases, which causes the rate of alignment for the vortex to increase through emission of sheared VRWs. This is shown in Figs. 3.36-3.40, where sheared VRWs are emitted as the vortex aligns. Furthermore, according to Schecter (2008), when the Rossby deformation radius decreases, the critical radius of damping moves inward. As the critical radius moves inward, it will move to an area of greater PV gradient and thus critical layer damping will increase. As a result, the vortex's tilt will decrease.

As shown in Chapter 2, the internal Rossby deformation radius also affects another parameter called the vortex beta Rossby number, R_β (Moller and Montgomery 2000; Enagonio and Montgomery 2001). In the nondivergent limit, the vortex beta Rossby number scales as:

$$R_\beta \approx \frac{V'}{L'^2 \frac{d\bar{\zeta}}{dr}} \tag{3.23}$$

R_β provides a measure of how important nonlinear advection is compared to the VRW restoring mechanism. For R_β much less than unity, perturbations on an everywhere monotonic mean vortex are expected to disperse as VRWs. For our experiment, diabatic heating causes an increase in the mean vorticity gradient near the surface, as the vortex relaxes to a monopole. This causes R_β to decrease during the model simulation, whereby perturbations caused by shear forcing are dispersed as sheared VRWs.

Reasor and Montgomery (2001) demonstrated that as λ_R tends to 0, R_β tends to 0, implying that the VRW restoring mechanism dominates over nonlinear advection. Another consequence of this dependence of R_β on λ_R is that the linear VRW dynamics will accurately capture the alignment process for a wider range of shear strength, the smaller λ_R is. Our results are consistent with these observations. As PV evolves during the model simulation, we see that sheared VRWs are emitted by the vortex. Furthermore, during the model simulation, the resistance to alignment disappears, as the quasi-mode disappears in the continuous spectrum of VRWs.

3.3 Summary and Application to Tropical Cyclones

In this chapter, we have extended the results from Chapter 2, namely the effect of diabatic forcing on the evolution of a baroclinic hollow PV tower in zero environmental flow and in external zonal shear. For our first series of experiments, we applied a specified source of diabatic heating similar to the heating profile of Yanai et al. (1973) at various locations within our vortex and illustrated how the vortex response to diabatic heating depends on the location of the heating. The vortex is very sensitive to the placement of the diabatic heating relative to the vortex profile. For heating contained within the RMW, there was a sharp increase in velocity and PV, whereas heating contained outside the RMW produced a minimal increase in velocity and PV. Using the energy

efficiency argument of Hack and Schubert (1986), heating within the RMW enables an efficient extraction of kinetic energy from the diabatic heating source. This efficiency leads to a nonlinear coupling between the vortex strength and the diabatic heating source. Heating outside the RMW causes an inefficient extraction of kinetic energy from the diabatic heating source. Therefore, the diabatic heating outside of the RMW has little influence on the development of the vortex.

For our second series of experiments, we represented the diabatic heating by a CISK-type parameterization. Because the diabatic forcing is proportional to the boundary layer convergence (and thus the Ekman pumping), this implies that the location of the heating is within the RMW of the vortex. This produces a large increase of inertial stability, while causing a decrease in minimum surface pressure. The addition of surface friction enhances inward PV mixing of the hollow tower, whereas the addition of vertical diffusion helps to maintain the overall structure of the PV tower by transporting momentum from middle-levels to the upper-troposphere. For the vortex-in-shear experiment, the initial response of the vortex to the vertical shear is to tilt downshear. The upper- and lower-level centers then began to rotate cyclonically about the midlevel center, causing both leftward and rightward movement relative to the vertical shear. As the inertial stability of the vortex increases due to diabatic heating, the wavenumber-1 quasimode disappears into the continuous spectrum of VRWs, leading to vortex alignment. Because of the increase of inertial stability of the vortex, the resonant damping of the quasimode, as in Schecter et al. (2002), becomes very efficient as the critical radius moves inward to a higher region of PV gradient. Furthermore, since L/λ_R and R_β are small, the vortex resists shear by emitted sheared VRWs in accordance with linear VRW theory.

These results affirm the idea that strong tropical cyclones efficiently radiate sheared VRWs in order to resist vertical shear. Furthermore, since strong tropical cyclones will also have strong PV gradients outside of the RMW, this suggests that strong tropical cyclones also have strong decay rates of the quasi-mode structure induced by the vortex tilt. When the inertial stability of a tropical

cyclone increases such that the horizontal scale is a non-negligible fraction of the global internal deformation scale, then the inviscid damping by sheared VRWs leads to rapid reduction of the tilt. From the results of this chapter, diabatic heating simply increases the efficiency of resonance damping mechanism through the emission of VRWs.

When a hurricane is forced by vertical shear, the observations suggest that the vortex tilt is generally oriented downshear to downshear-left when the decay rate of the quasi-mode is non-negligible, consistent with the results from Chapter 2. Diabatic forcing enables a higher decay rate of the quasi-mode, which allows the vortex to resist the effects of vertical shear. For a mature tropical cyclone whose structure is maintained by moist convection, the results in this chapter indicate that a tropical cyclone will resist the effects of vertical shear by the emission of convectively-coupled VRWs and through the resonant damping of the quasi-mode induced by the vertical shear. Therefore, for a given environmental vertical shear profile, the mature tropical cyclone will be less prone to breakdown and dissipation. As stated in Chapter 2, the downshear-left location of convective asymmetry observed in hurricanes forced by vertical shear may be in the first approximation a consequence of dry adiabatic VRW dynamics; however, diabatic heating and Ekman pumping play a vital role in the maintenance of a tropical cyclone in vertical shear.

Table 3.1: Specification of diabatic heating $\hat{Q}(r)$ used in model. The first column uniquely identifies the bounding radii r_1, r_2, r_3, r_4 used in any given case.

Label	$r_1(km)$	$r_2(km)$	$r_3(km)$	$r_4(km)$
DH1	5	9	20	24
DH2	23	27	38	42
DH3	41	45	56	60

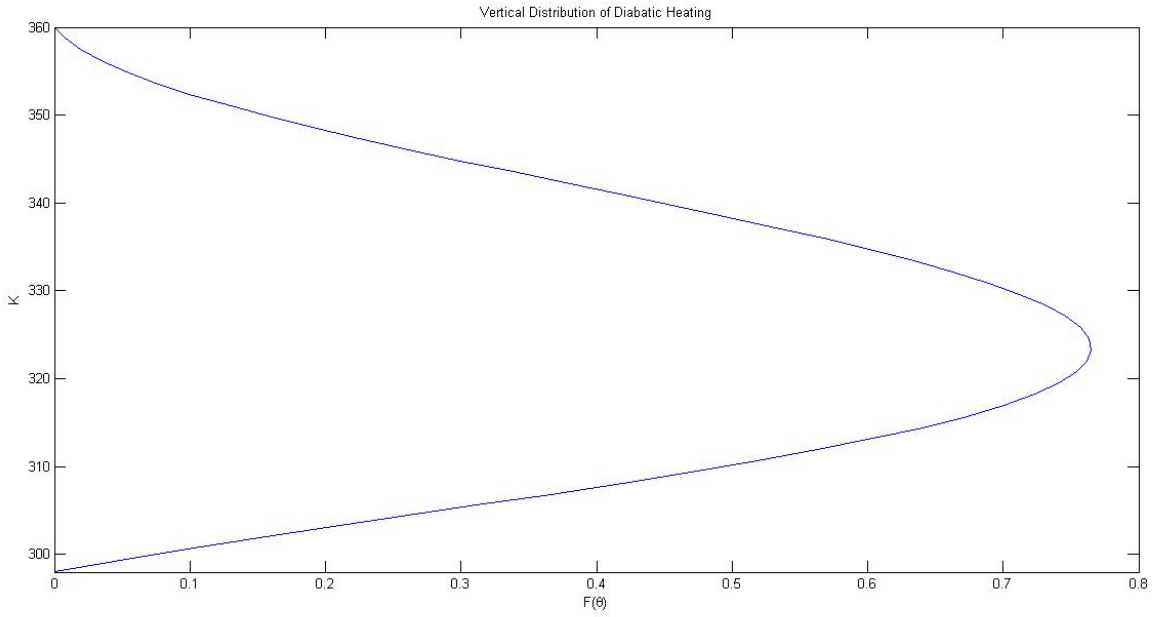

Figure 3.1: The vertical structure of diabatic heating as a function of θ.

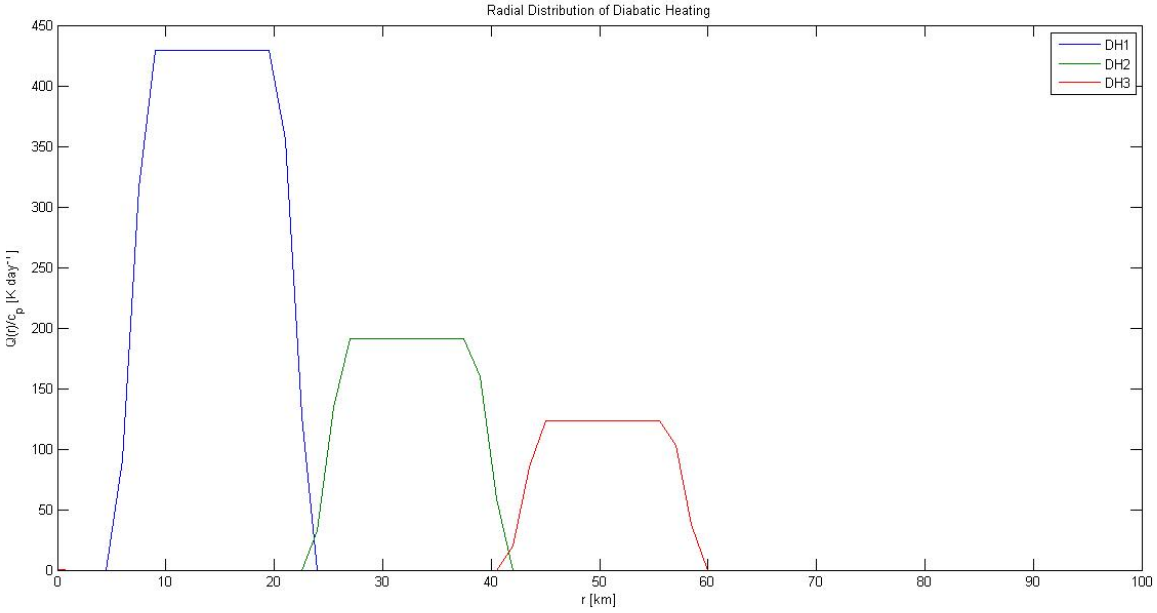

Figure 3.2: The radial distribution of diabatic heating $\hat{Q}(r)/c_p$ as a function of radius.

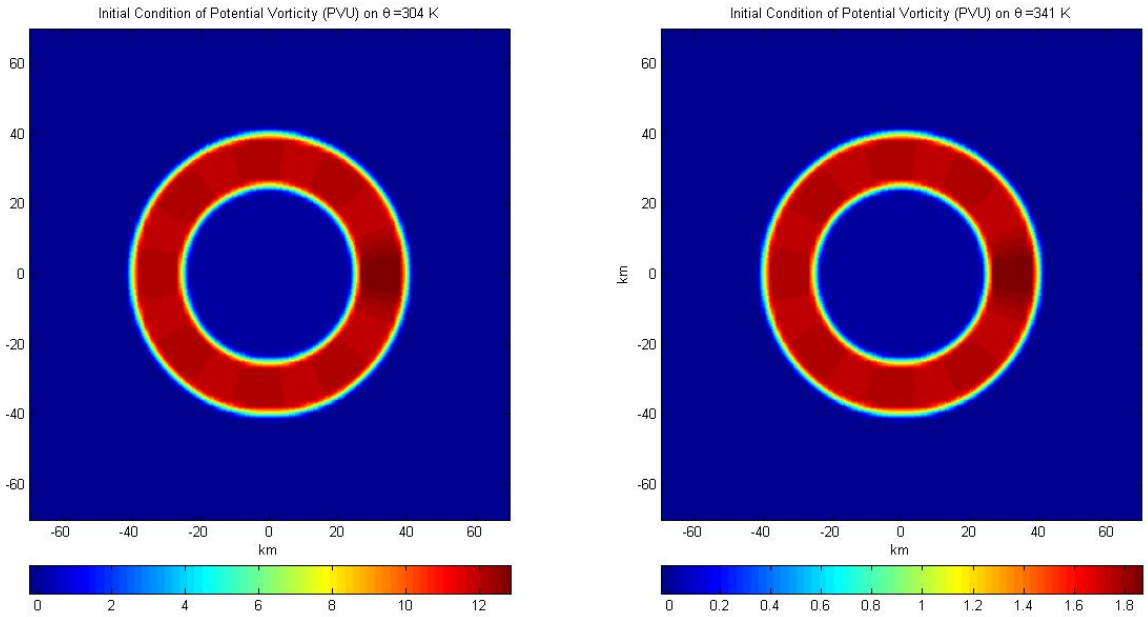

Figure 3.3: The initial condition for the hollow PV tower.

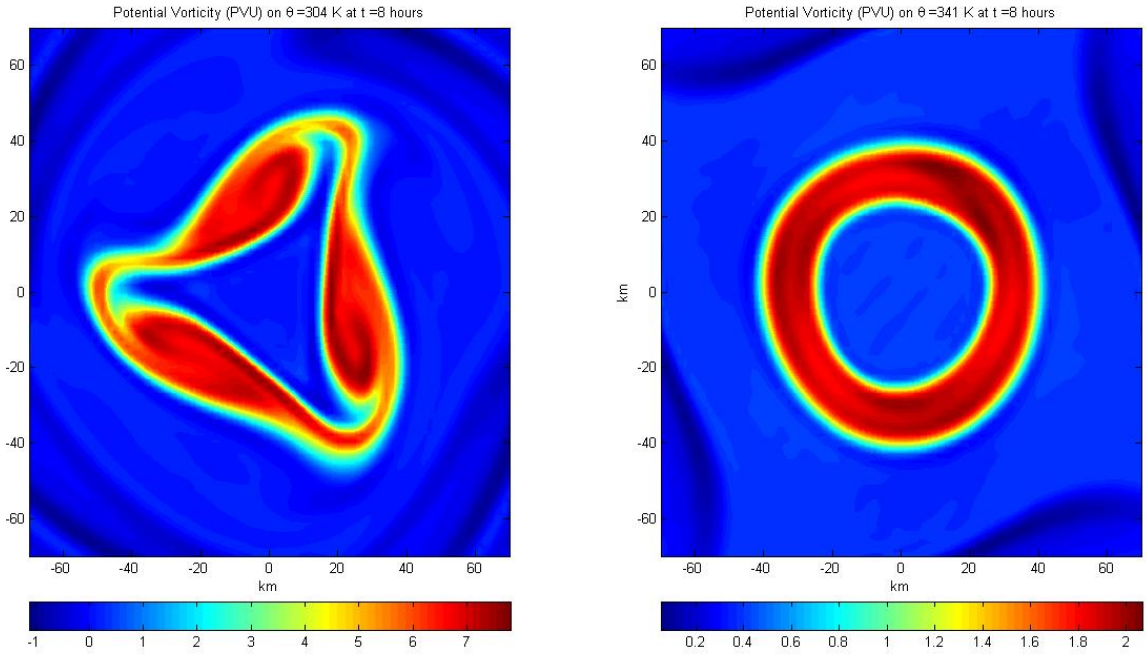

Figure 3.4: Evolution of PV Tower at 8 hours.

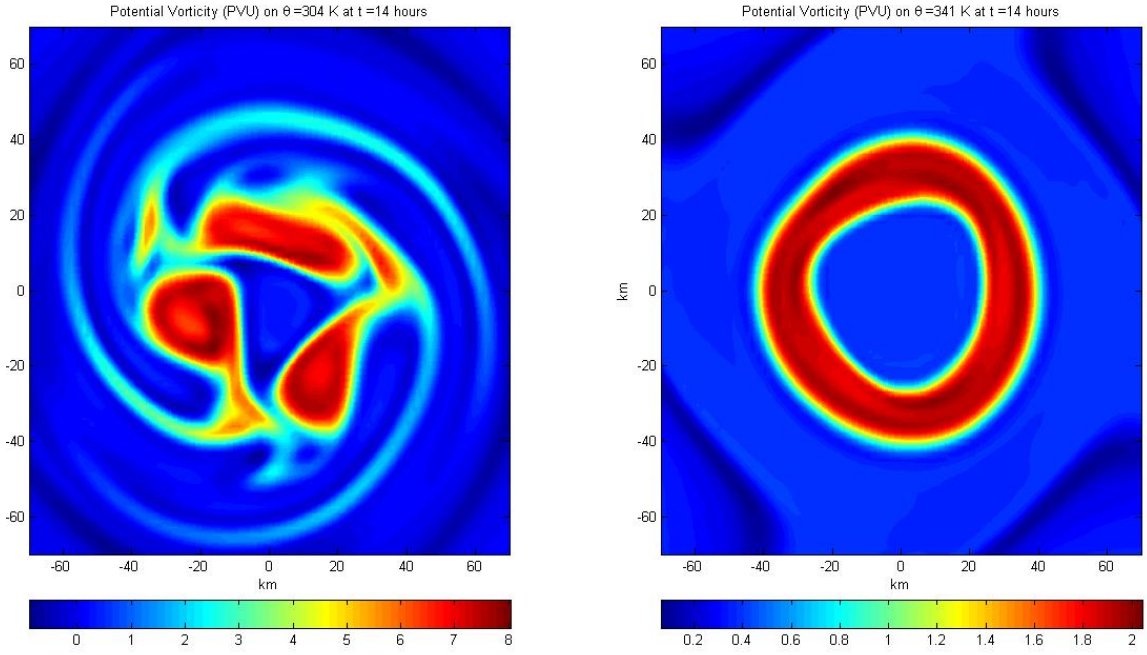

Figure 3.5: PV Evolution of $\theta = 304$ K and $\theta = 341$ at 14 hours.

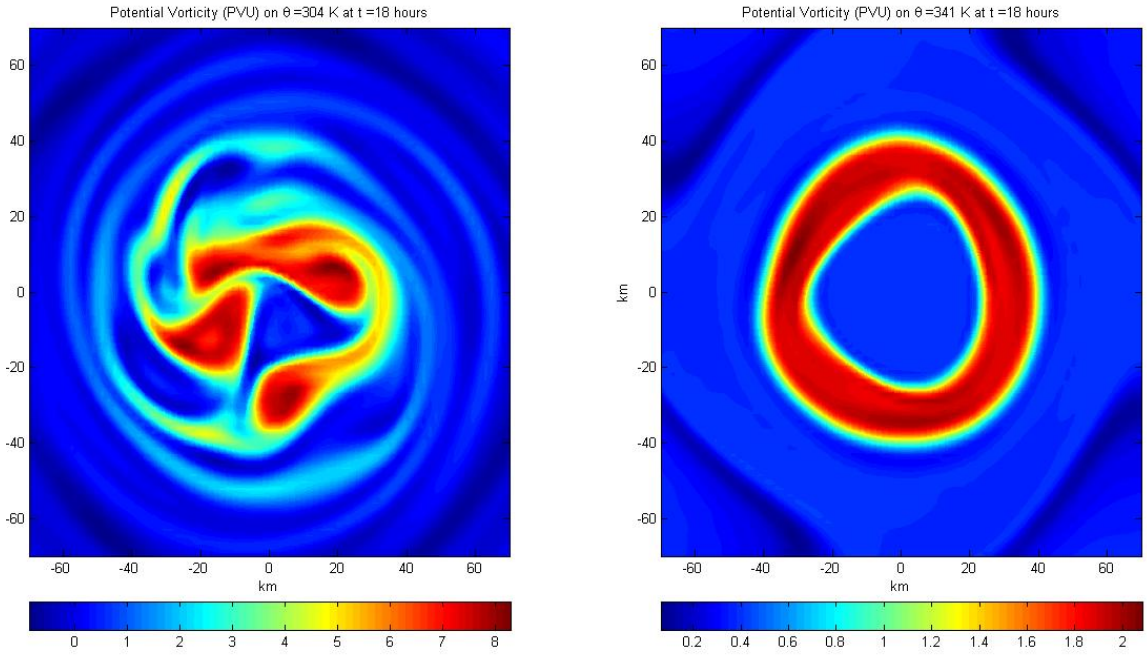

Figure 3.6: PV Evolution of $\theta = 304$ K and $\theta = 341$ at 18 hours.

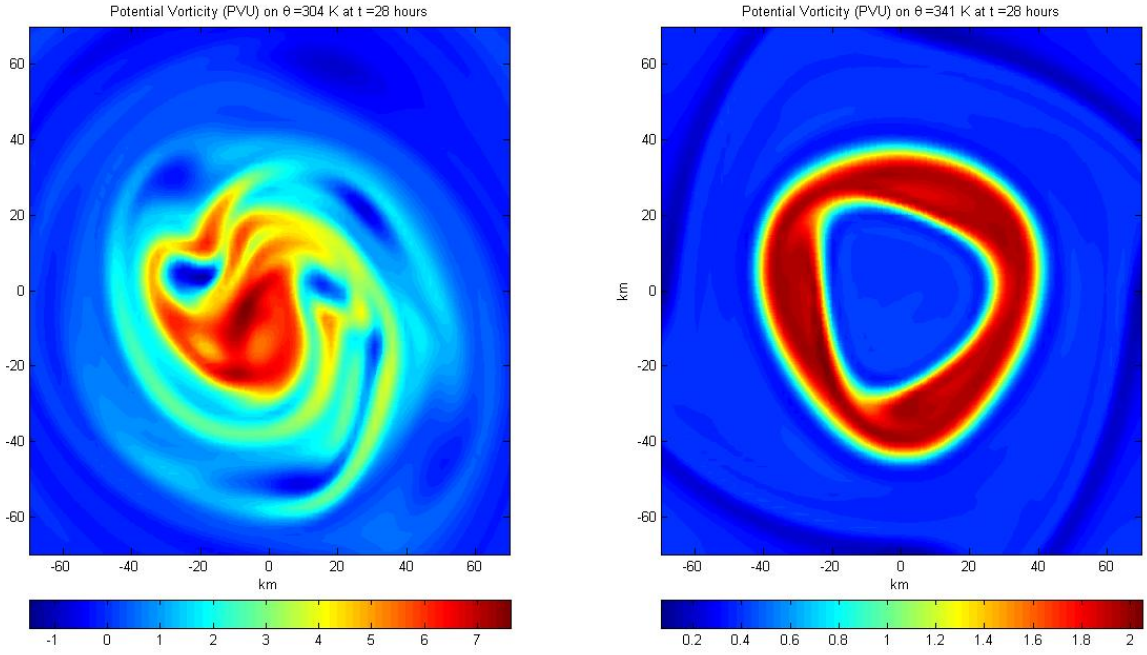

Figure 3.7: PV Evolution of $\theta = 304$ K and $\theta = 341$ at 28 hours.

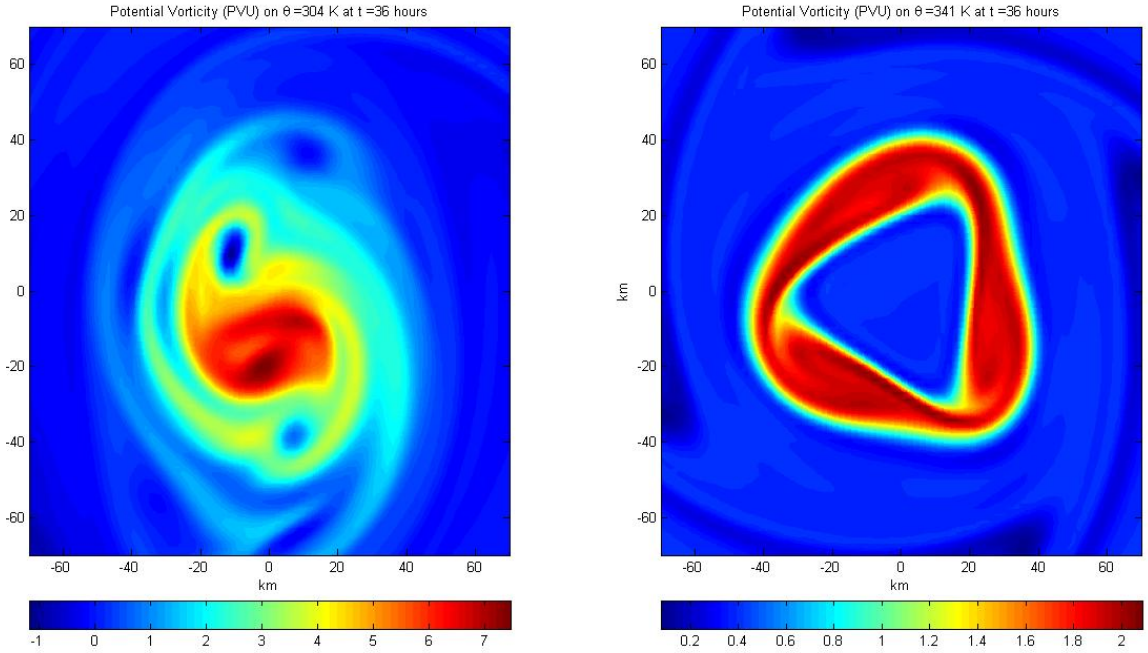

Figure 3.8: PV Evolution of $\theta = 304$ K and $\theta = 341$ at 36 hours.

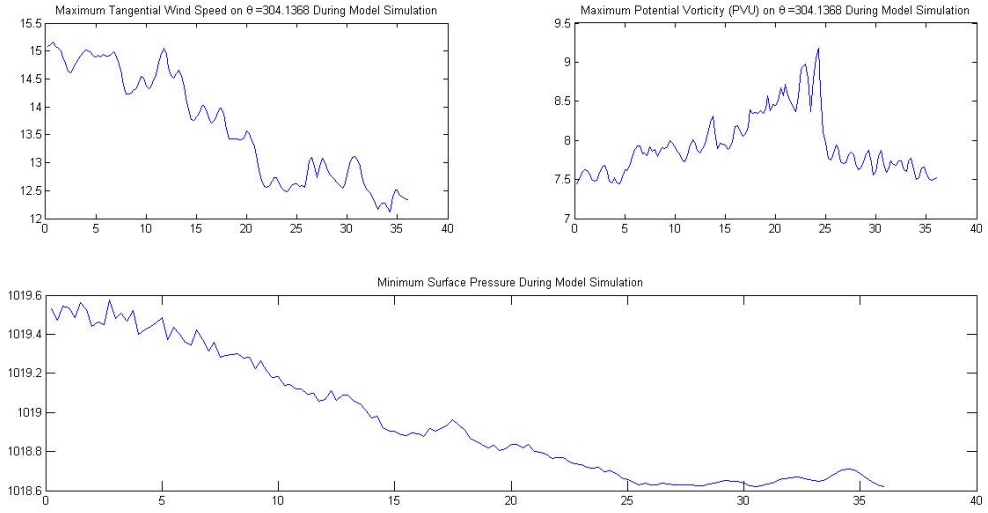

Figure 3.9: Time evolution of maximum tangential velocity, minimum surface pressure, and maximum potential vorticity for control experiment.

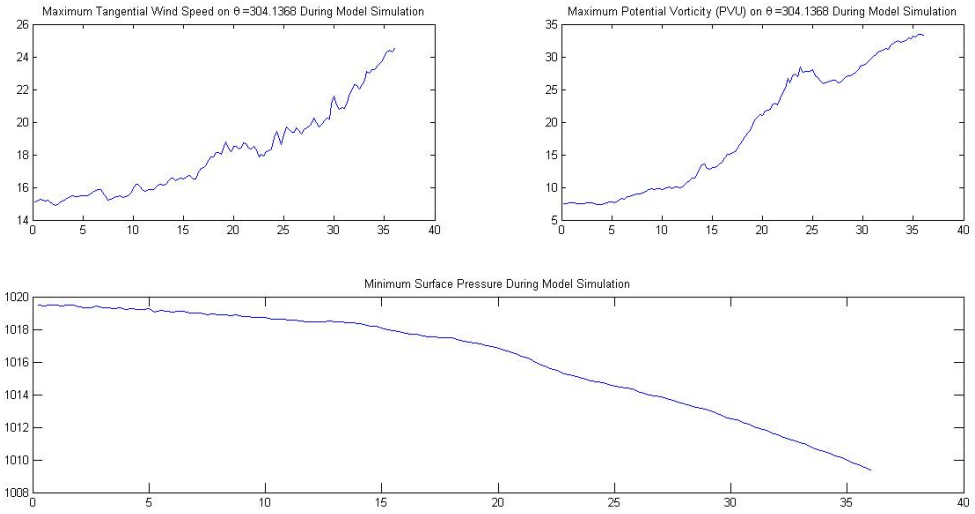

Figure 3.10: Time evolution of maximum tangential velocity, minimum surface pressure, and maximum potential vorticity for DH1.

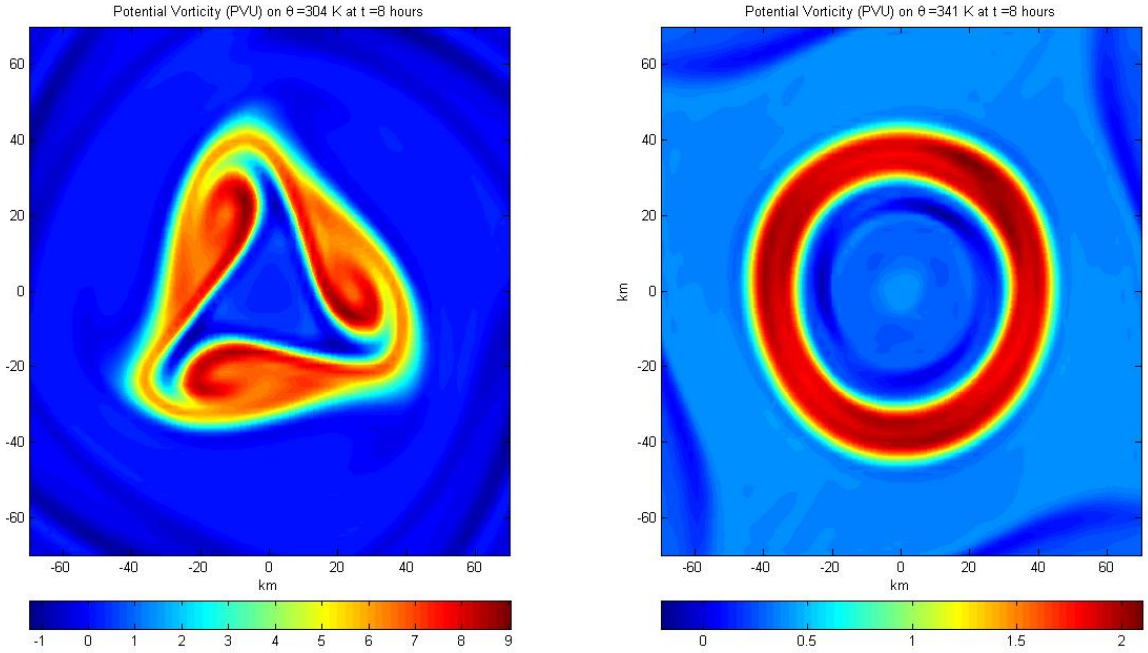

Figure 3.11: PV Evolution of DH1 on $\theta = 304$ K and $\theta = 341$ at 8 hours.

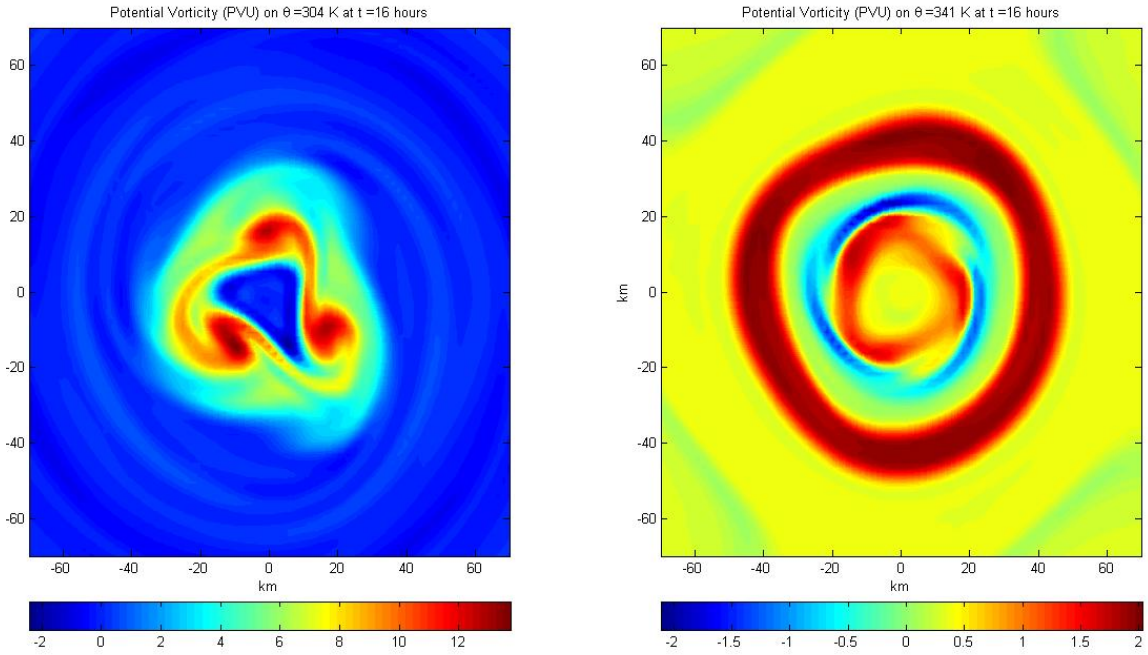

Figure 3.12: PV Evolution of DH1 on $\theta = 304$ K and $\theta = 341$ at 16 hours.

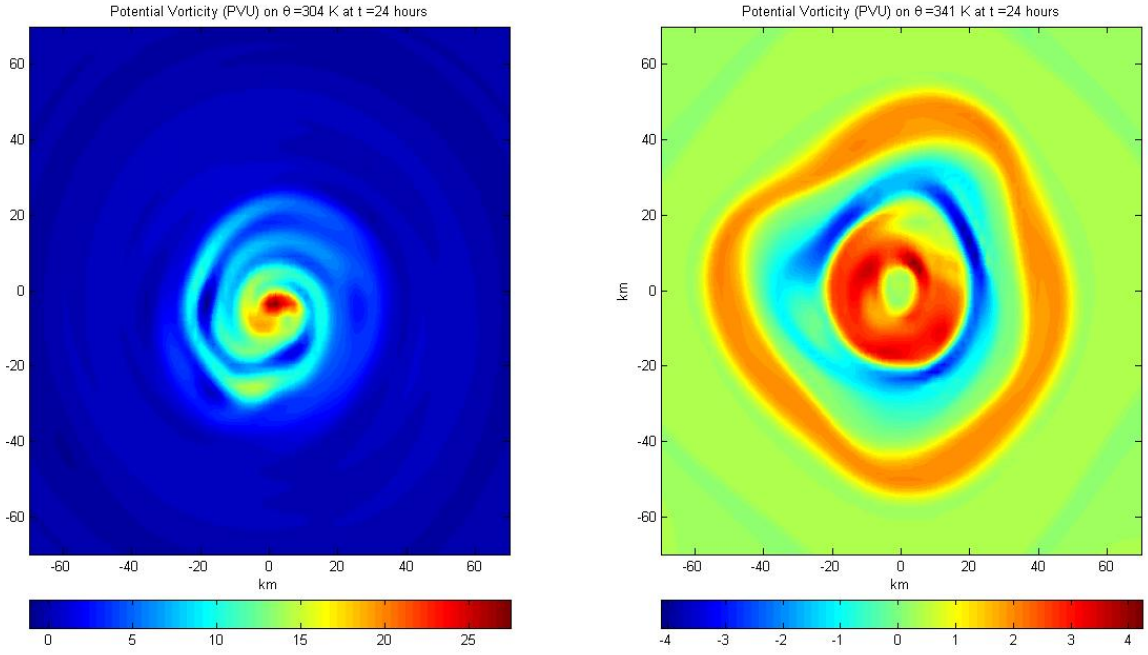

Figure 3.13: PV Evolution of DH1 on $\theta = 304$ K and $\theta = 341$ at 24 hours.

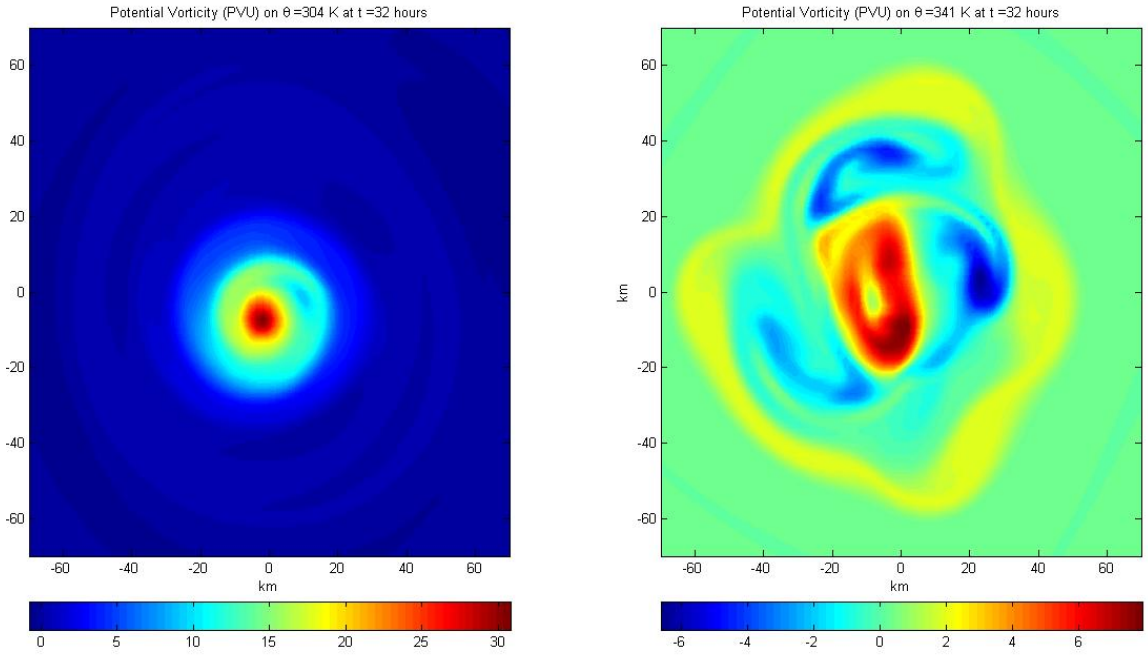

Figure 3.14: PV Evolution of DH1 on $\theta = 304$ K and $\theta = 341$ at 32 hours.

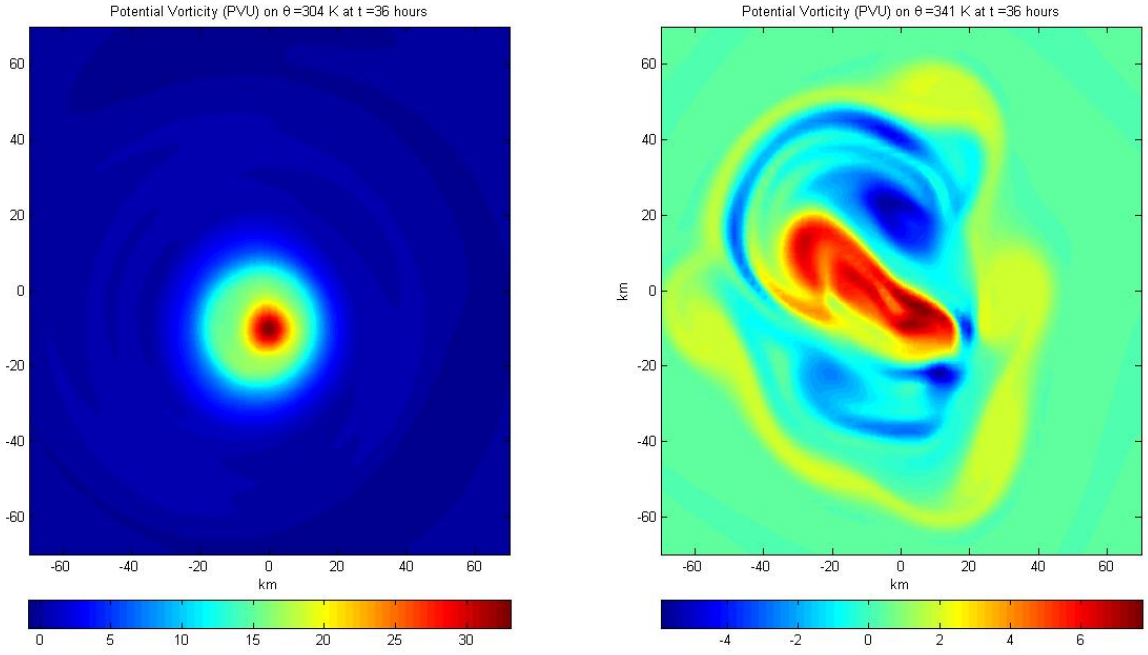

Figure 3.15: PV Evolution of DH1 on $\theta = 304$ K and $\theta = 341$ at 36 hours.

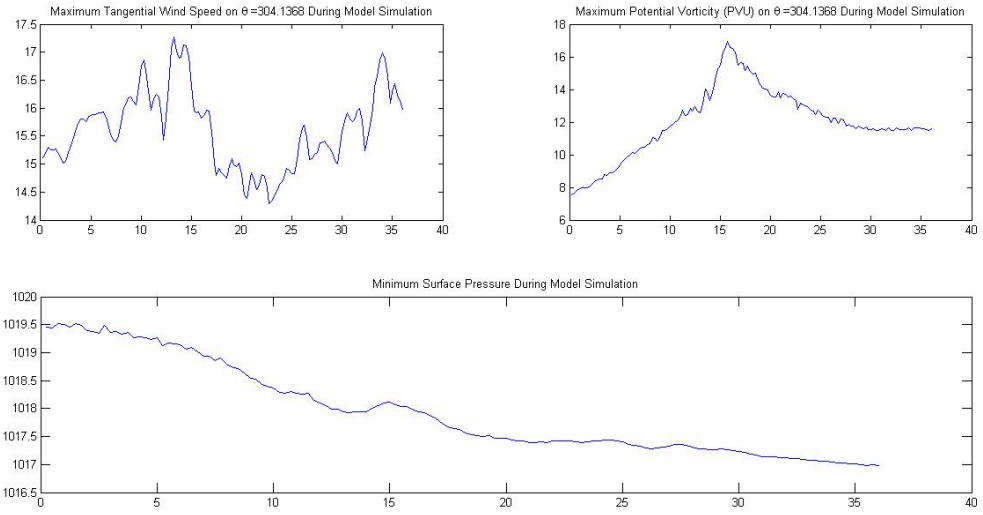

Figure 3.16: Time evolution of maximum tangential velocity, minimum surface pressure, and maximum potential vorticity for DH2.

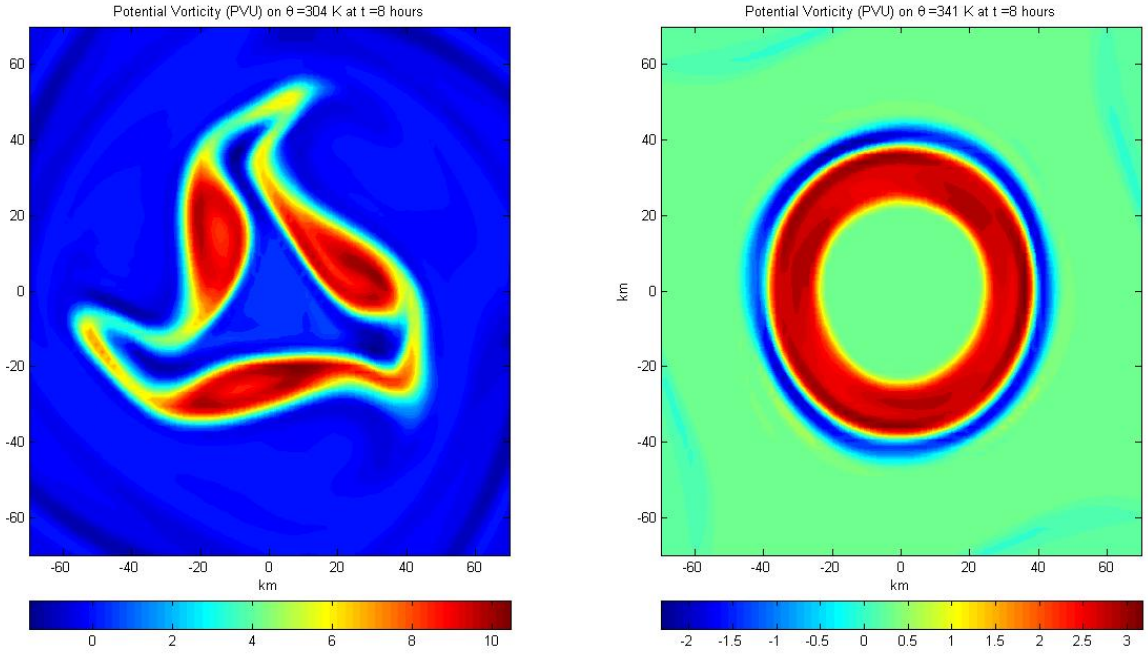

Figure 3.17: PV Evolution of DH2 on $\theta = 304$ K and $\theta = 341$ at 8 hours.

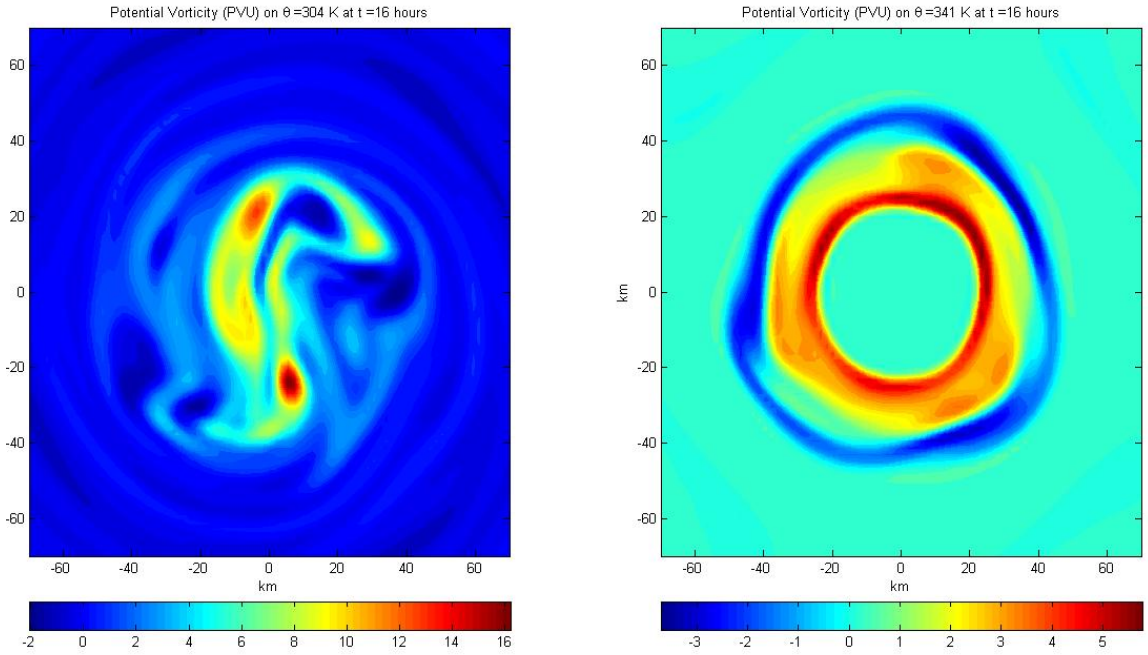

Figure 3.18: PV Evolution of DH2 on $\theta = 304$ K and $\theta = 341$ at 16 hours.

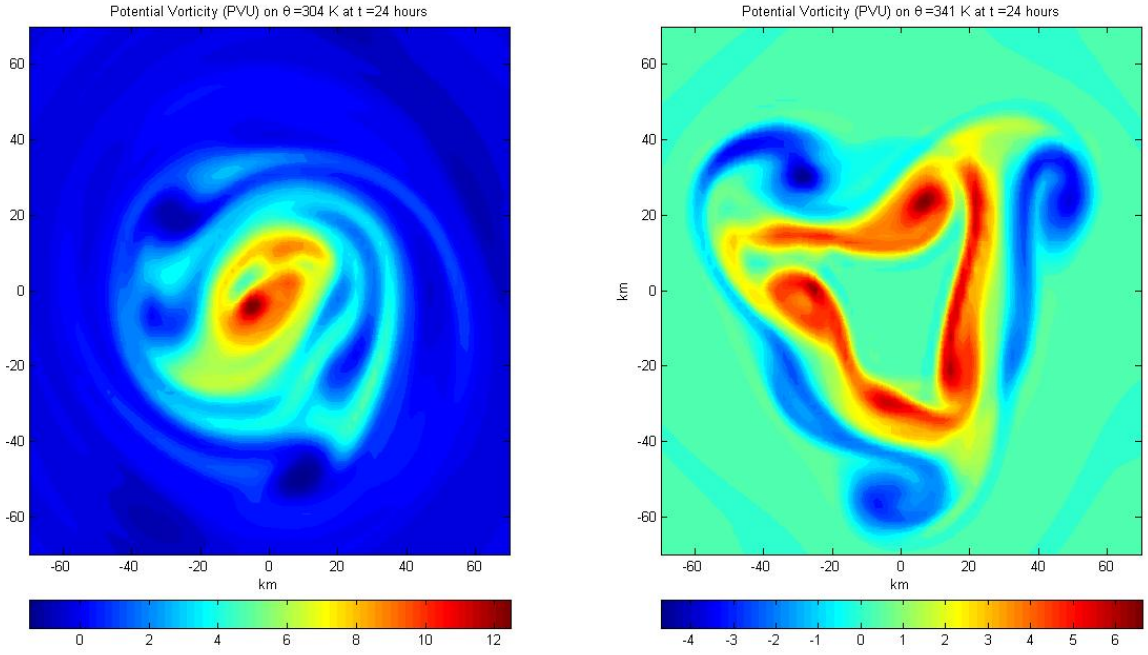

Figure 3.19: PV Evolution of DH2 on $\theta = 304$ K and $\theta = 341$ at 24 hours.

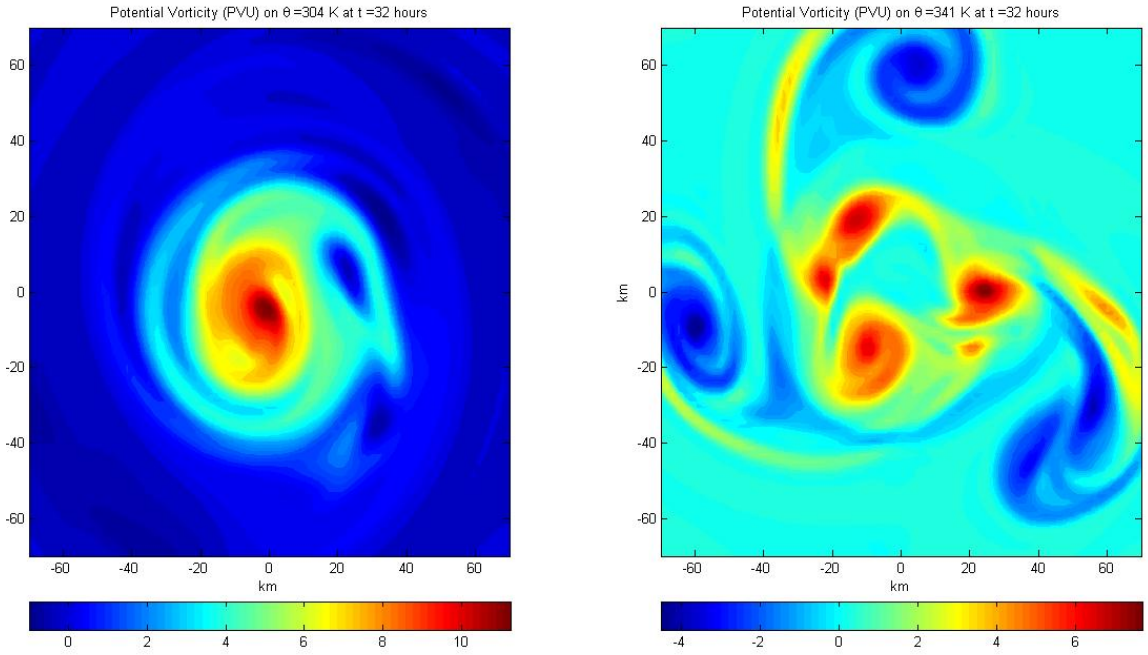

Figure 3.20: PV Evolution of DH2 on $\theta = 304$ K and $\theta = 341$ at 32 hours.

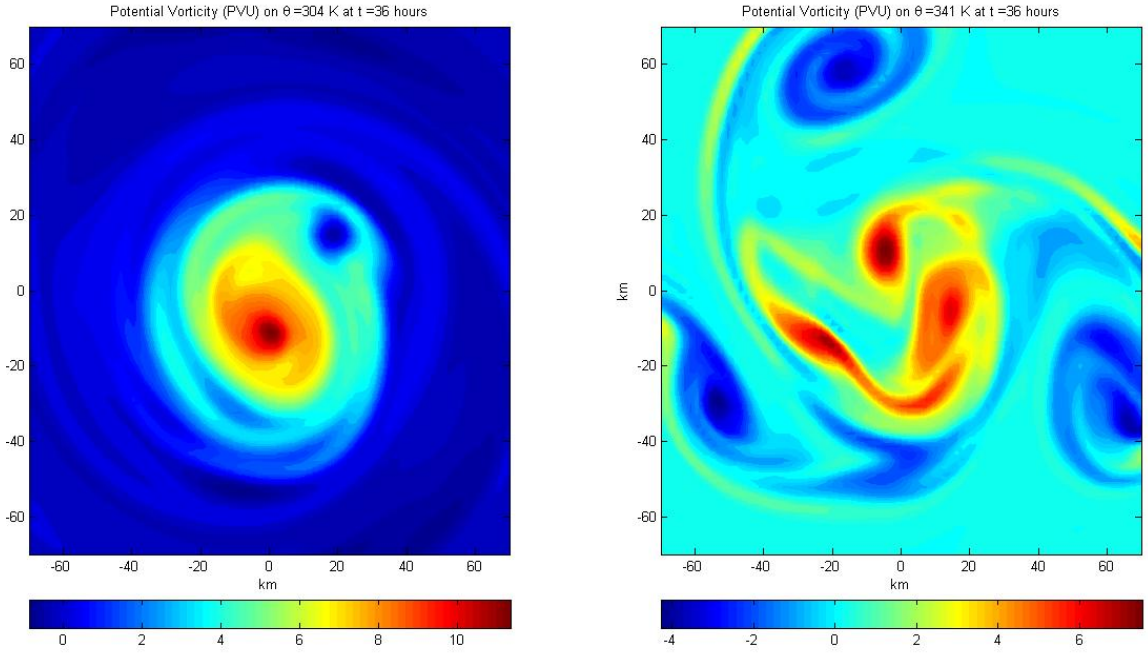

Figure 3.21: PV Evolution of DH2 on $\theta = 304$ K and $\theta = 341$ at 36 hours.

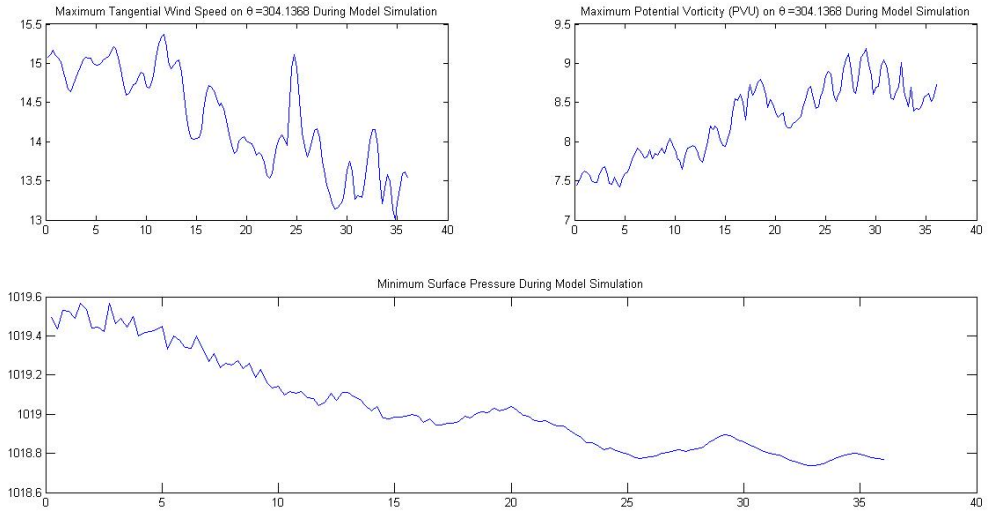

Figure 3.22: Time evolution of maximum tangential velocity, minimum surface pressure, and maximum potential vorticity for DH3.

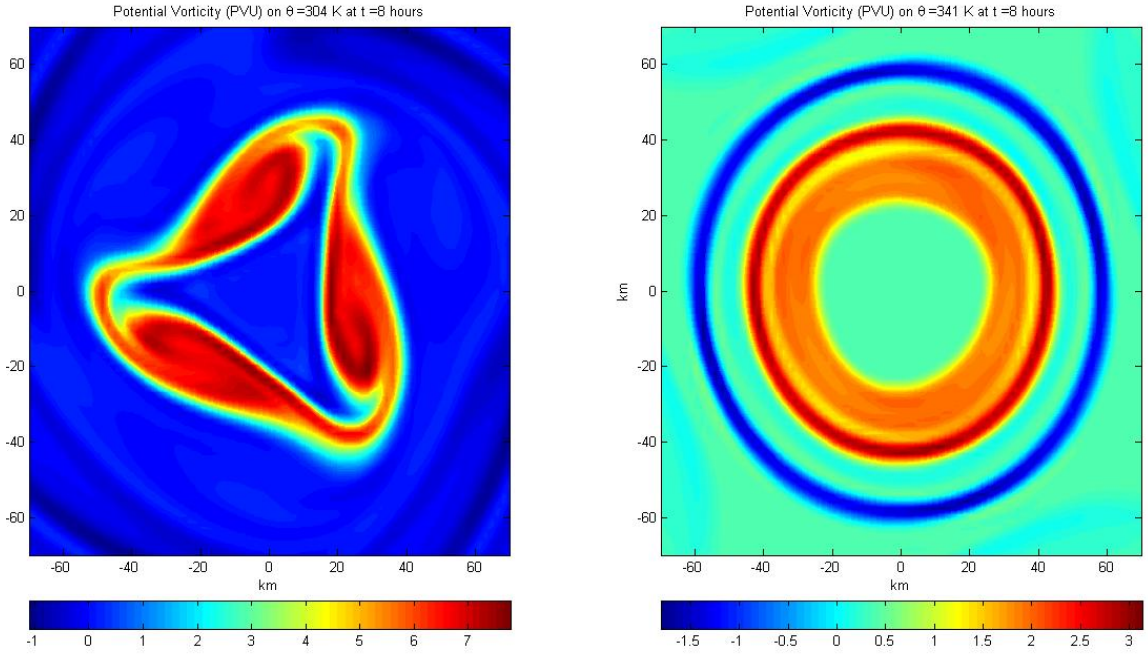

Figure 3.23: PV Evolution of DH3 on $\theta = 304$ K and $\theta = 341$ at 8 hours.

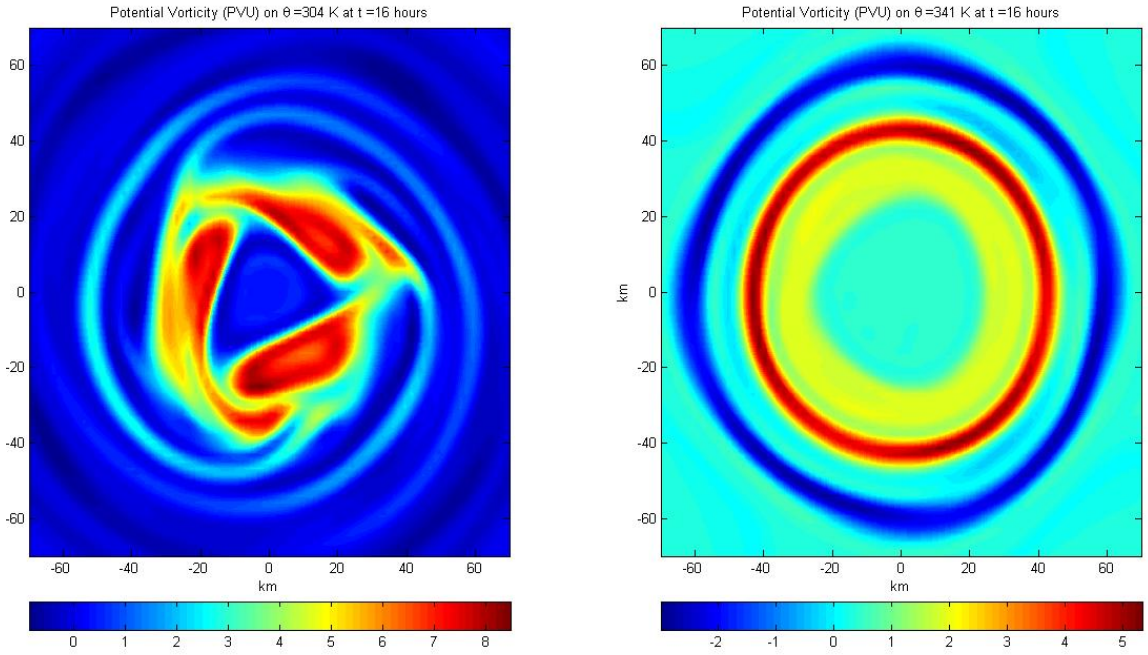

Figure 3.24: PV Evolution of DH3 on $\theta = 304$ K and $\theta = 341$ at 16 hours.

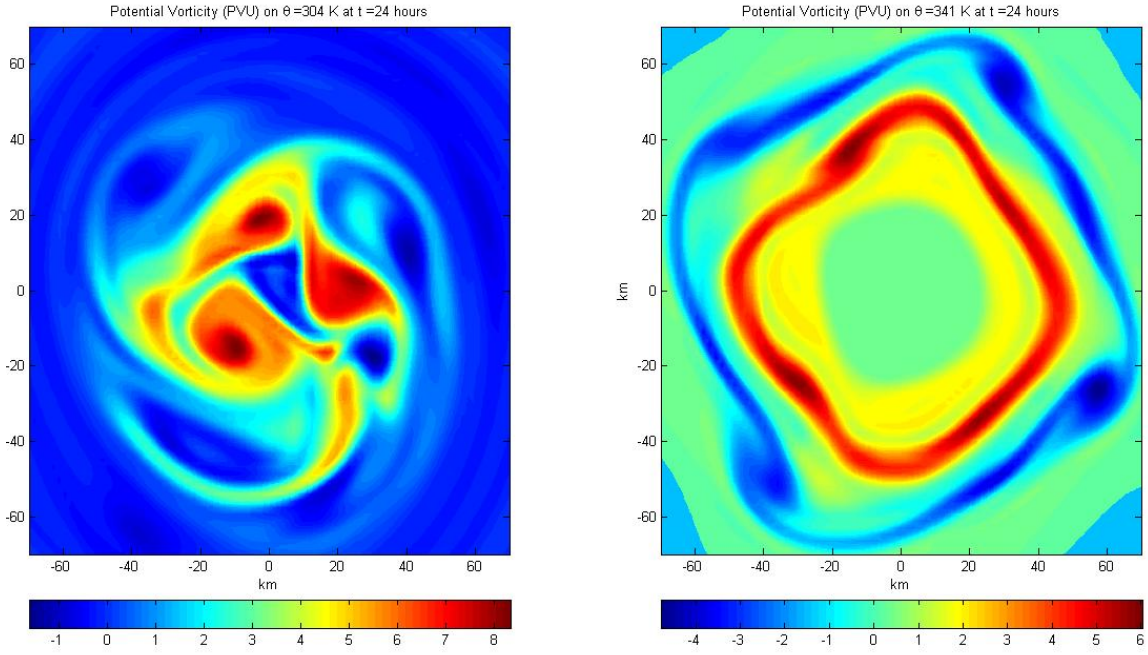

Figure 3.25: PV Evolution of DH3 on $\theta = 304$ K and $\theta = 341$ at 24 hours.

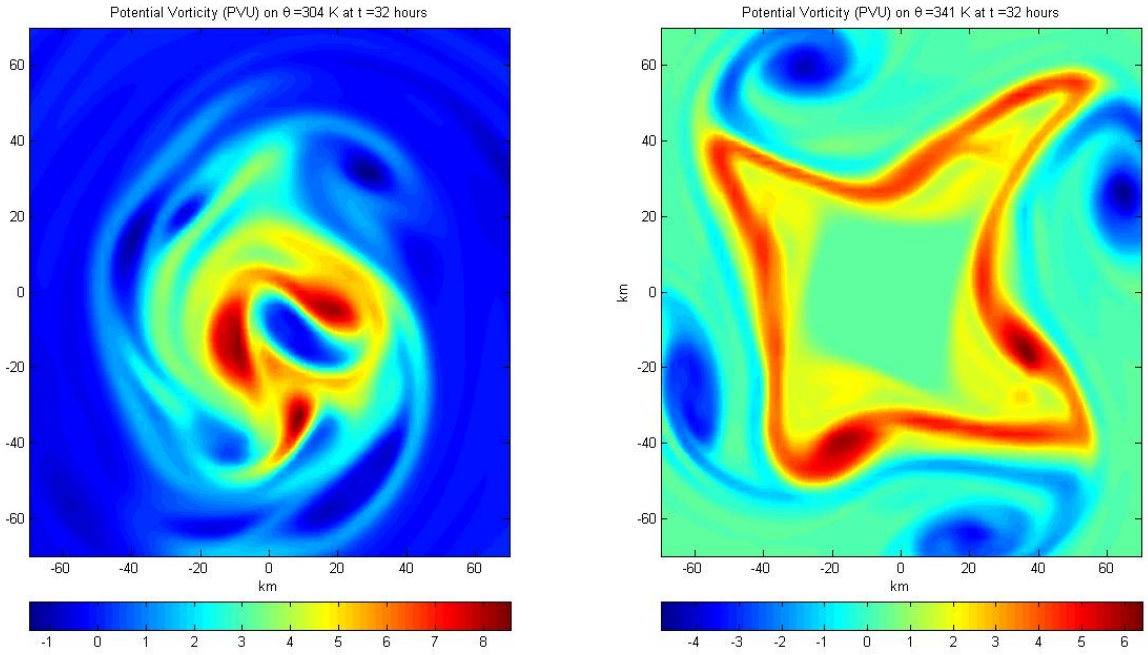

Figure 3.26: PV Evolution of DH3 on $\theta = 304$ K and $\theta = 341$ at 32 hours.

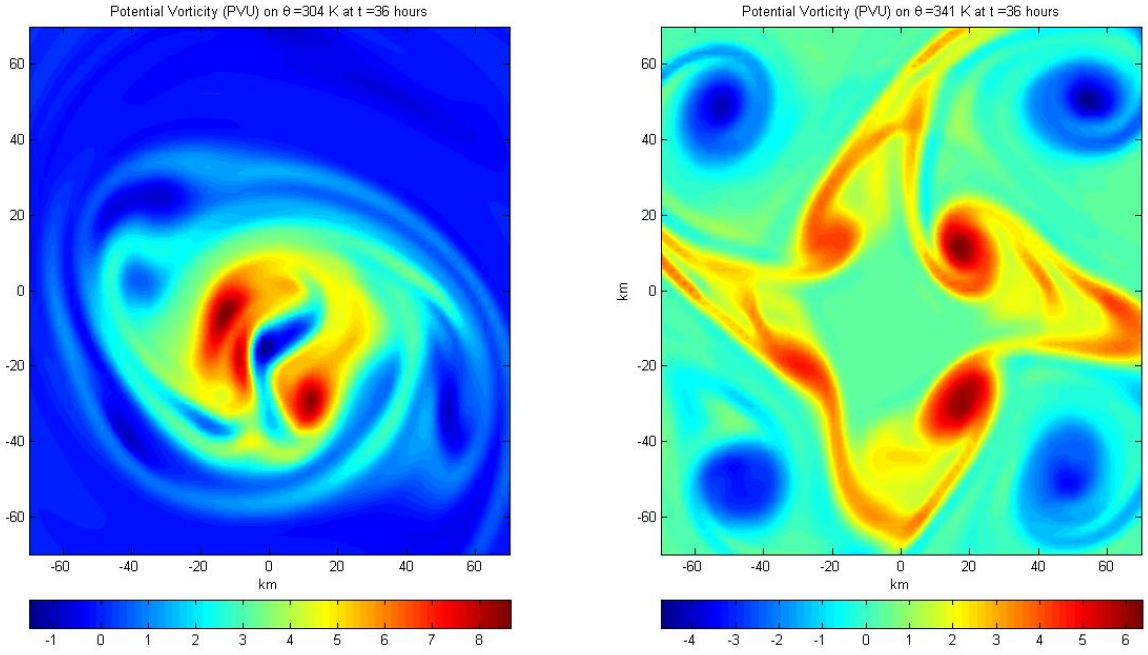

Figure 3.27: PV Evolution of DH3 on $\theta = 304$ K and $\theta = 341$ at 36 hours.

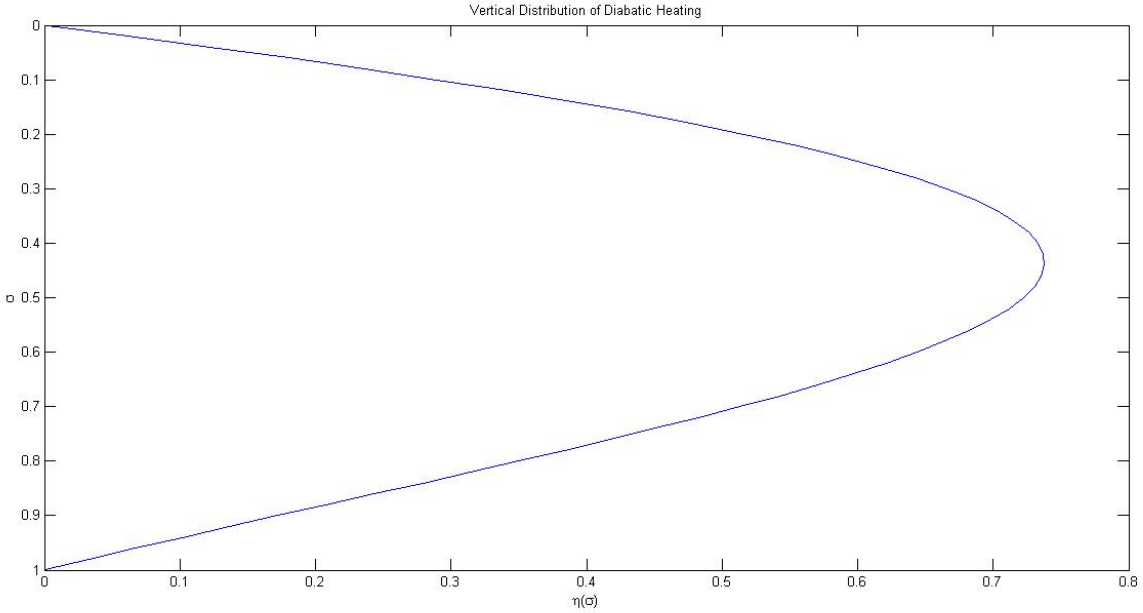

Figure 3.28: The vertical structure of diabatic heating $\eta(\sigma)$ as a function of σ.

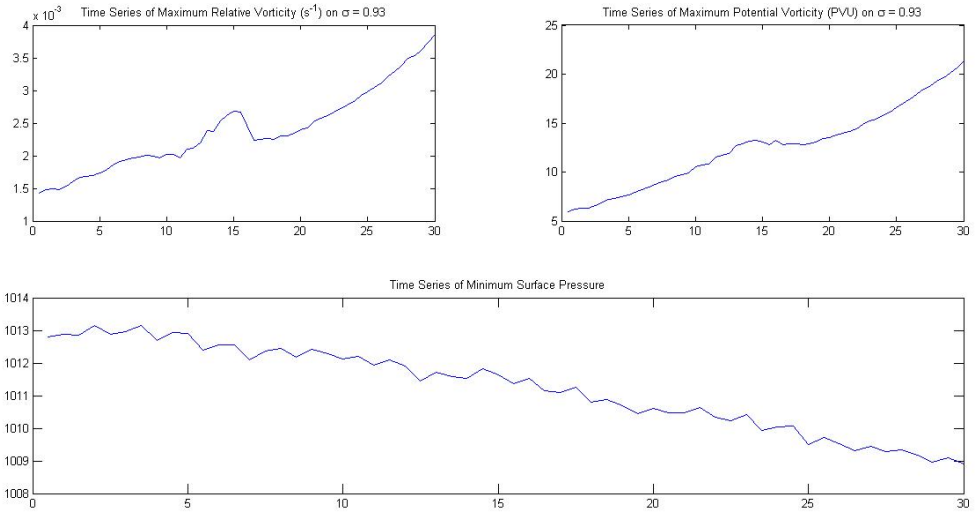

Figure 3.29: Time evolution of maximum relative vorticity, minimum surface pressure, and maximum potential vorticity for CH0.

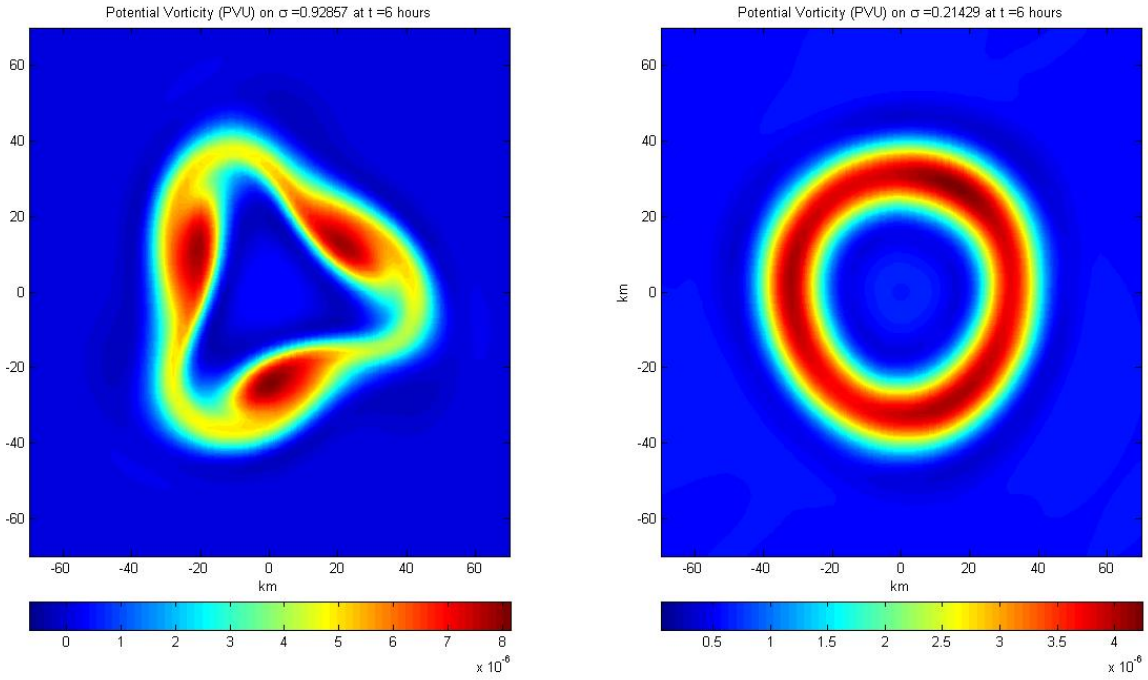

Figure 3.30: PV Evolution of CH0 on $\sigma = 0.21$ and $\sigma = 0.93$ at 6 hours.

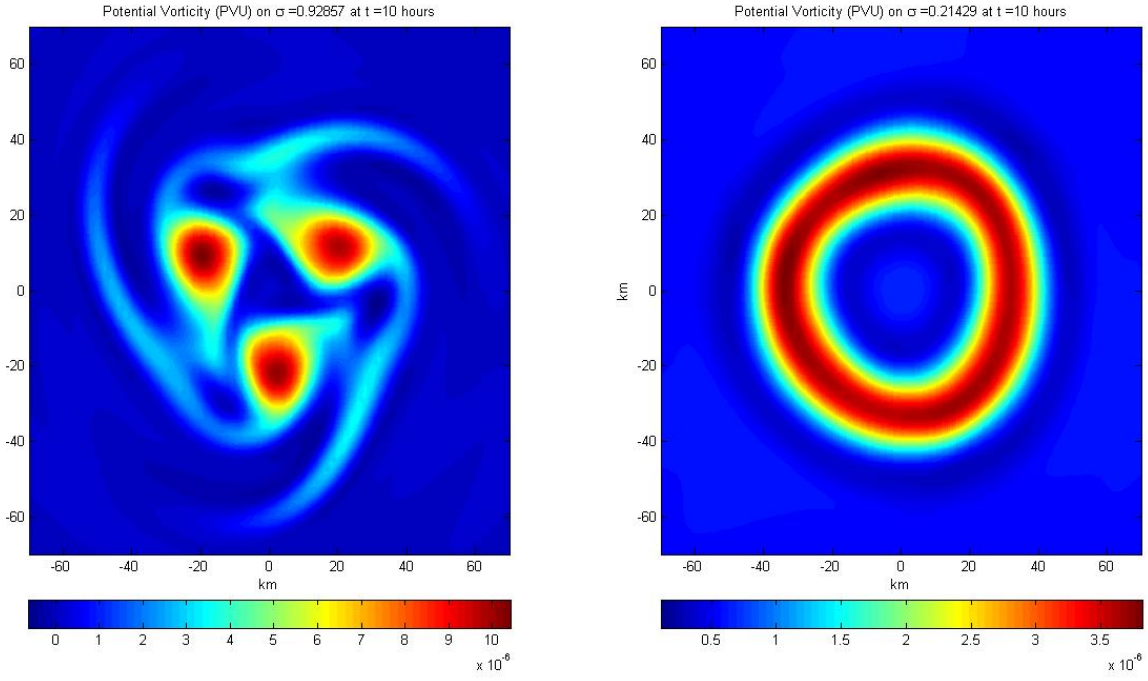

Figure 3.31: PV Evolution of CH0 on $\sigma = 0.21$ and $\sigma = 0.93$ at 10 hours.

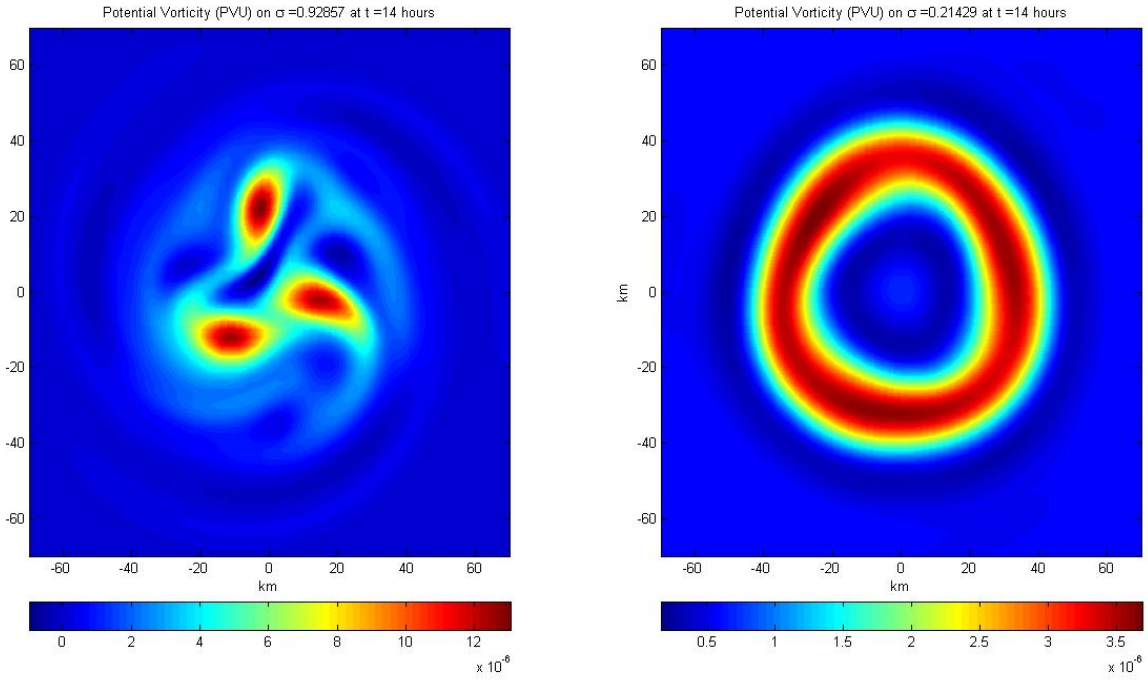

Figure 3.32: PV Evolution of CH0 on $\sigma = 0.21$ and $\sigma = 0.93$ at 14 hours.

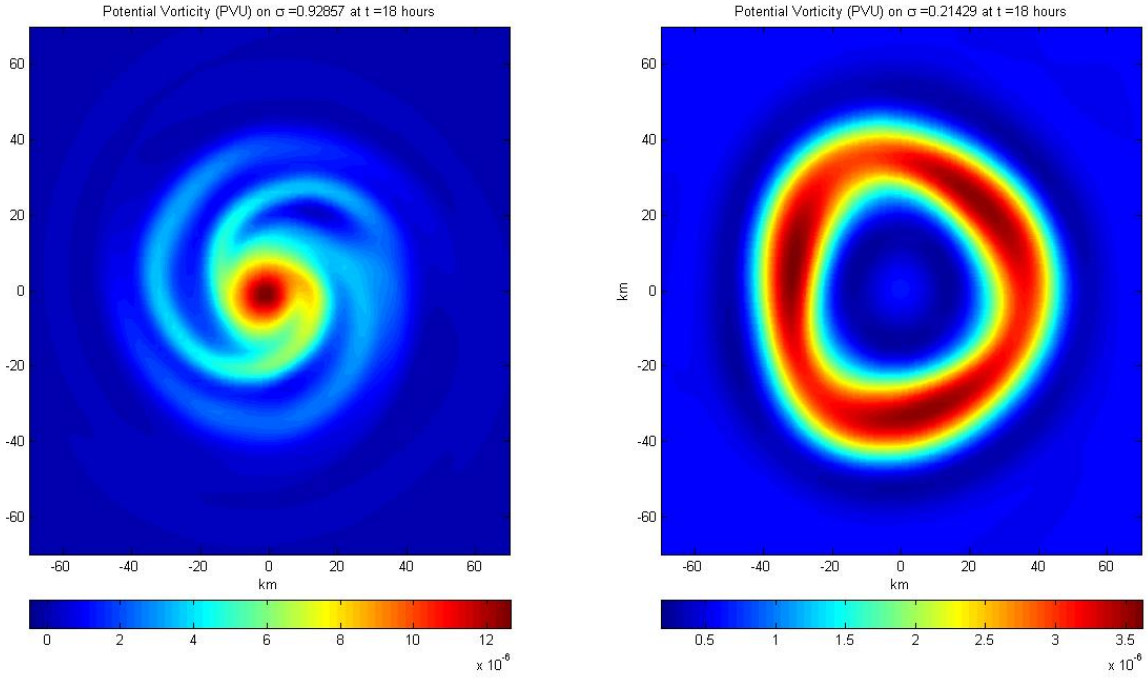

Figure 3.33: PV Evolution of CH0 on $\sigma = 0.21$ and $\sigma = 0.93$ at 18 hours.

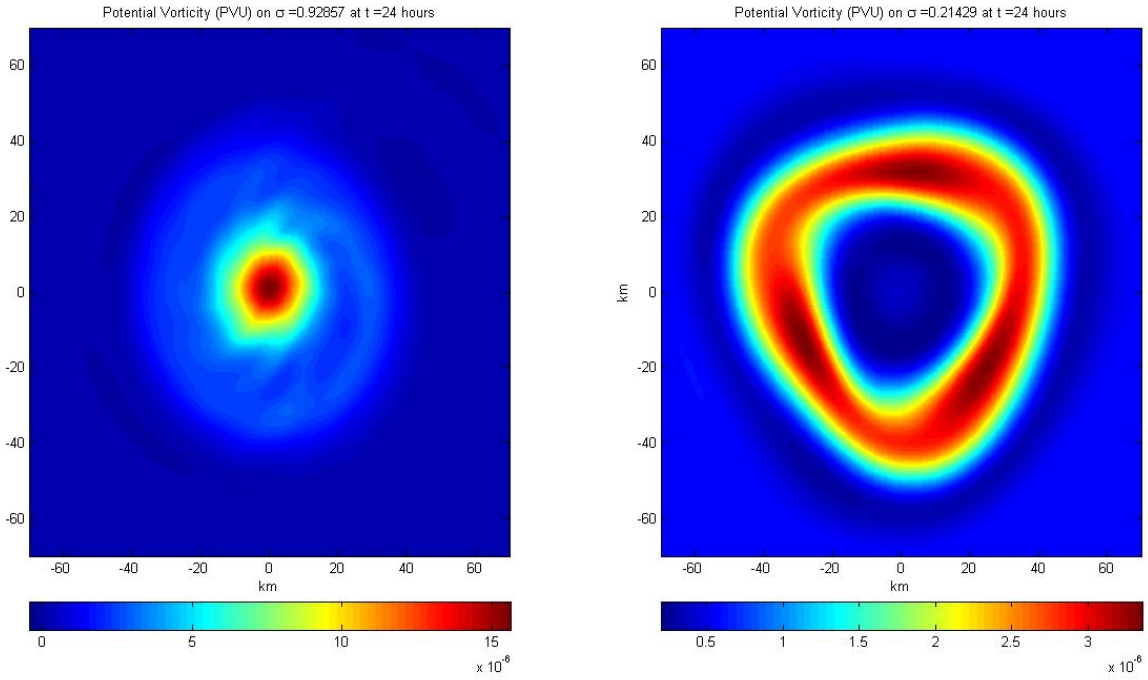

Figure 3.34: PV Evolution of CH0 on $\sigma = 0.21$ and $\sigma = 0.93$ at 24 hours.

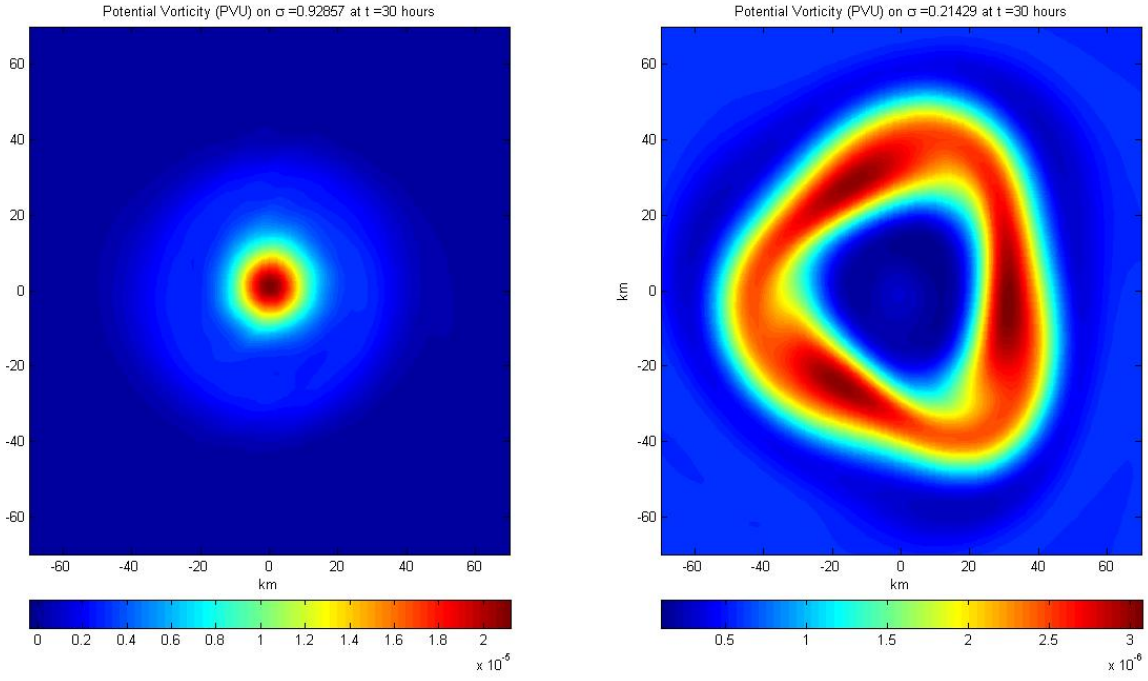

Figure 3.35: PV Evolution of CH0 on $\sigma = 0.21$ and $\sigma = 0.93$ at 30 hours.

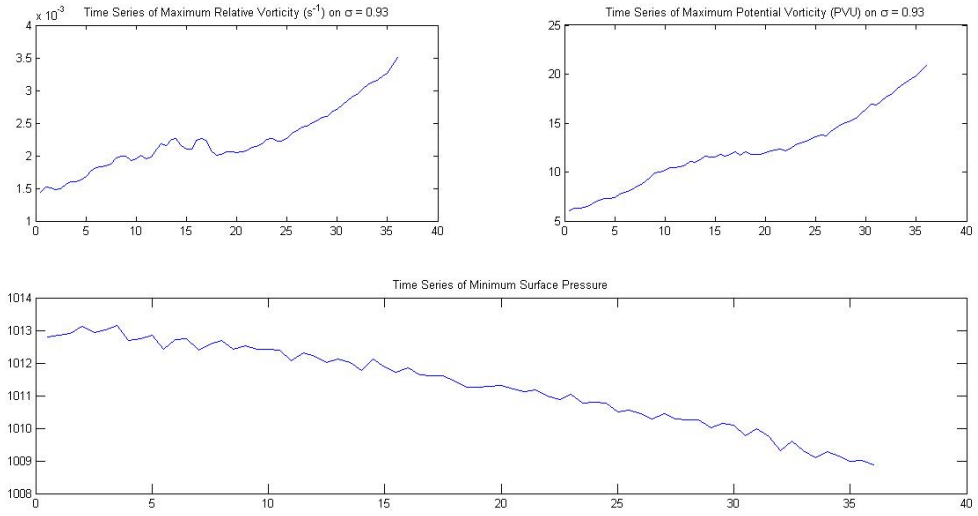

Figure 3.36: Time evolution of maximum relative vorticity, minimum surface pressure, and maximum potential vorticity for CH1.

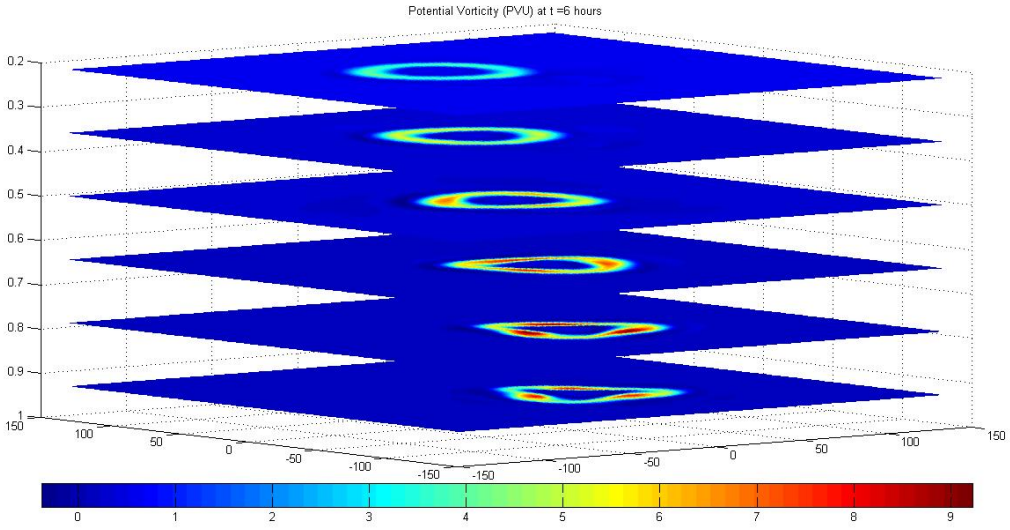

Figure 3.37: The evolution of the hollow PV tower for CH1 at 6 hours.

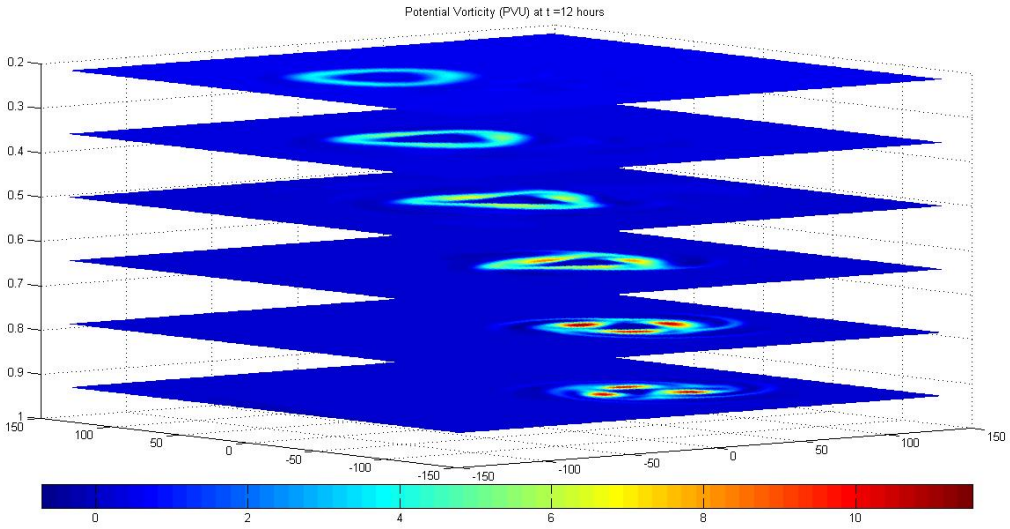

Figure 3.38: The evolution of the hollow PV tower for CH1 at 12 hours.

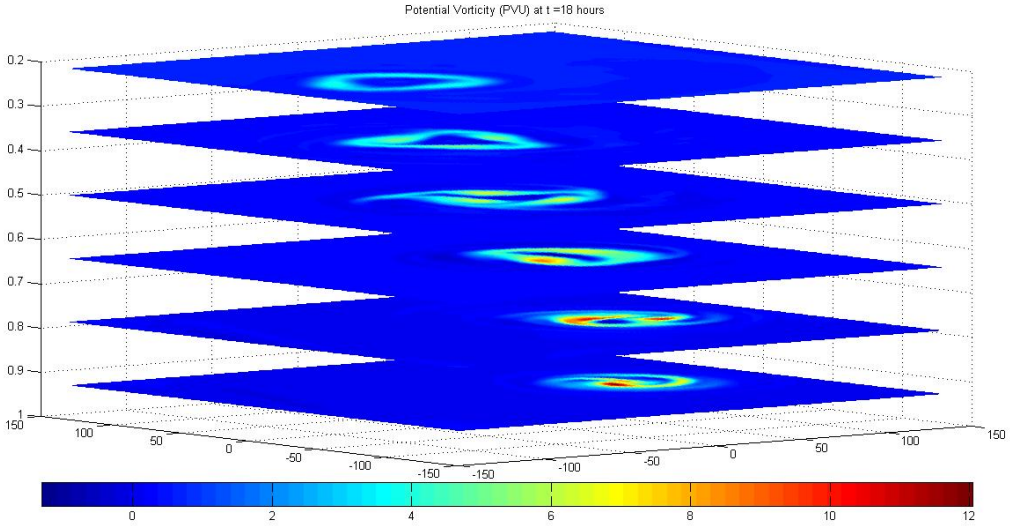

Figure 3.39: The evolution of the hollow PV tower for CH1 at 18 hours.

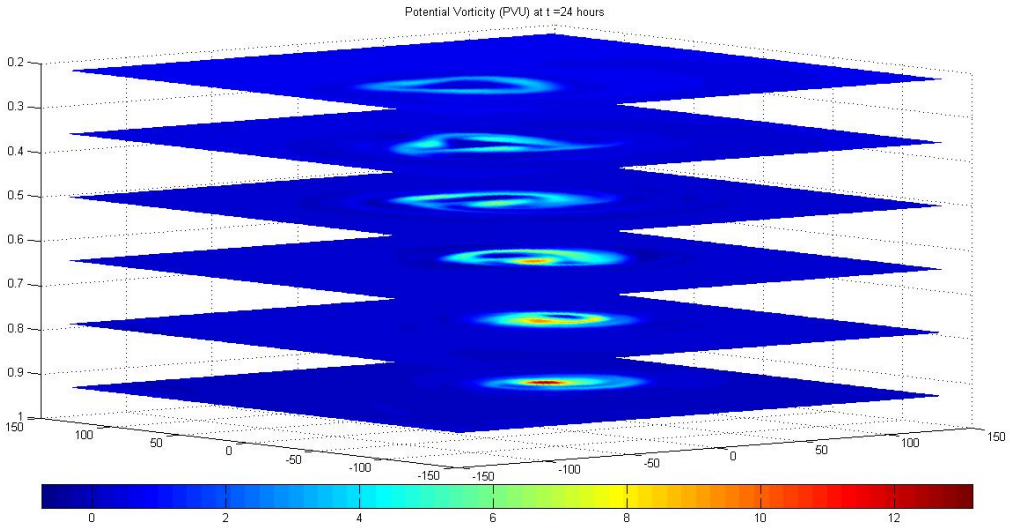

Figure 3.40: The evolution of the hollow PV tower for CH1 at 24 hours.

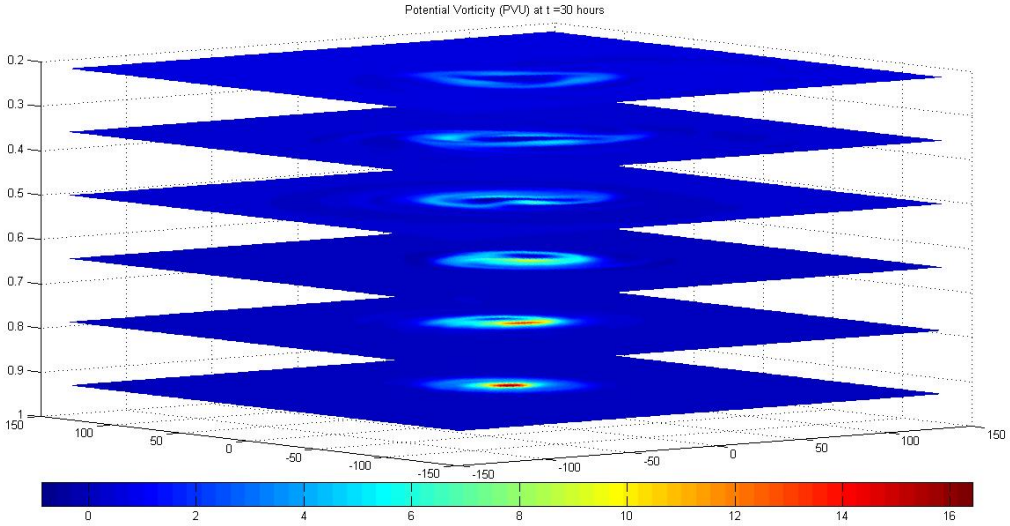

Figure 3.41: The evolution of the hollow PV tower for CH1 at 30 hours.

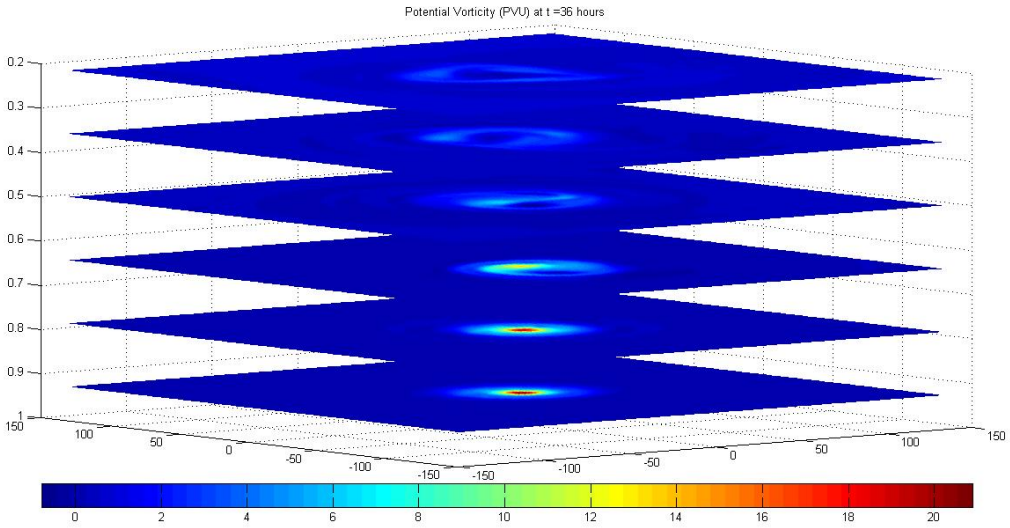

Figure 3.42: The evolution of the hollow PV tower for CH1 at 36 hours.

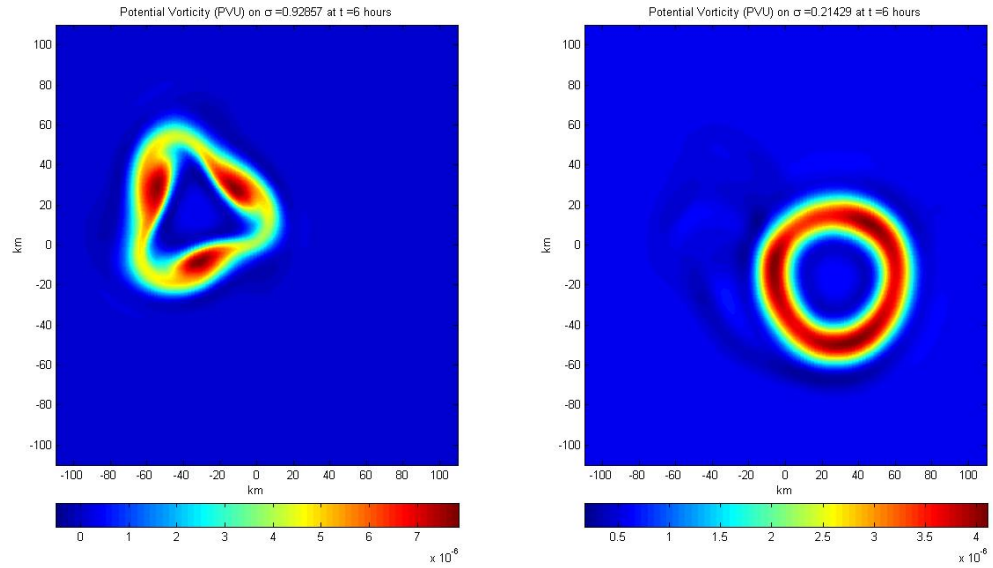

Figure 3.43: PV Evolution of CH1 on $\sigma = 0.21$ and $\sigma = 0.93$ at 6 hours.

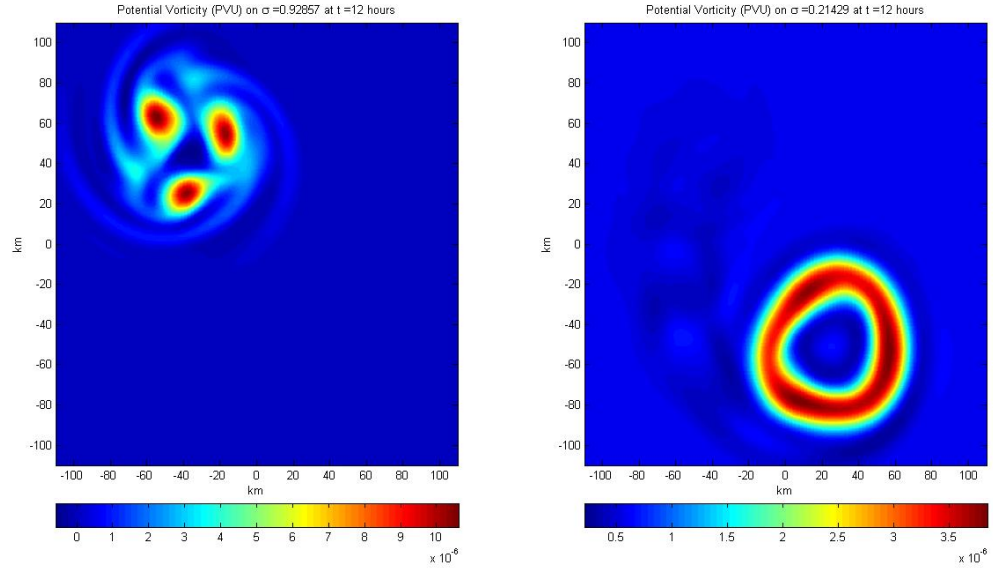

Figure 3.44: PV Evolution of CH1 on $\sigma = 0.21$ and $\sigma = 0.93$ at 12 hours.

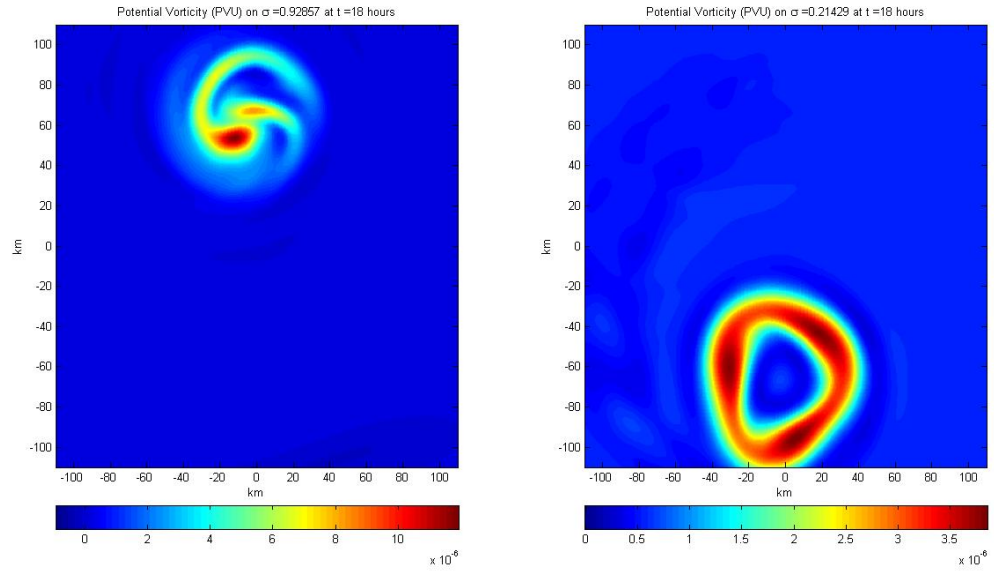

Figure 3.45: PV Evolution of CH1 on $\sigma = 0.21$ and $\sigma = 0.93$ at 18 hours.

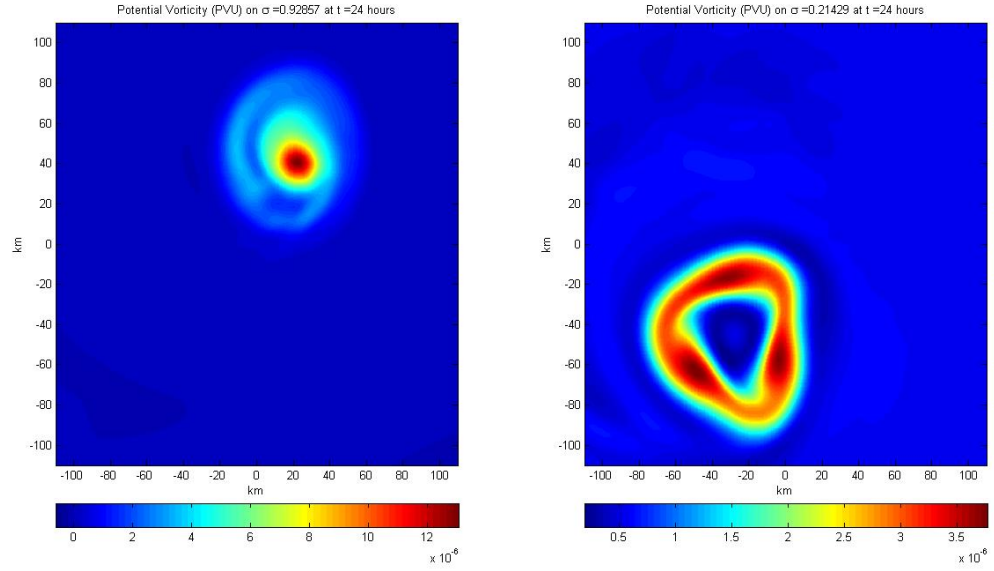

Figure 3.46: PV Evolution of CH1 on $\sigma = 0.21$ and $\sigma = 0.93$ at 24 hours.

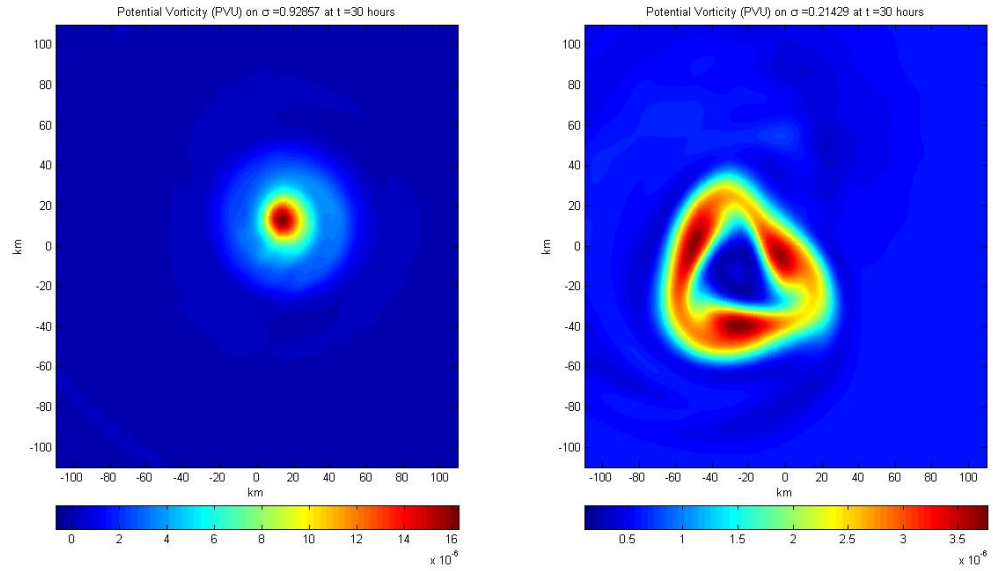

Figure 3.47: PV Evolution of CH1 on $\sigma = 0.21$ and $\sigma = 0.93$ at 30 hours.

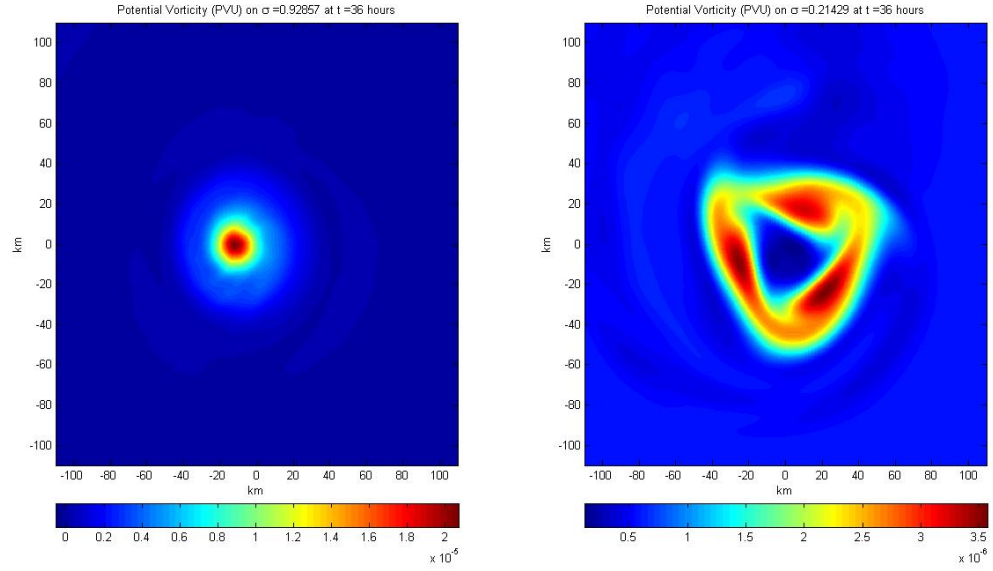

Figure 3.48: PV Evolution of CH1 on $\sigma = 0.21$ and $\sigma = 0.93$ at 36 hours.

Chapter 4

THE 2D EVOLUTION OF SHOCK-LIKE STRUCTURES IN THE TROPICAL CYCLONE BOUNDARY LAYER

4.1 Introduction and Motivation

The boundary layer of a mature hurricane has been long recognized as an important feature of the storm. In particular, it controls the radial distribution of moisture, vertical motion, and absolute angular momentum that ascends into the eyewall clouds. In addition, turbulent processes within the boundary layer transfer momentum to the ocean, generating damaging storm surge and waves, and also transfer energy from the oceanic reservoir to the TC heat engine, generating and maintaining the storm (Emanuel 1986). Yet, apart from the immediate surface, the structure of the tropical cyclone boundary layer has been less thoroughly characterized by observations than the rest of the storm. This lack of observational coverage is partly due to safety, since aircraft are unable to fly too near the surface in an intense TC. In addition, Doppler radar is subject to sea clutter and has insufficient resolution to resolve the large gradients in the boundary layer. Finally, the previous generation of aircraft-deployed dropsondes, which used the Omega radio navigation system, required heavy vertical filtering to remove noise, and so had insufficient vertical resolution to resolve the strong gradients near the surface (Hock and Franklin 1999). However, a considerable proportion of those early observations show the presence of low-level jets, variously reported as being at 60 m (Wilson 1979), 200 m (Korolev et al. 1990), and 550 m (Moss and Merceret 1976).

The recent advent of the global positioning system (GPS) dropsonde (Hock and Franklin 1999) has provided unprecedented observational coverage in the tropical cyclone boundary layer.

This instrument uses GPS navigation and radiosonde-type pressure, temperature, and humidity sensors to provide soundings with the unprecedented vertical sampling rate of 2 Hz, or approximately 6 m. These instruments have been routinely deployed from U.S. hurricane reconnaissance aircraft since 1997, with over 5000 having been used to date in the North Atlantic Ocean. They have proved to be highly reliable, with the only significant problem being a tendency for the wind measurements to fail in the lowest few tens of meters in the eyewall of intense hurricanes (Franklin et al. 2003; Powell et al. 2003), and a dry humidity bias in the early models, since corrected (Wang et al. 2002). In particular, GPS dropsondes have provided new data on the occurrence of low-level jets in the tropical cyclone boundary layer. For instance, Black and Shay (1998) in an initial report on recent observations from this instrument, state that "nearly all high wind soundings show this feature [a low-level jet]." Finally, the high-resolution modeling study of Li et al. (1997) shows a similar feature.

Kepert (2001) and Kepert and Wang (2001) describe a physical mechanism for producing such a jet in which strong inward advection of angular momentum leads to supergradient flow. The processes that maintain the necessary inflow against the outward acceleration due to gradient wind imbalance were identified as being vertical diffusion, vertical advection, and horizontal advection. In the case of a moving Northern Hemisphere storm, it is found that the jet is most supergradient – several times stronger than in a stationary storm – at the eyewall to the left and front of the storm, as well as extending into a significant area around to the left of the storm. To test the prediction of the boundary layer theory of Kepert and Wang (2001), Kepert (2006a,b) compared the detailed analyses of the wind field in the boundary layer of two intense TCs - Hurricane Georges (1998) and Hurricane Mitch (1998) - when they were close to maximum intensity.

The spatial variability of the boundary layer wind structure for Hurricane Georges is found to agree very well with the theoretical predictions of Kepert and Wang (2001). In particular, the ratio of the near-surface wind speed to that above the boundary layer is found to increase inward

toward the radius of maximum winds and to be larger to the left of the track than to the right, while the low-level wind maximum is both more marked and at lower altitude on the left of the storm track than on the right. However, the expected supergradient flow in the upper boundary layer is not found, with the winds being diagnosed as close to gradient balance. It is argued by Kepert that this lack of supergradient flow is a consequence of the particular radial structure in Georges, which had a comparatively slow decrease of wind speed with radius outside the eyewall. This radial profile leads to a relatively weak gradient of inertial stability near the eyewall and a strong gradient at larger radii, and hence the tropical cyclone boundary layer dynamics described by Kepert and Wang (2001) can produce only marginally supergradient flow near the radius of maximum winds. The lack of supergradient flow, diagnosed from the observational analysis, is thus attributed to the large-scale structure of this particular storm.

In contrast to Hurricane Georges, the flow in the middle to upper boundary layer near the eyewall of Hurricane Mitch was found to be strongly supergradient. The reason for the difference is shown to be the different radial structure of the storms, in that outside of the radius of maximum winds, the wind decreases much more quickly in Mitch than in Georges. Hurricane Mitch was close to inertially neutral at large radius, with a strong angular momentum gradient near the radius of maximum winds. Kepert and Wang (2001) predict strongly supergradient flow in the upper boundary layer near the radius of maximum winds in this situation; the observational analysis is thus in good agreement with their theory. The surface wind factor is found to increase inward toward the radius of maximum winds, in accordance with the analysis by Franklin et al. (2003). Marked asymmetries in the boundary layer wind field and in the eyewall convection are shown to be consistent with asymmetric surface friction due to the storm's proximity to land, rather than to motion.

Another common feature seen in the boundary layer of tropical cyclones is the existence of spatial oscillations in vertical velocity. Figure 4.1, reproduced from Marks et al. (2008), shows aircraft data from a low level (450 m) inward radial penetration of Hurricane Hugo on 15 Septem-

ber 1989. As the aircraft traversed the eyewall ($10 < r < 22$ km) the wind speed increased from 55 m s^{-1} to a maximum of 89 m s^{-1}. Near the inner edge of the eyewall there were multiple updraft-downdraft couplets (the strongest updraft being 21 m/s), with associated oscillations of the horizontal wind speed and a very rapid 60 m/s drop in wind speed near 8 km radius. Figure 4.2 shows the velocity fields from the 434 m and 2682 m flight legs in Hurricane Hugo on 15 September 1989. After the aircraft ascends to 2682 m in the eye, the aircraft departed the eye to the northeast, obtaining the wind speed and vertical velocity data shown by the blue curves in Fig. 4.2. The extreme horizontal wind shears and large vertical velocities observed at 434 m in the southwest sector were not observed at 2682 m in the northeast sector, primarily because the aircraft is above the boundary layer and the velocity field is approximately in gradient wind balance.

Since this complicated structure of the three-dimensional wind field occurs in the region of highest radar reflectivity (upper panel Fig. 4.1), it is natural to attribute it to moist convective dynamics. However, the purpose of this chapter is to explore the possibility that this behavior can be explained by nonlinear effects in a simple dry model of the hurricane boundary layer. In particular the emphasis here is on interpreting the observations shown in Fig. 4.1 and 4.2 in terms of shock-like structures that emerge from the fact that the horizontal momentum equation contains an embedded Burgers' equation. This chapter is organized in the following way. Section 4.2 presents and derives the governing set of partial differential equations for the slab model. Section 4.3 presents a mathematical discussion of the viscous Burgers' equation and its associated shock effects. Sections 4.4 and 4.5 present the evolution of shock-like structures for a hurricane-like vortex with a single concentric eyewall and a double concentric eyewall, respectively. The goal of these sections is to better understand the changes in boundary layer radial inflow and Ekman pumping that occur during an eyewall replacement cycle and how the radial distribution of Ekman pumping in an axisymmetric vortex depends on the radial distribution of vorticity. Section 4.6 examines the evolution of shock-like structures for a translating hurricane-like vortex.

4.2 The Primitive Equation Slab Boundary Layer Model

We consider motions in the frictional boundary layer of an incompressible fluid on an f-plane. The layer is assumed to have constant depth h, with eastward and northward velocities $u(x, y, t)$ and $v(x, y, t)$ that are independent of height between the surface and height h, and with vertical velocity $w(x, y, t)$ at height h. The horizontal velocity components are discontinuous across the top of the boundary layer. In the overlying layer, frictional effects vanish, the radial flow is assumed to be negligible, and the azimuthal velocity v_{gr} is assumed to be in gradient balance and constant in time. The boundary layer flow is driven by the same pressure gradient force that occurs in the overlying fluid. To derive the boundary layer model, we begin with the primitive equations written in flux form:

$$\frac{\partial u}{\partial t} = -\frac{\partial (u^2)}{\partial x} - \frac{\partial (uv)}{\partial y} - \frac{\partial (uw)}{\partial z} + fv - \frac{1}{\rho}\frac{\partial p_c}{\partial x} + K_H \nabla^2 u + \frac{\partial}{\partial z}\left(K_M \frac{\partial u}{\partial z} \right), \tag{4.1}$$

$$\frac{\partial v}{\partial t} = -\frac{\partial (uv)}{\partial x} - \frac{\partial (v^2)}{\partial y} - \frac{\partial (vw)}{\partial z} - fu - \frac{1}{\rho}\frac{\partial p_c}{\partial y} + K_H \nabla^2 v + \frac{\partial}{\partial z}\left(K_M \frac{\partial v}{\partial z} \right). \tag{4.2}$$

The continuity equation takes the form

$$\frac{\partial u}{\partial x} + \frac{\partial v}{\partial y} + \frac{\partial w}{\partial z} = 0 \tag{4.3}$$

As in Chow (1971) and Shapiro (1983), the pressure field is specified as the sum of a translating, axisymmetric, cyclonic part $p_c(x, y, t)$ and a stationary large-scale part with constant gradient, so that

$$\frac{\partial p}{\partial x} = \frac{\partial p_c}{\partial x} + \rho f v_g, \qquad \frac{\partial p}{\partial y} = \frac{\partial p_c}{\partial y} + \rho f v_g,$$

where ρ is the constant boundary layer density, and where the constants u_g and v_g are the geostrophic components associated with the stationary large-scale part of the pressure field. Because the boundary layer flow is driven by same pressure gradient force that occurs in the overlying fluid, we can write p_c in terms of a specified gradient wind v_{gr} via

$$\frac{1}{\rho}\frac{\partial p_c}{\partial r} = \left(f + \frac{v_{gr}}{r}\right)v_{gr} \tag{4.4}$$

Integration of (4.1)-(4.3) with respect to z gives

$$\frac{\partial u_b}{\partial t} = -\frac{\partial (u^2)_b}{\partial x} - \frac{\partial (uv)_b}{\partial y} - [uw]\Big|_{z=h} + fv_b - \frac{x}{r}\left(f + \frac{v_{gr}}{r}\right)v_{gr} + K_H\nabla^2 u_b - K_M\frac{\partial u}{\partial z}\Big|_{z=0}, \tag{4.5}$$

$$\frac{\partial v_b}{\partial t} = -\frac{\partial (uv)_b}{\partial x} - \frac{\partial (v^2)_b}{\partial y} - [vw]\Big|_{z=h} - fu_b - \frac{y}{r}\left(f + \frac{v_{gr}}{r}\right)v_{gr} + K_H\nabla^2 v_b - K_M\frac{\partial v}{\partial z}\Big|_{z=0}, \tag{4.6}$$

$$\frac{\partial u_b}{\partial x} + \frac{\partial v_b}{\partial y} + [w]\Big|_{z=h} = 0, \tag{4.7}$$

where

$$(u, v, w)_b = \int_0^h (u, v, w)dz. \tag{4.8}$$

Because the radial flow in the overlying fluid is assumed to be negligible, the horizontal velocities in the overlying fluid can be written solely in terms of the gradient wind profile:

$$u(x, y, t)\Big|_{z>h} = -\frac{y}{r}v_{gr}, \qquad v(x, y, t)\Big|_{z>h} = \frac{x}{r}v_{gr},$$

This implies that

$$[uw]\Big|_{z=h} = u_b w_{h+} + u_{z>h} w_{h-}, \tag{4.9}$$

$$[vw]\Big|_{z=h} = v_b w_{h+} + v_{z>h} w_{h-}, \tag{4.10}$$

where $w_{h+} = 0.5(w + |w|)$ and $w_{h-} = 0.5(w - |w|)$. To parameterize the air-sea interaction, we use the bulk drag law

$$K_M\frac{\partial \mathbf{u_b}}{\partial z}\Big|_{z=0} = C_D|U|\mathbf{u_b}, \tag{4.11}$$

where $U = 0.78(u_b^2 + v_b^2)^{1/2}$ is the wind speed at 10 m height, which is assumed to be seventy eight percent of the mean boundary layer wind speed (as supported by the dropwindsonde data of Powell et al. 2003). Concerning the dependence of C_D on wind speed we use

$$C_D = 10^{-3} \begin{cases} 2.70/U + 0.142 + 0.0764U & U \leq 25 \\ 2.16 + 0.5406\big[1 - \exp\big(-\dfrac{U-25}{7.5}\big)\big] & U \geq 25 \end{cases} \tag{4.12}$$

where the 10 m wind speed U is expressed in m s^{-1}. The $U \leq 25$ m s^{-1} part is based on Large et al. (1994) and has been constructed to make C_D go to its theoretical infinite value at zero wind speed. The $U \geq 25$ m s^{-1} part is based on Powell et al. (2003) and Donelan et al. (2004), who argue that C_D reaches a saturation value between 2.5×10^{-3} and 2.8×10^{-3} for high wind speeds. Now in Eqs. (4.5) – (4.7), the integrals can be explicitly solved giving:

$$\frac{\partial u}{\partial t} = -\frac{\partial(u^2)}{\partial x} - \frac{\partial(uv)}{\partial y} - \frac{1}{h}\left(u w_{h+} + u_{z>h} w_{h-}\right) + fv - \frac{x}{r}\left(f + \frac{v_{gr}}{r}\right) v_{gr} + K_H \nabla^2 u - C_D |U| \frac{\mathbf{u}}{h}, \tag{4.13}$$

$$\frac{\partial v}{\partial t} = -\frac{\partial(uv)}{\partial x} - \frac{\partial(v^2)}{\partial y} - \frac{1}{h}\left(v w_{h+} + v_{z>h} w_{h-}\right) - fu - \frac{y}{r}\left(f + \frac{v_{gr}}{r}\right) v_{gr} + K_H \nabla^2 v - C_D |U| \frac{\mathbf{v}}{h}, \tag{4.14}$$

$$-h\left(\frac{\partial u}{\partial x} + \frac{\partial v}{\partial y}\right) = [w]\Big|_{z=h}, \tag{4.15}$$

where u, v, w denote the values of the horizontal and vertical velocities inside the boundary layer. The slab boundary layer model will be solved using 4th-order centered differencing on the square domain $-591 \leq x, y \leq 591$ km with a grid spacing of 500 m in the region $-50 \leq x, y \leq 50$, increasing to 2 km using a variable-resolution stretched grid with a constant local stretching rate of 7.5 percent. The model uses a third-order Adams-Bashforth time differencing with a time step of 1.5 s.

Smith (2003; updated in Smith and Vogl 2008) used a high-resolution steady, two-dimensional, moist, axisymmetric, depth-averaged model to resolve the tangential wind speed and thermodynamic structure of the boundary layer. Smith and Vogl (2008) discovered a failure in their numerical integration procedure, which occurs when the radial wind begins to wildly oscillate near the radius of maximum gradient wind. Similar difficulties have been described by Kepert (2010a,b). Such difficulties are associated with the tendency of these equations to produce a Burgers' shock in the radial velocity field. In the absence of horizontal diffusion or some type of shock fitting procedure, the inward radial integration procedure generally fails. For this reason, we have included time-dependence and horizontal diffusion, so that the problem can be treated as a well-posed initial value problem describing the time dependent approach to a steady state solution with one or more shocks. Using this model, the goals of this chapter are:

- How does the shock structure of the boundary layer affect the vertical velocity in the boundary layer?
- How does the shock structure of the boundary layer depend upon the translation velocity of the storm?
- How does the radial distribution of vorticity affect the development of shock-like structures in the tropical cyclone boundary layer?

4.3 Review of the Viscous Burgers Equation

As mentioned above, the velocity and vorticity field of the tropical cyclone boundary layer can be interpreted in terms of "Burgers' shock-like" structures that emerge from the fact that the boundary layer momentum equations contain an embedded Burgers' equation. In this section, we give a brief review of the Burgers' equation. The one-dimensional inviscid Burgers' equation can be written as

$$u_t + uu_x = 0. \tag{4.16}$$

The one-dimensional Burgers equation is the simplest, nonlinear conservation equation. Although it is simple, it is a very important equation in the study of nonlinear waves and exhibits one of the most important features of nonlinear waves, i.e., the development of shocks. The corresponding equation with diffusion is given as

$$u_t + uu_x - \nu u_{xx} = 0, \tag{4.17}$$

where $\nu > 0$. Equation (4.17) is called the viscous Burgers equation. On physical grounds alone, one would expect viscosity to have a smoothing effect. Advection, on the other hand, does not smooth. To check this, consider the simplest, linear advection equation

$$w_t + cw_x = 0, \qquad w(x,0) = \delta(x)$$

The solution is $w(x,t) = \delta(x - ct)$, which is no smoother than its initial value. In particular, solutions of $u_t + uu_x = 0$ develop singularities and admit shock solutions no matter how smooth the initial conditions (see Whitham 1974, Chapter 4). The viscous Burgers' equation contains the combined effects of diffusion and nonlinear advection. In order to understand the formation and propagation of shocks in the viscous Burgers' equation, we'll seek special solutions in the form of traveling waves $u(x,t) = g(x - ct)$.

Let $z = x - ct$. Then $u_x = g'(z)$ and $u_t = cg'(z)$ and the viscous Burgers' equation becomes

$$cg' + gg' - \nu g'' = 0$$

.

Integration with respect to z yields

$$g' = \frac{1}{2\nu}(g^2 - 2cg - 2A) = \frac{1}{2\nu}(g - g_1)(g - g_2),$$

where A is a constant of integration, $g_1 = c - \sqrt{c^2 + 2A}$, and $g_2 = c + \sqrt{c^2 + 2A}$. Integrating again with respect to z yields

$$\frac{1}{g_2 - g_1} \ln \left| \frac{g_2 - g}{g - g_1} \right| = \frac{z}{2\nu} + B$$

where B is a constant of integration and $g_1 < g < g_2$. Assuming that $B = 0$ and setting $K = \frac{g_2 - g_1}{2\nu} > 0$ yields

$$g(z) = \frac{g_2 + g_1 e^{Kz}}{1 + e^{Kz}} \tag{4.18}$$

Thus g is a smooth function that decreases monotonically from $g(-\infty) = g_2$ to $g(\infty) = g_1$. The solution is given as

$$u(x,t) = g(x - ct) = \frac{g_2 + g_1 e^{K(x-ct)}}{1 + e^{K(x-ct)}}. \tag{4.19}$$

This is called the shock structure solution to the viscous Burgers' equation, which represents a wavefront moving with velocity $c = \dfrac{g_1 + g_2}{2}$. Note that

$$\lim_{\nu \to 0^+} u(x,t) = \begin{cases} g_2 & x < ct \\ g_1 & x > ct \end{cases} \tag{4.20}$$

Therefore, as the viscosity tends to zero, its smoothing effect is lost, and the solution becomes discontinuous (or multiple-valued). As the viscosity term increases, the viscous Burgers' equation behaves very much like the diffusion equation, which will smooth out the initial data. As the viscosity term decreases, the viscous Burgers' equation behaves very much like the inviscid Burgers' equation, which will produce a shock. For the viscous Burgers' equation, there is still a sharp gradient in velocity, but this sharp gradient is not discontinuous. In the neighborhood of the shock, where u_x is extremely large, the diffusion term νu_{xx} will not be small compared to the nonlinear advection term uu_x. With the inclusion of dissipation, $u(x,t)$ is no longer multiple-valued, nor discontinuous. Shocks will develop because of the nonlinearity, but the shock has a continuous structure.

For the tropical cyclone boundary layer, if the dominant processes are advection and diffusion, then the boundary layer equations will resemble the viscous Burgers' equation. This means

that a vortex will develop a continuous shock structure in the horizontal velocity fields. Since the shock structure will cause a sharp gradient in horizontal velocity, this will create strong Ekman pumping in the vortex. Based on the above analysis, the strength of the shock and the propagation speed of the shock will depend on the magnitude of the horizontal velocity in the initial condition and the magnitude of the horizontal diffusion. Based on Ekman layer dynamics for a circular vortex (e.g. Eliassen 1971), Ekman pumping will occur at the RMW and the vortex will develop a circular shock structure. In the following sections, we will analyze the evolution of these shocks for a vortex with a single eyewall and three vortices with double eyewalls. Finally, we will analyze how vortex motion affects the evolution and structure of shocks for a vortex with a single eyewall.

4.4 The Single Eyewall Case

To illustrate how the boundary layer flow and Ekman pumping evolve into a steady state for a vortex with a single eyewall, the initial conditions have been chosen to be $u(x, y, 0) = -(y/r)v_{gr}$ and $v(x, y, 0) = (x/r)v_{gr}$. The forcing v_{gr} is specified by:

$$v_{gr,sce}(r) = v_1 s \exp(-\alpha_1 s) + v_2 s \exp(-\alpha_2 s) \tag{4.21}$$

where $s = r/r_m$ and r_m, v_1, v_2, α_1 and α_2 are constants to make $v_{gr} = v_m = 55$ m s^{-1} at $r = r_m = 17$ km. With $\mu = v_2/v_m$ and α_2 specified, the values of v_1 and α_1 are given by

$$\alpha_1 = (1 - \mu\alpha_2 \exp(-\alpha_2))/(1 - \mu \exp(-\alpha_2)), \qquad v_1 = v_m \exp(\alpha_1)(1 - \mu \exp(\alpha_2)).$$

For the following experiment, we use $\mu = 0.3$ and $\alpha_2 = 0.5$. Figures 4.3 – 4.7 show the two-dimensional evolution of the radial wind V_R, tangential wind V_T, vertical velocity w, and relative vorticity ζ. Here, we see that strong radial inflow causes a circular shock that shrinks the RMW of the vortex. Within the first 3 hours of the model simulation, there are rapid changes in the velocity and vorticity fields. Radial inflow velocities exceeding 25 m s^{-1} quickly develop and circular shock structures form around 10 km, as shown in Figure 4.4. Since vertical velocity is the radial gradient

of radial inflow, the shock structures leads to vertical velocities exceeding 20 m/s around 10 km, shown in Figure 4.5. Furthermore, the vertical velocity, which signifies Ekman pumping, shrinks to smaller radius. Note that the peak Ekman pumping lies on the inside edge of the RMW. Since Ekman pumping is usually related to diabatic heating for a tropical cyclone, this implies that the shock effect helps to place the diabatic heating to the region of high inertial stability so that the central pressure falls more rapidly.

Figure 4.8 shows the horizontal cross-section at $y = 0$ of V_R, V_T, w, and ζ at times $t = 0, 3, 6, 9, 12$ hours. During the first 3 hours of the simulation, the boundary layer tangential wind field becomes supergradient in the region $13 \leq r \leq 17$ km and subgradient for $r \geq 17$ km. In response to the tangential wind field, the vorticity gradient rapidly increases by a factor of 4 over a 2 km range and the region of highest vorticity gradient moves radially inward. This implies that the shock effect causes a rapid increase of inertial stability for the vortex. The Burgers' shock continues to amplify during the simulation until reaching a steady state at 12 hours. At the end of the simulation, the radial inflow velocities exceed 30 m s^{-1}, vertical velocities exceed 15 m s^{-1}, and tangential velocity remains strongly supergradient. The radial inflow velocities cause the RMW of the vortex to move inward, contracting the vortex. For a tropical cyclone, the shock effect must play an important role in determining the eyewall radius.

4.5 The Double Eyewall Case

Intense hurricanes often form an outer (or secondary) concentric eyewall, which leads to dissipation of the inner eyewall. Well-documented cases of this eyewall replacement processes include those of Willoughby et al. (1982), Black and Willoughby (1992), Samsury and Zipser (1995), and Didlake and Houze (2011). Our goal here is to better understand the changes in boundary layer inflow and Ekman pumping that occur during an eyewall replacement cycle. In order to accomplish this, we consider the family of gradient balanced flows given by

$$v_{gr}(r) = v_{gr,sce} + v_3\left(\frac{n(r/a_2)^{n-1}}{1+(n-1)(r/a_2)^n}\right), \tag{4.22}$$

where the details of the vortex structure are controlled by the three parameters v_3, a_2, and n. Using this forcing, we run a series of experiments with $n = 20$ and $a_2 = 50$ km. The varying parameters in each experiment are v_m, the velocity at the RMW of the inner eyewall, and v_3, the velocity at the RMW of the outer eyewall. For the first experiment, $v_m = 45$ m/s and $v_3 = 20$ m/s. The gradient wind profile for the first experiment is shown in Figure 4.9. This experiment mimics the scenario where the maximum velocity at the outer eyewall is approximately equal to the maximum velocity at the inner eyewall.

Figures 4.10 – 4.14 show the two-dimensional evolution of the radial wind V_R, tangential wind V_T, vertical velocity w, and relative vorticity ζ. Within the first 3 hours of the model simulation, radial inflow velocities exceeding 17 m s^{-1} develop near the outer eyewall, whereas weak radial inflow (approximately 6 m s^{-1}) develop near the inner eyewall. In response to the radial inflow, strong Ekman pumping occurs at the outer eyewall with weak Ekman pumping occurring near the inner eyewall. As the vortex evolves, the outer eyewall contracts and intensifies, whereas the inner eyewall diminishes. Also, as the vortex evolves, the tangential wind near the outer eyewall becomes supergradient, whereas the tangential flow near the inner eyewall remains close to gradient flow. These results suggest that the outer eyewall chokes off the radial inflow to the inner eyewall, thus weakening Ekman pumping in the inner eyewall.

This behavior can be explained using the shock effect where we visualize an eyewall replacement cycle as two isolated shocks connected by a smooth ramp. In the boundary layer, a shock is characterized by a sharp gradient in radial velocity. On the outer edge of the shock, there is strong radial inflow, and on inner edge of the shock, there is weak radial outflow. For the outer eyewall, radial inflow outside of the outer eyewall creates a shock that propagates radially inward. As the outer shock propagates inward, it cuts off the region of radial inflow for the inner eyewall and the

weak radial outflow on the leading edge of the outer shock weakens the radial gradient of radial velocity for the inner eyewall. Therefore, the shock structure for the inner eyewall is inhibited by the propagating shock of the outer eyewall. This behavior is verified by Figure 4.15, which shows the horizontal cross-section at $y = 0$ of V_R, V_T, w, and ζ at times $t = 0, 3, 6, 9, 12$ hours. We see that the outer eyewall develops a shock structure that propagates radially inward, whereas the inner eyewall does not develop a strong shock structure.

The second experiment mimics the scenario where the maximum velocity at the outer eyewall is greater than the maximum velocity at the inner eyewall. For the second experiment, $v_m = 45$ m s^{-1} and $v_3 = 30$ m s^{-1}. The gradient wind profile for the second experiment is shown in Figure 4.16. Figures 4.17 – 4.21 show the two-dimensional evolution of the radial wind V_R, tangential wind V_T, vertical velocity w, and relative vorticity ζ. The evolution of this vortex is similar to the previous experiment, except the shock structure in the outer eyewall develops faster and is stronger. Within the first 3 hours of the model simulation, radial inflow velocities exceeding 20 m s^{-1} develop near the outer eyewall, whereas weak radial inflow develops near the inner eyewall. In response to the radial inflow, strong Ekman pumping occurs at the outer eyewall with weak Ekman pumping occurring near the inner eyewall. As the vortex evolves, the outer eyewall contracts and intensifies, whereas the inner eyewall diminishes. Also, as the vortex evolves, the tangential wind near the outer eyewall becomes supergradient, whereas the tangential flow near the inner eyewall remains close to gradient flow. This behavior is verified by Figure 4.22, which shows the horizontal cross-section at $y = 0$ of V_R, V_T, w, and ζ at times $t = 0, 3, 6, 9, 12$ hours. We see that the outer eyewall develops a shock structure that propagates radially inward, whereas the inner eyewall does not develop a shock.

The third experiment mimics the scenario where the maximum velocity at the outer eyewall is smaller than the maximum velocity at the inner eyewall. For the third experiment, $v_m = 60$ m s^{-1} and $v_3 = 10$ m s^{-1}. The gradient wind profile for the third experiment is shown in Figure 4.23. Figures 4.24 – 4.28 show the two-dimensional evolution of the radial wind V_R, tangential wind V_T,

vertical velocity w, and relative vorticity ζ. The evolution of this vortex is qualitatively different than the previous two experiments. Here, the shock structure develops in the inner eyewall, whereas there is no shock structure in the outer eyewall. Within the first 3 hours of the model simulation, radial inflow velocities exceeding 25 m s^{-1} develop near the inner eyewall. In response to the radial inflow, strong Ekman pumping occurs at the inner eyewall with weak Ekman pumping occurring near the inner eyewall. As the vortex evolves, the inner eyewall contracts and intensifies. Also, as the vortex evolves, the tangential wind near the outer eyewall becomes supergradient, whereas the tangential flow near the inner eyewall remains close to gradient flow.

This behavior can also be explained using the shock effect. On the outer edge of the shock on the inner eyewall, there is strong radial inflow, and on inner edge of the shock, there is weak radial outflow. As the shock propagates radially inward, the region behind the shock develops a strong radial velocity gradient, which weakens the radial velocity gradient near the outer eyewall. In this case, the shock associated with the inner eyewall chokes the development of a shock for the outer eyewall. This behavior is verified by Figure 4.29, which shows the horizontal cross-section at $y = 0$ of V_R, V_T, w, and ζ at times $t = 0, 3, 6, 9, 12$ hours. We see that the inner eyewall develops a shock structure that propagates radially inward, whereas the outer eyewall does not develop a shock structure.

This experiment suggests that the development and propagation of shock-like structures in the boundary layer depends sensitively on the radial structure of the gradient wind profile (or radial distribution of vorticity) for the vortex. For strong, inertially stable vortices, the above analysis suggests a small time-scale for shock formation, whereas there will be a long time-scale for shock formation for weak vortices. The dynamics of an eyewall replacement cycle can be simplified to the development of isolated shocks connected by smooth ramps. The location and propagation of the shock depends on the relative strength of the tangential velocity of the inner and outer eyewall.

4.6 The Effect of Vortex Motion

We now consider the effect of cyclone movement by embedding a vortex in a 5 m s^{-1} and 10 m s^{-1} southerly flow. The initial condition is the same as the single eyewall case:

$$v_{gr,sce}(r) = v_1 s \exp(-\alpha_1 s) + v_2 s \exp(-\alpha_2 s) \tag{4.23}$$

where $r_m = 17$ km, $v_m = 55$ m s^{-1}, $\alpha_2 = 0.5$, $\mu = 0.3$, $s = r/r_m$, and

$$\alpha_1 = (1 - \mu\alpha_2 \exp(-\alpha_2))/(1 - \mu \exp(-\alpha_2)), \qquad v_1 = v_m \exp(\alpha_1)(1 - \mu \exp(\alpha_2)).$$

Figures 4.30– 4.33 show the evolution of the wind field and vorticity field for this vortex embedded in the 5 m s^{-1} southerly flow. Within the first 3 hours of the model simulation, asymmetries in the wind field and vorticity field begin to develop. The maximum tangential velocity is located in the left forward quadrant with the strongest winds just inside the radius of maximum gradient level winds. In response to the tangential velocity field, the maximum relative vorticity field is located in the front left quadrant of the vortex. In contrast, the vertical velocity is strongest in the right forward quadrant and in response to the vertical velocity fields, the maximum radial velocity is located in the front quadrant of the storm. As the vortex continues to evolve, the asymmetries become stronger. These distribution of velocity and vorticity are consistent with Kepert and Wang (2001). Figure 4.34 shows the horizontal cross-section at $y = 0$ of V_r, V_t, w, and ζ at times $t = 0, 3, 6, 9, 12$ hours. Here, we see the strength of the asymmetries caused by the vortex motion. To the left of the vortex, there is a region of weak radial outflow within the RMW of the vortex, which causes a region of weak subsidence. Therefore, the shock structure on the left side of the storm is slightly weaker than the right side of the storm. To the right of the vortex, the flow is supergradient and is accompanied by strong inflow. This causes the Burgers' shock structure on the right side of the storm to strengthen.

Figures 4.35 – 4.38 show the evolution of the wind field and vorticity field for this vortex embedded in the 10 m s^{-1} southerly flow. Here, we see the asymmetries begin to strength, as the nonlinear asymmetric advective interactions become stronger. For the vortex embedded in 5 m s^{-1} southerly flow, radial inflow and Ekman pumping are large in a broad arc ahead of the vortex. For the vortex embedded in 10 m s^{-1} southerly flow, radial inflow and Ekman pumping becomes concentrated more ahead and to the right of the storm. The anticyclonic spiral character of the vertical velocity field becomes more pronounced. Due to increased advection of momentum into the core, the RMW tends to contract. The anticyclonic spiral nature of the vertical velocity and the concentrated radial flow in the right front quadrant of the storm creates an anticyclonic Burgers' shock spiral, as shown in Figure 4.37. Figure 4.39 shows the horizontal cross-section at $y = 0$ of V_r, V_t, w, and ζ at times $t = 0, 3, 6, 9, 12$ hours. Due to the strength of the nonlinear asymmetric advective interactions, the strength of the asymmetries caused by the vortex motion dramatically increases. To the left of the vortex, radial inflow is virtually nonexistent within the RMW, which causes a region of strong subsidence shown. Therefore, the shock structure on the left side of the storm is slightly weaker than the right side of the storm. To the right of the vortex, the flow becomes strongly supergradient (approximately 20 m s^{-1} supergradient) and is accompanied by strong vertical motion (approximately 35 m s^{-1}) and strong radial inflow (approximately 50 m s^{-1}). This suggests that the Burgers' shock is relatively weak on the left side of the vortex and relatively strong on the right side of the vortex, indicating a strongly anticyclonic spiral shock structure.

4.7 Summary and Applications to the Tropical Cyclone Boundary Layer

In this chapter, we studied the 2D evolution of shock-like structures in tropical cyclones. Kepert and Wang (2001) stated that the two dominant physical processes necessary to produce supergradient winds in the tropical cyclone boundary layer are horizontal advection and horizontal diffusion. This suggests that the boundary layer model should resemble the nonlinear viscous Burgers' equation and for a given vortex, a shock-like structure should develop.

Our first experiment mimicked a vortex with a single eyewall. Here, we saw that strong radial inflow created a circular shock that shrinks the RMW of the vortex. Within the first 3 hours of the model simulation, there were rapid changes in the velocity and vorticity fields. Radial inflow velocities exceeding 25 m s^{-1} quickly develop and circular shock structures form at a radius of approximately 10 km. In response to the sharp gradient in radial velocity, the shock structures lead to strong Ekman pumping, with vertical velocities exceeding 20 m s^{-1} near the RMW of the vortex. Since Ekman pumping is usually related to diabatic heating for a tropical cyclone, this implies that the shock effect helps to place the diabatic heating to the region of high inertial stability so that the central pressure falls more rapidly. For a tropical cyclone, the shock effect must play an important role in determining the eyewall radius.

Our next series of experiments mimicked a vortex with a double eyewall in order to study the dynamics of an eyewall replacement cycle. When the maximum velocity of the outer eyewall was greater than or approximately equal to the maximum velocity of the inner eyewall, the outer eyewall contracted inward, choking the radial inflow to the inner eyewall. This caused the maximum velocity of the inner eyewall to diminish whereas the maximum velocity of the outer eyewall intensified. When the maximum velocity of the outer eyewall was weaker than the maximum velocity of the inner eyewall, the outer eyewall diminished in strength whereas a shock-like structure formed on the inner eyewall.

The behavior of the vortex with a double eyewall can be explained using the shock effect where we visualize an eyewall replacement cycle as two isolated shocks connected by smooth ramps. In the boundary layer, a shock is characterized by a sharp gradient in radial velocity. For the outer eyewall, radial inflow outside of the outer eyewall creates a shock that propagates radially inward. As the outer shock propagates inward, it cuts off the region of radial inflow for the inner eyewall and the weak radial outflow on the leading edge of the outer shock weakens the radial gradient of radial velocity for the inner eyewall. Therefore, the shock structure for the inner eyewall is

inhibited by the propagating shock of the outer eyewall. When the maximum velocity at the inner eyewall is greater than the maximum velocity at the outer eyewall, the strong radial inflow into the eyewall region causes a shock structure. As the shock propagates radially inward, the region behind the shock develops a strong radial velocity gradient, which weakens the radial velocity gradient near the outer eyewall. In this case, the shock associated with the inner eyewall chokes the development of a shock for the outer eyewall. As predicted, the development and propagation of shock-like structures in the boundary layer depends sensitively on the radial structure of the gradient wind profile (or radial distribution of vorticity) for the vortex and the relative strength of the tangential velocity of the inner and outer eyewall.

Finally, we studied the effect of vortex motion on the evolution of shock-like structures in the boundary layer. The asymmetry in the boundary layer response is forced by the asymmetry in frictional drag due to the translation of the vortex. For a relatively slow moving vortex (5 m s^{-1} translation), the nonlinear asymmetric advective interactions remain relatively weak. Inflow is maximum in the right-front quadrant and Ekman pumping is large in a broad arc ahead of the center of the vortex. The maximum winds lie nearly ahead of the vortex due to horizontal advection into the inertially stable core region. When the translation speed is increased to 10 m s^{-1}, the nonlinear asymmetric advective interactions become stronger. Inflow and Ekman pumping become concentrated more ahead and to the right of the storm. Due to increased horizontal advection into the core, the RMW tends to contract. As the translation speed of the vortex increases, the anticyclonic spiral in the vertical velocity field becomes more pronounced and the circular shock becomes an anticyclonic spiral with maximum strength in the right quadrant. This suggests that vortex motion will cause asymmetries in convective heat release for a tropical cyclone.

The above analysis focused only on dynamical effects on the tropical cyclone boundary layer. It is assumed that diabatic heating will have a significant influence on the evolution of shocks in the boundary layer. However, the role of moist convection on the development and evolution of shocks

in the boundary layer is beyond the scope of this dissertation and will be a subject of future research. Another important limitation is the lack of vertical structure in the vortex. In the next chapter, we will study the role of vertical advection in the development of shock-like structures in the boundary layer and determine how the development of these shocks influence the thermodynamic structure of the tropical cyclone.

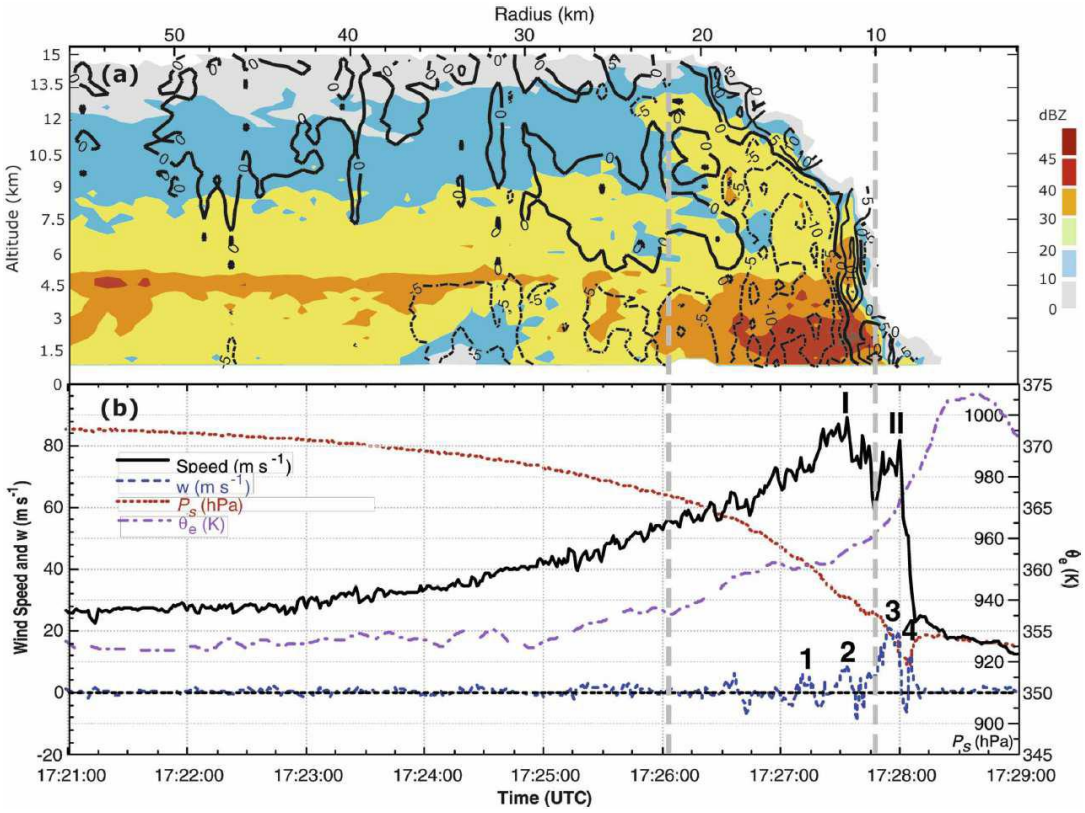

Figure 4.1: Data from the low level (450 m) flight leg into Hurricane Hugo on 15 September 1989. The upper panel shows radar reflectivity (dBZ scale on right), while the lower panel shows horizontal wind speed, vertical velocity w, surface pressure p_s, and equivalent potential temperature θ_e. The thick dashed vertical lines denote the edges of the eyewall at low levels. From Marks et al. (2008)

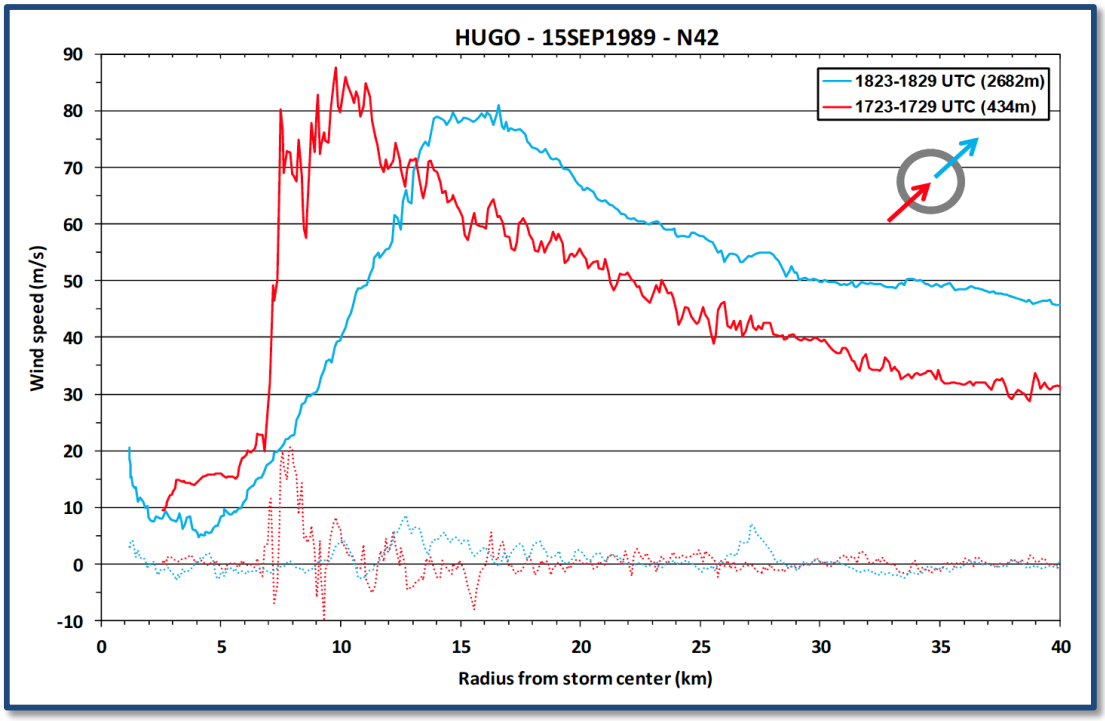

Figure 4.2: NOAA WP-3D (N42RF) aircraft data from 434 m (red, inbound, southwest quadrant) and 2682 m (blue, outbound, northeast quadrant) flight legs in Hurricane Hugo on 15 September 1989. Solid curves show horizontal wind speed while dotted curves show vertical velocity. The curves are based on 1 second flight data, which corresponds to a spatial resolution of approximately 100 m.

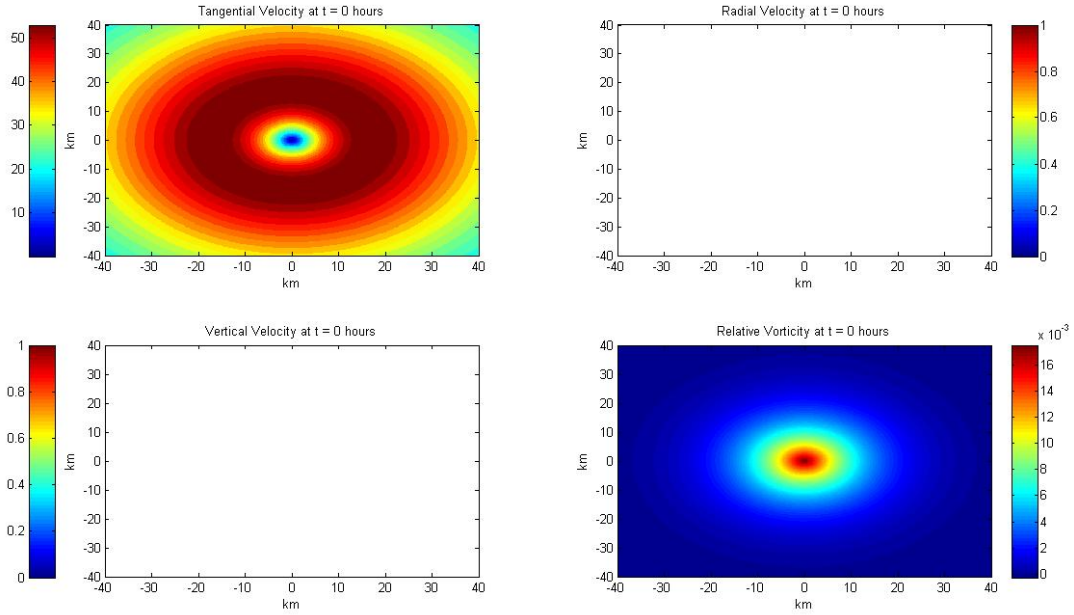

Figure 4.3: Initial condition of the single eyewall case.

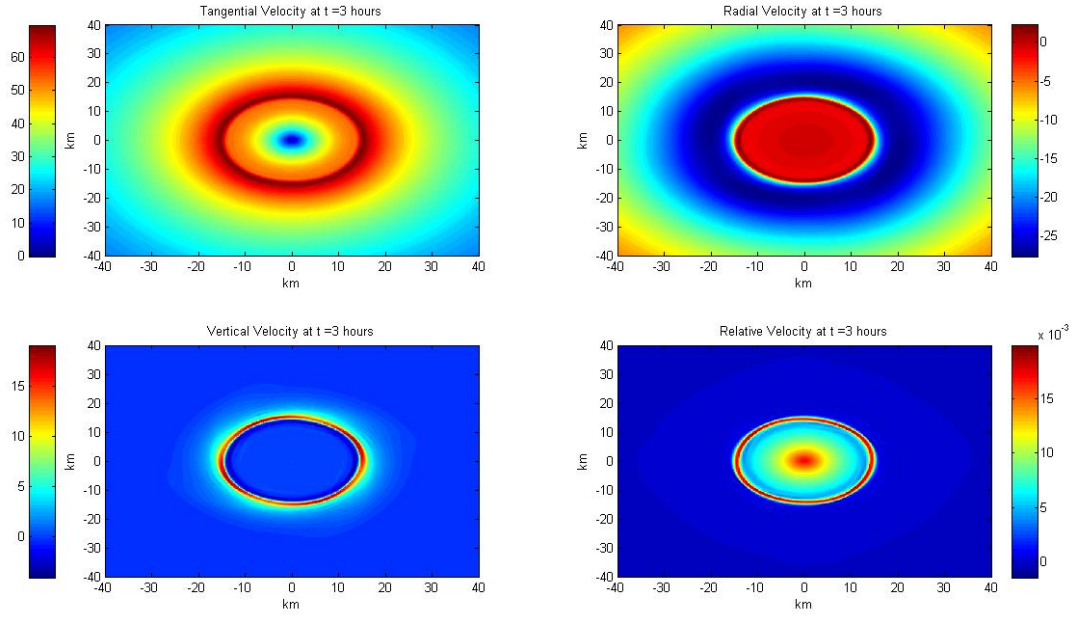

Figure 4.4: Evolution of the single eyewall at t = 3 hr.

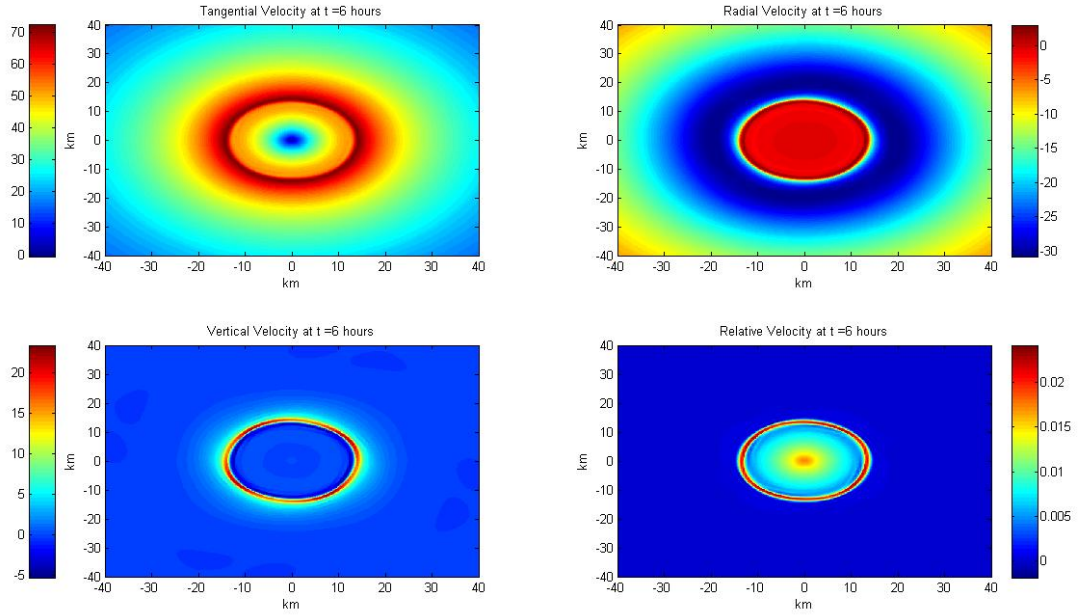

Figure 4.5: Evolution of the single eyewall at t = 6 hr.

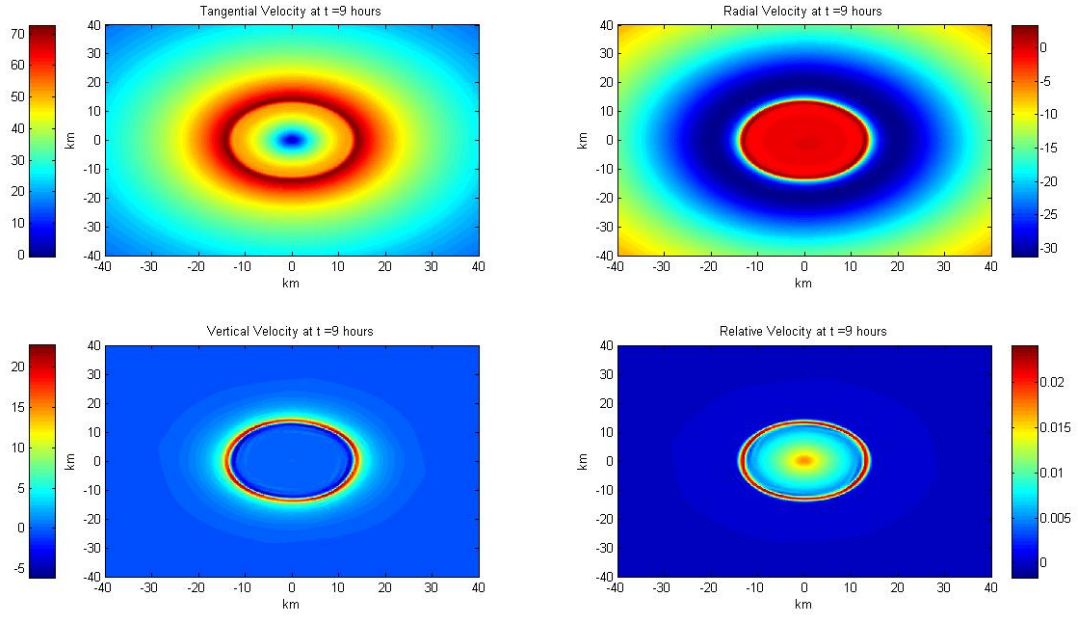

Figure 4.6: Evolution of the single eyewall at t = 9 hr.

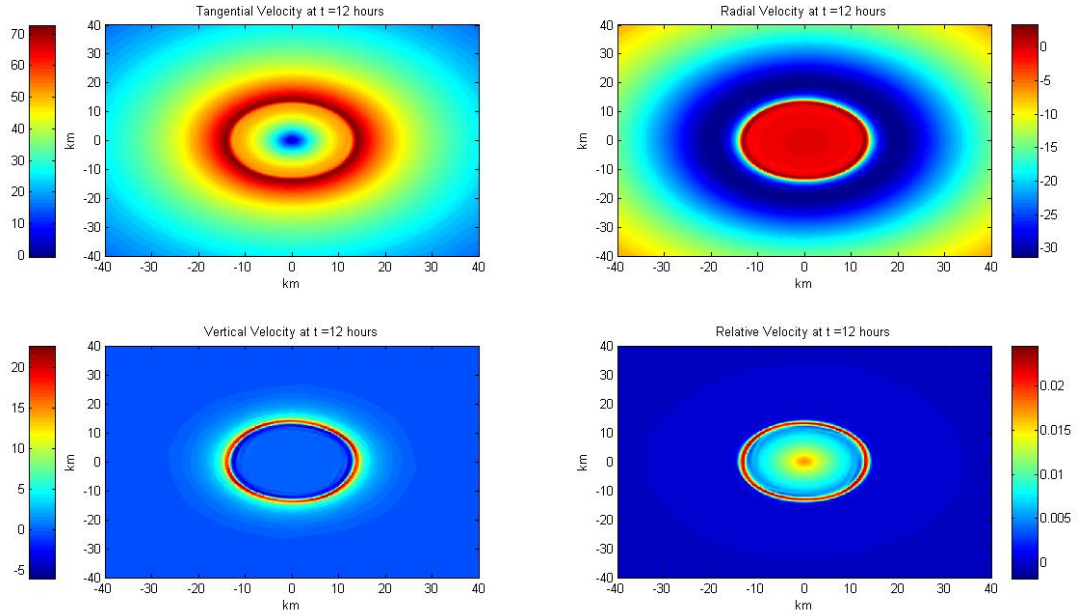

Figure 4.7: Evolution of the single eyewall at t = 12 hr.

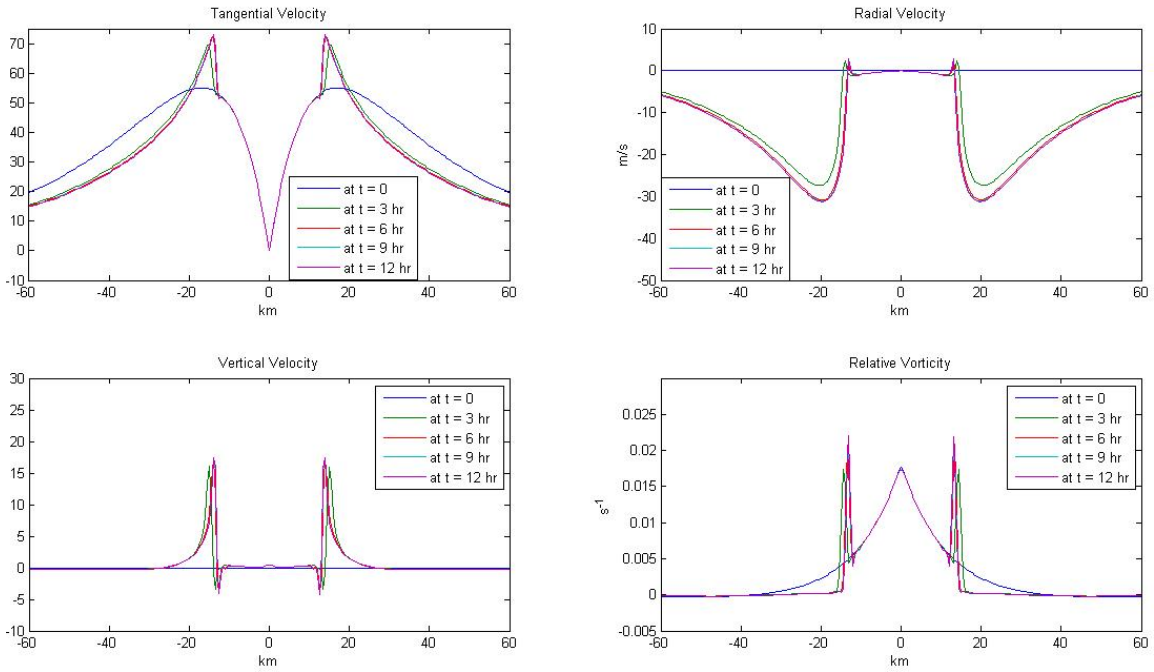

Figure 4.8: Horizontal cross-section of the velocity field and vorticity field for the single eyewall case.

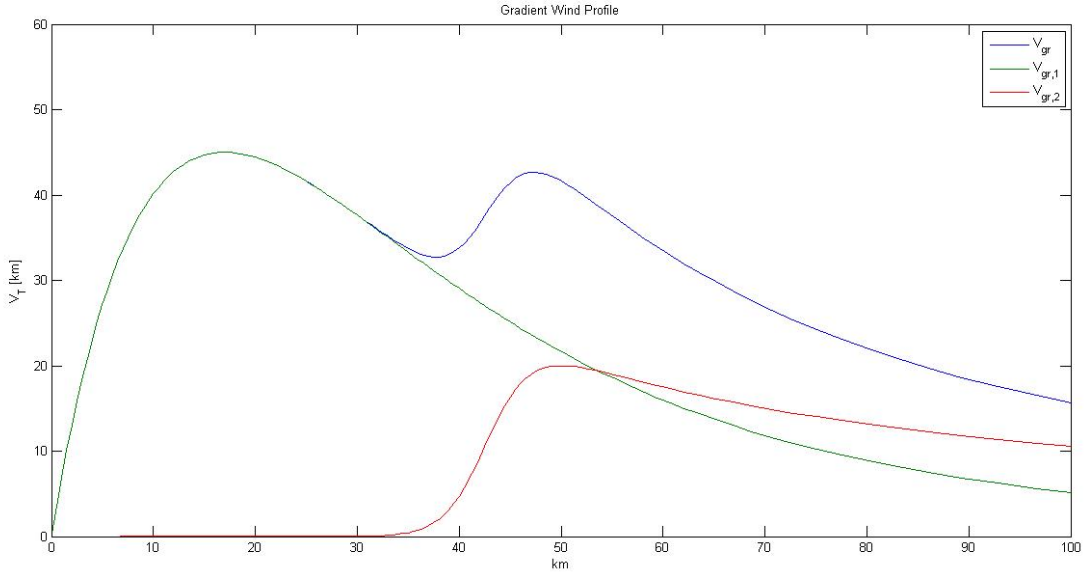

Figure 4.9: Gradient wind profile for experiment 1.

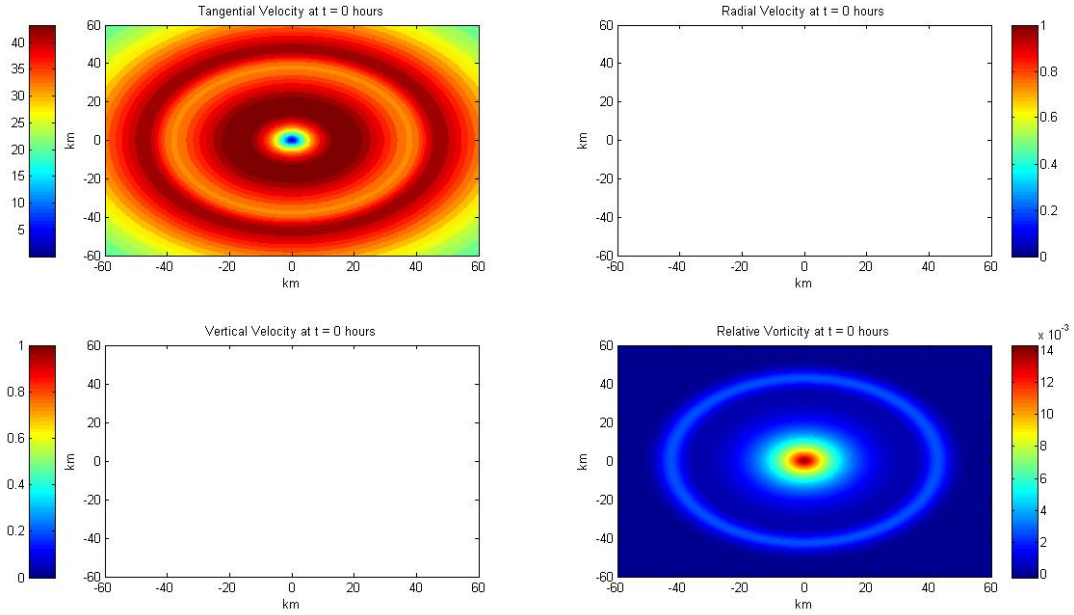

Figure 4.10: Initial condition for experiment 1.

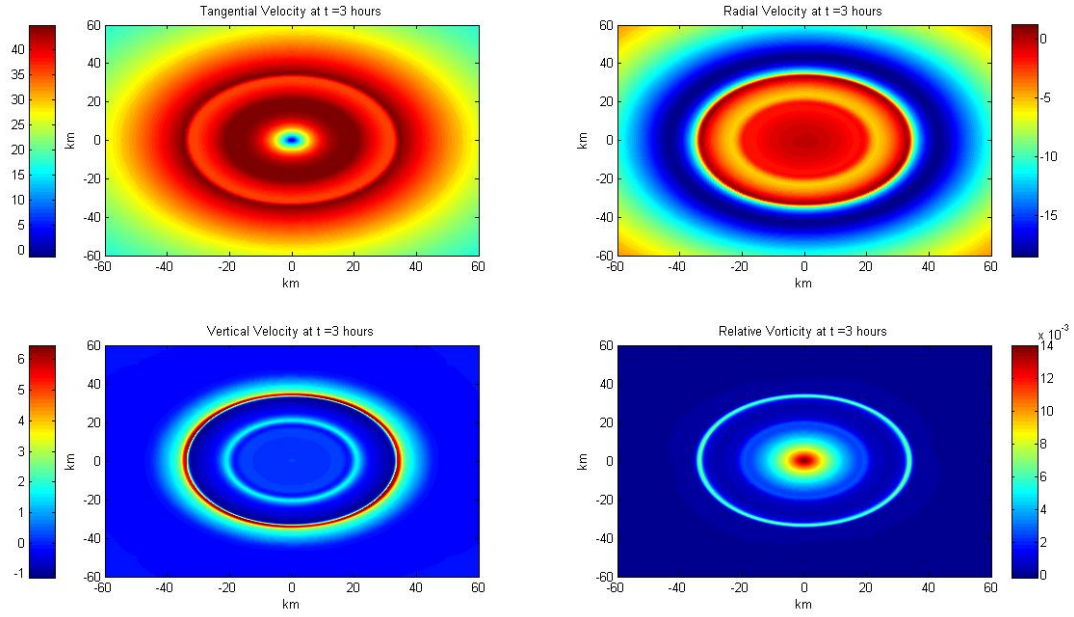

Figure 4.11: Evolution of experiment 1 at t = 3 hr.

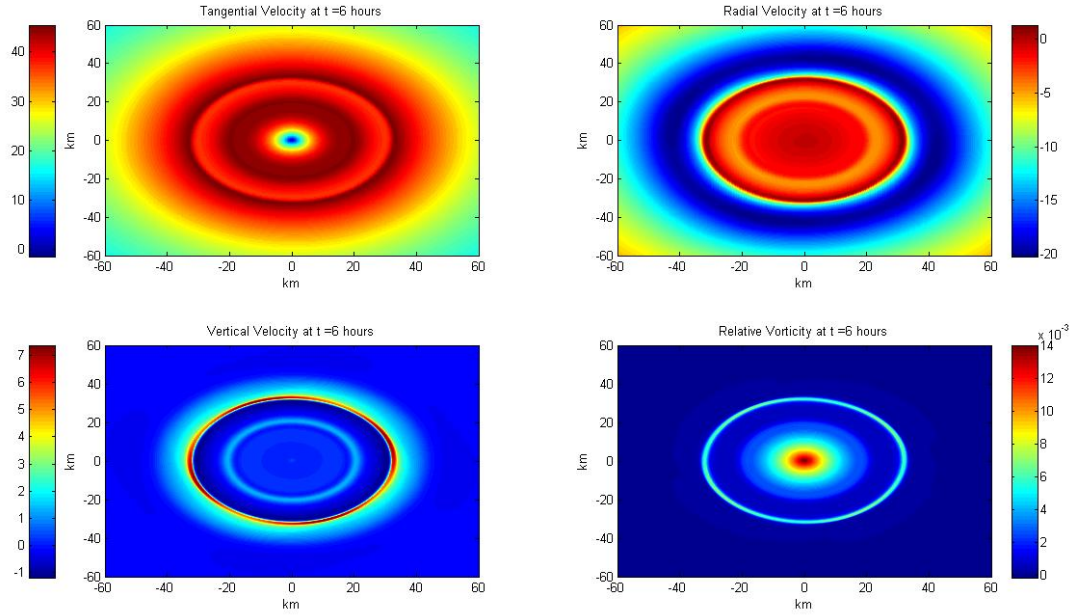

Figure 4.12: Evolution of experiment 1 at t = 6 hr.

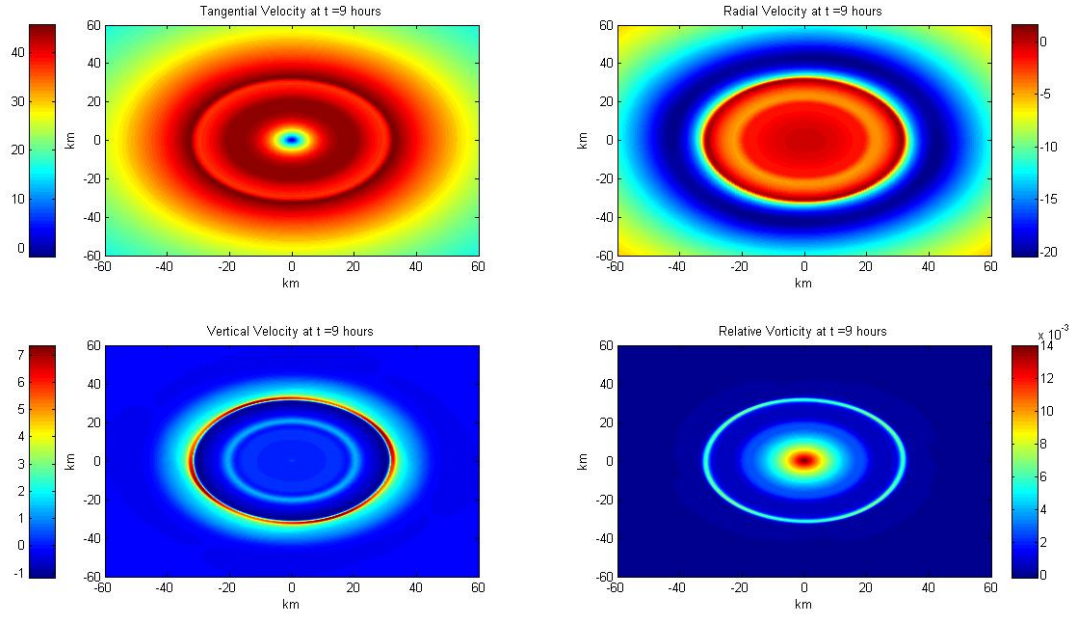

Figure 4.13: Evolution of experiment 1 at t = 9 hr.

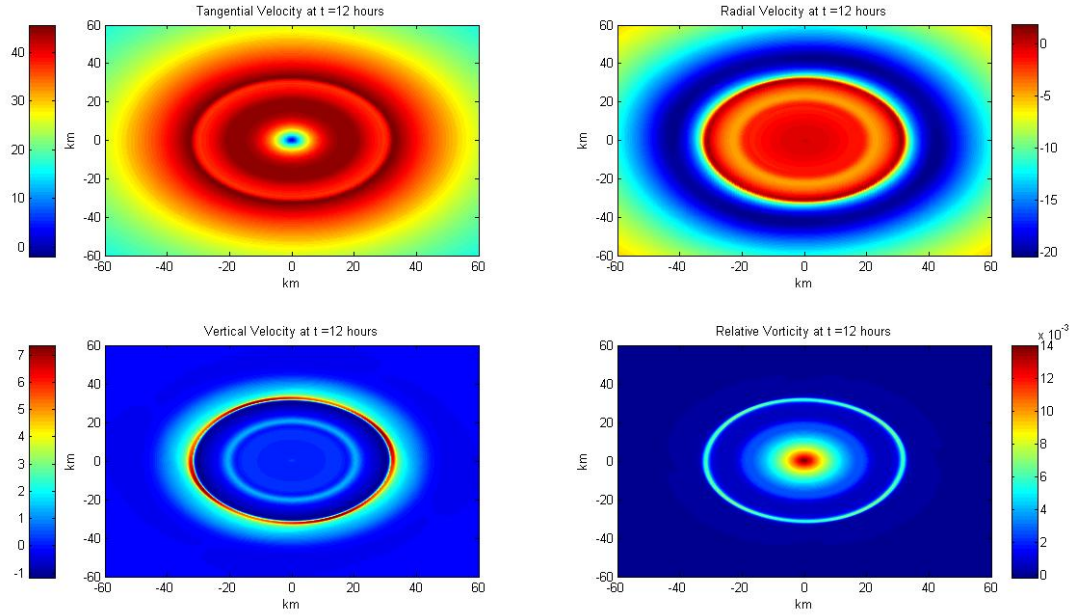

Figure 4.14: Evolution of experiment 1 at t = 12 hr.

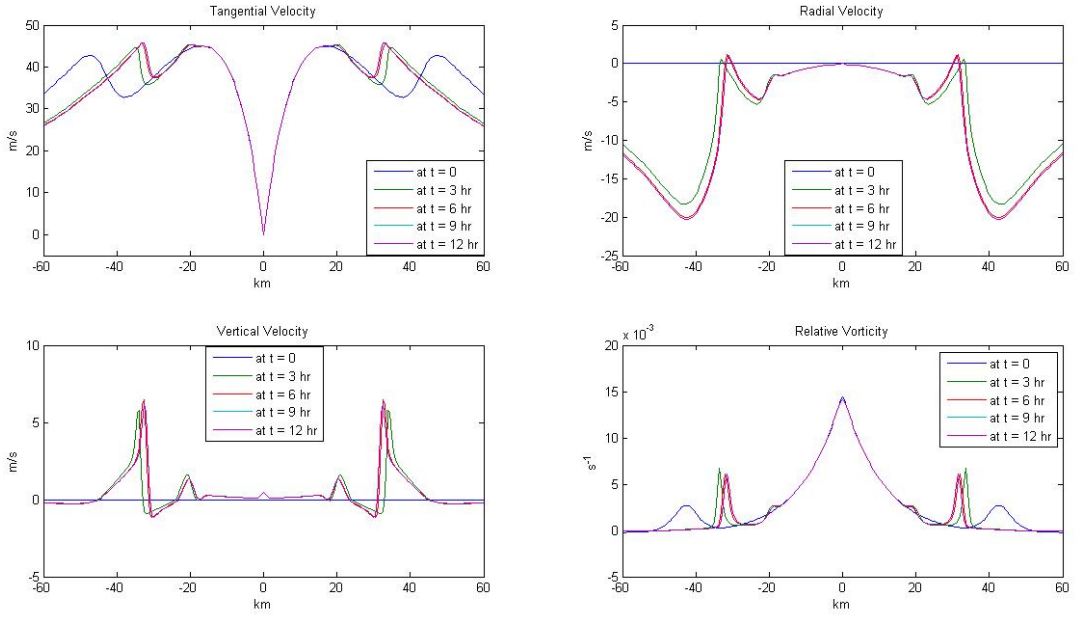

Figure 4.15: Horizontal cross-section of the velocity field and vorticity field for experiment 1.

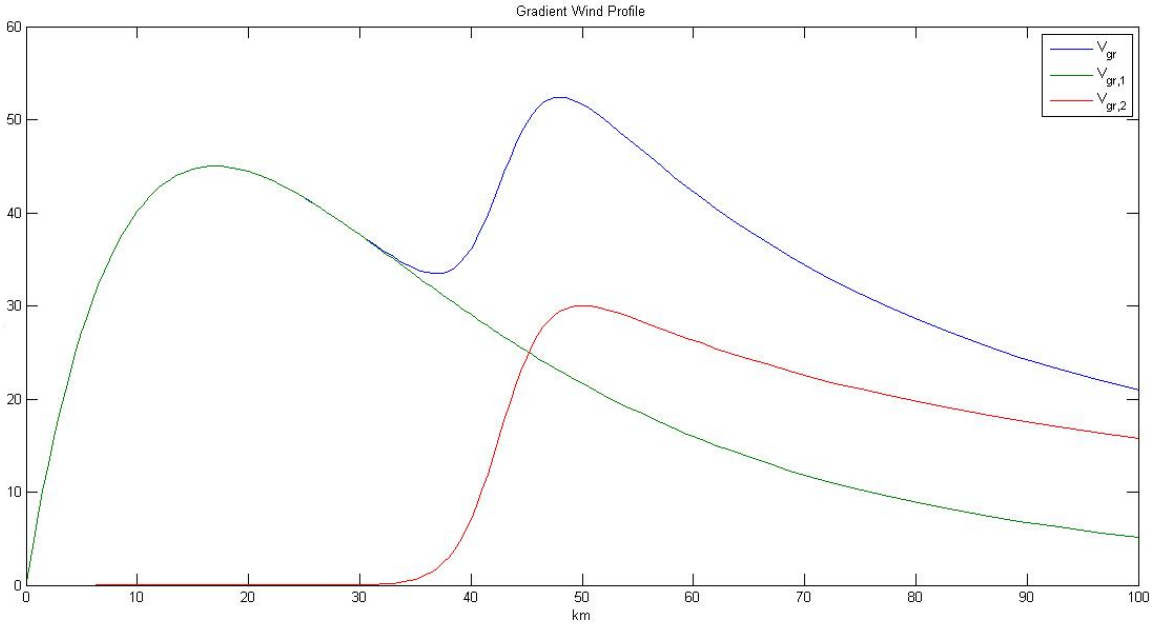

Figure 4.16: Gradient wind profile for experiment 2.

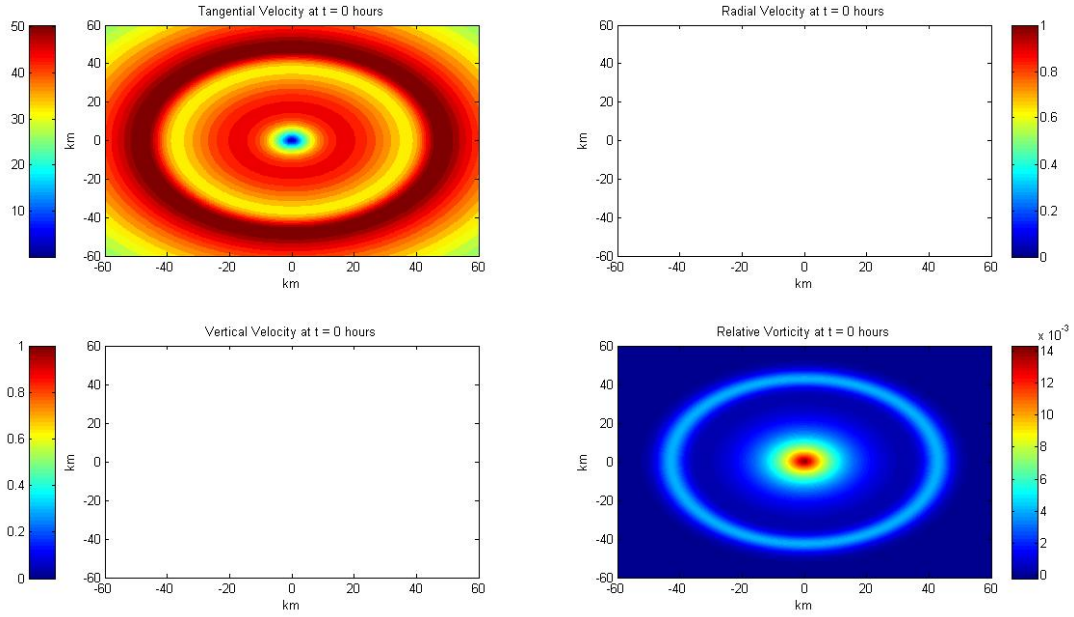

Figure 4.17: Initial condition for experiment 2.

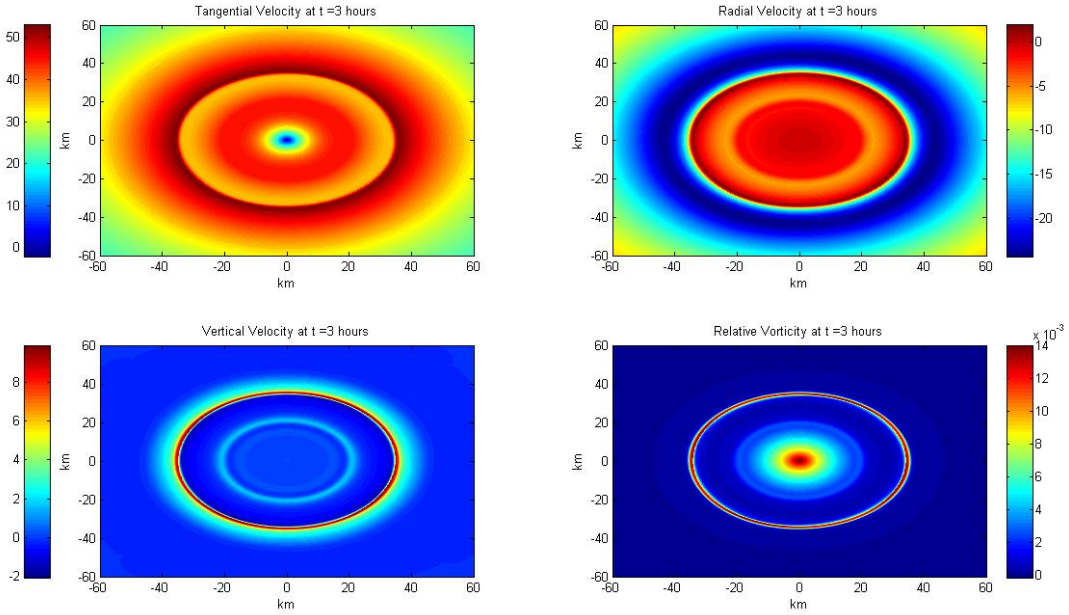

Figure 4.18: Evolution of experiment 2 at t = 3 hr.

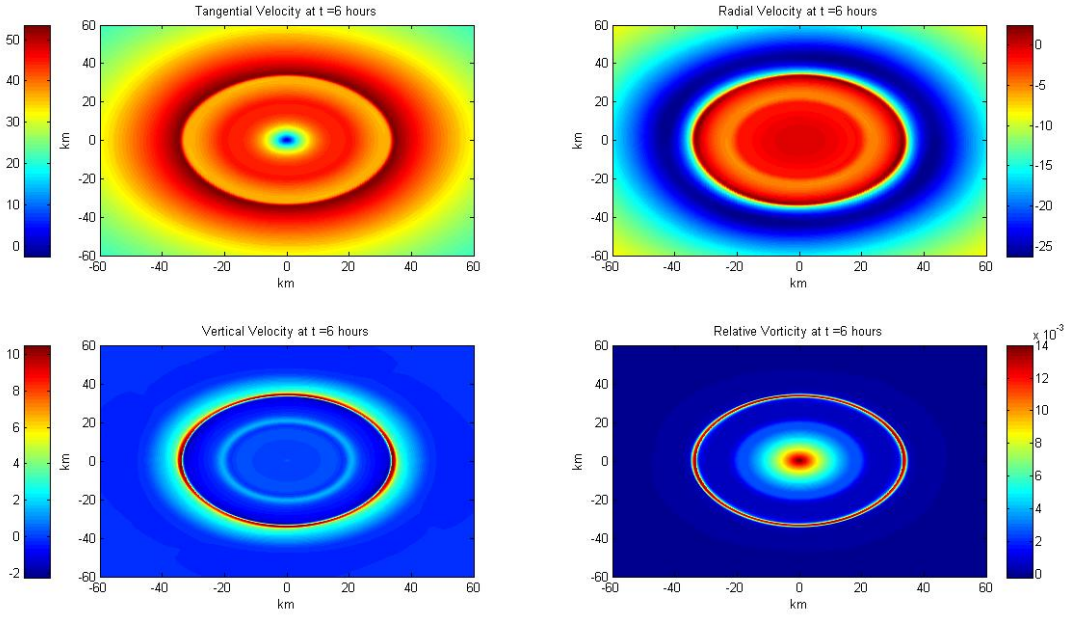

Figure 4.19: Evolution of experiment 2 at t = 6 hr.

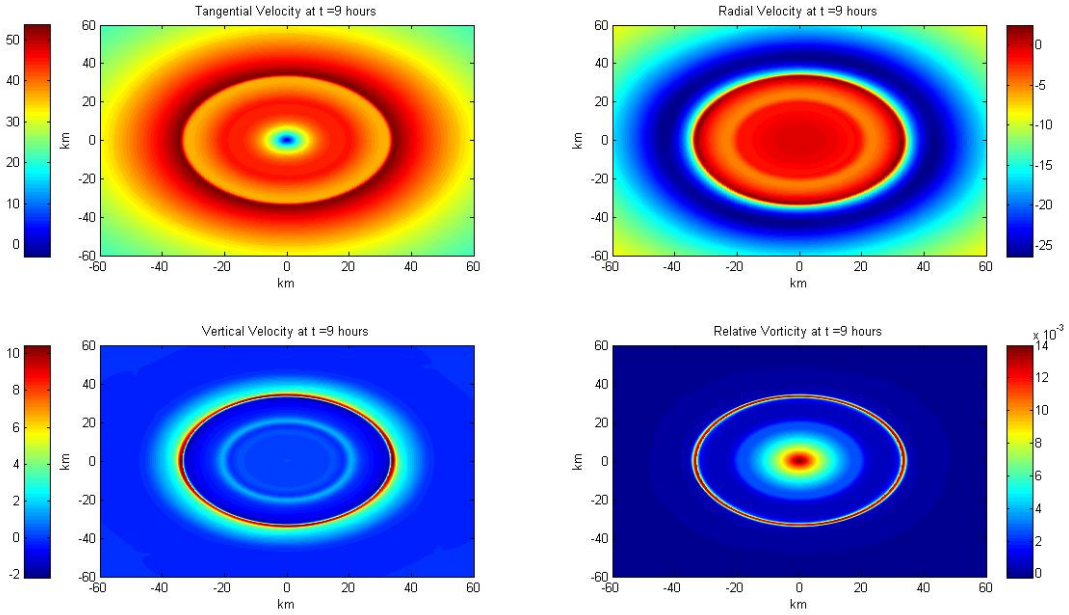

Figure 4.20: Evolution of experiment 2 at t = 9 hr.

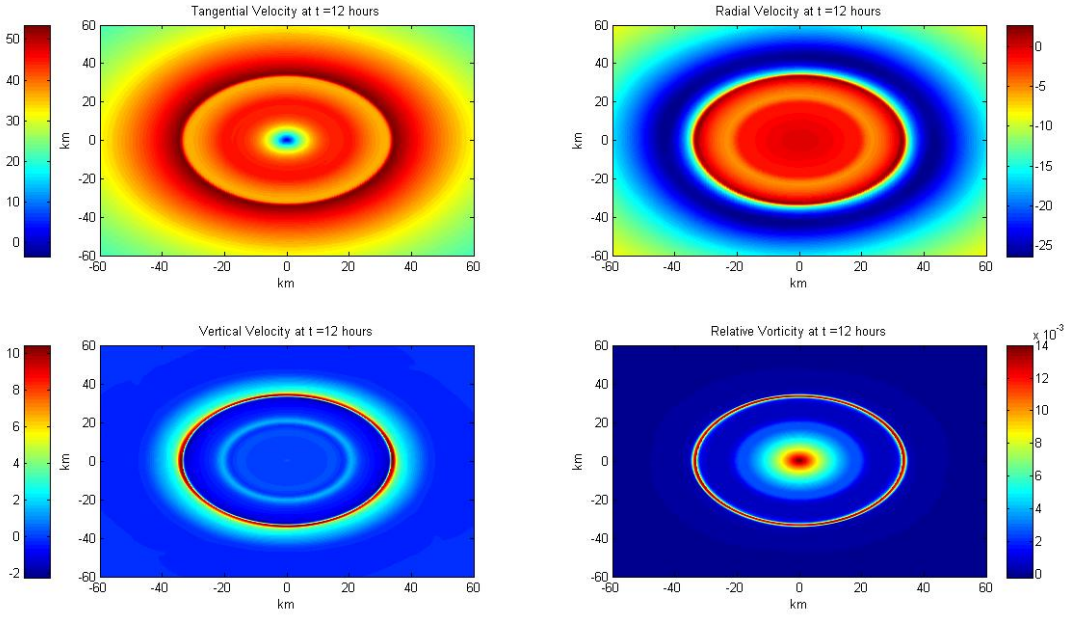

Figure 4.21: Evolution of experiment 2 at t = 12 hr.

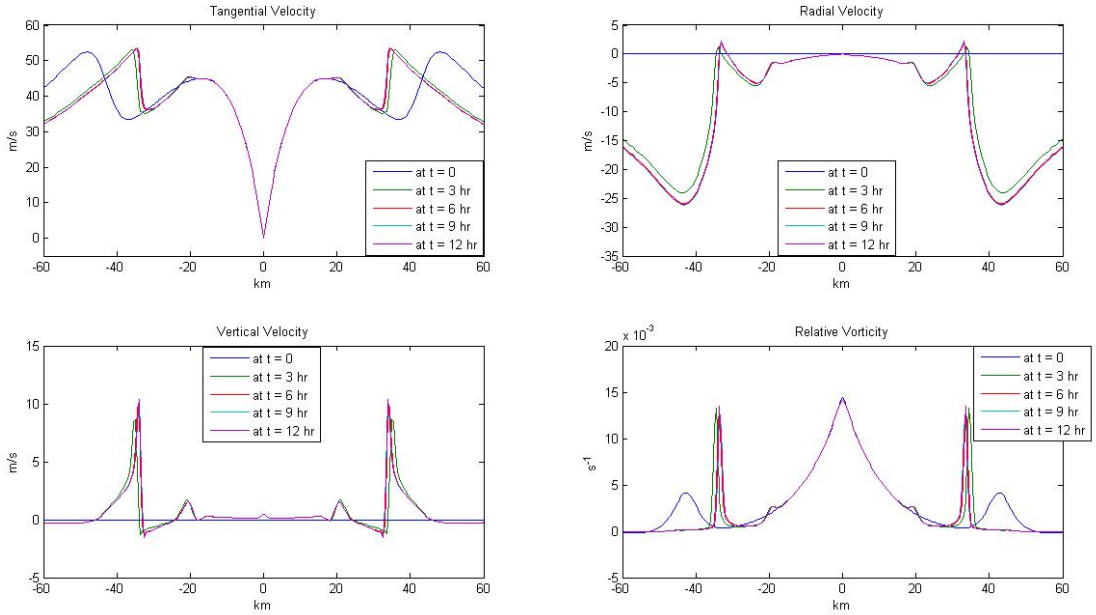

Figure 4.22: Horizontal cross-section of the velocity field and vorticity field for experiment 2.

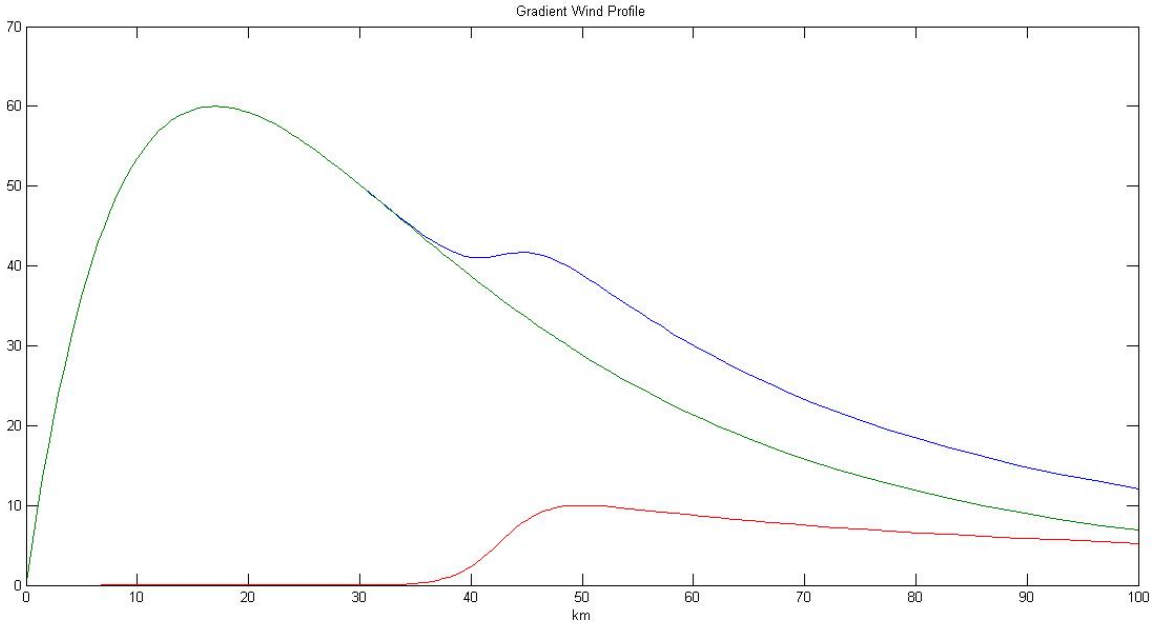

Figure 4.23: Gradient wind profile for experiment 3.

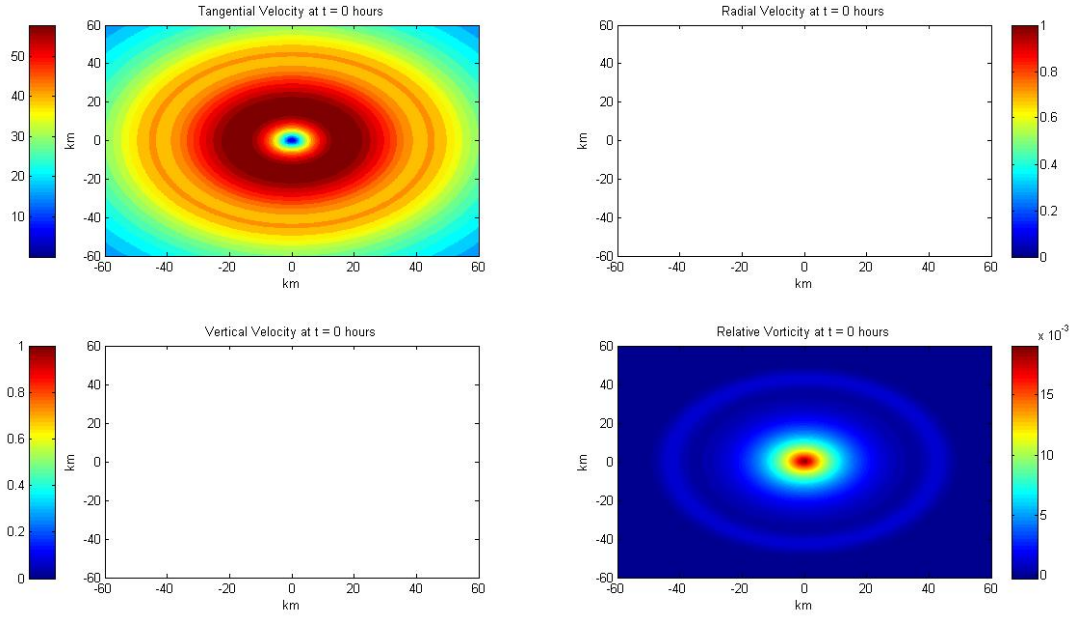

Figure 4.24: Initial condition for experiment 3.

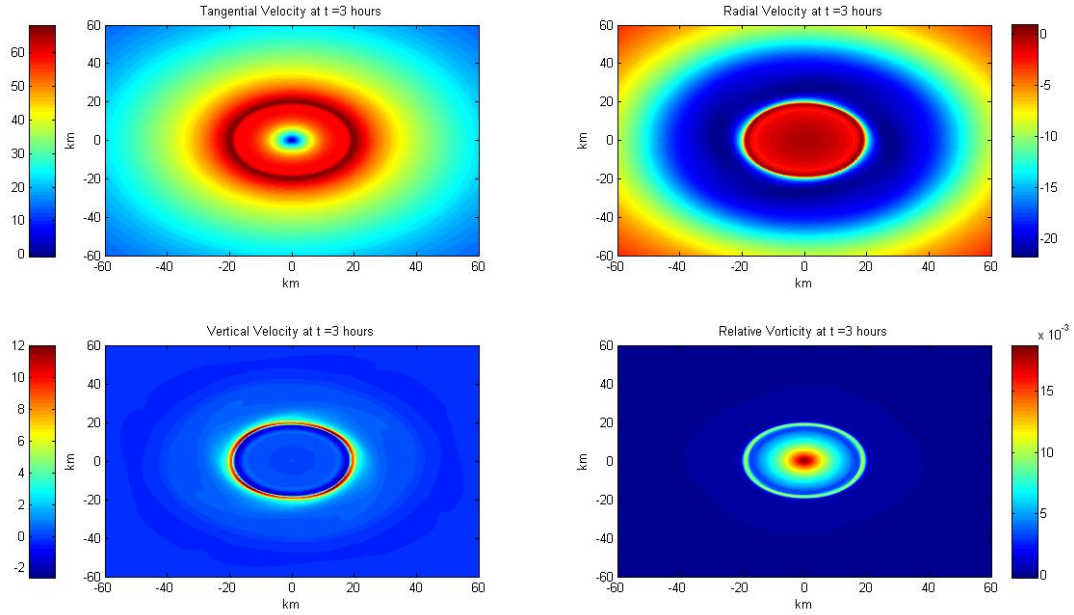

Figure 4.25: Evolution of experiment 3 at t = 3 hr.

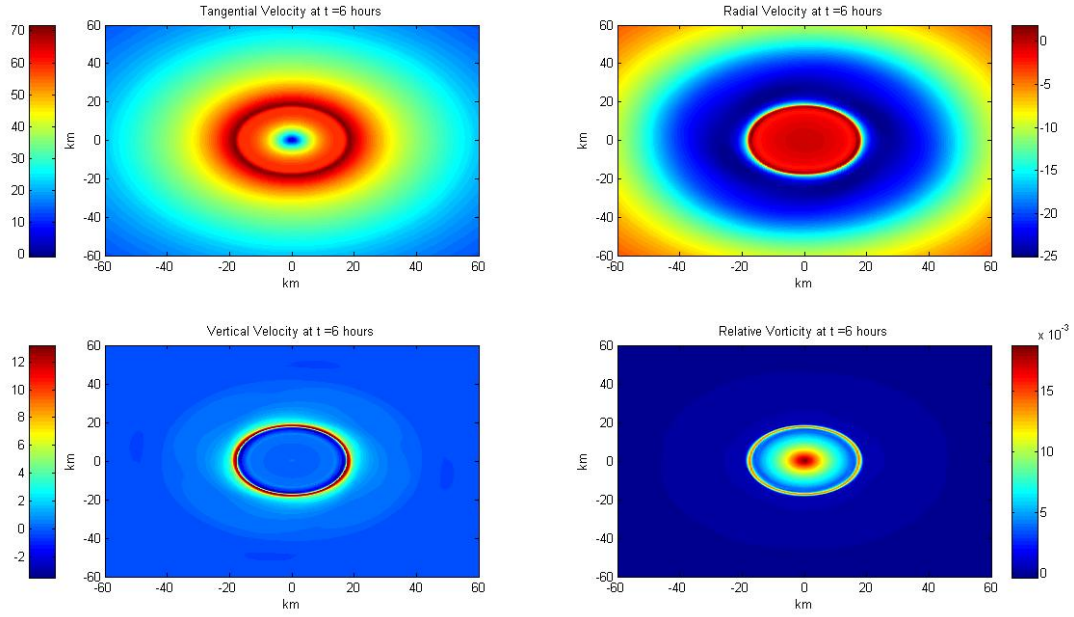

Figure 4.26: Evolution of experiment 3 at t = 6 hr.

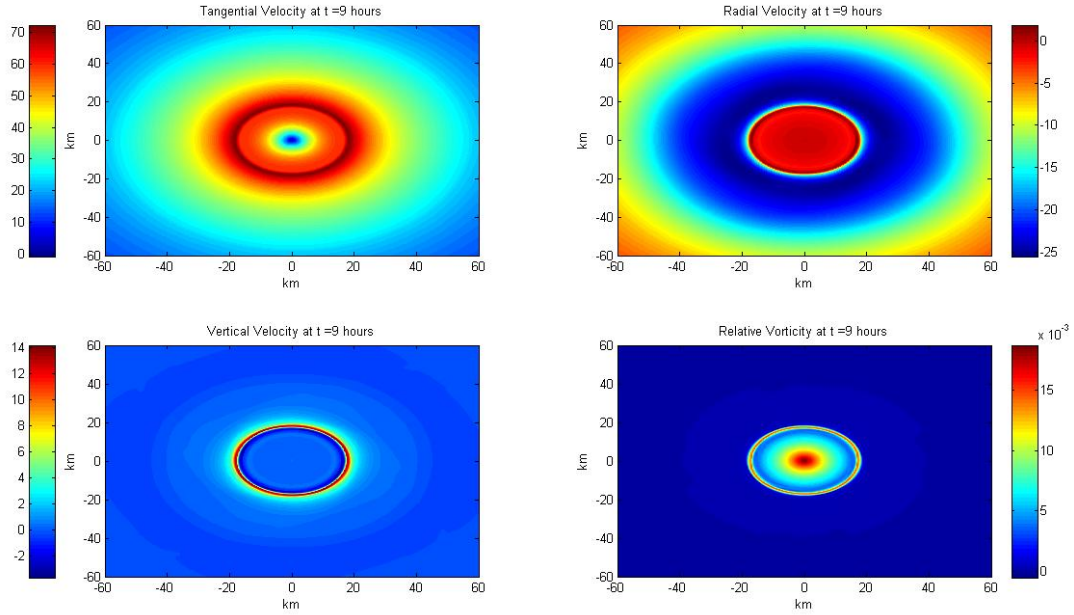

Figure 4.27: Evolution of experiment 3 at t = 9 hr.

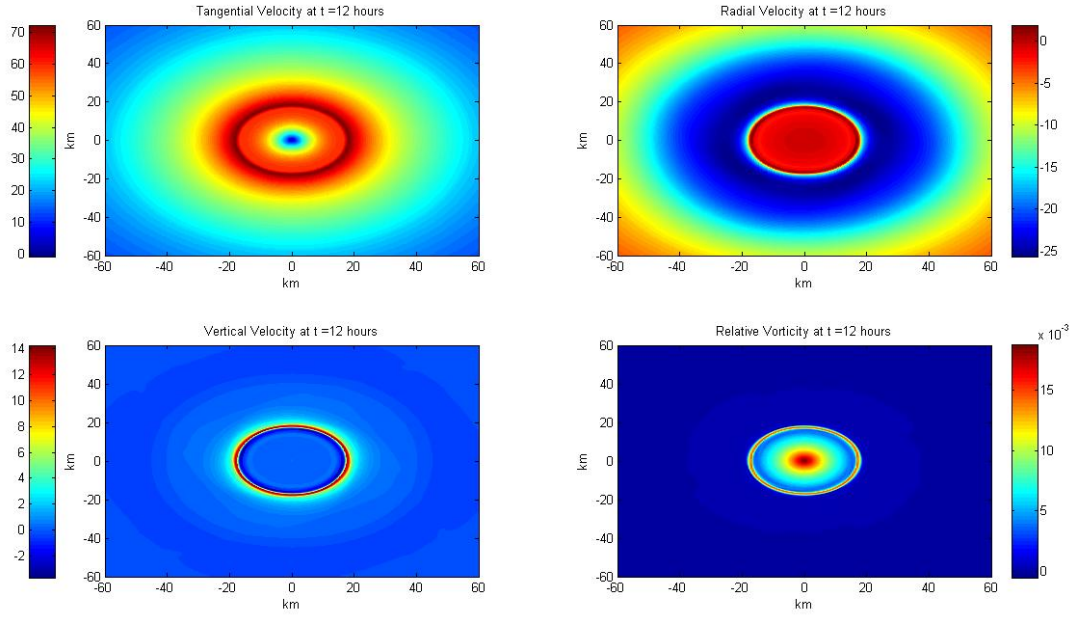

Figure 4.28: Evolution of experiment 3 at t = 12 hr.

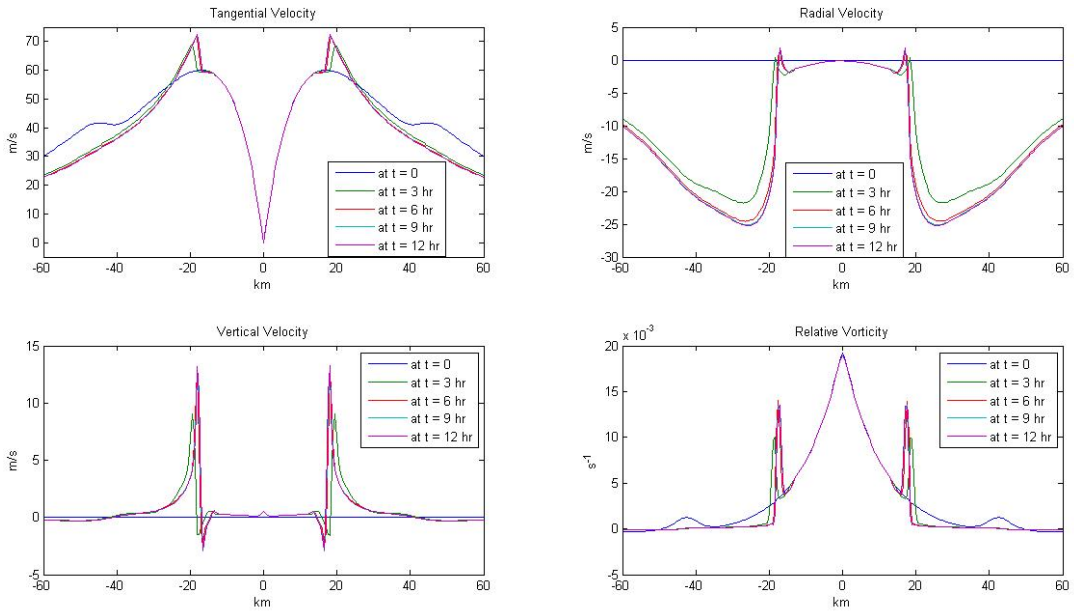

Figure 4.29: Horizontal cross-section of the velocity field and vorticity field for experiment 3.

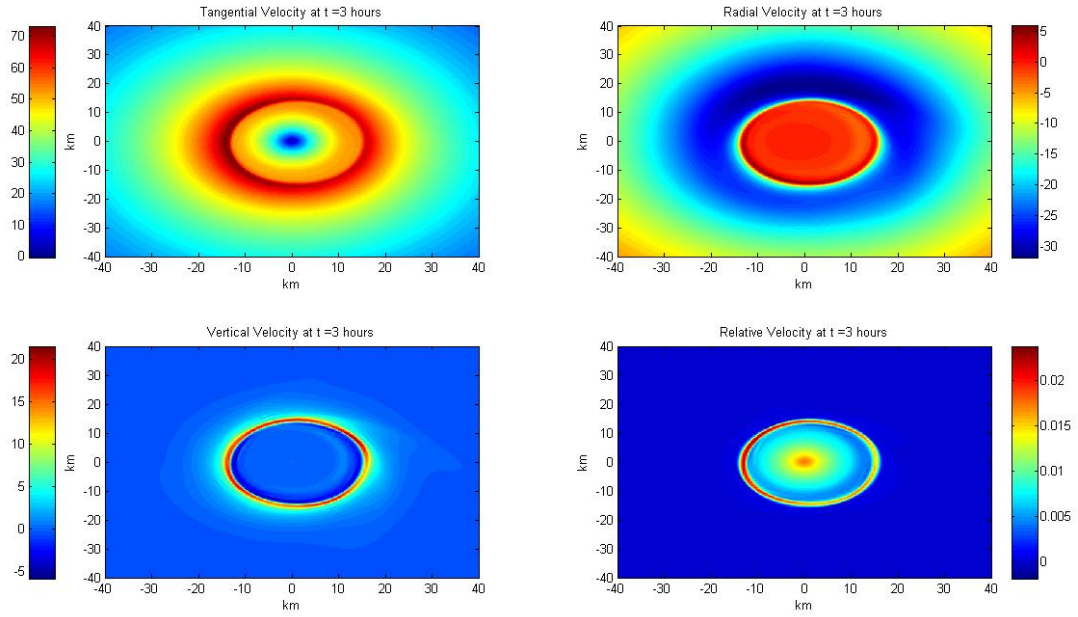

Figure 4.30: Evolution of single eyewall translating with a 5 m s^{-1} southerly flow at t = 3 hr.

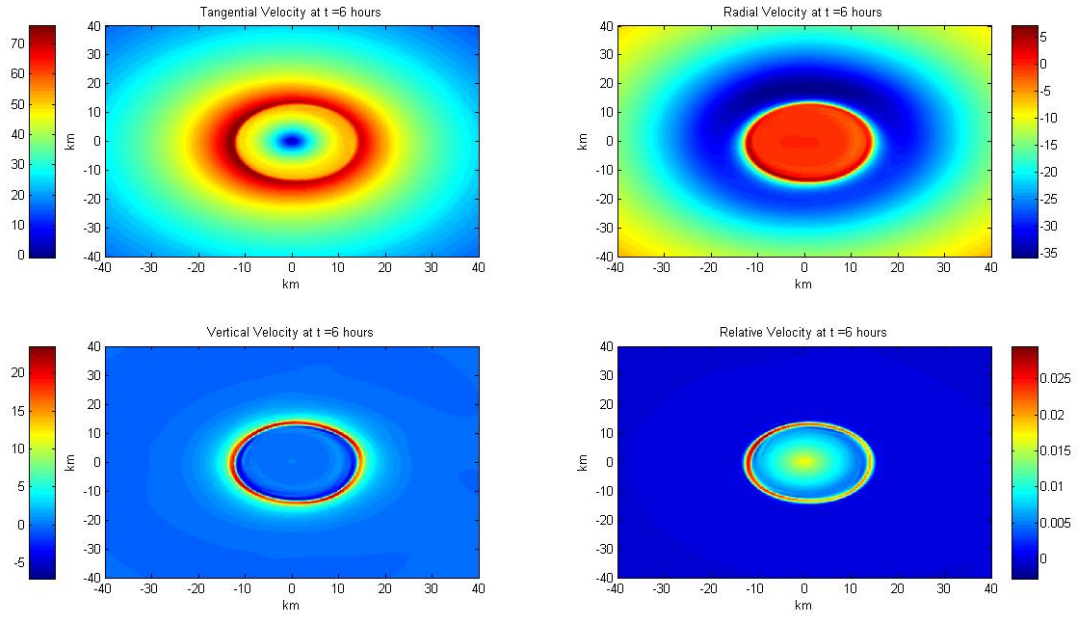

Figure 4.31: Evolution of single eyewall translating with a 5 m s^{-1} southerly flow at t = 6 hr.

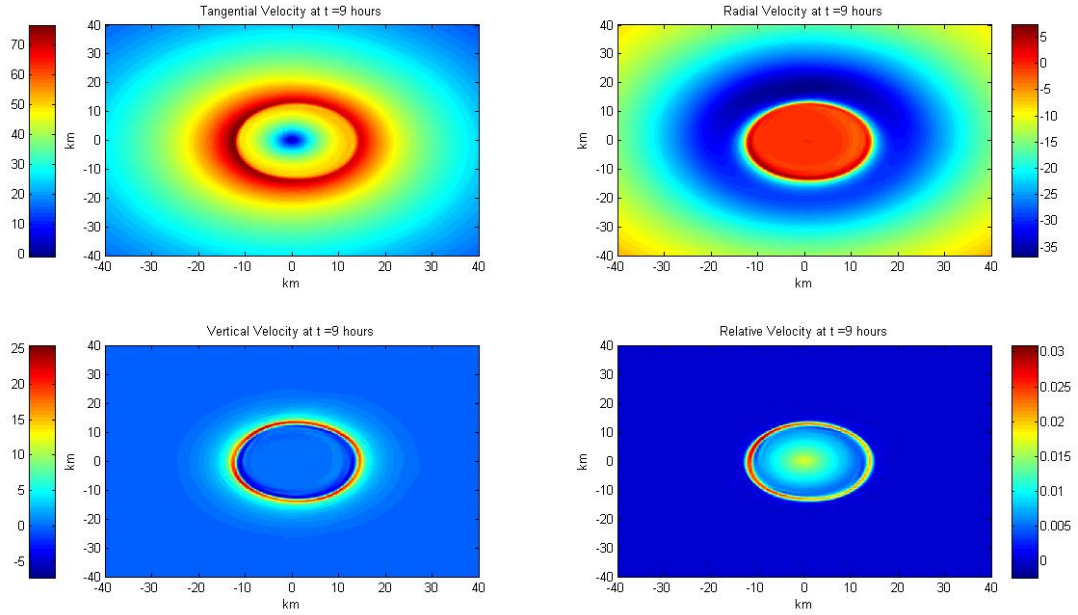

Figure 4.32: Evolution of single eyewall translating with a 5 m s^{-1} southerly flow at t = 9 hr.

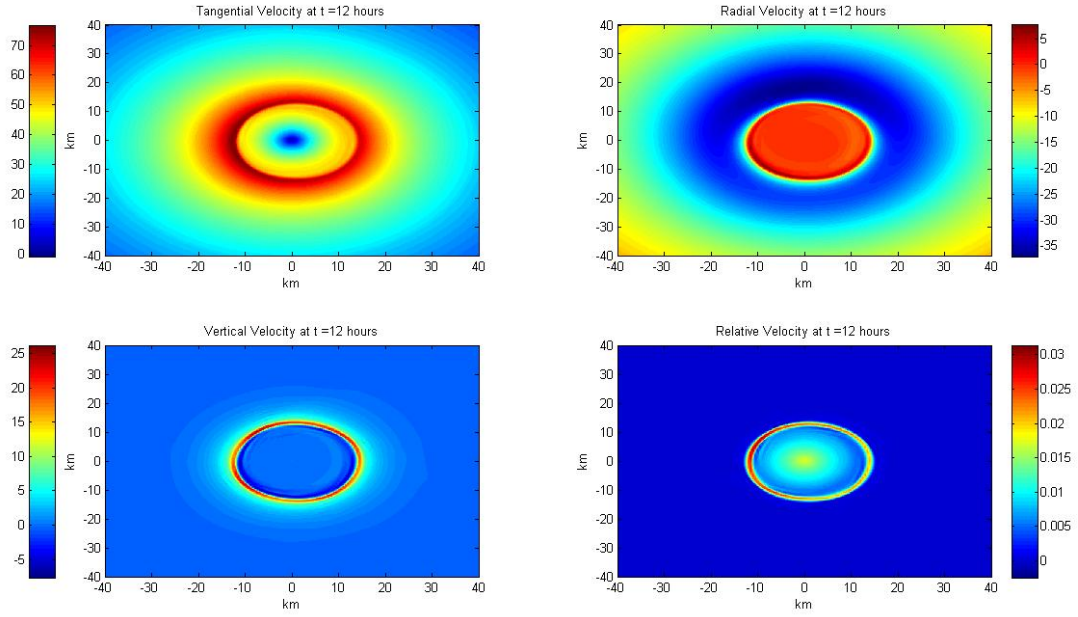

Figure 4.33: Evolution of single eyewall translating with a 5 m s^{-1} southerly flow at t = 12 hr.

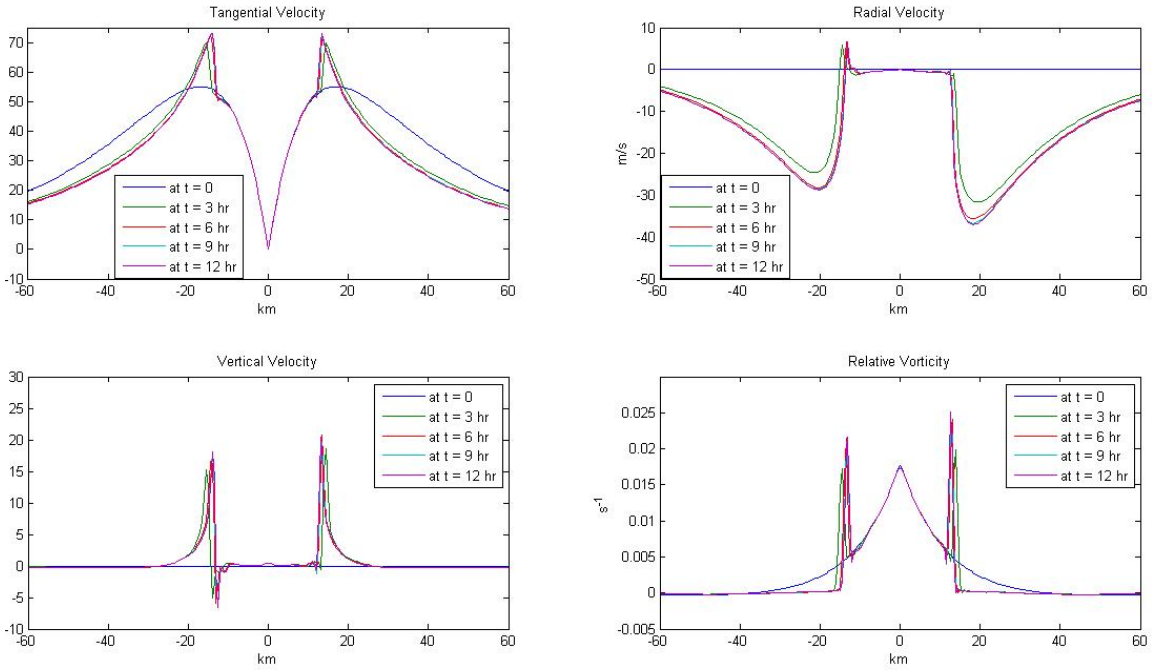

Figure 4.34: Horizontal cross-section of the velocity field and vorticity field for single eyewall translating with a 5 m s^{-1} southerly flow.

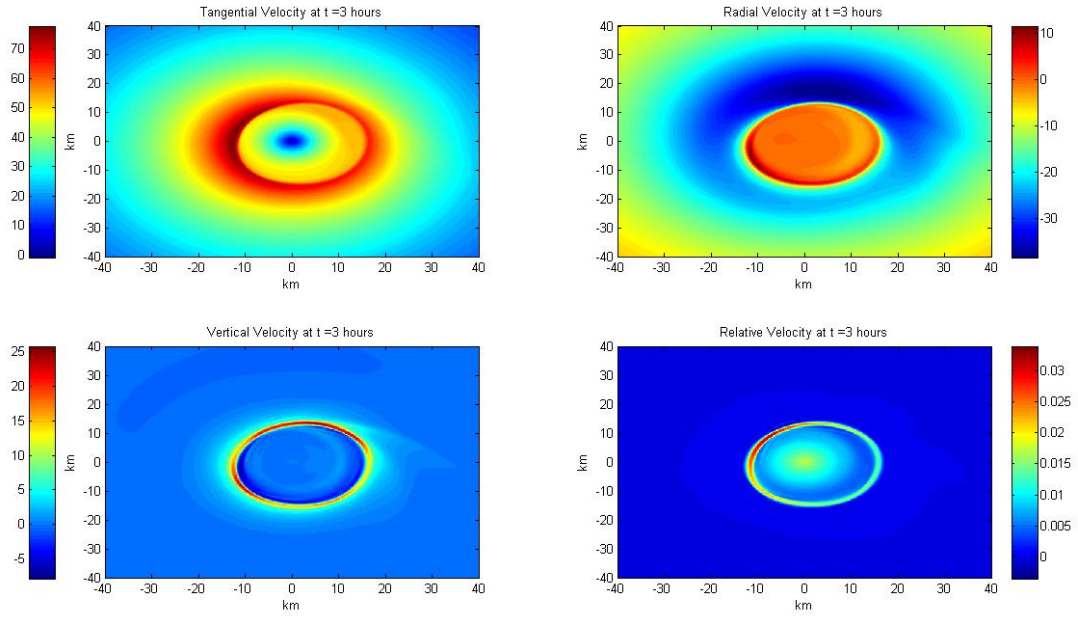

Figure 4.35: Evolution of single eyewall translating with a 10 m s^{-1} southerly flow at t = 3 hr.

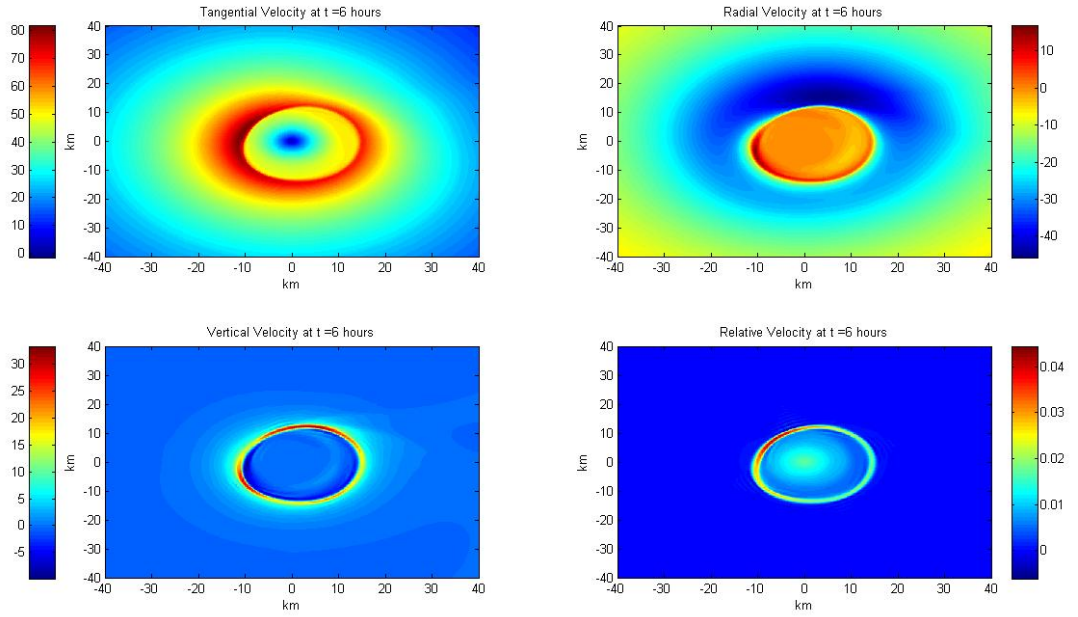

Figure 4.36: Evolution of single eyewall translating with a 10 m s^{-1} southerly flow at t = 6 hr.

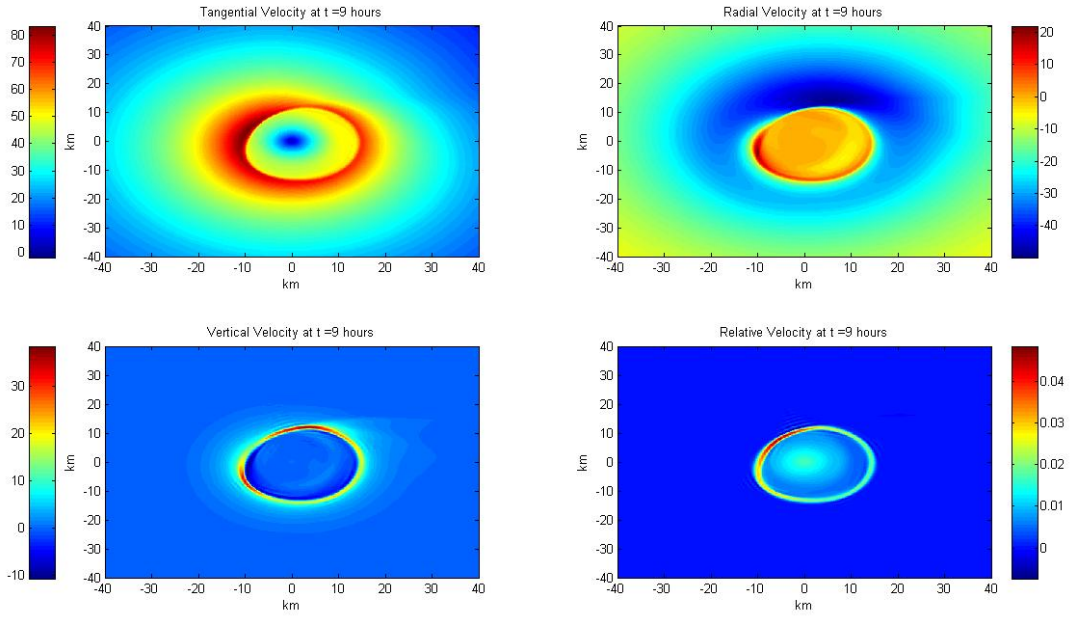

Figure 4.37: Evolution of single eyewall translating with a 10 m s^{-1} southerly flow at t = 9 hr.

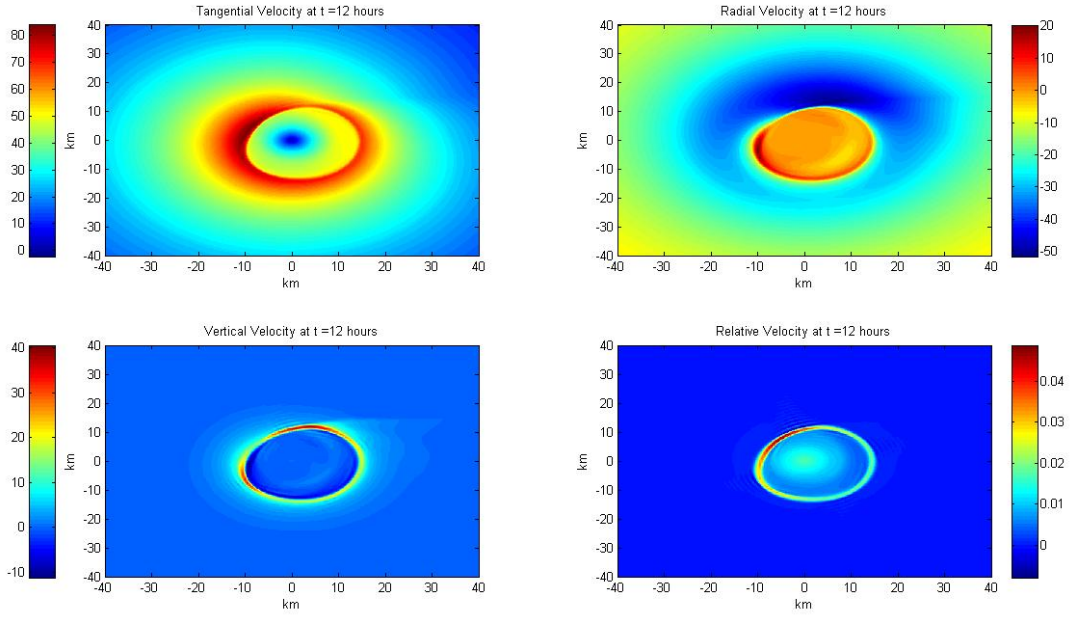

Figure 4.38: Evolution of single concentric eyewall translating with a 10 m s^{-1} southerly flow at t = 12 hr.

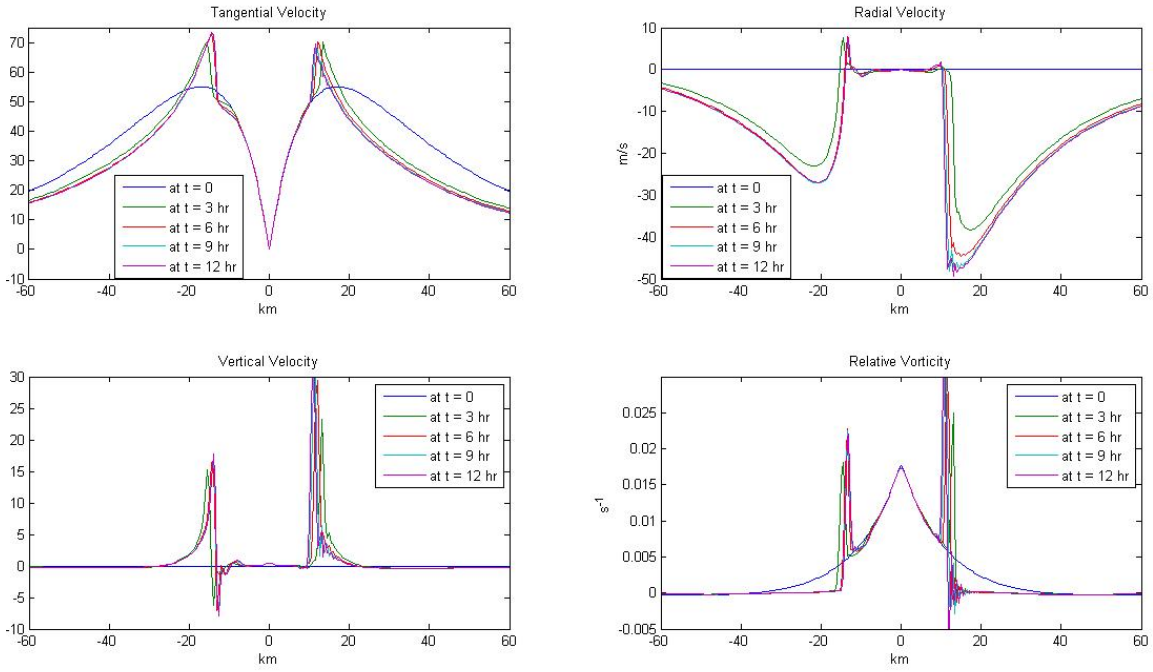

Figure 4.39: Horizontal cross-section of the velocity field and vorticity field for single concentric eyewall translating with a 10 m s^{-1} southerly flow.

Chapter 5

THE 3D EVOLUTION OF SHOCK-LIKE STRUCTURES IN THE TROPICAL CYCLONE BOUNDARY LAYER

As mentioned in the Introduction of Chapter 4, Kepert and Wang (2001) proposed that the dominant processes necessary to produce boundary layer jets are horizontal advection, vertical advection, and vertical diffusion. In this section, we investigate the effect of vertical advection and vertical diffusion in the evolution of shock-like structures in the tropical cyclone boundary layer.

5.1 3D Primitive Equation Boundary Layer Model

The boundary layer model is based on the three-dimensional primitive equations of a continuously stratified, hydrostatic, Boussinesq atmosphere in height coordinates. The governing equations are:

$$\frac{Du}{Dt} = fv - c_p\theta\frac{\partial \Pi}{\partial x} + D_u + F_u, \tag{5.1}$$

$$\frac{Dv}{Dt} = -fu - c_p\theta\frac{\partial \Pi}{\partial y} + D_v + F_v, \tag{5.2}$$

$$\frac{D\theta}{Dt} = D_\theta + F_\theta, \tag{5.3}$$

$$\frac{\partial \Pi}{\partial z} = -\frac{g}{c_p\theta}, \tag{5.4}$$

$$\frac{\partial u}{\partial x} + \frac{\partial v}{\partial y} + \frac{\partial w}{\partial z} = 0. \tag{5.5}$$

As in the 2D boundary layer model, the boundary layer flow is driven by the same pressure gradient force that occurs in the overlying fluid. The pressure field at the top of the model is prescribed using the analytical profile of Holland (1980):

$$p = p_c + (p_n - p_c)\exp(-A/r^B), \tag{5.6}$$

where p_c is the central pressure, p_n is the ambient pressure, and A and B are scaling parameters. Using the gradient wind equations, the gradient wind profile is

$$V_{gr} = \left(\frac{AB(p_n - p_c)\exp(-A/r^B)}{\rho r^B} + \frac{r^2 f^2}{4}\right)^{1/2} - \frac{rf}{2} \tag{5.7}$$

where ρ is the air density, assumed constant at 1.15 kg m^{-3}. In the region of maximum winds, the Coriolis force is small in comparison to the pressure gradient and centrifugal forces and the flow is in cyclostrophic balance. These winds are given by

$$V_c = \left(\frac{AB(p_n - p_c)\exp(-A/r^B)}{\rho r^B}\right)^{1/2} \tag{5.8}$$

By setting $\frac{dV_c}{dr} = 0$ where V_c is the cyclostrophic wind speed, it can be shown that the RMW and maximum wind speed of this profile is given by:

$$R_w = A^{\frac{1}{B}}, \qquad V_m = \left(\frac{B(p_n - p_c)}{\rho e}\right)^{1/2}, \tag{5.9}$$

where e is the base of natural logarithms. Physically, *B* defines the shape or "peakedness" of the gradient wind profile and *A* determines its location relative to the origin. More information on the model discretization and the model characteristics can be found in Appendix C.

5.2 The Stationary Vortex Case

To illustrate how the boundary layer flow evolves into a steady state, the initial conditions have been chosen to be $u(x, y, 0) = -(y/r)V_{gr}$ and $v(x, y, 0) = (x/r)V_{gr}$ where v_{gr} has the form

given in (5.7). The scaling parameters A and B have been designed such that the maximum wind of the vortex is 55 m s $^{-1}$ and the radius of maximum wind of the vortex is 17 km. The boundary layer flow is forced by the pressure field at the top of the model which is given by (5.6), where p_n = 1015.1 mb and p_c is determined by V_m and B.

5.2.1 Dynamical Structure of Vortex

Figures 5.1 – 5.3 show the three-dimensional evolution of the radial velocity V_R. As in the 2D boundary layer model simulations, we see that strong radial inflow causes a circular shock that shrinks the RMW of the vortex. Within the first 15 minutes of the model simulation, there are rapid changes in the radial velocity field. Radial inflow velocities exceeding 14 m s^{-1} quickly develop near the surface and the radial inflow decreases with height in the boundary layer. Within the next 4 hours of the model simulation, the vertical gradient of radial inflow increases. The radial inflow velocity exceeds 30 m s^{-1} near the surface and decreases with height. Radial inflow ceases around 650 m and radial outflow begins to develop in the upper boundary layer. The vortex reaches a steady state around 8 hr in the model simulation. At this time, radial inflow velocities approach 35 m s^{-1} near the surface and radial outflow velocities approach 15 m s^{-1} at approximately 1200 m.

Figures 5.4 and 5.5 show radial profiles of V_R at t = 4 hr and t = 8 hr, respectively. Here, we can see the development of a shock structure as the radial inflow velocity at 125 m increases from 0 to 30 m s^{-1} near the eyewall. This horizontal gradient in radial velocity causes a strong updraft and strong Ekman pumping, as shown in Figures 5.6 and 5.7. Strong radial inflow near the surface causes strong Ekman pumping near the surface and at 625 m. Furthermore, the vertical velocity, which signifies Ekman pumping, shrinks to smaller radius. Similar to the 2D boundary layer model simulation, the peak Ekman pumping lies on the inside edge of the RMW, implying that the shock effect helps to place the diabatic heating to the region of inertial stability for a tropical cyclone. Contrary to the 2D boundary layer model simulation, the magnitude of the vertical velocity is smaller. This is due to the larger grid spacing of the model (1 km compared to 500 m for the 2D boundary

layer model simulation) and due to vertical diffusion, which will be shown below.

Figures 5.8 – 5.10 show the three-dimensional evolution of the tangential wind V_T. Due to the strong gradient of radial velocity near the surface, we see strong supergradient winds near the surface and due to vertical advection, we see strong supergradient winds throughout the boundary layer. The tangential velocity maximizes around 650 m and gradually decreases with height above 1 km. The strongest contraction of the RMW occurs near the surface and the contraction weakens with height. This is expected since the strongest gradient of radial inflow occurs near the surface and radial inflow decreases with height. This implies that the shock develops primarily near the surface and vertical transport processes transfer the shock effect throughout the boundary layer. Figures 5.11 and 5.12 show radial profiles of V_T at t = 4 hr and t = 8 hr, respectively. Similar to the 2D boundary layer model, we see that the tangential wind near the surface becomes strongly supergradient in the region $14 < r < 17$ km and subgradient in the region $r > 17$ km. The tangential wind remains largely supergradient in the region $14 < r < 17$ km throughout the depth of the boundary layer but outside the RMW, the tangential wind approaches gradient balance above 650 m. This reaffirms the suggestion that the shock effect caused by radial inflow occurs near the surface.

As mentioned before, the vertical structure of the boundary layer wind fields signify the importance of vertical advection and vertical diffusion. Figures 5.13 – 5.15 show the three-dimensional evolution of the turbulent diffusivity of momentum K_m. We note first that the Richardson number is very small in the region $r < 100$ km, suggesting that shear production will dominate over buoyancy production in the boundary layer. During the first 15 minutes of the model simulation, we see that turbulent mixing occurs primarily in the eyewall region and is coincident with the location of surface radial inflow. This implies that surface radial inflow causes vertical shear near the surface, which initiates vertical turbulent mixing in the lower boundary layer. In the first 4 hours of the model simulation, we see that vertical diffusion of momentum occurs throughout the entire boundary layer and maximizes at approximately 625 m. We also note the peak of maximum turbulent mixing, the

maximum tangential wind, and the maximum vertical velocity all occur at this height. This suggests that the boundary layer jet maximum is located at approximately 625 m and occurs in a region of strong turbulent transport. Thus, as the circular shock develops near the surface, vertical diffusion and vertical advection transfer momentum from the surface to the jet location.

To further explain the location of the boundary layer jet, we note that this vortex has a strongly peaked radial wind profile, which produces a region of zero radial angular momentum gradient outside of the RMW. With no possibility for advection of radial velocity outside of the RMW, the jet is confined to the immediate vicinity of the RMW, where the steep, shock-like gradient in radial velocity produces a marked jet with tangential wind component at 625 m just inside the RMW. The updraft is likewise now restricted to the vicinity of the RMW. The strength of the jet and the strength of the near-surface inflow is accompanied by substantial increases in nonlinear advection. In particular, vertical advection is now approximately as important as vertical diffusion in balancing the inward radial advection below the jet, while above the jet, there is now substantial outflow as the strongly supergradient flow in the updraft returns to balance.

The role of the shock effect in producing the boundary layer jet can also be explained in terms of angular momentum conservation. Frictional destruction of angular momentum near the surface produces subgradient flow there and consequently a strong inward acceleration caused by gradient adjustment. Since the radial gradient of angular momentum outside of the RMW is close to zero for this vortex, the gradient adjustment process only produces weak advection of angular momentum. Since this advection is not strong enough to balance the frictional destruction of angular momentum, the radial inflow continues to accelerate. As the inrushing air encounters the inertially stable core, overshoot leads to a shock structure, producing a very strong jet and near-surface winds. Gradient adjustment of these winds eventually stops the radial inflow producing a strong updraft and outflow returns the updraft back into balance.

5.2.2 Thermodynamic Structure of Vortex

Figures 5.16 – 5.18 show the three-dimensional evolution of potential temperature θ. As stated previously, the Richardson number in the boundary layer is very small in the region $r < 100$ km, suggesting that the hurricane boundary layer is close to a neutral boundary layer. During the first 4 hours of the model simulation, since the vertical diffusion of heat maximizes at 625 m, we have upward mixing of low-θ air in the eyewall region. Furthermore, with the secondary maximum of turbulent diffusivity at the top of the boundary layer, there is downward mixing of high-θ air into the eye region above the jet. For a tropical cyclone, the upward flux of moisture and heat is overwhelmed by the mixing of dryer air downward in the eye (cf. Rotunno and Emanuel 1987). Figures 5.19 and 5.20 show the horizontal cross-section of potential temperature for t = 4 hr and t = 8 hr, respectively. Because of the shock structure near the surface, vertical transport of heat produce potential temperature gradients throughout the boundary layer.

5.3 The Effect of Vortex Translation

We now consider the effect of vortex movement by embedding the vortex in a 5 m s^{-1} southerly flow. The initial condition is the same as the vortex used in Section 5.2.

5.3.1 Dynamical Structure of Vortex

Figures 5.21 – 5.23 show the three-dimensional evolution of the radial wind V_R. Due to the translation of the vortex, the maximum radial inflow components lie in the right forward quadrant whereas the maximum radial outflow components lie in the right rear quadrant. As in the stationary vortex case, we see that strong radial inflow causes a circular shock that shrinks the RMW of the vortex. Within the first 15 minutes of the model simulation, there are rapid changes in the radial velocity field. Radial inflow velocities exceeding 16 m s^{-1} quickly develop near the surface and weak radial inflow occurs throughout the lower boundary layer. Within the next 4 hours of the model simulation, the radial inflow exceeds 35 m s^{-1} near the surface with weak radial inflow in the lower boundary layer. Radial inflow ceases around 650 m and radial outflow begins to develop

in the upper boundary layer. The vortex reaches a steady state in approximately 8 hr. At this time, radial inflow velocities exceed 40 m s^{-1} near the surface and radial outflow velocities approach 15 m s^{-1} near the top of the boundary layer.

Figures 5.24 and 5.25 show radial profiles of V_R at t = 4 hr and t = 8 hr, respectively. Here, we can see the development of an asymmetric shock structure as the radial inflow velocity at 125 m increases from 0 to 30 m s^{-1} near the eyewall. This gradient in radial velocity causes a strong updraft and strong Ekman pumping, as shown in Figures 5.26 and 5.27. Strong radial inflow near the surface causes strong Ekman pumping near the surface and at 625 m. As in the stationary vortex case, the vertical velocity shrinks to smaller radius and the peak Ekman pumping lies on the inside edge of the RMW.

Figures 5.28 – 5.30 show the three-dimensional evolution of the tangential wind V_T. The maximum tangential wind is located in the left forward quadrant near the surface, with the strongest winds just inside the radius of maximum gradient level winds, and the maximum tangential wind is located in the left rear quadrant near the top of the boundary layer. This is downstream of the maximum storm-relative inflow, in the right forward quadrant. As in the stationary vortex case, we see strong supergradient winds near the surface. The tangential velocity maximizes around 650 m and gradually decreases with height above 1 km. As expected, the RMW strongly contracts near the surface due to radial inflow, whereas there is a slight expansion of the RMW at the top of the boundary layer. Figures 5.31 and 5.32 show radial profiles of V_t at t = 4 hr and t = 8 hr, respectively. Similar to the stationary vortex case, we see that the tangential wind near the surface becomes strongly supergradient in the region $14 < r < 17$ km and subgradient in the region $r > 17$ km. The tangential wind remains largely supergradient in the region $14 < r < 17$ km throughout the depth of the boundary layer but outside the RMW, the tangential wind approaches gradient balance above 650 m.

Figures 5.33 – 5.35 show the three-dimensional evolution of the turbulent diffusivity of momentum K_m. During the first 15 minutes of the model simulation, surface radial inflow causes vertical shear near the surface, which causes vertical turbulent mixing, and the motion of the vortex causes asymmetries in the turbulent diffusivity. In the first 4 hours of the model simulation, we see that vertical diffusion of momentum maximizes at 625 m. This suggests that the boundary layer jet maximum occurs in a region of strong turbulent transport. The maximum turbulent diffusivity maximizes in the right front quadrant near the surface and in the right rear quadrant near the top of the boundary layer.

The strength of the jet and the strength of the near-surface inflow is accompanied by substantial increases in nonlinear advection caused by the storm motion. Below the jet, the asymmetries in horizontal advection produce asymmetries in vertical advection and vertical diffusion. Above the jet, there is now substantial outflow as the strongly supergradient flow in the updraft returns to balance. The balance creates an anticyclonic spiral character to the velocity field. The anticyclonic spiral in radial velocity creates an anticyclonic shock structure, both horizontally and vertically. This is demonstrated in the vertical velocity field, radial velocity field, and in the turbulent diffusivity of momentum.

5.3.2 Thermodynamic Structure of Vortex

Figures 5.37 – 5.39 show the three-dimensional evolution of potential temperature θ. The results are similar to the stationary vortex case, except the asymmetries produce an anticyclonic spiral nature to the potential temperature field. During the first 4 hours of the model simulation, since the vertical diffusion of heat maximizes at 625 m, we have upward mixing of low-θ air in the eyewall region. Furthermore, with the secondary maximum of turbulent diffusivity at the top of the boundary layer, there is downward mixing of high-θ air. Figures 5.40 and 5.41 show the horizontal cross-section of potential temperature for t = 4 hr and t = 8 hr, respectively. In these figures, the asymmetries in potential temperature become clear. Because of the shock structure near the surface,

vertical transport of heat produce potential temperature gradients throughout the boundary layer.

5.4 Summary and Application to the Tropical Cyclone Boundary Layer

In this chapter, we studied the 3D evolution of shock-like structures in tropical cyclones. Kepert and Wang (2001) stated that the two dominant physical processes necessary to produce supergradient winds in the tropical cyclone boundary layer are horizontal advection and horizontal diffusion. This suggests that the boundary layer model should resemble the nonlinear viscous Burgers' equation and for a given vortex, a shock-like structure should develop.

Our first experiment mimicked a stationary vortex with a single eyewall. Here, we saw that strong radial inflow created a circular shock that shrinks the RMW of the vortex. Within the first 3 hours of the model simulation, there were rapid changes in the velocity fields. Radial inflow velocities exceeding 30 m s^{-1} quickly developed near the surface and radial outflow developed near the top of the boundary layer. Circular shock structures formed at a radius of approximately 15 km. In response to the sharp gradient in radial velocity, the shock structures led to strong Ekman pumping near the surface, with vertical velocities exceeding 8 m s^{-1} near the RMW of the vortex. For a tropical cyclone, the shock effect must play an important role in determining the eyewall radius. The jet maximum occurred around 650 m, which was confirmed by examining the location of maximum turbulent transport, the location of maximum tangential winds, and the location of radial outflow. Because the tropical cyclone boundary layer resembles a neutral boundary layer, the production of turbulence (and thus vertical mixing) was caused predominately by vertical shear within the boundary layer. The circular shock structure influenced the radial and vertical distribution of potential temperature. Due to turbulent transport, there was significant downward mixing of high-θ air into the eye region from the top of the boundary layer and significant upward mixing of low-θ air into the eyewall region.

Finally, we studied the effect of vortex motion on the 3D evolution of shock-like structures in the tropical cyclone boundary layer. The asymmetry in the boundary layer response is forced by the asymmetry in frictional drag due to the translation of the vortex. Near surface inflow is maximum in the right-front quadrant whereas outflow near the top of the boundary layer is maximum in the right-rear quadrant. Ekman pumping is large in a broad arc ahead of the center of the vortex. The maximum winds lie nearly ahead of the vortex due to horizontal advection into the inertially stable core region. Because of the vortex translation, the asymmetries in the velocity field develop an anticyclonic spiral horizontally and vertically. This indicates that vortex translation will induce a spiral shock structure in the tropical cyclone boundary layer and will cause asymmetries in the convective heat release for a tropical cyclone. The spiral shock structure also influenced the radial and vertical distribution of potential temperature. Due to turbulent transport, there was significant downward mixing of high-θ air into the eye region toward the right-rear quadrant from the top of the boundary layer and significant upward mixing of low-θ air into the eyewall region toward the right-front quadrant from the surface.

These results also indicate that the development of boundary layer shocks depend on the radial wind profile. Kepert and Wang (2001) analyze the 3D evolution of the tropical cyclone boundary layer using an inertially stable vortex. Compared to their model simulation, the strength of the jet and the strength of the near-surface inflow have more than doubled and vertical advection plays a smaller role. Kepert and Wang (2001) indicates that the weakness of the jet is caused by the lack of vertical advection of the inertially stable vortex and by the lack of imbalance between frictional destruction of radial angular momentum and nonlinear production of radial angular momentum. For our vortex, frictional destruction of radial angular momentum outside the RMW produces inflow and only weak advection of radial angular momentum arises. Therefore, the inflow continues to accelerate and when the inrushing air encounters the core, overshoot creates a large gradient in radial velocity creating the shock-like structures observed in our model simulation.

As a final note, these results indicate that the tropical cyclone boundary layer jet is distinct from the nocturnal jet. First, the tropical cyclone boundary level jet forms when the Richardson number is very small, indicating a nearly neutral boundary layer. This is completely contrary to the situation in the nocturnal jet, where strong stabilization and buoyant suppression of turbulence are necessary for the decoupling, which then allows the inertial oscillation that produces the jet. Second, the turbulent diffusivity has a maximum immediately below the jet. This confirms that the jet is in a region of strong turbulent transport, and is therefore not a consequence of frictional decoupling. These points indicate that vertical advection and vertical diffusion are crucial for the development of the tropical cyclone boundary layer jet, whereas static stability is the crucial ingredient needed for the nocturnal jet. Furthermore, without the accelerating radial inflow by surface friction creating shocks near the surface, the boundary layer jet cannot form.

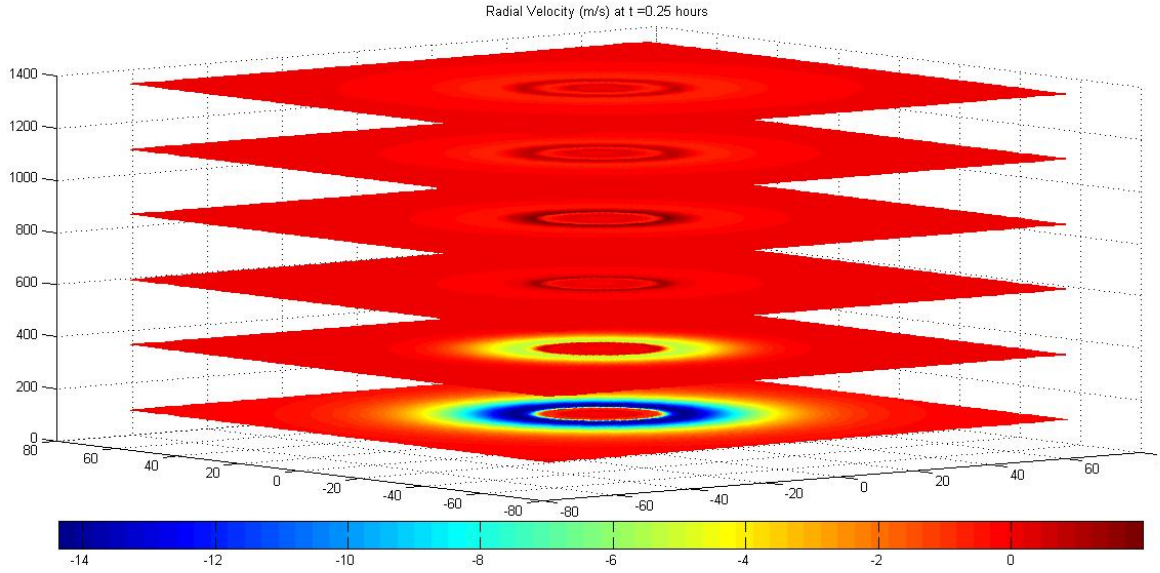

Figure 5.1: Evolution of radial velocity at $t = 0.25$ hr for the stationary vortex case.

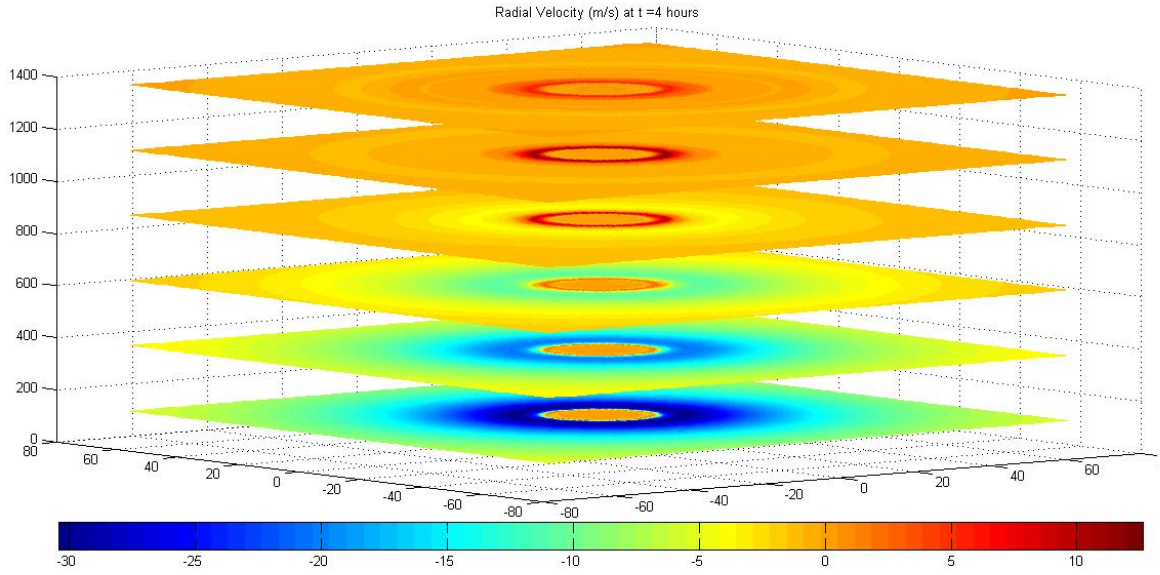

Figure 5.2: Evolution of radial velocity at $t = 4$ hr for the stationary vortex case.

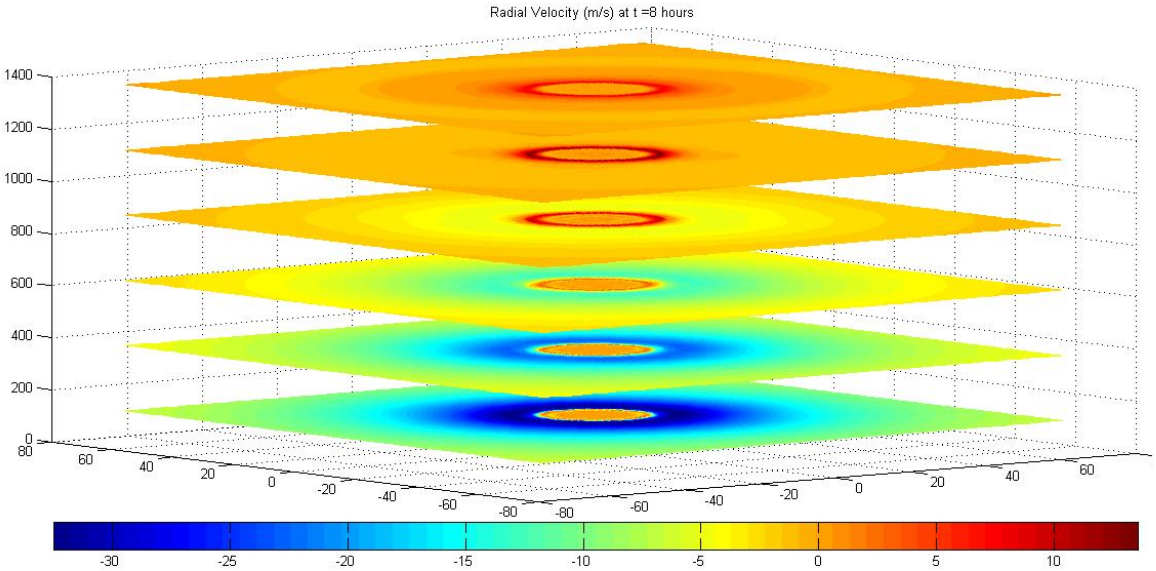

Figure 5.3: Evolution of radial velocity at $t = 8$ hr for the stationary vortex case.

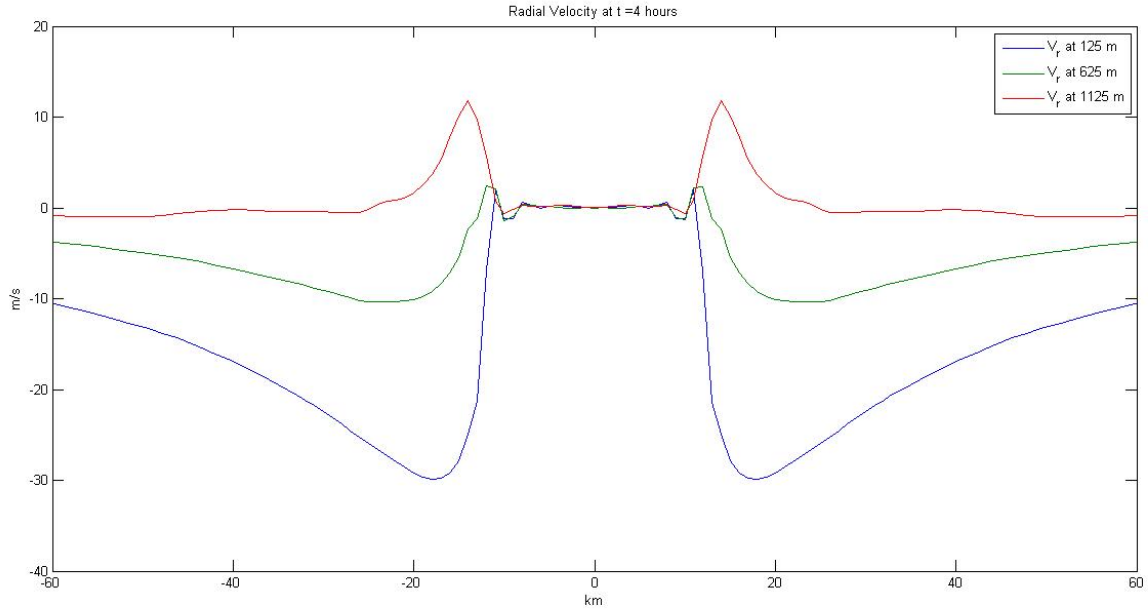

Figure 5.4: Horizontal cross-section of radial velocity at $t = 4$ hr for the stationary vortex case.

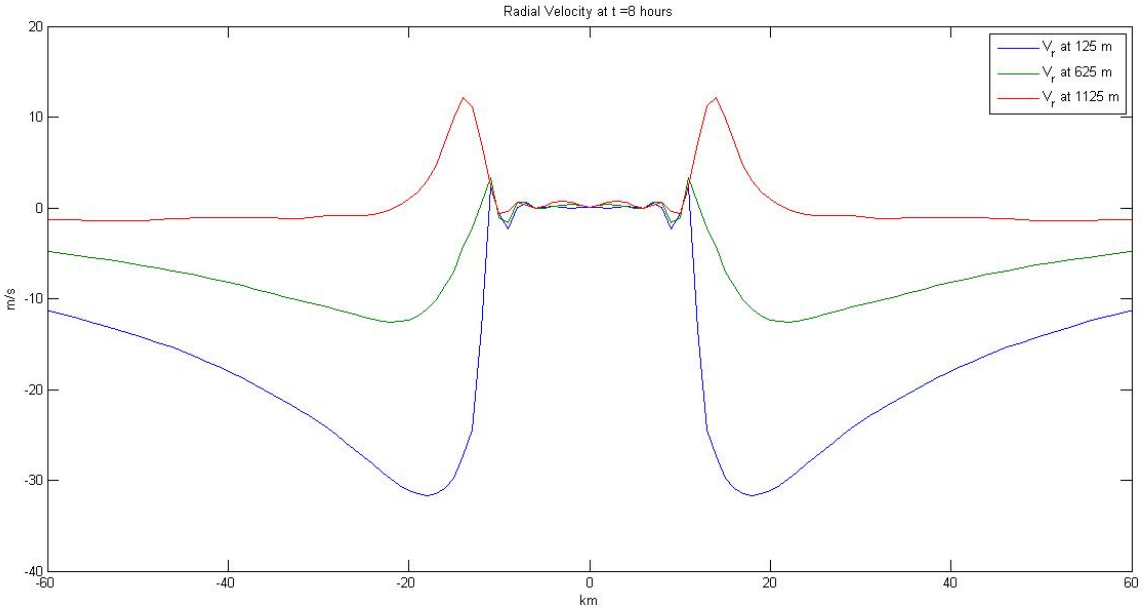

Figure 5.5: Horizontal cross-section of radial velocity at $t = 8$ hr for the stationary vortex case.

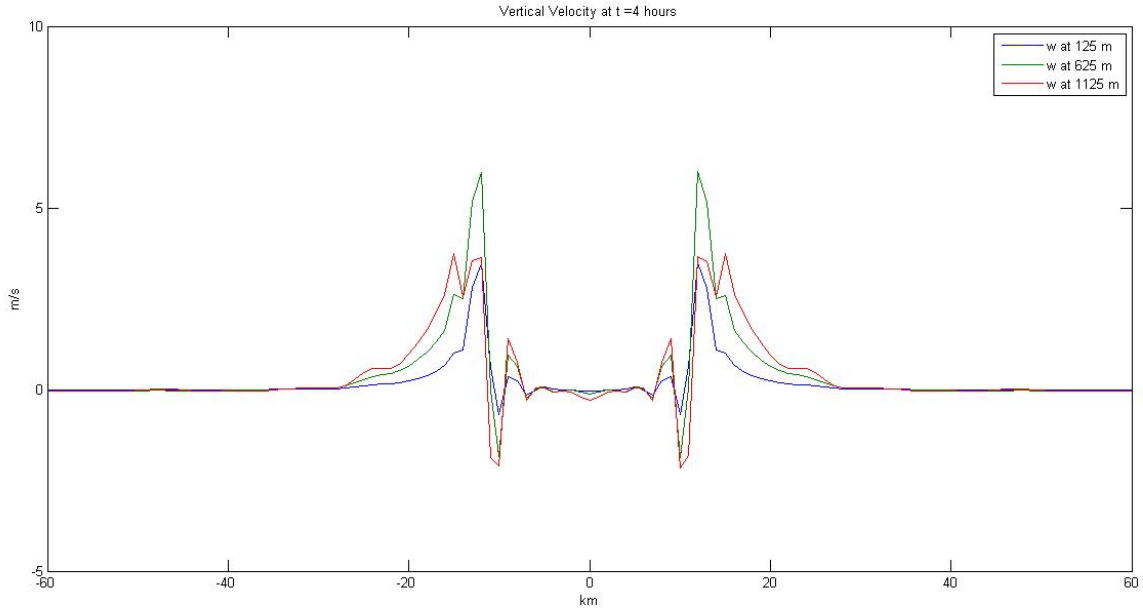

Figure 5.6: Horizontal cross-section of vertical velocity at $t = 4$ hr for the stationary vortex case.

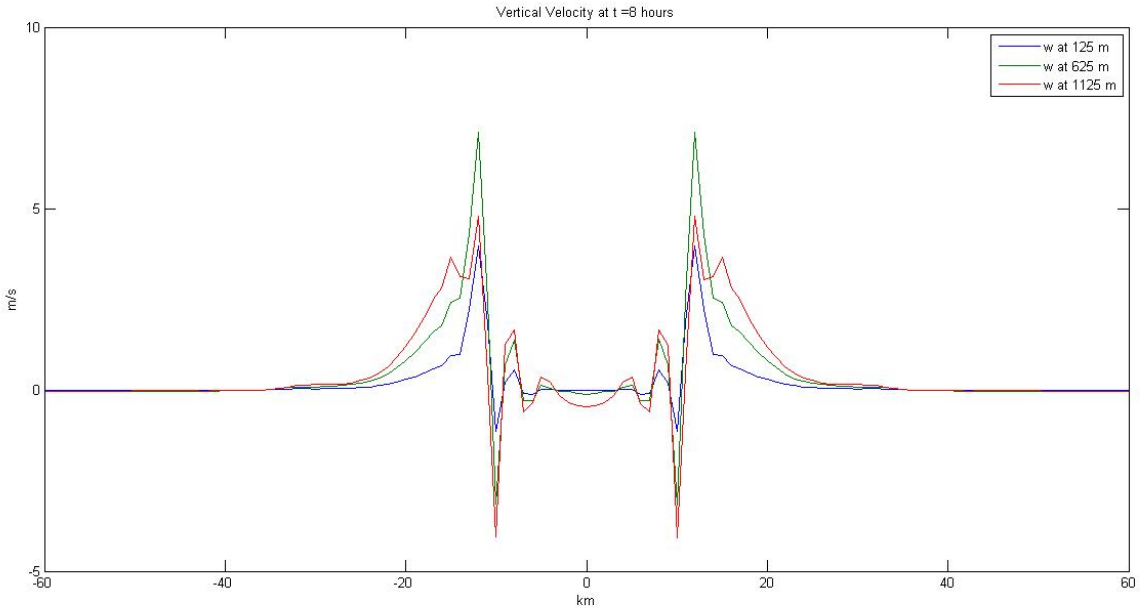

Figure 5.7: Horizontal cross-section of vertical velocity at $t = 8$ hr for the stationary vortex case.

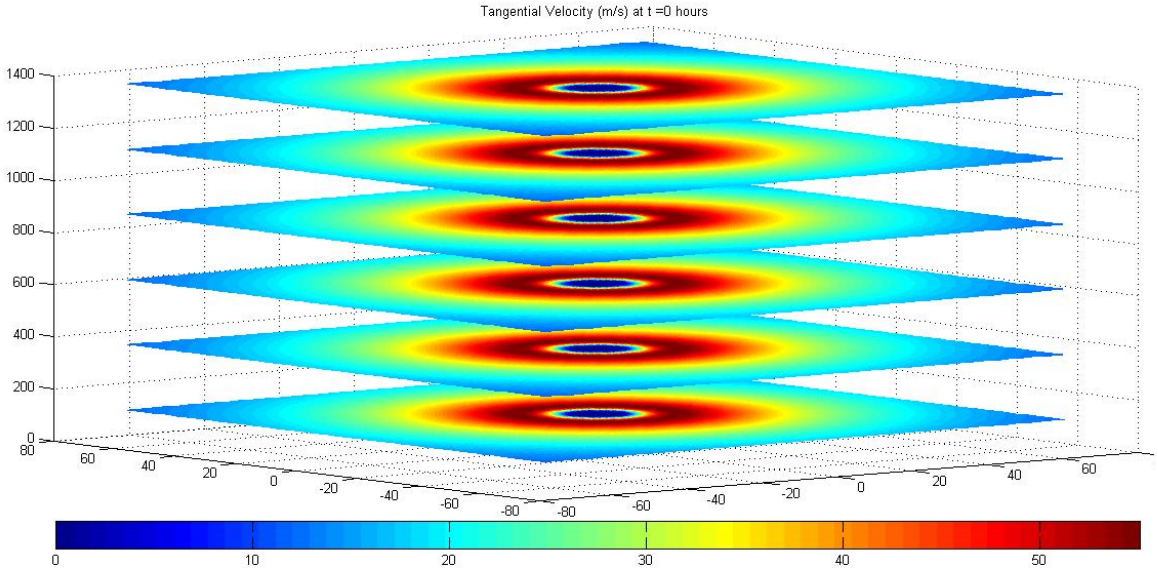

Figure 5.8: Evolution of tangential velocity at $t = 0$ hr for the stationary vortex case.

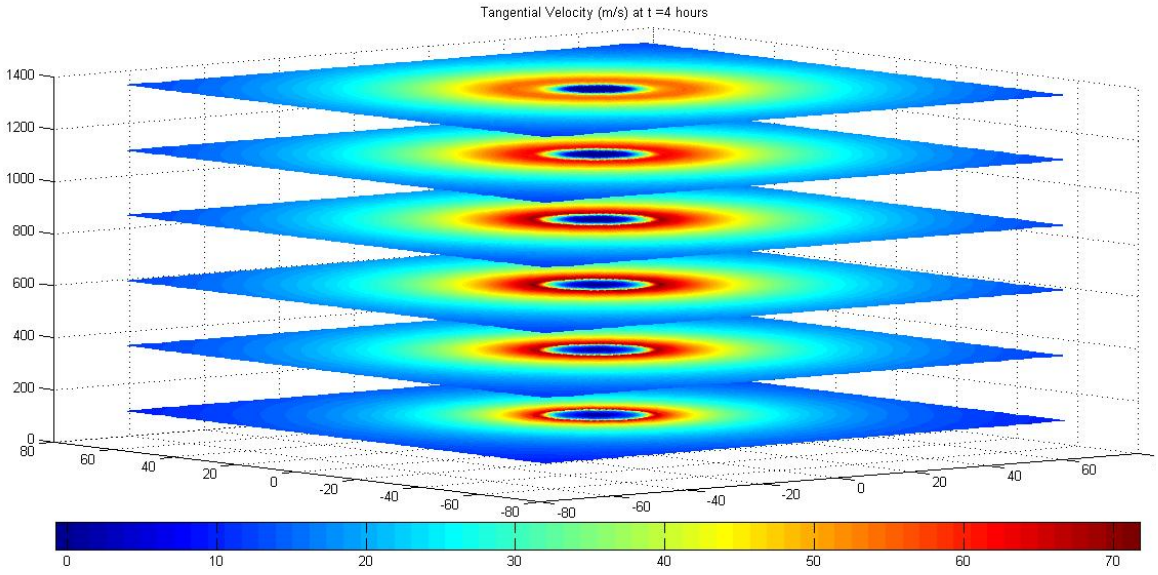

Figure 5.9: Evolution of radial velocity at $t = 4$ hr for the stationary vortex case.

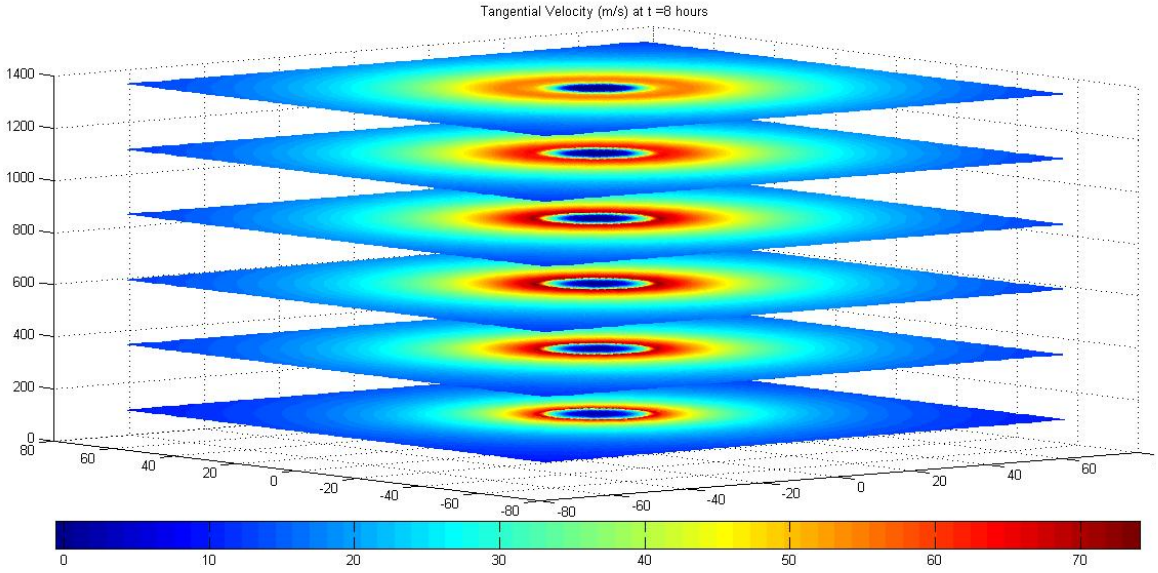

Figure 5.10: Evolution of radial velocity at $t = 8$ hr for the stationary vortex case.

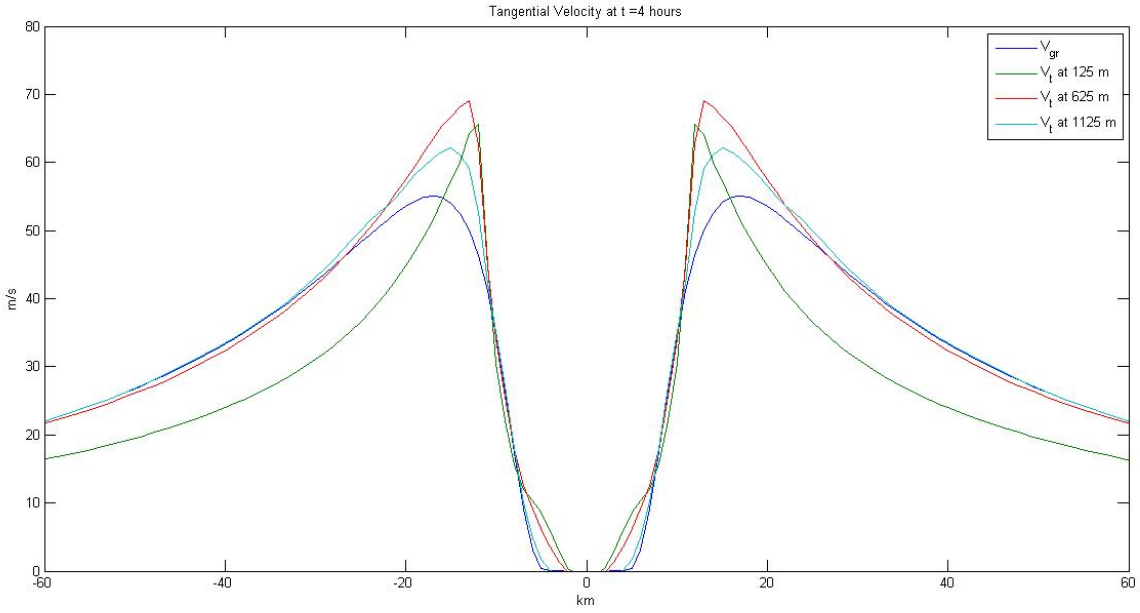

Figure 5.11: Horizontal cross-section of tangential velocity at $t = 4$ hr for the stationary vortex case.

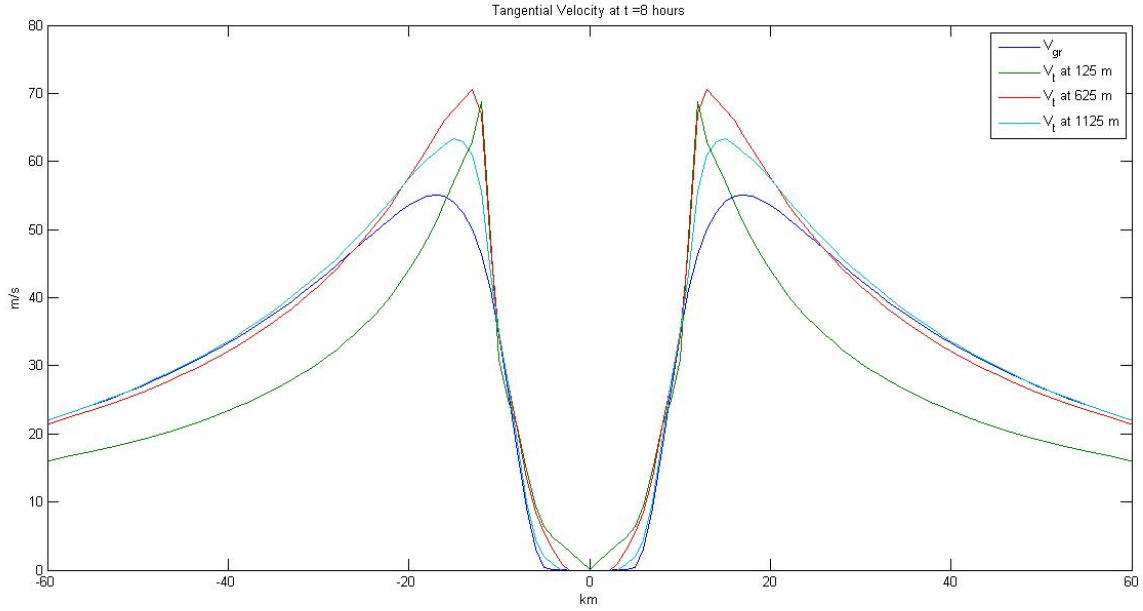

Figure 5.12: Horizontal cross-section of tangential velocity at $t = 8$ hr for the stationary vortex case.

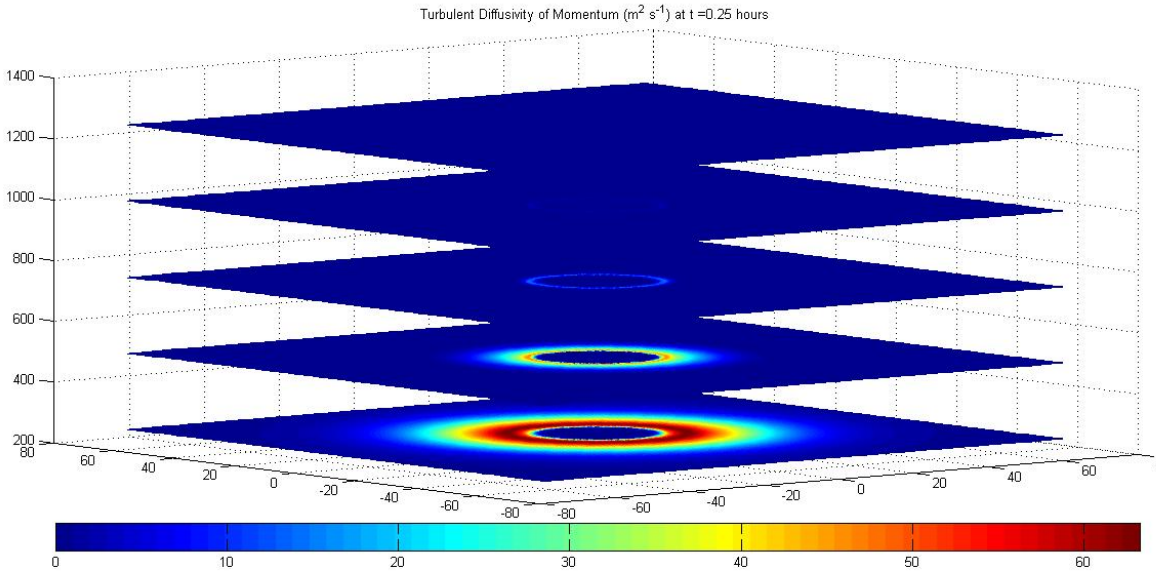

Figure 5.13: Evolution of turbulent diffusivity of momentum at $t = 0.25$ hr for the stationary vortex case.

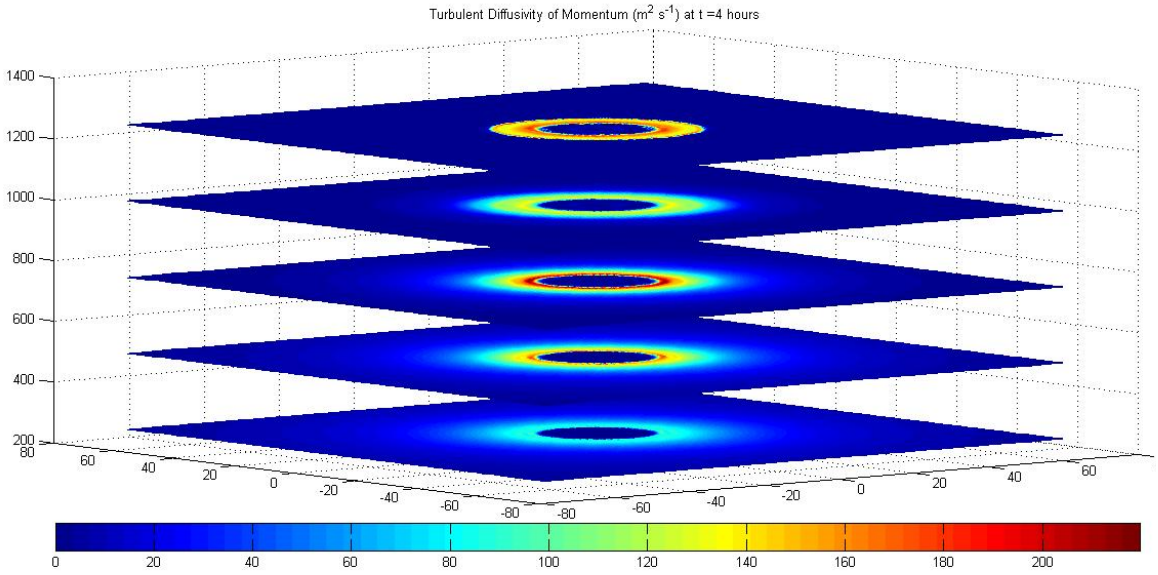

Figure 5.14: Evolution of turbulent diffusivity of momentum at $t = 4$ hr for the stationary vortex case.

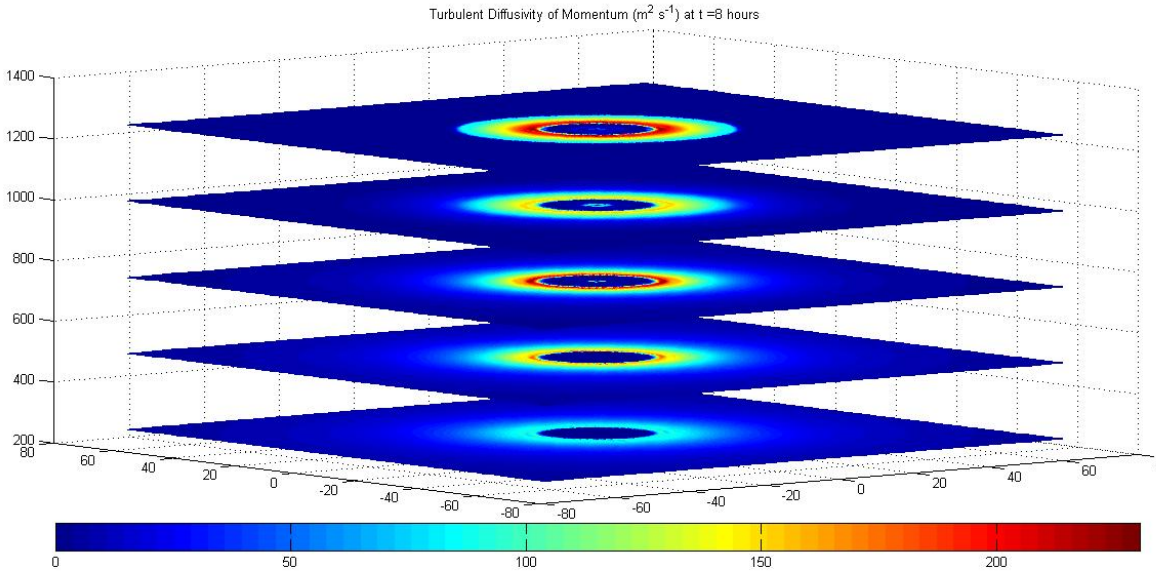

Figure 5.15: Evolution of turbulent diffusivity of momentum at $t = 8$ hr for the stationary vortex case.

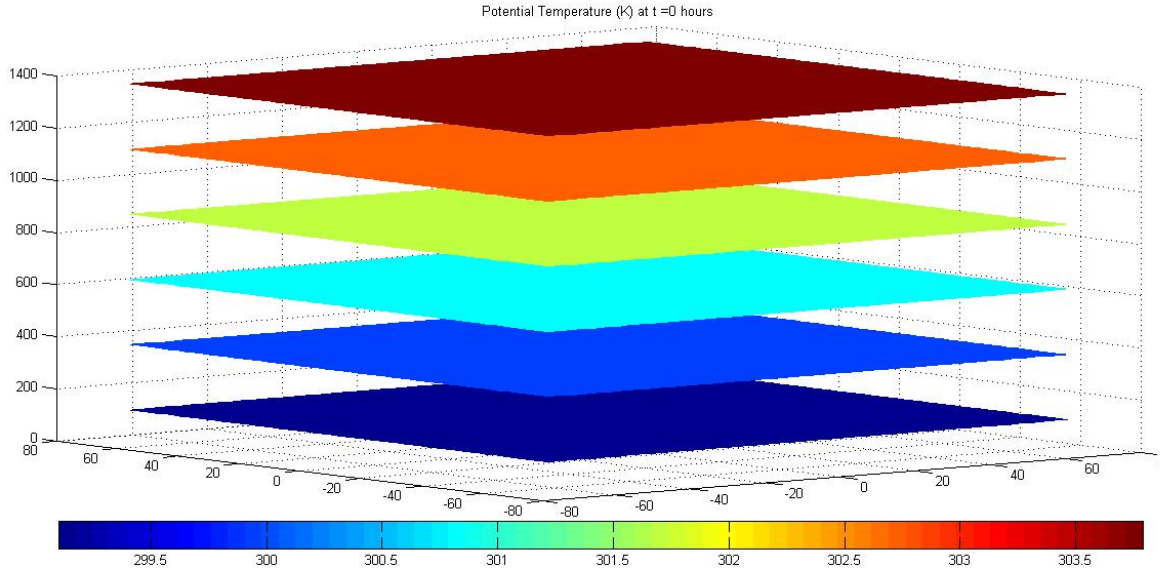

Figure 5.16: Evolution of potential temperature at $t = 0$ hr for the stationary vortex case.

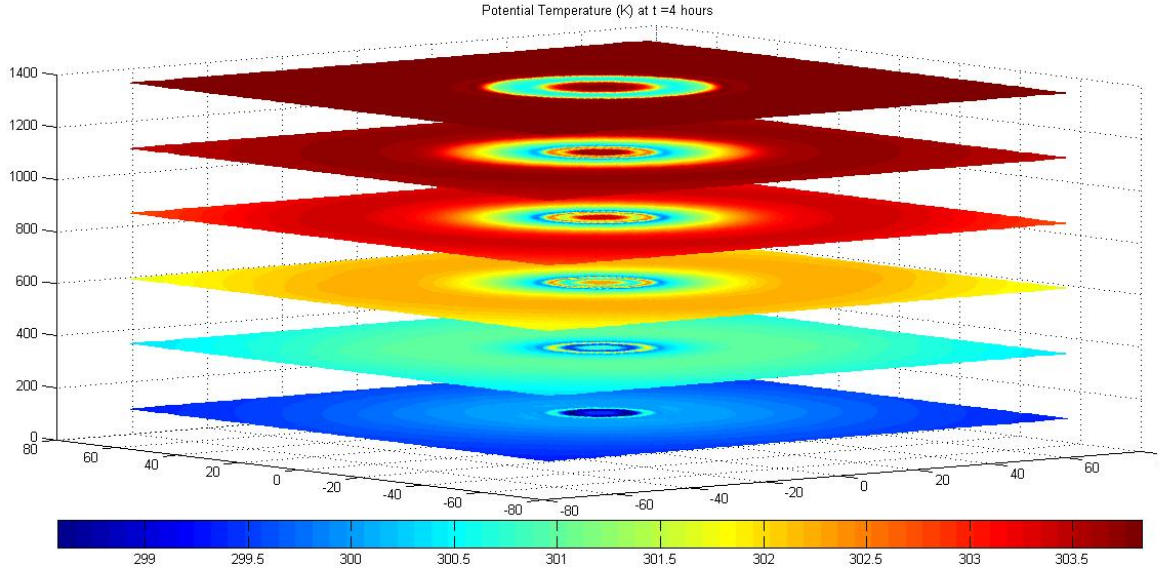

Figure 5.17: Evolution of potential temperature at $t = 4$ hr for the stationary vortex case.

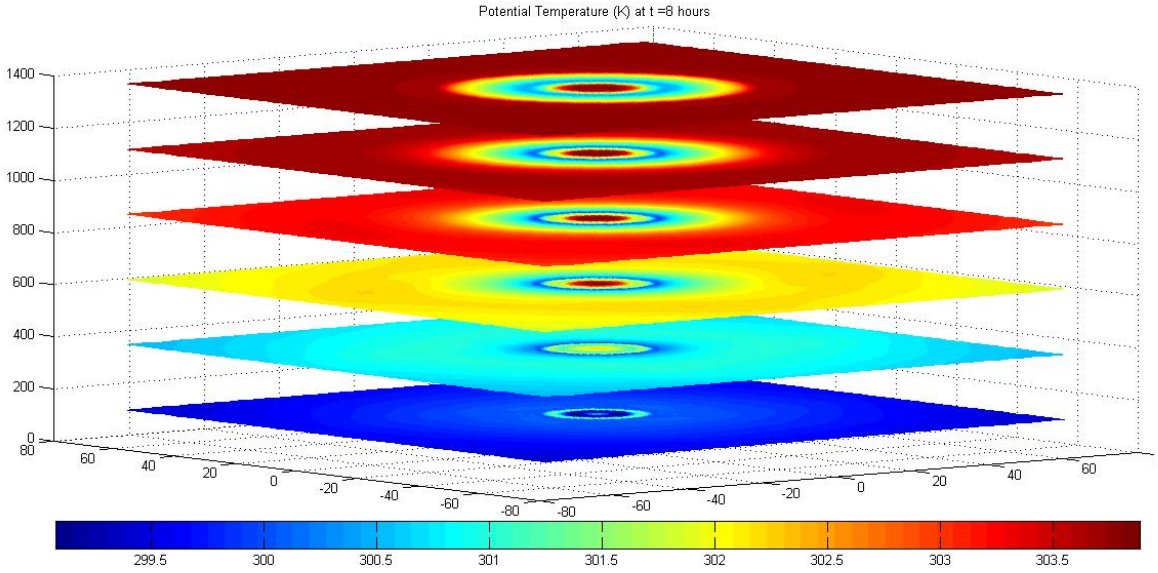

Figure 5.18: Evolution of potential temperature at $t = 8$ hr for the stationary vortex case.

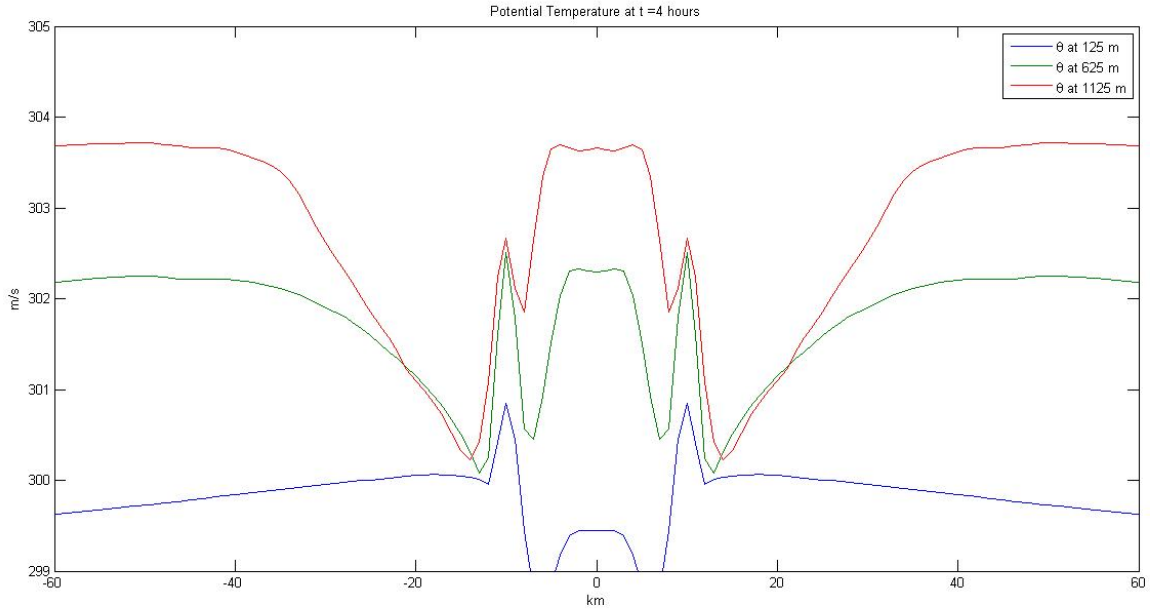

Figure 5.19: Horizontal cross-section of potential temperature at $t = 4$ hr for the stationary vortex case.

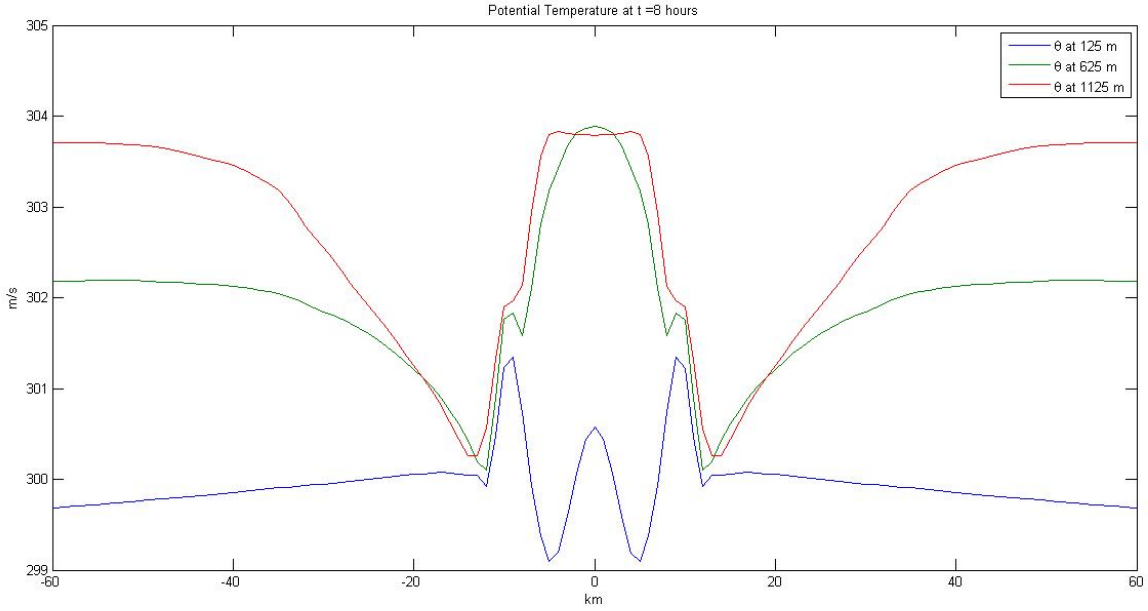

Figure 5.20: Horizontal cross-section of potential temperature at $t = 8$ hr for the stationary vortex case.

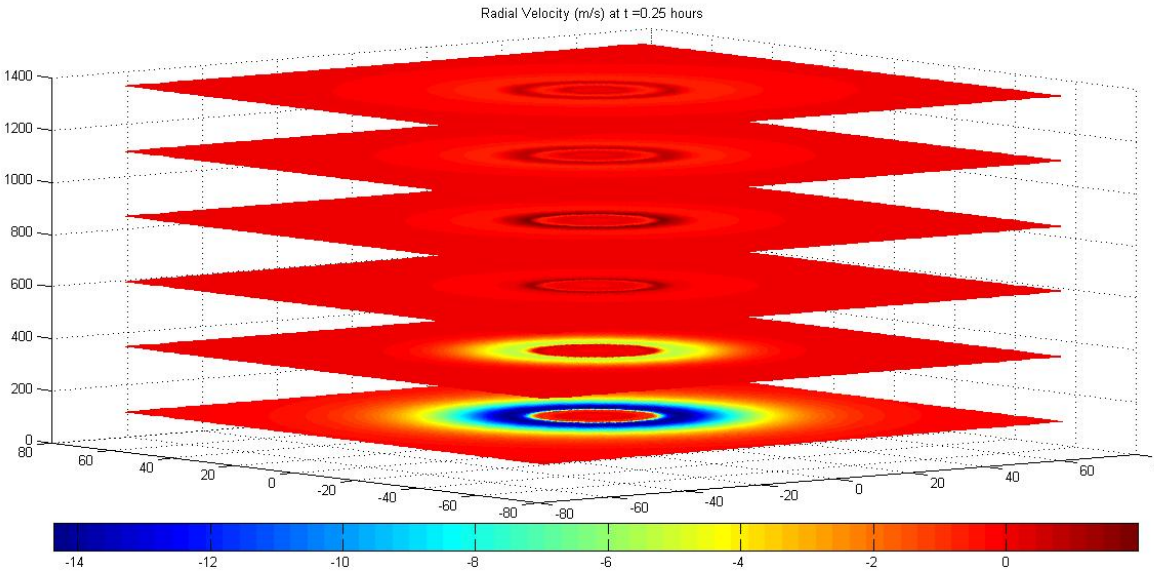

Figure 5.21: Evolution of radial velocity at $t = 0.25$ hr for the vortex embedded in 5 m s^{-1} southerly flow.

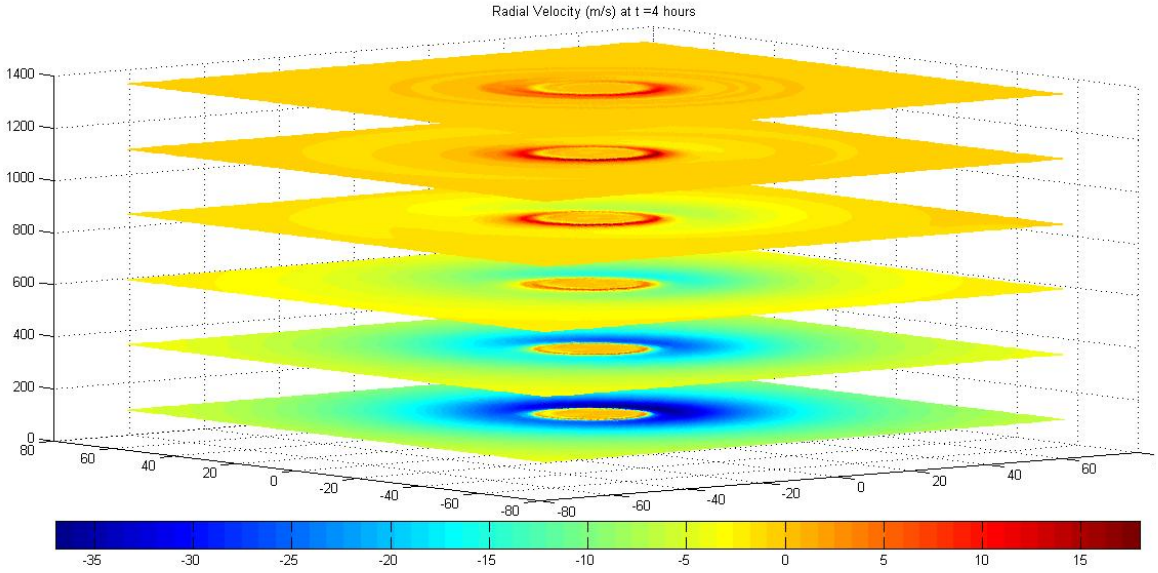

Figure 5.22: Evolution of radial velocity at $t = 4$ hr for the vortex embedded in 5 m s^{-1} southerly flow.

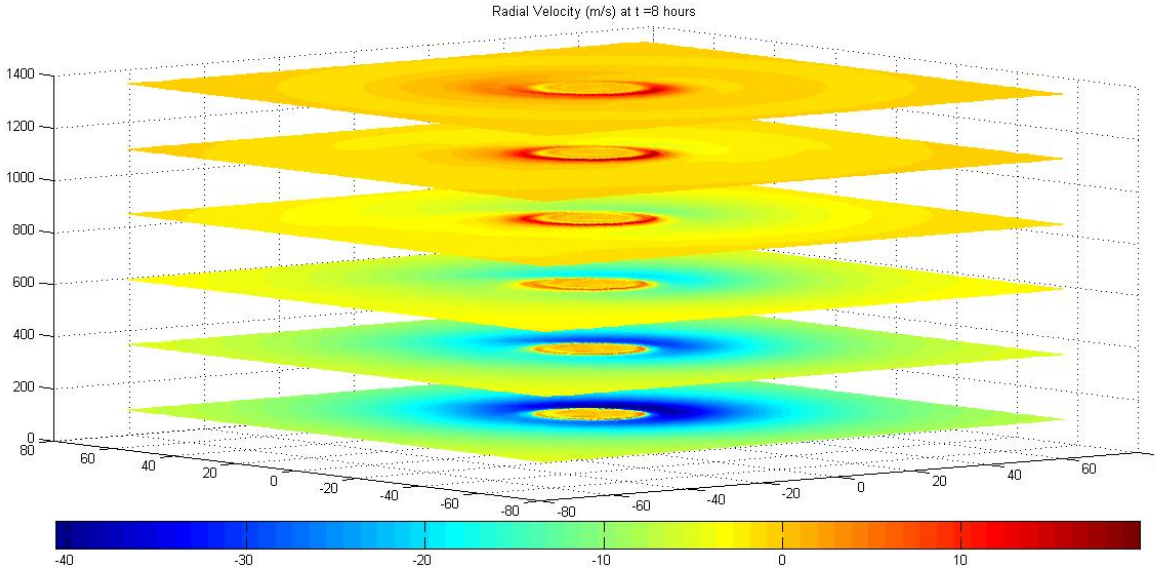

Figure 5.23: Evolution of radial velocity at $t = 8$ hr for the vortex embedded in 5 m s^{-1} southerly flow.

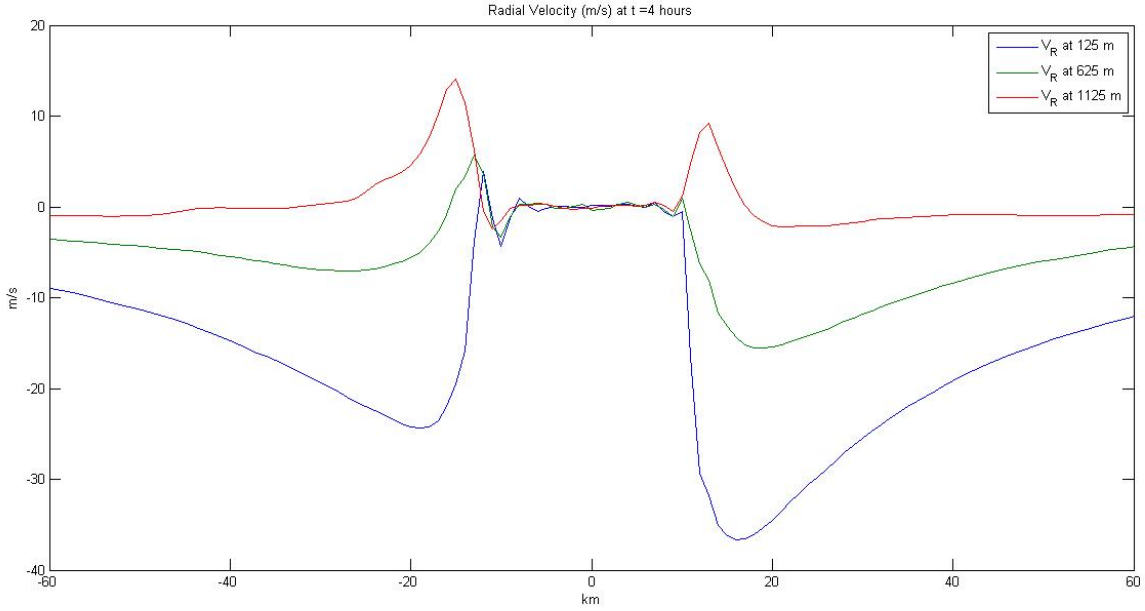

Figure 5.24: Radial profiles of radial velocity at $t = 4$ hr for the vortex embedded in 5 m s^{-1} southerly flow.

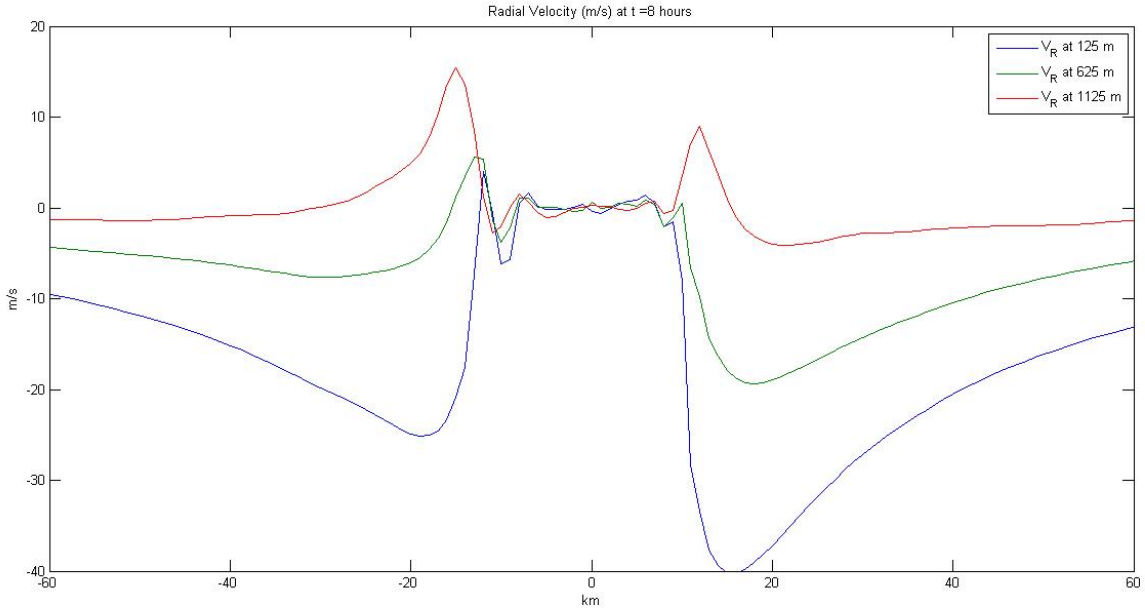

Figure 5.25: Radial profiles of radial velocity at $t = 8$ hr for the vortex embedded in 5 m s^{-1} southerly flow.

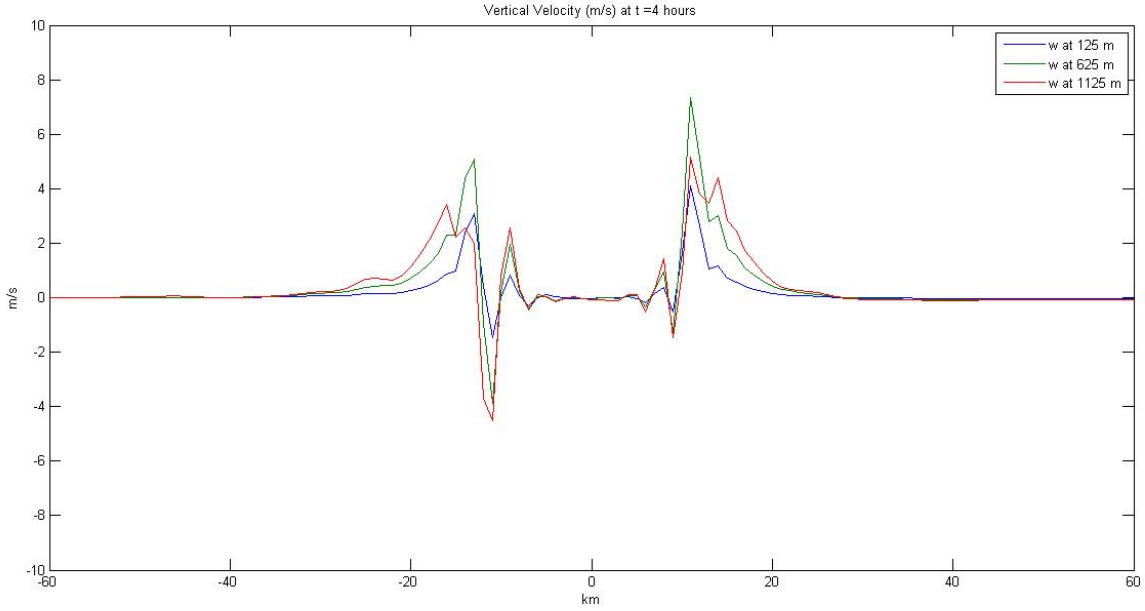

Figure 5.26: Radial profiles of vertical velocity at $t = 4$ hr for the vortex embedded in 5 m s^{-1} southerly flow.

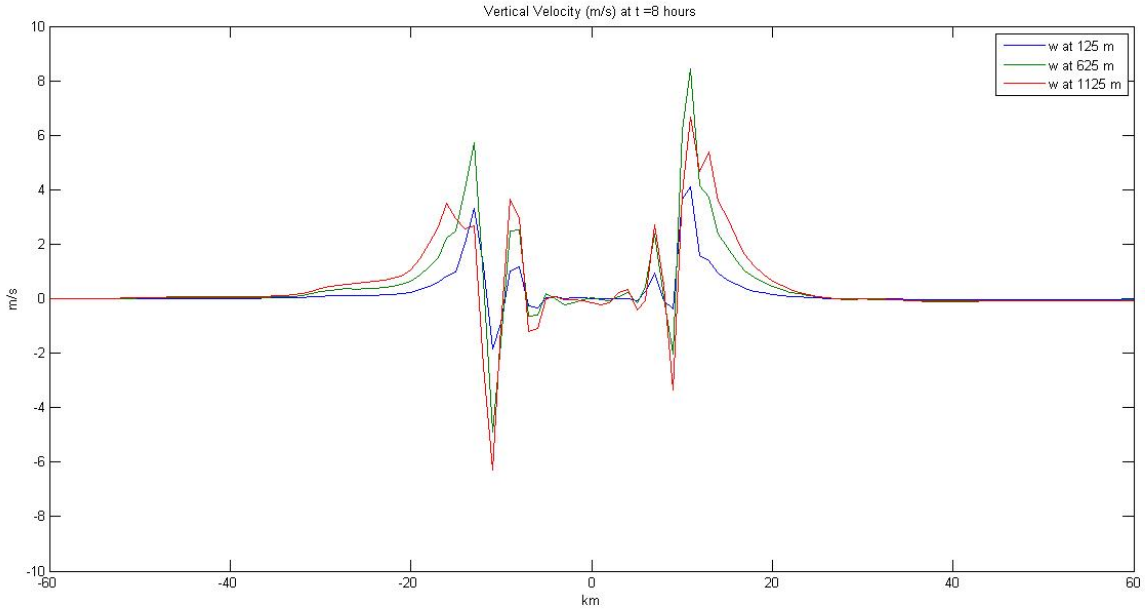

Figure 5.27: Radial profiles of vertical velocity at $t = 8$ hr for the vortex embedded in 5 m s^{-1} southerly flow.

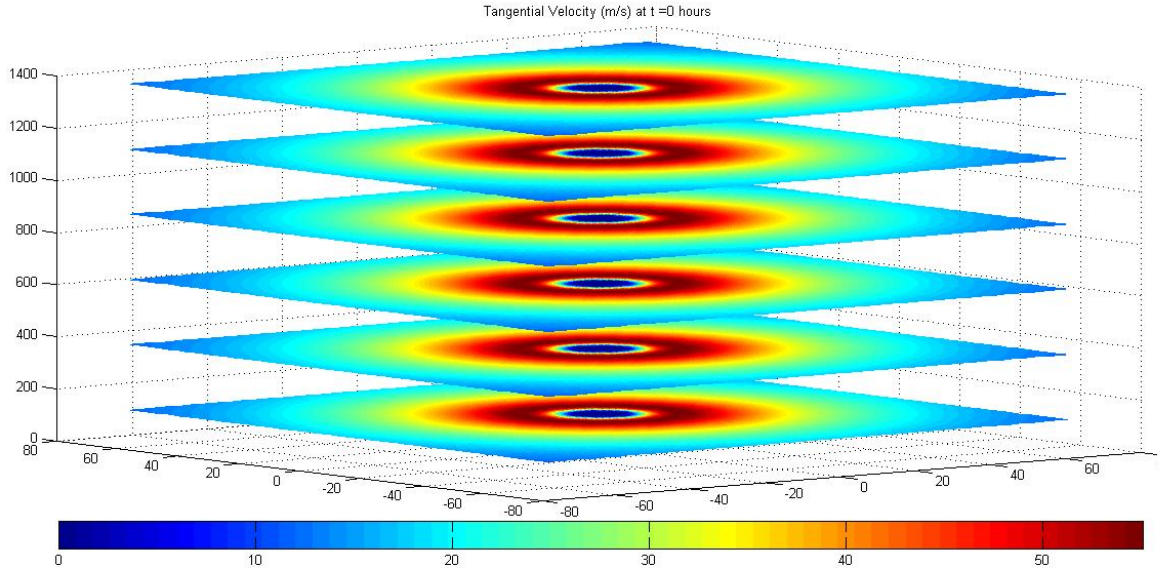

Figure 5.28: Evolution of tangential velocity at $t = 0$ hr for the vortex embedded in 5 m s^{-1} southerly flow.

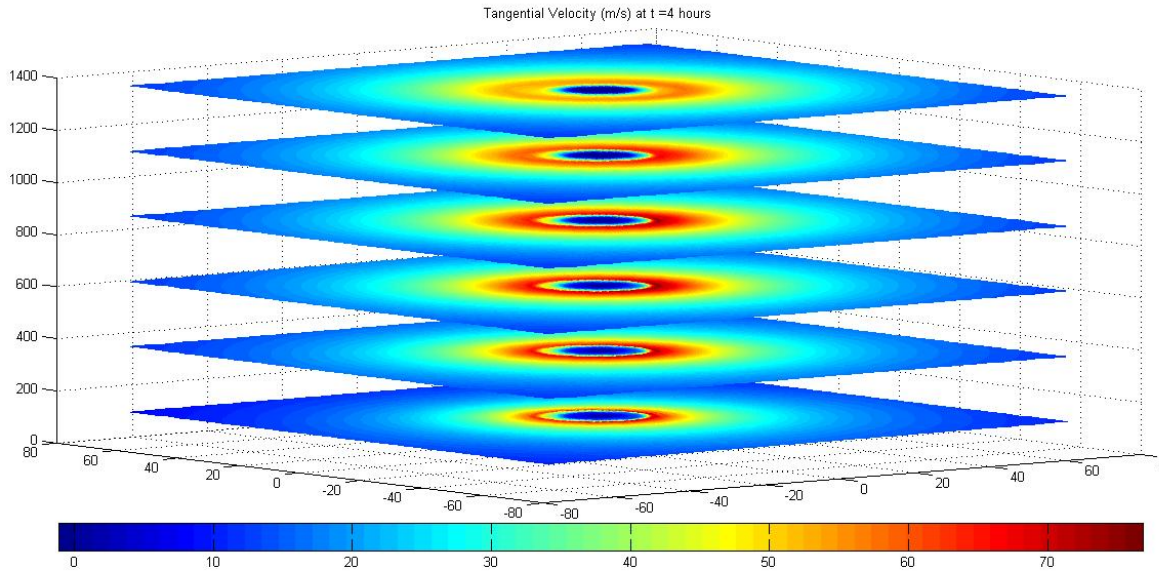

Figure 5.29: Evolution of tangential velocity at $t = 4$ hr for the vortex embedded in 5 m s^{-1} southerly flow.

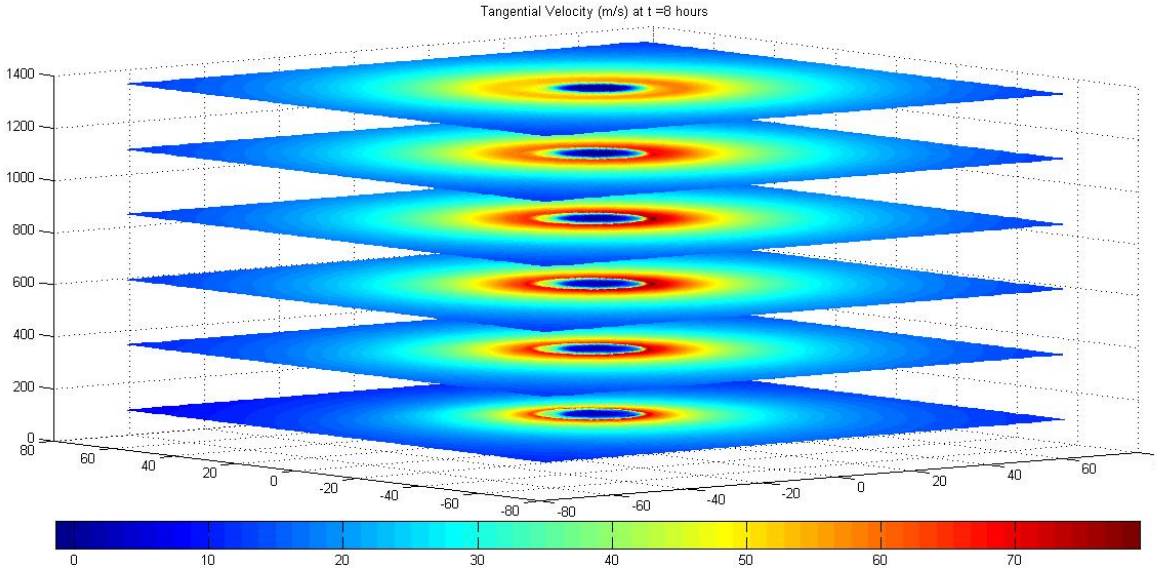

Figure 5.30: Evolution of tangential velocity at $t = 8$ hr for the vortex embedded in 5 m s^{-1} southerly flow.

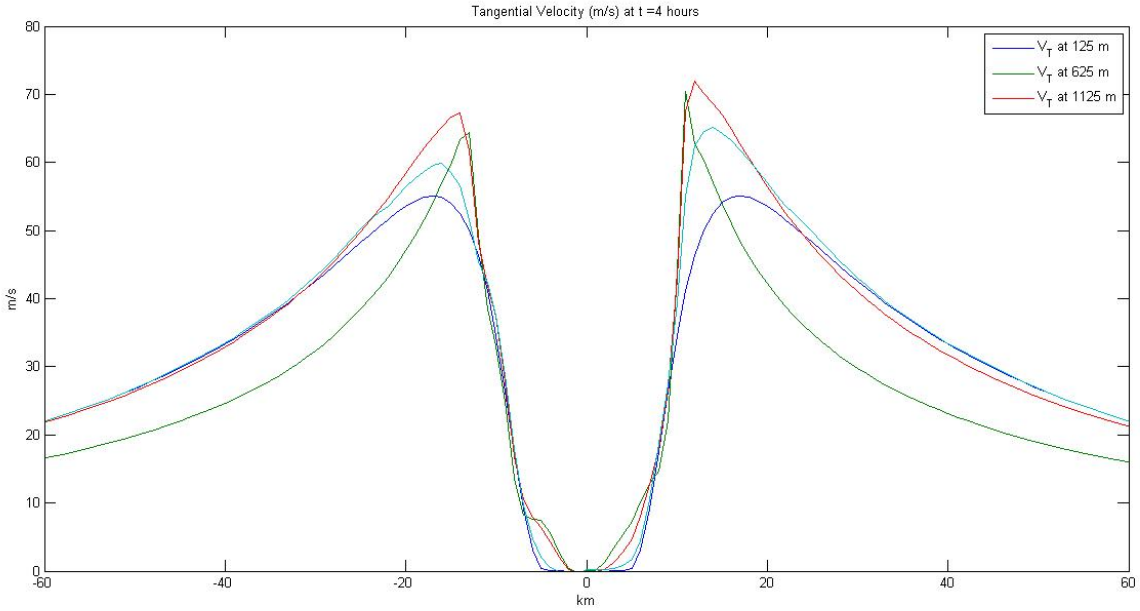

Figure 5.31: Radial profiles of tangential velocity at $t = 4$ hr for the vortex embedded in 5 m s^{-1} southerly flow.

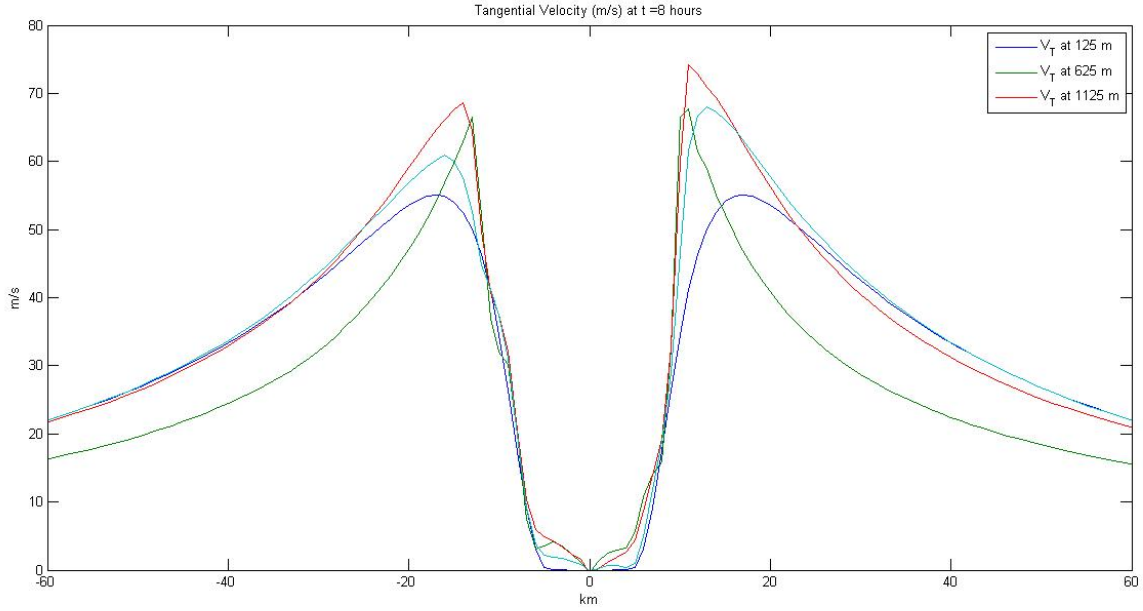

Figure 5.32: Radial profiles of tangential velocity at $t = 8$ hr for the vortex embedded in 5 m s^{-1} southerly flow.

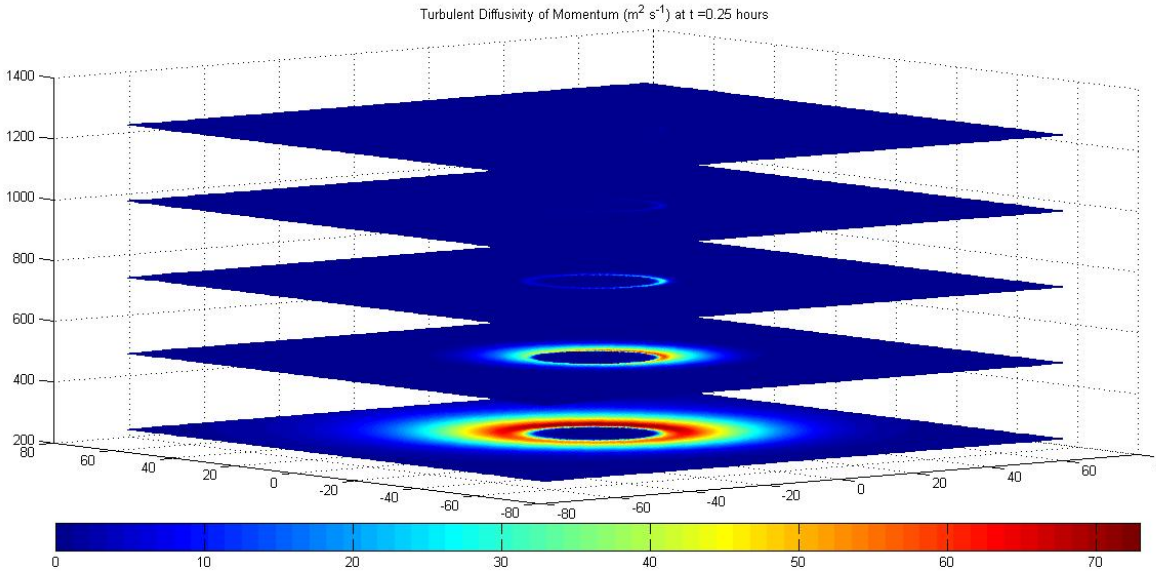

Figure 5.33: Evolution of turbulent diffusivity of momentum at $t = 0.25$ hr for the vortex embedded in 5 m s^{-1} southerly flow.

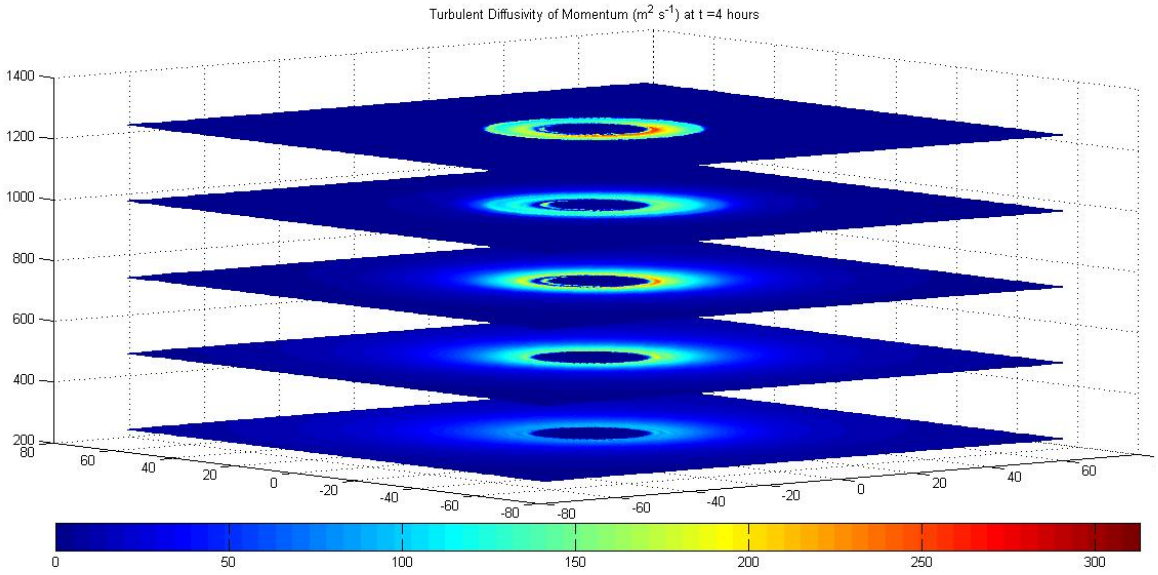

Figure 5.34: Evolution of turbulent diffusivity of momentum at $t = 4$ hr for the vortex embedded in 5 m s^{-1} southerly flow.

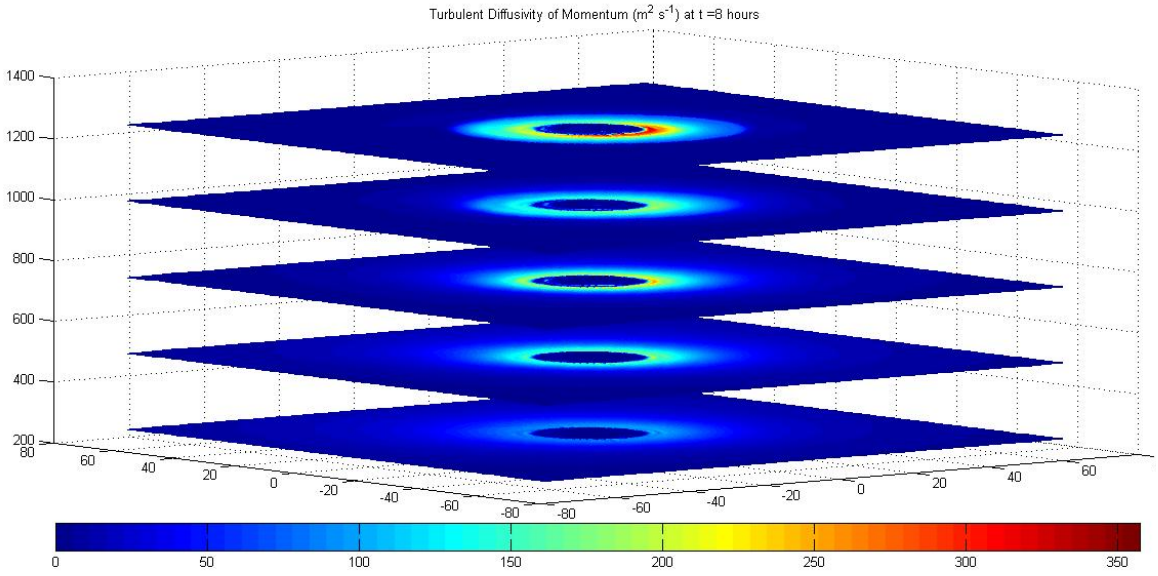

Figure 5.35: Evolution of turbulent diffusivity of momentum at $t = 8$ hr for the vortex embedded in 5 m s^{-1} southerly flow.

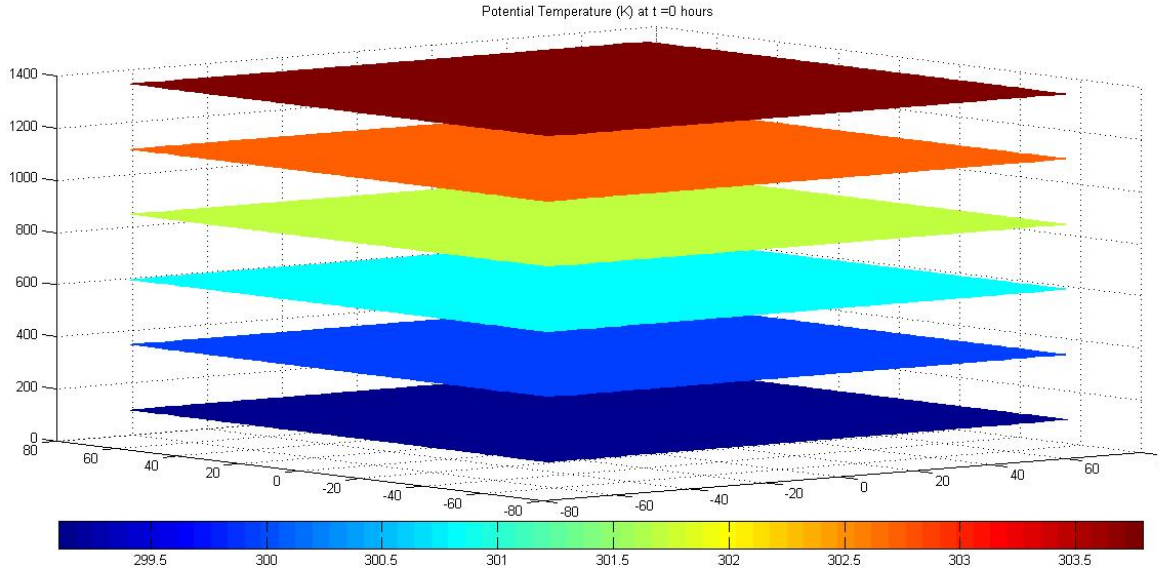

Figure 5.36: Evolution of potential temperature at $t = 0$ hr for the vortex embedded in 5 m s^{-1} southerly flow.

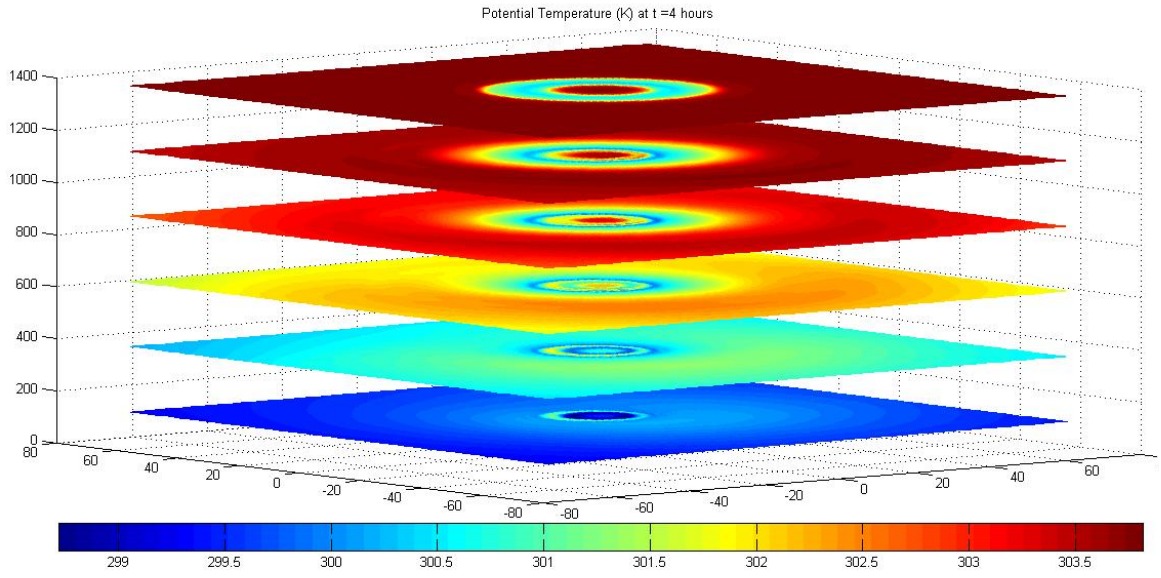

Figure 5.37: Evolution of potential temperature at $t = 4$ hr for the vortex embedded in 5 m s^{-1} southerly flow.

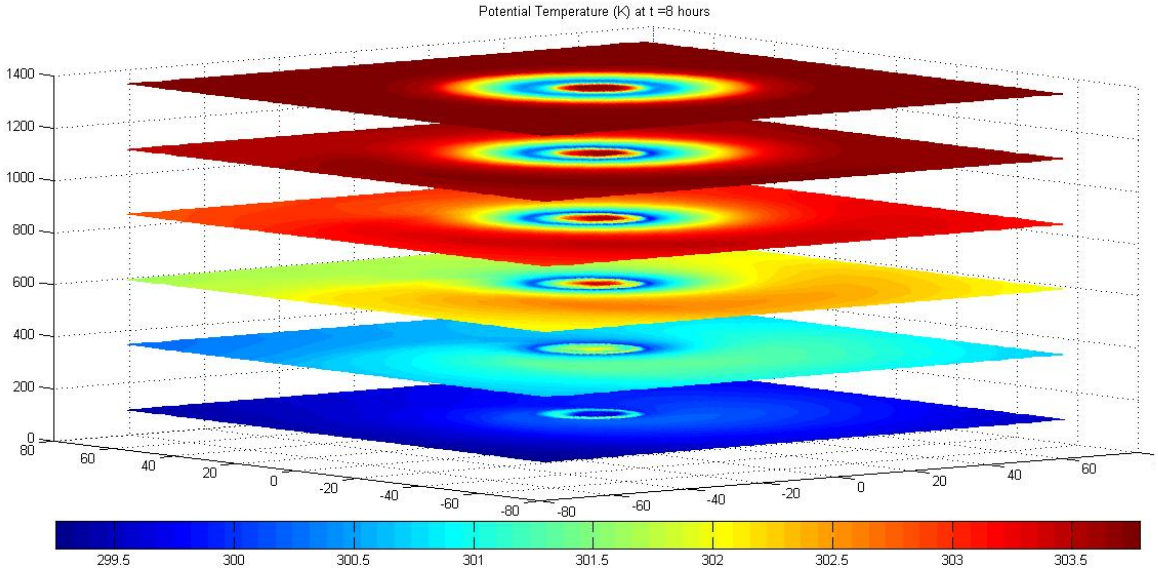

Figure 5.38: Evolution of potential temperature at $t = 8$ hr for the vortex embedded in 5 m s^{-1} southerly flow.

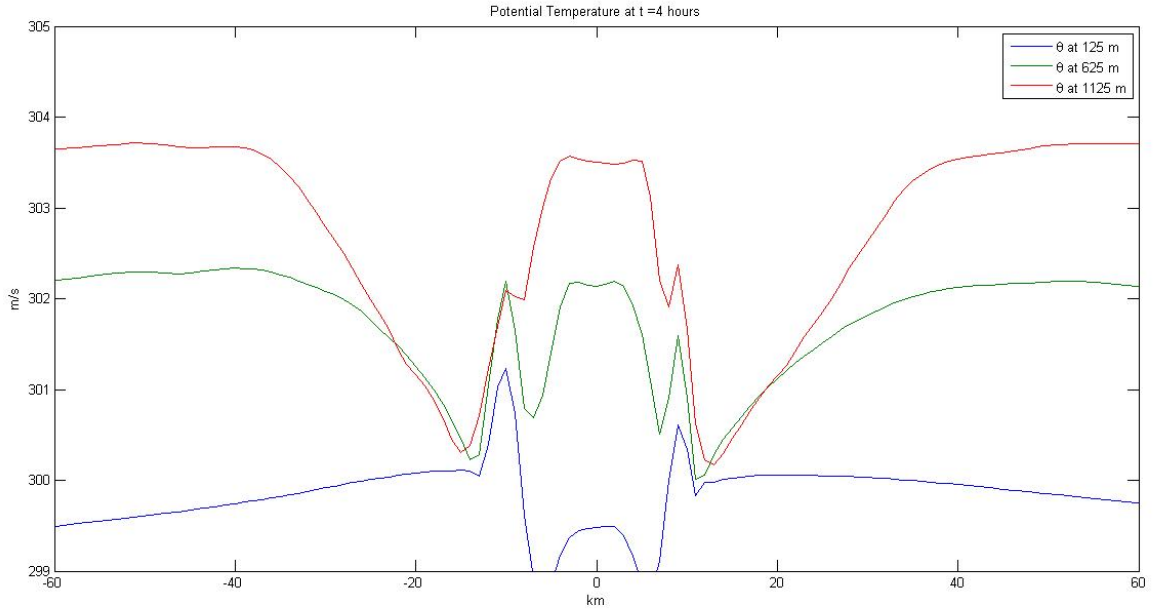

Figure 5.39: Horizontal cross-section of potential temperature at $t = 4$ hr for the vortex embedded in 5 m s^{-1} southerly flow.

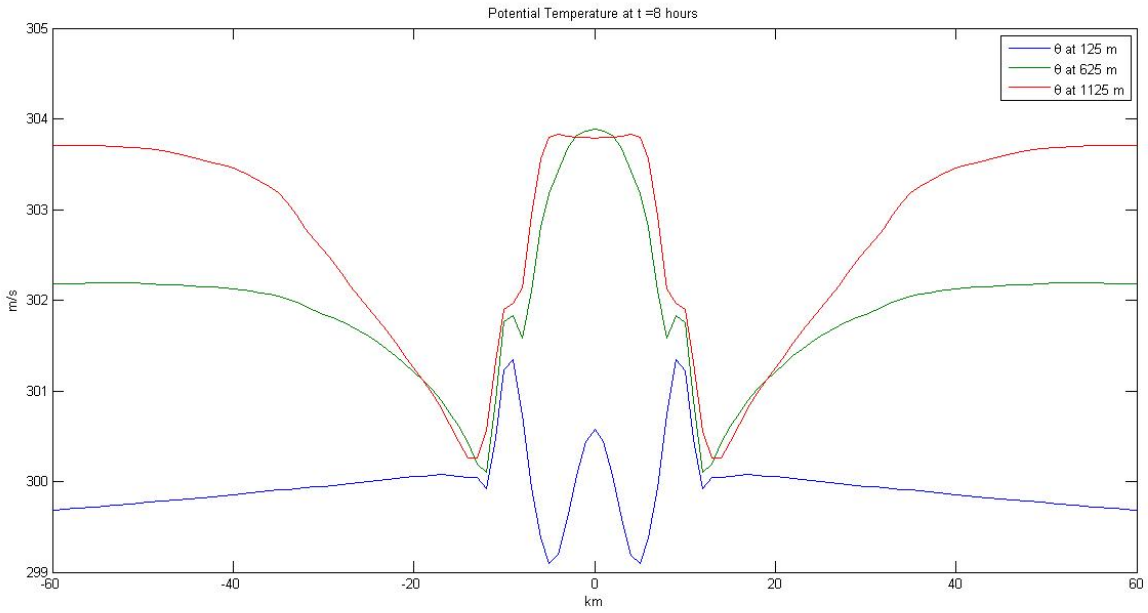

Figure 5.40: Horizontal cross-section of potential temperature at $t = 8$ hr for the vortex embedded in 5 m s^{-1} southerly flow.

Chapter 6

SUMMARY AND CONCLUSIONS

Tropical cyclones (TCs) may change in structure and intensity due to environmental factors, ocean surface fluxes, and internal dynamics. In this dissertation, aspects of the evolution of TCs due to internal dynamical processes and environmental forcing have been assessed. The first half of the dissertation focused on idealized studies of the effect of vertical shear on PV mixing in the hurricane inner-core and the second part focused on the development of shock-like structures in the tropical cyclone boundary layer for a stationary and a moving tropical cyclone.

In chapter 2, we studied the evolution of a baroclinic hollow PV tower in zero environmental flow and in external zonal shear. For the baroclinic hollow PV tower in zero environmental flow, barotropic instability caused air parcels with high PV to be mixed into the eye preferentially at lower levels, where unstable PV wave growth rates are the largest. During the model simulation, little mixing is found to occur at upper levels. The rearrangement of PV affects the structure and intensity of the vortex by causing a simultaneous decrease in minimum central pressure and maximum tangential velocity and by forming a PV bridge at lower levels. For the baroclinic hollow PV tower in zonal shear, the shear forcing caused an internal oscillation (wavenumber-1 structure) and a damping of the unstable mode during the nonlinear mixing of the vortex. The initial response of the vortex to the vertical shear is to tilt downshear. The upper- and lower-level centers then began to rotate cyclonically about the midlevel center, causing both leftward and rightward movement relative to the vertical shear. The cyclonic precession of the vortex around the center demonstrates the existence of an azimuthal wavenumber-1 quasimode that prevents the vertical alignment of the

vortex. Because of the radial structure of our vortex, the resonant damping of the quasimode, as in Schecter et al. (2002), becomes very efficient as the critical radius moves outward to a region of weakened PV gradient. The persistence of the quasi-mode also demonstrates that nonlinear advection does not play a dominant role in the vertical alignment process. Since the Rossby radius of deformation λ_R of our vortex is large and the vortex beta Rossby number R_β is small, the dynamics of a sheared vortex can be described in terms of linear VRW theory.

In Chapter 3, we studied the evolution of sheared PV towers under simple diabatic forcing, which is an extension of the results from Chapter 2. For our first series of experiments, we applied a specified source of diabatic heating similar to the heating profile of Yanai et al. (1973) at various locations within our vortex and illustrated how the vortex response to diabatic heating depends on the location of the heating. For heating contained within the RMW, there was a sharp increase in velocity and PV, whereas heating contained outside the RMW produced a minimal increase in velocity and PV. Using the energy efficiency argument of Hack and Schubert (1986), heating within the RMW enables an efficient extraction of kinetic energy from the diabatic heat source. This efficiency leads to a nonlinear coupling between the vortex strength and the diabatic heat source. Heating outside the RMW causes an inefficient extraction of kinetic energy from the diabatic heat source. Therefore, the diabatic heating outside of the RMW has little influence on the development of the vortex.

For our second series of experiments, we represented the diabatic heating by a CISK-type parameterization. The addition of surface friction enhances inward PV mixing of the hollow tower, whereas the addition of vertical diffusion helps to maintain the overall structure of the PV tower by transporting momentum from middle-levels to the upper-troposphere. For the vortex in simple vertical shear, the initial response of the vortex to the vertical shear is to tilt downshear. The upper- and lower-level centers then began to rotate cyclonically about the midlevel center, causing both leftward and rightward movement relative to the vertical shear. As the inertial stability of the vor-

tex increases due to diabatic heating, the wavenumber-1 quasimode disappears into the continuous spectrum of VRWs, leading to vortex alignment. Because of the increase of inertial stability of the vortex, the resonant damping of the quasi-mode, as in Schecter et al. (2002), becomes very efficient as the critical radius moves inward to a region of higher PV gradient. Furthermore, since L/λ_R and R_β are small, the vortex resists shear by emitted sheared VRWs in accordance with linear VRW theory.

The results from Chapters 2 and 3 can be extended to tropical cyclones. In particular, our results imply that strong tropical cyclones efficiently radiate sheared VRWs in order to resist vertical shear. Also, since strong tropical cyclones have strong PV gradients outside of the RMW, this suggests that strong tropical cyclones also have strong decay rates of the quasi-mode structure induced by the vertical tilt. When the inertial stability of a tropical cyclone increases such that the horizontal scale is a non-negligible fraction of the global internal deformation scale, then the inviscid damping of the sheared VRWs leads to rapid reduction of the tilt. Diabatic forcing enables a higher decay rate of the quasi-mode, which allows the vortex to resist the effects of vertical shear. For a mature tropical cyclone whose structure is maintained by moist convection, the results in this chapter indicate that a tropical cyclone will resist the effects of vertical shear by the emission of convectively-coupled VRWs and through the resonant damping of the quasi-mode induced by the vertical shear. Therefore, for a given environmental vertical shear profile, the mature tropical cyclone will be less prone to breakdown and dissipation. When a hurricane is forced by vertical shear, observations suggest that the vortex tilt is generally oriented downshear to downshear-left when the decay rate of the quasi-mode is non-negligible, consistent with our results. This suggests that the downshear-left location of convective asymmetry observed in hurricanes forced by vertical shear may be in the first approximation a consequence of dry adiabatic VRW dynamics.

In Chapter 4, we studied the 2D evolution of shock-like structures in the tropical cyclone boundary layer. Since the dominant physical processes necessary to produce boundary layer jets

are horizontal advection, vertical advection, and vertical diffusion, this suggests that the boundary layer model should resemble the nonlinear viscous Burgers' equation and for a given vortex, shock-like structures should develop. For the single eyewall experiment, we saw that strong radial inflow created a circular shock that shrunk the RMW of the vortex, which produced supergradient winds near the RMW and strong Ekman pumping. For the single eyewall experiment under vortex translation, we saw that the asymmetry in the boundary layer response is forced by the asymmetry in frictional drag due to the translation of the vortex. For a relatively slow moving vortex, the nonlinear asymmetric advective interactions remain relatively weak where inflow is maximum in the right-front quadrant and Ekman pumping is large in a broad arc ahead of the center of the vortex. As the translation speed increases, the nonlinear asymmetric advective interactions become stronger where inflow and Ekman pumping become concentrated more ahead and to the right of the vortex. Furthermore, as the translation speed of the vortex increases, the anticyclonic spiral in the vertical velocity field becomes more pronounced and the circular shock becomes an anticyclonic spiral with maximum strength in the right quadrant. This suggests that vortex motion will cause asymmetries in convective heat release for a tropical cyclone.

For the double eyewall experiments, we observed two general cases. When the maximum velocity of the outer eyewall was greater than or approximately equal to the maximum velocity of the inner eyewall, the outer eyewall contracted inward, choking the radial inflow to the inner eyewall. This caused the maximum velocity of the inner eyewall to diminish whereas the maximum velocity of the outer eyewall intensified. When the maximum velocity of the outer eyewall was weaker than the maximum velocity of the inner eyewall, the outer eyewall diminished in strength whereas a shock-like structure formed on the inner eyewall. As shown in Chapter 4, the behavior of the vortex with a double eyewall can be explained using the shock effect where we visualize an eyewall replacement cycle as two isolated shocks connected by a smooth ramp. The development of shock-like structures in the boundary layer depends sensitively on the radial structure of the gradient wind profile for the vortex and the relative strength of the inner and outer eyewall.

In Chapter 5, we studied the 3D evolution of shock-like structure in the tropical cyclone boundary layer. In particular, we studied the effect of vertical advection and vertical diffusion on the development of shock-like structures in the boundary layer. For the single eyewall experiment, we saw that strong radial inflow created a circular shock near the ocean surface, leading to strong Ekman pumping. Even though the shock occurred near the surface, the jet maximum occurred around 650 m, which was confirmed by examining the location of maximum turbulent transport, the location of maximum tangential winds, and the location of radial outflow. The production of turbulent transport was caused predominately by vertical shear within the boundary layer, indicating that the tropical cyclone boundary layer resembles a neutral boundary layer. These results suggest that the shock structure develops near the surface due to strong radial inflow and vertical diffusion and vertical advection communicates the shock effect to the depth of the tropical cyclone boundary layer. The circular shock structure influenced the radial and vertical distribution of potential temperature. Due to turbulent transport, there was significant downward mixing of high-θ air into the eye region from the top of the boundary layer and significant upward mixing of low-θ air into the eyewall region. The effect of vortex translation was very similar to the effect of vortex translation for the 2D boundary layer. As the translation speed increased, the circular shock structure became an anticyclonic spiral structure horizontally and vertically. Near surface inflow is maximum in the right-front quadrant whereas outflow near the top of the boundary layer is maximum in the right-rear quadrant. These results indicate that vortex translation will induce a spiral shock structure in the tropical cyclone boundary layer and will cause asymmetries in the convective heat release for a tropical cyclone.

For future research, I would like to examine the effect of multi-directional shear on the rearrangement of hollow PV towers. As shown in Chapter 2, a vortex resists the effects of zonal shear by projecting the tilt asymmetry onto the wavenumber-1 quasimode and depending on the Rossby number and the Rossby deformation radius, the vortex will damp the tilt asymmetry through resonant damping of the quasimode or through the emission of sheared VRWs from the vortex. Since the

core of a TC-like vortex is dominated by low wavenumber discrete VRWs, multi-directional shear may cause a vortex to project its tilt asymmetry onto higher wavenumber. An interesting question would be to determine whether or not a vortex will become more resilient or less resilient under multi-directional shear.

There are five future research projects that can be extended from the results of this dissertation. First, I would like to examine the role of moisture and moist convection upon the evolution of sheared hollow PV towers. As mentioned in Chapter 1, moist processes in the eyewall region give rise to a reduced effective static stability, which should suppress discrete VRW development and improve vortex resiliency. In order to truly examine how moist convection affects the PV mixing process and the vortex resiliency process, moist physics through explicit cloud microphysics must be implemented into the models used in this study. An interesting and relevant question would be to determine the role of ice and liquid water processes in the vortex resiliency and PV mixing process. Moist processes will change the vertical and radial distribution of heating through the secondary circulation compared to the CISK-type parameterized heating given in Chapter 3. Therefore, the evolution of sheared VRWs and discrete VRWs (and thus, the resonant damping mechanism) should be significantly altered in comparison to the results from Chapter 3.

Second, I would like to examine the sensitivity of the PV mixing process and vortex resiliency process to the radial and vertical structure of the vortex. As mentioned in Chapter 1, the end state of the mixing process for an annular vorticity ring depends on the hollowness and the thickness of the vorticity ring. Hendricks and Schubert (2010) discovered that a thin, hollow PV tower develops a PV bridge faster and has a greater decrease in tangential velocity than a thick, hollow PV tower. Based on the arguments of Chapter 2, this suggests that a thin, hollow PV tower would be less resistant to vertical shear than a thick, hollow PV tower. It would be interesting to compare the results from Chapter 2 and 3 for a barotropic PV tower, a baroclinic PV tower, and for PV towers of varying hollowness and thickness.

Third, I would like to examine how deep convection would influence the development of shocks in the TC boundary layer. As mentioned in Chapter 4, the shock effect helps to place Ekman pumping to the region of high inertial stability so that the central pressure falls more rapidly. This suggests that the shock effect must play an important role in determining the eyewall radius and may help to organize convection within the TC boundary layer. Conversely, deep convection could alter the development of boundary layer shocks through the secondary circulation in the boundary layer and through the feedback between the surface entropy fluxes and the primary circulation. I would also like to examine how the development of shocks in the boundary layer contribute to outer eyewall formation. As mentioned in Chapters 4 and 5, translating vortices caused the shock to arranged itself into anticyclonic spirals that resembled the principal rainband of a TC. This may suggest that due to the embedded Burgers' equation, the boundary layer likes to form shocks which both cause low-level supergradient winds and localize convection so that the balanced Sawyer-Eliassen process can spin up a lower-middle tropospheric wind maximum. It is an interesting and relevant question to determine whether the 3D boundary layer model of Chapter 5 can produce this effect.

Fourth, I would like to extend this research to include the role of upper-level troughs. I would like to study the evolution of baroclinic hollow PV towers during a hurricane-trough interaction. Since upper-level troughs are often accompanied with strong vertical shear, a first step in addressing this question involves understanding the evolution of hollow PV towers in sheared vortices, which was done in this dissertation. The future goals of this research are to answer the following questions:

- How does the presence of an upper-level trough affect the shear forcing on a vortex?
- How does the presence of an upper-level trough affect the inner core PV mixing dynamics of a TC?

Kimball and Evans (2002) simulated a tropical cyclone interacting with an idealized trough and discovered that during the interaction, the troughs are deformed by the tropical cyclone flow. In particular, they found that when a strong and shallow trough merges with a tropical cyclone, the

trough splits and causes a reduction of vertical shear over the vortex. This suggests that troughs have the ability to both amplify and reduce vertical shear over tropical cyclones. I would like to extend this research by studying how the internal dynamics are affected by an upper-level trough interaction.

Finally, I would like to examine how the shock effect in the tropical cyclone boundary layer affects the evolution of a hollow PV tower. As mentioned above, the shock effect plays an important role in determining the eyewall radius of a TC and thus should affect the rearrangement of PV in a hollow PV tower. Furthermore, as seen in Chapter 2, the rearrangement of PV into a monopole state tends to weaken vorticity gradients throughout the vortex, which may affect the development and propagation of boundary layer shocks. An important and relevant question is to determine how barotropic instability affects the structure of the tropical cyclone boundary layer and the development of boundary layer jets.

BIBLIOGRAPHY

Anthes, R. A., 1970: The role of large-scale asymmetries and internal mixing in computing meridional circulations associated with the steady-state hurricane. *Mon. Wea. Rev.*, **98**, 521-528.

Arakawa, A., and V. Lamb, 1977: Computational design of the basic dynamical processes of the UCLA general circulation model. *Methods in Computational Physics*, **Vol. 17**, J. Chang, Ed., Academic Press, 173-265.

Arakawa, A., and S. Moorthi, 1988: Baroclinic instability in vertically discrete systems. *J. Atmos. Sci.*, **45**, 1688-1707.

Black, P. G., and R. A. Anthes, 1971: On the asymmetric structure of the tropical cyclone outflow layer. *J. Atmos. Sci.*, **28**, 1348-1366.

Black, P. G., and L. K. Shay, 1998: Air-sea interaction processes relevant to tropical cyclone intensity change. Preprints, *Symp. on Tropical Cyclone Intensity Change*, Phoenix, AZ. Amer. Meteor. Soc., 161-168.

Black, M. L., and H. E. Willoughby, 1992: The concentric eyewall cycle of Hurricane Gilbert. *Mon. Wea. Rev.*, **120**, 947-957.

Bosart, L. F., and J. A. Bartlo, 1991: Tropical storm formation in a baroclinic environment. *Mon. Wea. Rev.*, **119**, 1979-2013.

Bosart, L. F., and G. M. Lackmann, 1995: Post-landfall tropical cyclone intensification in a weakly baroclinic environment: A case study of Hurricane David (September 1979). *Mon. Wea. Rev.*, **123**, 3268-3291.

Bosart, L. F., C. S. Velden, W. E. Bracken, J. Molinari, and P. G. Black, 2000: Environmental Influences on the Rapid Intensification of Hurricane Opal (1995) over the Gulf of Mexico. *Mon. Wea. Rev.* **128**, 322-352.

Braun, S. A., 2002: A cloud-resolving simulation of Hurricane Bob (1991): Storm structure and eyewall buoyancy. *Mon. Wea. Rev.*, **130**, 1573-1592.

Braun, S. A., 2006: High-resolution simulations of Hurricane Bonnie (1998). Part II: Water budget. *J. Atmos. Sci.*, **63**, 43-64.

Braun, S. A., and L. Wu, 2007: A numerical study of Hurricane Erin (2001). Part II: Shear and the organization of eyewall vertical motion. *Mon. Wea. Rev.*, **135**, 1179-1194.

Briggs, R. J., J. D. Daugherty, and R. H. Levy, 1970: Role of Landau damping in crossed-field electron beams and inviscid shear flow. *Phys. Fluids*, **13**, 421-432.

Bryan, G. H., and R. Rotunno, 2010: The maximum intensity of tropical cyclones in axisymmetric numerical model simulation. *Mon. Wea. Rev.*, **137**, 1770-1789.

Challa M., and R. L. Pfeffer , 1980: Effects of eddy fluxes of angular momentum on model hurricane development. *J. Atmos Sci.*, **37**: 1603-1618.

Challa M., R. L. Pfeffer, Q. Zhao, and S. W. Chang, 1998: Can eddy fluxes serve as a catalyst for hurricane and typhoon formation? *J. Atmos. Sci.*, **55**, 22012219.

Chen L., and W. M. Gray, 1984: Global view of the upper level outflow patterns associated with tropical cyclone intensity changes. Preprint, *15th Conference on Hurricanes and Tropical Meteorology*, Miami, FL, AMS, Boston, 224-231.

Chen Y., and M. K. Yau, 2001: Spiral bands in a simulated hurricane. Part I: Vortex Rossby wave verification. *J. Atmos. Sci.*, **58**: 2128-2145.

Chen Y., G. Brunet, and M. K. Yau, 2003: Spiral bands in a simulated hurricane. Part II: Wave activity diagnostics. *J. Atmos. Sci.*, **60**, 12391256.

Chow, S., 1971: A study of the wind field in the planetary boundary layer of a moving tropical cyclone. M. S. Thesis, Department of Meteorology and Oceanography, New York University, 59 pages.

Colon, J. A., and W. R. Nightingale, 1963: Development of tropical cyclones in relation to circulation patterns at the 200 millibar level. *Mon. Wea. Rev.*, **91**, 329-336.

Corbosiero, K. L., and J. Molinari, 2002: The effects of vertical wind shear on the distribution of convection in tropical cyclones. *Mon. Wea. Rev.*, **130**, 2110-2123.

Corbosiero, K. L., and J. Molinari, 2003: The relationship between storm motion, vertical wind shear, and convective asymmetries in tropical cyclones. *J. Atmos. Sci.*, **60**, 366-376.

Corbosiero, K. L., J. Molinari, and A. R. Aiyyer, 2006: The structure and evolution of Hurricane Elena (1985). Part II: Convective Asymmetries and Evidence for Vortex Rossby Waves. *Mon. Wea. Rev.*, **134**, 3073-3091.

Cram, T. A., J. Persing, M. T. Montgomery, and S. A. Braun, 2007: A Lagrangian Trajectory View on Transport and Mixing Processes between the Eye, Eyewall, and Environment Using a High-Resolution Simulation of Hurricane Bonnie (1998). *J. Atmos. Sci.*, **64**, 1835-1856.

Davidson, N. E., G. J. Holland, J. L. McBride, T. D. Keenan, 1990: On the formation of AMEX tropical cyclones Irma and Jason. *Mon. Wea. Rev.*, **118**, 1981-2000.

Davis, C., S. C. Jones, and M. Riemer, 2008: Hurricane vortex dynamics during Atlantic extratropical transition. *J. Atmos. Sci.*, **65**, 714-736.

DeMaria, M., J-J Baik, and J. Kaplan, 1993: Upper-level eddy angular momentum fluxes and tropical cyclone intensity change. *J. Atmos. Sci.*, **50**, 1133-1147.

DeMaria, M., 1996: The effect of vertical shear on tropical cyclone intensity change. *J. Atmos. Sci.*, **53**, 2076-2087.

Didlake, A. C., and R. A. Houze, 2011: Kinematics of the secondary eyewall observed in Hurricane Rita (2005). *J. Atmos. Sci.*, **68**, 1620-1636.

Donelan, M. A., B. K. Haus, N. Reul, W. J. Plant, M. Stiassnie, H. C. Graber, O. B. Brown, and E. S. Saltzman, 2004: On the limiting aerodynamic roughness of the ocean in very strong winds. *J. Geophys. Res.*, **31**, L18306.

Eliassen, A., 1952: Slow thermally or frictionally controlled meridional circulation in a circular vortex. *Astrophys. Norv.*, **5**, 19-60.

Eliassen, A., 1971: On the Ekman layer in a circular vortex. *J. Meteor. Soc. Japan.*, **49**, 784-789.

Elsberry, R. L., G. J. Holland, H. Gerrish, M. DeMaria, C. P. Guard, and K. Emanuel, 1992: Is there any hope for tropical cyclone intensity prediction? - A panel discussion. *Bull. Amer. Meteor. Soc.*, **73**, 264-275.

Emanuel, K. A., 1986: An air-sea interaction theory for tropical cyclones. Part I: Steady-state maintenance. *J. Atmos. Sci.*, **43**, 2044-2061.

Emanuel, K. A. 1991: The theory of hurricanes. *Annu. Rev. Fluid Mech.*, **23**, 585-604.

Emanuel, K. A., M. Fantini, and A. J. Thorpe, 1987: Baroclinic instability in an environment of small stability to slantwise moist convection. Part I: Two-dimensional models. *J. Atmos. Sci.*, **44**, 1559-1573.

Enagonio, J., and M. T. Montgomery, 1988: Tropical cyclogenesis via convectively forced Rossby waves in a shallow water primitive equation model. *J. Atmos. Sci.*, **58**, 685-706.

Erickson, C. O., 1967: Some aspects of the development of Hurricane Dorothy. *Mon. Wea. Rev.*, **95**, 121-130.

Fett, R. W., 1966: Upper-level structure of the formative tropical cyclone. *Mon. Wea. Rev.*, **94**, 9-18.

Frank, W. M., 1977: The structure and energetics of the tropical cyclone II: Dynamics and energetics. *Mon. Wea. Rev.*, **105**, 1136-1150.

Frank, W. M., and E. A. Ritchie, 2001: Effects of vertical wind shear on the intensity and structure of numerical simulated hurricanes. *Mon. Wea. Rev.*, **129**, 2249-2269.

Franklin, J. L., M. L. Black, and K. Valde, 2003: GPS dropwindsonde wind profiles in hurricanes and their operational implications. *Wea. Forecasting*, **18**, 32-44.

Guinn, T. A., and W. H. Schubert, 1993: Hurricane spiral bands. *J. Atmos. Sci.*, **50**, 3380-3404.

Hack, J. J., and W. H. Schubert 1986: Nonlinear response of atmospheric vortices to heating by organized cumulus convection. *J. Atmos. Sci.*, **43**, 1559-1573.

Hanley, D. E., 1999: The effect of trough interactions on tropical cyclone intensity change. PhD Thesis, State University of New York at Albany, 164 pp.

Hanley, D. E., J. Molinari, and D. Keyser, 2001: A composite study of the interactions between tropical cyclones and upper-tropospheric troughs. *Mon. Wea. Rev.*, **129**, 2570-2584.

Hebert, P. J., 1978: Intensification criteria for tropical depressions of the Western North Atlantic. *Mon. Wea. Rev.*, **106**, 831-840.

Hendricks, E. A., W. H. Schubert, R. K. Taft, H. Wang, and J. P. Kossin, 2009: Lifecycles of hurricane-like vorticity rings. *J. Atmos. Sci.*, **66**, 705-722.

Hendricks, E. A., and W. H. Schubert, 2010: Adiabatic rearrangement of hollow PV towers. *J. Adv. Model. Earth Syst.*, **2**, Art. 8, 19 pp.

Hock, T.F. and J. L. Franklin, 1999: The NCAR GPS dropwindsonde. *Bull. Amer. Meteor. Soc.*, **80**, 407-420.

Holland, G. J., 1980: An analytic model of the wind and pressure profiles in hurricanes. *Mon. Wea. Rev.*, **108**, 1212-1218.

Holland, G. J., and R. T. Merrill, 1984: On the dynamics of tropical cyclone structural changes. *Quart. J. Roy. Meteor. Soc.*, **110**, 723745.

Hoskins, B. J., M. E. McIntyre, and A. W. Robertson, 1985: On the use and significance of isentropic potential vorticity maps. *Quart. J. Roy. Meteor. Soc.*, **111**, 877-946.

Houze R. A., S. S. Chen, and Smull B. F., Lee W-C., and M. M. Bell, 2007: Hurricane intensity and eyewall replacement. *Science*, **315**, 12351239.

Jones, S. C., 1995: The evolution of vortices in vertical shear. I: Initially barotropic vortices. *Quart. J. Roy. Meteor. Soc.*, **126**, 3137-3159.

Jones, S. C., 2000: The evolution of vortices in vertical shear: III: Baroclinic vortices. *Quart. J. Roy. Meteor. Soc.*, **126**, 3161-3185.

Jones, S. C., 2004: On the ability of dry tropical cyclone like vortices to withstand vertical shear. *J. Atmos. Sci.*, **61**, 114-119.

Kaplan, J. 1995: An examination of the role of large-scale forcing on the rapid intensification of Hurricane Emily (1987). Preprints, *21st Conference on Hurricanes and Tropical Meteorology*, Miami FL, AMS, Boston, 332-334.

Kepert, J. D., 2001: The dynamics of boundary layer jets within the tropical cyclone core. Part I: Linear theory. *J. Atmos. Sci.*, **58**, 2469-2484.

Kepert, J. D., 2006a: Observed boundary layer wind structure and balance in the hurricane core. Part I: Hurricane Georges. *J. Atmos. Sci.*, **63**, 2169-2193.

Kepert, J. D., 2006b: Observed boundary layer wind structure and balance in the hurricane core. Part II: Hurricane Mitch. *J. Atmos. Sci.*, **63**, 2194-2211.

Kepert, J. D., 2010a: Comparing slab and height-resolving models of the tropical cyclone boundary layer. Part I: Comparing the simulations. *Quart. J. Roy. Meteor. Soc.*, **136**, 1689-1699.

Kepert, J. D., 2010b: Comparing slab and height-resolving models of the tropical cyclone boundary layer. Part II: Why the simulations differ. *Quart. J. Roy. Meteor. Soc.*, **136**, 1700-1711.

Kepert, J. D., 2012: Choosing a boundary layer parameterization for tropical cyclone modeling. *Mon. Wea. Rev.*, **140**, 1427-1445.

Kepert J.D., and Y. Wang., 2001: The dynamics of boundary layer jets within the tropical cyclone core. Part II; Nonlinear enhancement. *J. Atmos. Sci.*, **58**, 2485-2501.

Kimball, S. K., and Evans J. L., 2002: Idealized simulations of hurricane-trough interaction. *Mon. Wea. Rev.*, **130**, 2210-2227.

Knaff, J. A., J. P. Kossin, and M. DeMaria, 2003: Annular hurricanes. *Wea. Forecasting*, **18**, 204-223.

Korolev, V.S., S. A. Petrichenko, and V. D. Pudov, 1990: Heat and moisture exchange between the ocean and atmosphere in tropical storms Tess and Skip. *Meteor. Gidrol.*, **2**, 108-111. (English translation in Sov. Meteor. Hydrol., 2, 92-94.

Kossin, J. P., and M. D. Eastin, 2001: Two distinct regimes in kinematic and thermodynamic structure of the hurricane eye and eyewall. *J. Atmos. Sci.*, **41**, 1268-1285.

Kossin, J. P., and M. D. Eastin, 2004: Mesovortices in Hurricane Isabel. *Bull. Amer. Meteor. Soc.*, **85**, 151-153.

Kossin, J. P., B. D. McNoldy, and W. H. Schubert, 2002: Vortical swirls in hurricane eye clouds. *Mon. Wea. Rev.*, **130**, 3144-3149.

Kossin J. P., and W. H. Schubert, 2001: Mesovortices, polygonal flow patterns, and rapid pressure falls in hurricane-like vortices. *J. Atmos. Sci.*, **58**, 2196-2209.

Kuo H. C., Williams R. T., and J-H Chen, 1999: A possible mechanism for the eye rotation of typhoon Herb. *J. Atmos. Sci.*, **56**, 1659-1673.

Kwon, Y. C., and W. M. Frank, 2005: Dynamic instabilities of simulated hurricane-like vortices and their impacts on the core structure of hurricanes. Part I: Dry experiments. *J. Atmos. Sci.*, **62**, 3955-3973.

Kwon, Y. C., and W. M. Frank, 2008: Dynamic instabilities of simulated hurricane-like vortices and their impacts on the core structure of hurricanes. Part II: Moist experiments. *J. Atmos. Sci.*, **65**, 106-122.

Lewis, B. M., and D. P. Jorgensen, 1978: Study of the dissipation of Hurricane Gertrude (1974). *Mon. Wea. Rev.*, **106**, 1288-1306.

Li, J., N. E. Davidson, G. D. Hess, and G. Mills, 1997: A high-resolution prediction study of two typhoons at landfall. *Mon. Wea. Rev.*, **125**, 2856-2878.

MacDonald, N. J., 1968: The evidence for the existence of Rossby-like waves in the hurricane vortex. *Tellus*, **20**, 138-150.

Mallen, K. J., Montgomery M. T., and B. Wang, 2005: Re-examining the near-core radial structure of the tropical cyclone primary circulation: Implications for vortex resiliency. *J. Atmos. Sci.*, **62**, 408425.

Marks, F. D., P. G. Black, M. T. Montgomery, and R. W. Burpee, 2008: Structure of the eye and eyewall of Hurricane Hugo (1989). *Mon. Wea. Rev.*, **136**, 1237-1259.

McBride, J. L., and R. Zehr, 1981: Observational analysis of tropical cyclone formation. Part II: Comparison of non-developing versus developing systems. *J. Atmos. Sci.*, **38**, 1132-1151.

McWilliams, J. C., Graves L. P., and M. T. Montgomery, 2003: A formal theory for vortex Rossby waves and vortex evolution. *Geophys. Astrophys. Fluid Dyn.*, **97**, 275309.

Merrill, R. T., 1988a: Characteristics of the upper-tropospheric environmental flow around hurricanes. *J. Atmos. Sci.*, **45**, 1665-1677.

Merrill, R. T., 1988b: Environmental influences on hurricane intensification. *J. Atmos. Sci.*, **45**, 1678-1687.

Miller, B. I., 1958: On the maximum intensity of hurricanes *J. Meteorol.*, **15**, 184-195.

Molinari, J., and D. Vollaro, 1989: External influences on hurricane intensity. Part I: Outflow layer eddy angular momentum fluxes. *J. Atmos. Sci.*, **46**, 1093-1105.

Molinari, J., and D. Vollaro, 1990: External influences on hurricane intensity. Part II: Vertical structure and response of hurricane vortex. *J. Atmos. Sci.*, **47**, 1902-1918.

Molinari, J., Skubis S., and D. Vollaro, 1995: External influences on hurricane intensity. Part III: Potential vorticity structure. *J. Atmos. Sci.*, **52**, 3593-3606.

Molinari, J., Skubis S., Vollaro D., Alsheimer F., and H. E. Willoughby, 1998: Potential vorticity analysis of tropical cyclone intensification. *J. Atmos. Sci.*, **55**, 2632-2644.

Moller, J. D., and M. T. Montgomery, 1999: Vortex Rossby waves and hurricane intensification in a barotropic model. *J. Atmos. Sci.*, **56**, 1674-1687.

Moller, J. D., and M. T. Montgomery, 2000: Tropical cyclone evolution via potential vorticity anomalies in a three-dimensional balance model. *J. Atmos. Sci.*, **57**, 3366-3387.

Moller, J. D., and L. J. Shapiro, 2002: Balanced contributions to the intensification of Hurricane Opal as diagnosed from a GFDL model forecast. *Mon. Wea. Rev.*, **130**, 18661881.

Montgomery, M. T., and B. F. Farrell, 1992: Polar low dynamics. *J. Atmos. Sci.*, **49**, 2484-2505.

Montgomery, M. T., and B. F. Farrell, 1993: Tropical cyclone formation. *J. Atmos. Sci.*, **50**, 285-310.

Montgomery, M. T., and J. Enagonio, 1998: Tropical cyclogenesis via convectively forced vortex Rossby waves in a three-dimensional quasi-geostrophic model. *J. Atmos. Sci.*, **55**, 3176-3207.

Montgomery, M. T., and J. D. Moller, and C. T. Nicklas, 1999: Linear and nonlinear vortex motion in an asymmetric balance shallow water model. *J. Atmos. Sci.*, **56**, 749-768.

Montgomery, M. T., and R. J. Kallenbach, 1997: A theory for vortex Rossby-waves and its application to spiral bands and intensity changes in hurricanes. *Quart. J. Roy. Meteor. Soc.*, **123**, 435-465.

Montgomery, M. T., V. A. Vladimirov, and P. V. Denissenko, 2002: An experimental study on hurricane mesovortices. *J. Fluid. Mech.*, **471**, 132.

Moss, M. S., and F. J. Merceret, 1976. A note on several low-level features of Hurricane Eloise (1975). *Mon. Wea. Rev.*, **104**, 967-971.

Muramatsu T., 1986: The structure of polygonal eye of a typhoon. *J. Meteor. Soc. Japan*, **64**, 913921.

Musgrave, K. D., R. K. Taft, J. L. Vigh, B. D. McNoldy, and W. H. Schubert, 2011: Time evolution of the intensity and size of tropical cyclones. *J. Adv. Model. Earth Syst.*, submitted.

Nolan, D. S., and M. T. Montgomery, 2002: Non-hydrostatic, Three-Dimensional Perturbations to Balanced, Hurricane-like Vortices. Part I: Linearized Formulation, Stability, and Evolution. *J. Atmos. Sci.*, **58**, 2989-3020.

Nolan, D. S., and L. D. Grasso, 2003. Non-hydrostatic, three-dimensional perturbations to hurricane-like vortices. Part II: Symmetric response and nonlinear simulations. *J. Atmos. Sci.*, **60**, 2717-2745.

Orr, W. M., 1907: The stability or instability of the steady motions of a perfect liquid and of a viscous liquid. *Proc. Roy. Irish Acad.*, **A27**, 9-138.

Orville, H. D., and F. I. Kopp, 1977: Numerical simulation of the life history of a hailstorm. *J. Atmos. Sci.*, **34**, 1596-1618.

Persing, J., and M. T. Montgomery, 2003: Hurricane superintensity. *J. Atmos. Sci.*, **60**, 2349-2371.

Pfeffer, R. L. 1958: Concerning the mechanism of hurricanes. *J. Meteorol.*, **15**, 113-120.

Pfeffer, R. L., and M. Challa, 1981: A numerical study of the role of eddy fluxes of momentum in the development of Atlantic hurricanes. *J. Atmos. Sci.*, **38**, 2392-2398.

Pfeffer R. L., and M. Challa, 1992: The role of environmental asymmetries in Atlantic hurricane formation. *J. Atmos. Sci.*, **49**, 1170-1178.

Powell, M.D., P. J. Vickery, and T. A. Reinhold, 2003: Reduced drag coefficient for high wind speeds in tropical cyclones. *Nature*, **422**, 279-283.

Reasor P. D., M. T. Montgomery, F. D. Marks Jr, and J. F. Gamache, 2000: Low-wavenumber structure and evolution of the hurricane inner core observed by airborne Daul-Doppler radar. *Mon. Wea. Rev.*, **128**, 1653-1680.

Reasor, P. D., and M. T. Montgomery, 2001: Three-dimensional alignment and corotation of weak TC-like vortices via linear vortex Rossby waves. *J. Atmos. Sci.*, **58**, 2306-2330.

Reasor, P. D., F. D. Marks, and L. D. Grasso, 2004: A new look at the problem of tropical cyclones in vertical shear flow: Vortex resiliency. *J. Atmos. Sci.*, **61**, 3-22.

Reasor, P. D., M. D. Eastin, and J. F. Gamache, 2009: Rapidly intensifying Hurricane Guillermo (1997). Part I: Low-wavenumber structure and evolution. *Mon. Wea. Rev.*, **137**, 603-631.

Riehl, H. 1950: A model of hurricane formation. *J. Appl. Phys.*, **21**, 917-925.

Riemer, M., M. T. Montgomery, and M. E. Nicholls, 2010: A new paradigm for intensity modification of tropical cyclones: thermodynamic impact of vertical wind shear on the inflow layer. *Atmos. Chem. Phys.*, **10**, 3163-3188.

Rotunno, R., and K. A. Emanuel, 1987: An air-sea interaction theory for tropical cyclones. Part II: Evolutionary study using a nonhydrostatic axisymmetric numerical model. *J. Atmos. Sci.*, **44**, 542-561.

Rozoff, C. M., J. P. Kossin, W. H. Schubert, and P. J. Mulero, 2009: Internal control of hurricane intensity variability: the dual nature of PV mixing. *J. Atmos. Sci.*, **66**, 133-147.

Rutherford, B., G. Danglemayr, J. Persing, W. H. Schubert, and M. T. Montgomery, 2009: Advective mixing in a nondivergent barotropic model. *Atmos. Chem. Phys.*, **9**, 16085-16129.

Samsury, C. E., and E. J. Zipser, 1995: Secondary wind maxima in hurricanes: Airflow and relationship to rainbands. *Mon. Wea. Rev.*, **123**, 3502-3517.

Shapiro, L. J., 1983: The asymmetric boundary layer flow under a translating hurricane. *J. Atmos. Sci.*, 40, 1984-1998.

Shapiro, L. J. and M. T. Montgomery, 1993: A three-dimensional balance theory for rapidly rotating vortices. *J. Atmos. Sci.*, **56**, 1197-1223.

Schecter, D. A., and M. T. Montgomery, 2003: On the symmetrization rate of an intense geophysical vortex. *Dyn. Atmos. Oceans*, **37**, 55-88.

Schecter, D. A., and M. T. Montgomery, 2004: Damping and pumping of a vortex Rossby wave in a monotonic cyclone: Critical layer stirring versus inertia-buoyancy wave emission. *Phys. Fluids*, **16**, 1334-1348.

Schecter, D. A., M. T. Montgomery, and P. D. Reasor, 2002: A theory for the vertical alignment of a quasigeostrophic vortex. *J. Atmos. Sci*, **59**, 150-168.

Schecter, D. A., and M. T. Montgomery, 2007: Waves in a cloudy vortex. *J. Atmos. Sci.*, **64**, 314-337.

Schubert W. H., Montgomery M. T., Taft R. K., Guinn T. A., Fulton S. R., Kossin J. P., and J. P. Edwards, 1999: Polygonal eyewalls, asymmetric eye contraction, and potential vorticity mixing in hurricanes. *J. Atmos. Sci.*, **56**, 1197-1223.

Shi J. J., Chang S. W., and S. Raman, 1990: A numerical study of the outflow layer of the tropical cyclone. *Mon. Wea. Rev.*, **118**, 20422055.

Shi J. J., Chang S. W., and S. Raman, 1997: Interaction between Hurricane Florence (1988) and an upper-tropospheric westerly trough. *J. Atmos. Sci.*, **54**, 12311247.

Smith, R. K., 1990: A numerical study of tropical cyclone motion using a barotropic model I: The role of vortex asymmetries. *Quart. J. Roy. Meteor. Soc.*, **116**, 337-362.

Smith, R. K., 2003: A simple model of the hurricane boundary layer. *Quart. J. Roy. Meteor. Soc.*, **129**, 1007-1027.

Smith, R. K., and M. T. Montgomery, 2008: Balanced boundary layers used in hurricane models. *Quart. J. Roy. Meteor. Soc*., **134**, 1385-1395.

Smith, R. K., and S. Vogl, 2008: A simple model of the hurricane boundary layer revisited. *Quart. J. Roy. Meteor. Soc.*, **134**, 337-351.

Thomson, W. W., 1887: Stability of fluid motion: Rectilinear motion of viscous fluid between two parallel plates. *Philos. Mag.*, **24**, 188-196.

Wang, Y., 2001: An explicit simulation of tropical cyclones with a triply nested movable mesh primitive equation model: TCM3. Part I: Model description and control experiment. *Mon. Wea. Rev.*, **129**, 1370-1394.

Wang, Y., 2002a: Vortex Rossby waves in a numerically simulated tropical cyclone. Part I: Overall structure, potential vorticity, and kinetic energy budgets. *J. Atmos. Sci.*, **59**, 1213-1238.

Wang, Y., 2002b: Vortex Rossby waves in a numerically simulated tropical cyclone. Part II: The role in tropical cyclone structure and intensity change. *J. Atmos. Sci.*, **59**, 1239-1262.

Wang, Y., 2008: How do spiral rain bands affect tropical cyclone structure and intensity? *J. Atmos. Sci.*, **66**, 12501273.

Wang, J., H. L. Cole, D. J. Carlson, E. R. Miller, K. Beierle, A. Paukkunen, and T. K. Laine, 2002: Corrections of humidity measurements errors from the Vaisala RS80 Radiosonde – Application to TOGA COARE data. *J. Atmos. Oceanic Technol.*, **19**, 981-1002.

Wang, Y., and G. Holland, 1995: On the interaction of tropical-cyclone scale vortices. IV: Baroclinic vortices. *Q. J. R. Meteorol. Soc.*, **121**, 95-126.

Wang, Y., and G. Holland, 1996: Tropical cyclone motion and evolution in vertical shear. *J. Atmos. Sci.*, **53**, 3313-3332.

Whitman, G. B., 1974: Linear and Nonlinear Waves. Wiley, New York.

Willoughby, H. E., J. A. Clos, and M. G. Shoreibah, 1982: Concentric eyewalls, secondary wind maxima, and the evolution of the hurricane vortex. *J. Atmos. Sci.*, **39**, 395411.

Wilson, K.J., 1979: Characteristics of the subcloud layer wind structure in tropical cyclones. Extended Abstracts, *Int. Conf. on Tropical Cyclones*, Perth, Australia, Roy. Meteor. Soc. (Australian Branch), 15II.

Wu, L., S. A. Braun, J. Halverson, and G. Heymsfield, 2006: A numerical study of Hurricane Erin (2001). Part I: Model verification and storm evolution. *J. Atmos. Sci.*, **63**, 65-86.

Yanai, M. 1968: Evolution of a tropical disturbance in the Caribbean Sea region. *J. Meteorol. Soc. Japan*, **46**, 86-108.

Yanai, M., S. Esbensen, and J. H. Chu, 1973: Determination of bulk properties of tropical cloud clusters from large-scale heat and moisture budgets. *J. Atmos. Sci.*, **30**, 611-627.

Yang, B., Y. Wang, and B. Wang, 2007: The effect of internally generated inner-core asymmetries on tropical cyclone potential intensity. *J. Atmos. Sci.*, **64**, 1165-1188.

Appendix A

3D HYDROSTATIC PRIMITIVE EQUATIONS IN ISENTROPIC COORDINATES

As stated in Chapter 2, the governing equations for this model are

$$\frac{Du}{Dt} = fv - \frac{\partial M}{\partial x}, \tag{A.1}$$

$$\frac{Dv}{Dt} = -fu - \frac{\partial M}{\partial y}, \tag{A.2}$$

$$\frac{\partial \sigma}{\partial t} + \frac{\partial(\sigma u)}{\partial x} + \frac{\partial(\sigma v)}{\partial y} + \frac{\partial(\sigma \dot{\theta})}{\partial \theta} = 0, \tag{A.3}$$

$$\frac{\partial M}{\partial \theta} = \Pi. \tag{A.4}$$

where $D/Dt = u\partial/\partial x + v\partial/\partial y + \dot{\theta}\partial/\partial\theta$. The model is horizontally staggered using the Arakawa C grid. We recognize that the horizontal advection terms play an important role in translating distances throughout the domain. Insufficient numerical resolution of these terms leads to phase errors which can significantly distort the smaller scale features of a simulation. For this reason, we seek to reduce these errors by approximating the horizontal advection terms with fifth-order finite differences. Although the horizontal fifth-order differences do not insure numerical conservation of certain second-order quantities (such as enstrophy), we feel that they are desirable because of the increase in numerical accuracy and the small implicit diffusion which they provide. For this model, we use a uniform grid spacing of 1.5 km over a square domain of 300 km by 300 km.

The model is vertically discretized using the conventions of Hsu and Arakawa (1990). The vertical grid is defined with a layer index *l* between two half-layer indices *l* + 1/2 and *l* - 1/2. The layers and half layers are indexed from the top of the atmosphere (*l* = 1/2) to the surface (*l* = L + 1/2). For our model, we use 5 vertical layers: $\theta = 304, 316, 328, 341, 353$ K. The half-layer potential temperature values are specified. The layer potential temperature values are computed using $\theta_l = \sqrt{\theta_{l+1/2}\theta_{l-1/2}}$ if $p_{1/2} \neq 0$ and $\theta_l = (1+\kappa)\theta_{l+1/2}$ if $p_{1/2} = 0$. For this model, the prognostic variables *u*, *v*, σ are carried on integer layers, whereas pressure and potential temperature are carried on the half-integer levels. The vertical discrete model is given as:

$$\frac{\partial u_l}{\partial t} = -u_l\frac{\partial u_l}{\partial x} - v_l\frac{\partial u_l}{\partial y} - \frac{1}{\sigma_l}\left[(\sigma\dot{\theta})_{l-1/2}\frac{u_{l-1/2}-u_l}{\theta_{l-1/2}-\theta_l} + (\sigma\dot{\theta})_{l+1/2}\frac{u_l-u_{l+1/2}}{\theta_l-\theta_{l+1/2}}\right] + fv_l - \frac{\partial M_l}{\partial x} \quad \text{(A.5)}$$

$$\frac{\partial v_l}{\partial t} = -u_l\frac{\partial v_l}{\partial x} - v_l\frac{\partial v_l}{\partial y} - \frac{1}{\sigma_l}\left[(\sigma\dot{\theta})_{l-1/2}\frac{v_{l-1/2}-v_l}{\theta_{l-1/2}-\theta_l} + (\sigma\dot{\theta})_{l+1/2}\frac{v_l-v_{l+1/2}}{\theta_l-\theta_{l+1/2}}\right] - fu_l - \frac{\partial M_l}{\partial y} \quad \text{(A.6)}$$

$$\frac{\partial \sigma_l}{\partial t} = -\frac{\partial(\sigma_l u_l)}{\partial x} - \frac{\partial(\sigma_l v_l)}{\partial y} - \frac{(\sigma\dot{\theta})_{l-1/2} - (\sigma\dot{\theta})_{l+1/2}}{\theta_{l-1/2}-\theta_{l+1/2}} \quad \text{(A.7)}$$

$$\dot{\theta}_{l+1/2} = \frac{Q_{l+1/2}}{\Pi_{l+1/2}} \quad \text{(A.8)}$$

$$M_L - \Phi_s = \theta_L \Pi_{L+1/2} \quad \text{(A.9)}$$

$$\frac{M_l - M_{l+1}}{\theta_l - \theta_{l+1}} = \Pi_{l+1/2} \quad \text{(A.10)}$$

The model is discretized in time using the third-order Adams-Bashforth scheme with a 1 second time step. The model is initialized by specifying $u(x, y, \theta)$ and $v(x, y, \theta)$. After the wind field is specified, one can obtain the mass field by the nonlinear balance equation and the hydrostatic equation. In isentropic coordinates, the nonlinear balance and hydrostatic equations are

$$2\left[\frac{\partial^2\psi}{\partial x^2}\frac{\partial^2\psi}{\partial y^2}-\left(\frac{\partial^2\psi}{\partial x\partial y}\right)^2\right]+f\left(\frac{\partial^2\psi}{\partial x^2}+\frac{\partial^2\psi}{\partial y^2}\right)=\nabla^2 M, \tag{A.11}$$

$$\frac{\partial M}{\partial\theta}=\Pi, \tag{A.12}$$

where $u = -\partial\psi/\partial y$ and $v = \partial\psi/\partial x$. Equations (A.10) and (A.11) can be solved to obtain the balanced Montgomery potential. Knowing $M(x, y, \theta)$, the corresponding balanced mass field, $m(x, y, \theta$, is obtained by

$$\sigma=-\frac{p}{\kappa\Pi}\frac{\partial^2 M}{\partial\theta^2}. \tag{A.13}$$

This model includes a sponge layer at the lateral boundaries. The sponge layer is necessary to damp outward propagating internal gravity eaves excited in the domain interior, especially in light of the periodic boundary condition.

Appendix B

3D HYDROSTATIC PRIMITIVE EQUATIONS IN SIGMA COORDINATES

As stated in Chapter 3, the governing equations for this model are

$$\frac{Du}{Dt} = fv - \frac{\partial \Phi}{\partial x} - \frac{RT\sigma}{p}\frac{\partial p_\star}{\partial x} + F_u, \tag{B.1}$$

$$\frac{Dv}{Dt} = -fu - \frac{\partial \Phi}{\partial y} - \frac{RT\sigma}{p}\frac{\partial p_\star}{\partial y} + F_v, \tag{B.2}$$

$$\frac{D\theta}{Dt} = S_\theta + F_\theta, \tag{B.3}$$

$$\frac{\partial p_\star}{\partial t} = -\int_0^1 \left(\frac{\partial u p_\star}{\partial x} + \frac{\partial v p_\star}{\partial y}\right) d\sigma, \tag{B.4}$$

$$p_\star \dot{\sigma} = \sigma \frac{\partial p_\star}{\partial t} - \int_0^\sigma \left(\frac{\partial u p_\star}{\partial x} + \frac{\partial v p_\star}{\partial y}\right) d\sigma, \tag{B.5}$$

$$\frac{\partial \Phi}{\partial \sigma} = -\frac{RTp_\star}{p}. \tag{B.6}$$

The subgrid-scale vertical diffusion of momentum and heat is estimated by the neutral version of the turbulence closure model derived by Louis et al. (1982). The vertical fluxes are expressed by

$$\tau = K_M \frac{\partial \mathbf{v}}{\partial z}, \tag{B.7}$$

$$H = K_H \frac{\partial \theta}{\partial z}, \tag{B.8}$$

where

$$K_M = l^2 \left| \frac{\partial \mathbf{U}}{\partial z} \right|, \tag{B.9}$$

$$K_M = l^2 \left| \frac{\partial \mathbf{U}}{\partial z} \right|. \tag{B.10}$$

where the mixing length l is calculated using Blackadar's (1962) formula. For the air-sea interaction, we use the standard bulk aerodynamic formulation

$$(\tau_{\mathbf{v}}, H) = \rho_s C_D |\mathbf{V}| (\mathbf{V}, \theta - \theta_s), \tag{B.11}$$

where

$$C_D = 10^{-3} \begin{cases} 2.70/U + 0.142 + 0.0764U & U \leq 25 \\ 2.16 + 0.5406\big[1 - \exp\big(-\dfrac{U-25}{7.5}\big)\big] & U \geq 25 \end{cases} \tag{B.12}$$

where U is the total wind speed. The source term, S_θ, for potential temperature comes through the specified diabatic forcing. The model is horizontally staggered using the Arakawa C grid on a doubly periodic horizontal domain of 450 km by 450 km with a grid spacing of 1.5 km. To avoid the reflection of internal gravity waves, a sponge layer is applied to the model. A third order Adams-Bashforth explicit scheme is used for the time discretization for the prognostic equations. Because this primitive equation model allows rapidly propagating Lamb waves and uses an explicit time differencing scheme, the CFL condition requires a small time step. The model simulations here used a time step of 1.5 s. The model is vertically discretized using the method of Arakawa and Konor (1996). The model is vertically discretized on 7 even σ-layers with $d\sigma = 1/7$. The vertical boundary conditions are $\dot{\sigma} = 0$ on $\sigma = 0, 1$.

The model is initialized based on the balance initialization from Sundqvist (1975) and Kurihara and Bender (1980). The model determines $\theta(x, y, \sigma)$ and $p_s(x, y)$ by specifying $u(x, y, \sigma)$ and $v(x, y, \sigma)$. The nonlinear balance equation is sigma coordinates is:

$$2\left[\frac{\partial^2\psi}{\partial x^2}\frac{\partial^2\psi}{\partial y^2} - \left(\frac{\partial^2\psi}{\partial x \partial y}\right)^2\right] + f\nabla^2\psi = \nabla^2\Phi + \nabla\cdot(\sigma\alpha\nabla p_s), \tag{B.13}$$

where $\alpha = RT/p$ and ψ is the streamfunction. This equation is solved by an overrelaxation method by first solving for p_s at $\sigma = 1$ assuming a surface temperature field and then solving for Φ and α at $\sigma < 1$.

Appendix C

3D HYDROSTATIC BOUNDARY LAYER MODEL

As stated in Chapter 5, the governing equations for this model are

$$\frac{Du}{Dt} = fv - c_p\theta_v\frac{\partial \Pi}{\partial x} + D_u + F_u \tag{C.1}$$

$$\frac{Dv}{Dt} = -fu - c_p\theta_v\frac{\partial \Pi}{\partial y} + D_v + F_v \tag{C.2}$$

$$\frac{D\theta}{Dt} = D_\theta + F_\theta \tag{C.3}$$

$$\frac{\partial \Pi}{\partial z} = -\frac{g}{c_p\theta} \tag{C.4}$$

$$\frac{\partial u}{\partial x} + \frac{\partial v}{\partial y} + \frac{\partial w}{\partial z} = 0 \tag{C.5}$$

The model is horizontally unstaggered on a doubly periodic horizontal domain of 500 km by 500 km with a grid spacing of 1 km using fourth-order advection. To avoid nonlinear instability, fourth order hyperdiffusion is applied to each prognostic equation and to avoid the reflection of internal gravity waves, a sponge layer is applied to the model. The model is vertically staggered on a Lorenz grid, where horizontal velocity and potential temperature are vertically staggered with vertical velocity and vertical turbulent fluxes. In this model, we have vertical grid spacing of 250 m, leading

to 6 vertical layers in the model. A third order Adams-Bashforth scheme is used for the time discretization for the governing equations.

The subgrid-scale horizontal diffusion, D_X, is treated by the nonlinear viscosity scheme given by Smagorinsky (1963). Based on computational resources and the recommendation from Kepert (2012), the subgrid-scale vertical diffusion of momentum and heat is estimated by the turbulence closure model derived by Louis et al. (1982). The vertical fluxes are expressed by

$$\tau = K_M \frac{\partial \mathbf{v}}{\partial z}, \tag{C.6}$$

$$H = K_H \frac{\partial \theta}{\partial z}, \tag{C.7}$$

where

$$K_M = l^2 F_M \left| \frac{\partial \mathbf{U}}{\partial z} \right|, \tag{C.8}$$

$$K_M = l^2 F_H \left| \frac{\partial \mathbf{U}}{\partial z} \right|. \tag{C.9}$$

where the mixing length l is calculated using Blackadar's (1962) formula. The stability functions, F_M and F_H, are given by

$$F_M = \begin{cases} 1 - \dfrac{10Ri}{1 + C_h\sqrt{-Ri}} & Ri < 0 \\ \dfrac{1}{1 + 10Ri\sqrt{1 + 5Ri}} & Ri > 0 \end{cases} \tag{C.10}$$

$$F_H = \begin{cases} 1 - \dfrac{15Ri}{1 + C_h\sqrt{-Ri}} & Ri < 0 \\ \dfrac{1}{1 + 15Ri\sqrt{1 + 5Ri}} & Ri > 0 \end{cases} \tag{C.11}$$

where $C_h = l^2/3z^2$ and Ri is the Richardson number. For the air-sea interaction, we use the standard bulk aerodynamic formulation

$$(\tau_{\mathbf{v}}, H) = \rho_s C_D |\mathbf{V}|(\mathbf{V}, \theta - \theta_s), \tag{C.12}$$

where

$$C_D = 10^{-3} \begin{cases} 2.70/U + 0.142 + 0.0764U & U \leq 25 \\ 2.16 + 0.5406\big[1 - \exp\big(-\dfrac{U-25}{7.5}\big)\big] & U \geq 25 \end{cases} \tag{C.13}$$

where *U* is the 10-m total wind speed.